QUANTUM MECHANICAL ORIGIN OF THE PLASMONIC PROPERTIES OF NOBLE METAL NANOPARTICLES

by

EMILIE BRIGITTE GUIDEZ

B.S., University of Geneva, 2008

AN ABSTRACT OF A DISSERTATION

submitted in partial fulfillment of the requirements for the degree

DOCTOR OF PHILOSOPHY

Department of Chemistry
College of Arts and Sciences

KANSAS STATE UNIVERSITY
Manhattan, Kansas

2014

Abstract

Small silver and gold clusters (< 2 nm) display a discrete absorption spectrum characteristic of molecular systems whereas larger particles display a strong, broad absorption band in the visible. The latter feature is due to the surface plasmon resonance, which is commonly explained by the collective dipolar motion of free electrons across the particle, creating charged surface states. The evolution between molecular properties and plasmon is investigated. Time-dependent density functional theory (TDDFT) calculations are performed to study the absorption spectrum of cluster-size silver and gold nanorods. The absorption spectrum of these silver nanorods exhibits high-intensity longitudinal and transverse modes (along the long and short axis of the nanorod respectively), similar to the plasmons observed experimentally for larger nanoparticles. These plasmon modes result from a constructive addition of the dipole moments of nearly degenerate single-particle excitations. The number of single-particle transitions involved increases with increasing system size, due to the growing density of states available. Gold nanorods exhibit a broader absorption spectrum than their silver counterpart due to enhanced relativistic effects, affecting the onset of the longitudinal plasmon mode.

The high-energy, high-intensity beta-peak of acenes also results from a constructive addition of single-particle transitions and I show that it can be assigned to a plasmon. I also show that the plasmon modes of both acenes and metallic nanoparticles can be described with a simple configuration interaction (CI) interpretation.

The evolution between molecular absorption spectrum and plasmon is also investigated by computing the density of states of spherical thiolate-protected gold clusters using a charge-perturbed particle-in-a-sphere model. The electronic structure obtained with this model gives good qualitative agreement with DFT calculations at a fraction of the cost. The progressive increase of the density of states with particle size observed is in accordance with the appearance of a plasmon peak.

The optical properties of nanoparticles can be tuned by varying their composition. Therefore, the optical behavior of the bimetallic $Au_{25-n}Ag_n(SH)_{18}^-$ cluster for different values of n using TDDFT is analyzed. A large blue shift of the HOMO-LUMO absorption peak is observed with increasing silver content, in accordance with experimental results.

QUANTUM MECHANICAL ORIGIN OF THE PLASMONIC PROPERTIES OF NOBLE METAL NANOPARTICLES

by

EMILIE BRIGITTE GUIDEZ

B.S., University of Geneva, 2008

A DISSERTATION

submitted in partial fulfillment of the requirements for the degree

DOCTOR OF PHILOSOPHY

Department of Chemistry
College of Arts and Sciences

KANSAS STATE UNIVERSITY
Manhattan, Kansas

2014

Approved by:

Major Professor
Christine M. Aikens

Copyright

EMILIE BRIGITTE GUIDEZ

2014

Abstract

Small silver and gold clusters (< 2 nm) display a discrete absorption spectrum characteristic of molecular systems whereas larger particles display a strong, broad absorption band in the visible. The latter feature is due to the surface plasmon resonance, which is commonly explained by the collective dipolar motion of free electrons across the particle, creating charged surface states. The evolution between molecular properties and plasmon is investigated. Time-dependent density functional theory (TDDFT) calculations are performed to study the absorption spectrum of cluster-size silver and gold nanorods. The absorption spectrum of these silver nanorods exhibits high-intensity longitudinal and transverse modes (along the long and short axis of the nanorod respectively), similar to the plasmons observed experimentally for larger nanoparticles. These plasmon modes result from a constructive addition of the dipole moments of nearly degenerate single-particle excitations. The number of single-particle transitions involved increases with increasing system size, due to the growing density of states available. Gold nanorods exhibit a broader absorption spectrum than their silver counterpart due to enhanced relativistic effects, affecting the onset of the longitudinal plasmon mode.

The high-energy, high-intensity beta-peak of acenes also results from a constructive addition of single-particle transitions and I show that it can be assigned to a plasmon. I also show that the plasmon modes of both acenes and metallic nanoparticles can be described with a simple configuration interaction (CI) interpretation.

The evolution between molecular absorption spectrum and plasmon is also investigated by computing the density of states of spherical thiolate-protected gold clusters using a charge-perturbed particle-in-a-sphere model. The electronic structure obtained with this model gives good qualitative agreement with DFT calculations at a fraction of the cost. The progressive increase of the density of states with particle size observed is in accordance with the appearance of a plasmon peak.

The optical properties of nanoparticles can be tuned by varying their composition. Therefore, the optical behavior of the bimetallic $Au_{25-n}Ag_n(SH)_{18}^-$ cluster for different values of n using TDDFT is analyzed. A large blue shift of the HOMO-LUMO absorption peak is observed with increasing silver content, in accordance with experimental results.

Table of Contents

List of Figures xi

List of Tables xvi

Acknowledgements xxii

Dedication xxiii

Chapter 1 - Introduction 1

- Plasmons in noble metal nanoparticles 1
- Theoretical modeling of plasmons in noble metal nanoparticles 2
    - Classical electromagnetic theory 2
    - First principle calculations on silver and gold nanoparticles 4
        - Spherical ligand-protected clusters 4
        - Elongated noble metal clusters 6
- Objectives and overview of the thesis 7

Chapter 2 - Theory and computational methods 9

- Theory of quantum mechanics 9
    - The Schrödinger equation 9
    - The Born-Oppenheimer approximation 10
    - Relativistic effects 12
- Computational methods 13
    - Density functional theory (DFT) 13
        - The Hohenberg-Kohn theorem 13
        - The Kohn-Sham (KS) method 14
        - Construction of the molecular orbitals. 17
    - Relativistic effects: The zeroth order regular approximations (ZORA) 18
    - Time-dependent density functional theory (TDDFT) 19
        - The Runge-Gross theorem 19
        - The time-dependent Kohn-Sham equations 19
        - Time-dependent density function response theory (TD-DFRT) 21
    - Configuration interaction 23

Chapter 3 - Theoretical analysis of the optical excitation spectra of silver and gold nanowires.. 25

  - Abstract 25
  - Introduction 25
  - Computational details 26
  - Results and discussion 27
    - Silver nanowires 27
      - Neutral nanowires 27
      - Positively and negatively charged nanowires 34
    - Gold nanowires 34
      - Neutral gold nanowires 35
      - Positively and negatively charged nanowires 40
  - Conclusions 41
  - Acknowledgements 41

Chapter 4 - Diameter-Dependence of the Excitation Spectra of Silver and Gold Nanorods

- Chapter 4 - Diameter-Dependence of the Excitation Spectra of Silver and Gold Nanorods 42
  - Abstract 42
  - Introduction 43
  - Computational methods 44
  - Results and discussion 45
    - Silver nanorods 45
    - Analysis of the longitudinal peak 50
    - Analysis of the transverse peak 52
    - Analysis of the Ag_{71}^{-3} spectrum 52
    - Gold nanorods 57
    - Analysis of the Au_{71}^{-3} nanorod 61
  - Conclusions 63
  - Acknowledgements 65
- Chapter 5 - Origin and TDDFT Benchmarking of the Plasmon Resonance in Acenes 66
  - Abstract 66
  - Introduction 67
  - Computational methods 69
  - Results and discussion 69
    - Theoretical explanation of plasmon resonance in acenes 69

Single-particle versus plasmonic character of the p-band ... 76
Benchmarking of exchange-correlation functionals ... 77
Conclusions ... 83
Acknowledgements ... 84
Chapter 6 - Plasmon Resonance Analysis with Configuration Interaction ... 86
Abstract ... 86
Introduction ... 86
Methods ... 88
Results and discussion ... 89
Case 1: Ideal case. ... 89
Case 2: Vary α_1 only. ... 91
Case 3: Vary α_1 and α_3. ... 94
Case 4: Vary β_{12} only. ... 96
Case 5: Vary β_{12} and β_{23} ... 98
Case 6: Varying the β/α ratio. ... 99
Case 7: Mixed-coupling systems. ... 101
Conclusions ... 102
Acknowledgements ... 103
Chapter 7 - Development of a charge-perturbed particle-in-a-sphere model for nanoparticle electronic structure ... 105
Abstract ... 105
Introduction ... 105
Method ... 106
Computational details ... 108
Description of the model systems ... 108
Test cases ... 108
$Au_{25}(SR)_{18}^-$ ... 110
$Au_{102}(SR)_{44}$ ... 110
$Au_{144}(SR)_{60}$ ... 111
3nm nanoparticle ... 112
Results and discussion ... 113

Test cases 113

$Au_{25}(SR)_{18}^{-}$ 115

$Au_{102}(SR)_{44}$ 117

$Au_{144}(SR)_{60}$ 119

Comparison between the PIS model and DFT electronic structures for the optimized structure (Cases A and B). 120

Comparison between the DFT optimized structure and uniformly spread perturbations (Cases A and C). 123

3 nm NP 123

Final considerations 125

Conclusions.. 125

Acknowledgement 126

Chapter 8 - Applications of the configuration interaction interpretation and extension to large nanoparticles 127

Introduction.. 127

Applications of the CI interpretation 127

Application of the CI interpretation to the nanowire Ag_6.. 128

Application of the CI interpretation to the nanorod Ag_{71}^{-3} 130

Application of the CI interpretation to the tetrahedral cluster Ag_{20}.............................. 132

Discussion: Extension of the CI interpretation to large nanoparticles.............................. 135

Chapter 9 - Effects of Silver Doping on the Geometric and Electronic Structure and Optical Absorption Spectra of the $Au_{25-n}Ag_n(SH)_{18}^{-}$ (n = 1, 2, 4, 6, 8, 10, 12) Bimetallic Nanoclusters 136

Abstract.. 136

Introduction.. 136

Computational details 138

Results and discussion 139

$Au_{24}Ag(SH)_{18}^{-}$.. 139

$Au_{23}Ag_2(SH)_{18}^{-}$ 144

$Au_{25-n}Ag_n(SH)_{18}^{-}$ (n=4, 6, 8, 10) 147

$Au_{13}Ag_{12}(SH)_{18}^{-}$ 151

Conclusions 152

Acknowledgements 153

Chapter 10 - Conclusions 154

References 156

Appendix A - Supporting information for “Theoretical analysis of the optical excitation spectra of silver and gold nanowires” 176

Appendix B - Supporting information for “Diameter-Dependence of the Excitation spectra of Silver and Gold Nanorods” 197

Appendix C - Supporting information for “Origin and TDDFT Benchmarking of the Plasmon Resonance in Acenes” 213

Appendix D - Supporting information for “Plasmon Resonance Analysis with Configuration Interaction” 214

Appendix E - Supporting Information for “Development of a charge-perturbed particle-in-a-sphere model for nanoparticle electronic structure” 238

Appendix F - Supporting information for “Effects of Silver Doping on the Geometric and Electronic Structure and Optical Absorption Spectra of the $Au_{25-n}Ag_n(SH)_{18}^-$ (n = 1, 2, 4, 6, 8, 10, 12) Bimetallic Nanoclusters” 239

List of Figures

Figure 1-1. Collective electron oscillation under electromagnetic radiation in spherical noble metal nanoparticles. 1

Figure 1-2. Structure of the thiol-protected $Au_{25}(SR)_{18}^{-}$ cluster. 5

Figure 1-3. A) Electronic structure and B) theoretical absorption spectrum of the $Au_{25}(SH)_{18}^{-}$ cluster. 6

Figure 3-1. Excitation spectra of A) Ag_{20} nanowire and B) Ag_{40} nanowire at the SAOP/DZ level of theory. 27

Figure 3-2. Longitudinal and transverse peak wavelengths (nm) for A) neutral B) positively charged and C) negatively charged silver nanowires. 28

Figure 3-3. Kohn-Sham orbital energy diagram of Ag_6 at the BP86/DZ level of theory. 29

Figure 3-4. Oscillator strength* of A) the longitudinal peak of silver nanowires with SAOP/DZ; B) the transverse peak of silver nanowires with SAOP/DZ; C) the longitudinal peak of silver nanowires with LB94/DZ; D) the transverse peak of silver nanowires with LB94/DZ. 30

Figure 3-5. A) SAOP/DZ excitation spectrum of the Au_{20} nanowire. B) Subset of SAOP/DZ transverse excitation modes for the Au_{20} nanowire. 35

Figure 3-6. Wavelengths of main longitudinal peak for A) neutral B) positively charged and C) negatively charged gold nanowires. 36

Figure 3-7. Weighted average of the HOMO-LUMO transition for A) neutral B) positively charged and C) negatively charged gold nanowires. 37

Figure 3-8. Oscillator strength of the longitudinal transition energy of gold nanowires with A) SAOP/DZ and B) LB94/DZ. 37

Figure 3-9. A) *d*-band of the neutral nanowires starting at a wire length of twelve atoms. B) Density of states of the *d* orbitals of gold nanowires. This data was plotted with SAOP/DZ. 40

Figure 4-1. Side view and end view of A) Ag_9^{+1} nanowire B) Ag_{37}^{+1} small pentagon C) Ag_{73}^{+1} star-shaped silver nanorod and D) Ag_{55}^{+1} large pentagon-shaped nanorod. The length and radius considered for each system are noted L and R respectively. 45

Figure 4-2. Excitation spectra of silver A) nanowires[195] B) small pentagonal nanorods[70] C) star-shaped nanorods and D) large pentagonal nanorods at the LB94/DZ level of theory. 48

Figure 4-3. Longitudinal peak wavelengths of positively charged silver nanorods at the LB94/DZ level of theory. 51

Figure 4-4. Excitation spectra of A) Ag_{71}^{-3} and B) Au_{71}^{-3} at the LB94/DZ level of theory. 52

Figure 4-5. Kohn-Sham orbitals involved in the high intensity transitions for Ag_{71}^{-3} at the LB94/DZ level of theory. Contour value=0.01. 53

Figure 4-6. Excitation spectra of gold A) nanowires[195] B) small pentagonal nanorods C) star-shaped nanorods and D) large pentagonal nanorods at the LB94/DZ level of theory. 57

Figure 4-7. Longitudinal peak wavelengths of positively charged gold nanorods. 60

Figure 4-8. Kohn-Sham orbitals involved in the high intensity transitions for Au_{71}^{-3} at the LB94/DZ level of theory. Contour value= 0.01. 63

Figure 5-1. Linear polycyclic aromatic hydrocarbons (acenes). 67

Figure 5-2. Natural transition orbitals involved in the α and β-peak at the LB94/cc-pVTZ level of theory. 74

Figure 5-3. Edge view and side view of the transition densities for the α- and β-peaks of naphthalene. 75

Figure 5-4. A) β-band B) p-band and C) α-band excitation energies of acenes with two to six rings at various levels of theory. 78

Figure 6-1. A) Peak energies and B) oscillator strengths for different values of α_1 (case 2). 92

Figure 6-2. A) Peak energies and B) oscillator strengths for different values of α_3 (case 3). (α_1=6.0 eV). 94

Figure 6-3. A) Peak energies and B) oscillator strengths for different values of β_{12} (case 4). 97

Figure 6-4. A) Peak energies and B) oscillator strengths for different values of β_{23} (case 5). (β_{12}=0.6 eV) 98

Figure 6-5. A) Peak energies and B) oscillator strengths for different values of $\beta=\beta_{12}=\beta_{13}=\beta_{23}$ and α_1=5.0 eV, α_2=5.1 eV, α_3=5.2 eV (case 6). Inset in A is an enlarged version of the region in the black square. 100

Figure 7-1. Test cases. A) Case 1a: Axial with perturbations aligned along the *z* axis. B) Case 1b: Axial with perturbations along a random axis. C) Case 2: Square planar. D) Case 3:

Octahedral. E) Case 4: Planar with eight perturbations. F) Case 5: Quasi-spherical with 18 perturbations. 109

Figure 7-2. Optimized Xα/TZP.4f structure of the $Au_{25}(SR)_{18}^-$ cluster. 110

Figure 7-3. $Au_{102}(SR)_{44}$ crystal structure. 111

Figure 7-4. A) $Au_{144}(SR)_{60}$ optimized structure. B) Spherically spread out perturbations. 112

Figure 7-5. Perturbations of the 3 nm sphere. A) 96 perturbations. B) 64 perturbations. 113

Figure 7-6. Orbital splitting for the test cases. A) Axial with perturbations along the z axis. B) Axial with perturbations along a random axis. C) Square planar. D) Octahedral. E) Planar with eight perturbations. F) Quasi-spherical with 18 perturbations. The orbital energies are in eV. 115

Figure 7-7. A) $Au_{25}(SR)_{18}^-$ 1P and 1D orbitals and their energies in eV for a 4.2 Å spherical core. B) $Au_{25}(SR)_{18}^-$ 1P and 1D orbital energies in eV for a 3 Å spherical core. 116

Figure 7-8. A) $Au_{102}(SR)_{44}$ density of states spectrum using the PIS model. B) Projected density of states within the gold core region. 118

Figure 7-9. A) $Au_{144}(SR)_{60}$ density of states spectrum using the PIS model. B) Projected density of states within the gold core region. C) $Au_{144}(SR)_{60}$ density of states spectrum using PIS model with uniformly spherically spread out perturbations. 120

Figure 7-10. Density of states spectra using PIS model of a 3 nm nanoparticle with A) 96 and B) 64 S-Au-S units. 124

Figure 9-1. Geometry of the $Au_{24}Ag(SH)_{18}^-$ isomers at the Xα/TZP level of theory. 140

Figure 9-2. Excitation spectra of the A) 1a, B) 1b and C) 1c $Au_{24}Ag(SH)_{18}^-$ isomers at the LB94/TZP level of theory. 143

Figure 9-3. Geometries of the $Au_{23}Ag_2(SH)_{18}^-$ isomers at the Xα/TZP level of theory. 144

Figure 9-4. Excitation spectra of the A) 2a, B) 2b and C) 2c $Au_{23}Ag_2(SH)_{18}^-$ isomers at the LB94/TZP level of theory. 146

Figure 9-5. Frontier orbitals of $Au_{23}Ag_2(SH)_{18}^-$ (2a) at the LB94/TZP level of theory. 147

Figure 9-6. Boltzmann-averaged excitation spectra of $Au_{25-n}Ag_n(SH)_{18}^-$ nanoclusters at the LB94/TZP level of theory. 150

Figure 9-7. Geometry of the $Au_{13}Ag_{12}(SH)_{18}^-$ nanocluster at the Xα/TZP level of theory. 151

Figure 9-8. Excitation spectrum of the $Au_{13}Ag_{12}(SH)_{18}^-$ nanocluster at the LB94/TZP level of theory. 152

Figure A-1. Neutral silver nanowires excitation spectra with SAOP/DZ. 176
Figure A-2. Positively charged silver nanowires excitation spectra with SAOP/DZ. 177
Figure A-3. Negatively charged silver nanowires excitation spectra with SAOP/DZ. 179
Figure A-4. Neutral silver nanowires excitation spectra with LB94/DZ. 181
Figure A-5. Positively chaged silver nanowires excitation spectra with LB94/DZ. 182
Figure A-6. Negatively charged silver nanowires excitation spectra with LB94/DZ. 184
Figure A-7. Neutral gold nanowires excitation spectra with SAOP/DZ. 186
Figure A-8. Positively charged gold nanowires excitation spectra with SAOP/DZ. 188
Figure A-9. Negatively charged gold nanowires excitation spectra with SAOP/DZ. 190
Figure A-10. Neutral gold nanowires excitation spectra with LB94/DZ. 191
Figure A-11. Positively charged gold nanowires excitation spectra with LB94/DZ. 193
Figure A-12. Negatively charged gold nanowires excitation spectra with LB94/DZ. 195
Figure B-1. Excitation spectra of star-shaped silver nanorods at the LB94/DZ level of theory. 197
Figure B-2. Excitation spectra of large pentagon-shaped silver nanorods at the LB94/DZ level of theory. 200
Figure B-3. Excitation spectra of small pentagon-shaped gold nanorods at the LB94/DZ level of theory. 202
Figure B-4. Excitation spectra of star-shaped nanorods at the LB94/DZ level of theory. 206
Figure B-5. Excitation spectra of large pentagon-shaped gold nanorods at the LB94/DZ level of theory. 209
Figure B-6. Longitudinal peak wavelengths of positively charged and negatively charged A) star-shaped and B) large pentagon-shaped silver nanorods. 210
Figure B-7. Kohn-Sham orbitals for the transitions involved in the high intensity longitudinal peak of the small pentagon-shaped nanorods Au_{67}^{+1}. Contour value=0.01. 212
Figure C-1. Natural transition orbitals involved in the α and β-peak at the ωPBEh/cc-pVTZ level of theory. 213
Figure E-1. A) P orbitals of test case 1a and B) P orbitals of test case 1b. Green: Orbitals. Magenta: Point charge perturbations. 238
Figure F-1. Excitation spectrum of $Au_{25}(SH)_{18}^-$ at the LB94/TZP level of theory. 239
Figure F-2. Geometries of the $Au_{21}Ag_4(SH)_{18}^-$ isomers at the Xα/TZP level of theory. 240
Figure F-3. Geometries of the $Au_{19}Ag_6(SH)_{18}^-$ isomers at the Xα/TZP level of theory 240

Figure F-4. Geometries of the $Au_{17}Ag_8(SH)_{18}^-$ isomers at the Xα/TZP level of theory. 241

Figure F-5. Geometries of the $Au_{15}Ag_{10}(SH)_{18}^-$ isomers at the Xα/TZP level of theory. 241

Figure F-6. Excitation spectra of the A) 4a, B) 4b and C) 4c D) 4d E) 4e and F) 4f $Au_{21}Ag_4(SH)_{18}^-$ isomers at the LB94/TZP level of theory. 242

Figure F-7. Excitation spectra of the A) 6a, B) 6b and C) 6c D) 6d E) 6e and F) 6f G) 6g and H) 6h $Au_{19}Ag_6(SH)_{18}^-$ isomers at the LB94/TZP level of theory. 243

Figure F-8. Excitation spectra of the A) 8a, B) 8b and C) 8c D) 8d E) 8e and F) 8f $Au_{17}Ag_8(SH)_{18}^-$ isomers at the LB94/TZP level of theory. 244

Figure F-9. Excitation spectra of the A) 10a, B) 10b and C) 10c $Au_{15}Ag_{10}(SH)_{18}^-$ isomers at the LB94/TZP level of theory. 245

List of Tables

Table 2.1 Jacob's ladder 17

Table 3.1. Transitions contributing to the high-intensity transverse peak in silver nanowires at the SAOP/DZ level of theory. 33

Table 3.2. Transitions with the highest oscillator strength occurring between 6 and 7 eV for the Au_{20} nanowire. 38

Table 3.3. $d\Sigma\rightarrow\Pi$ transitions involved in the transverse band of the Au_{20} nanowire at SAOP/DZ level of theory. 39

Table 4.1. Peak energies and HOMO-LUMO gaps of silver nanowires. 46

Table 4.2. Peak energies and HOMO-LUMO gaps of small positively charged pentagon-shaped silver nanorods. 46

Table 4.3. Peak energies and HOMO-LUMO gaps of positively charged star-shaped silver nanorods. 46

Table 4.4. Peak energies and HOMO-LUMO gaps of large positively charged pentagon-shaped silver nanorods. 47

Table 4.5. Energy, oscillator strength and transitions of the main A_2'' peaks of Ag_{71}^{-3}. 54

Table 4.6. Energy, oscillator strength and transitions of the low intensity A_2'' peaks involving the same transitions as the main A_2'' peaks for Ag_{71}^{-3}. 55

Table 4.7. Energy, oscillator strength and transitions of the main E_1' peaks of Ag_{71}^{-3}. 56

Table 4.8. Longitudinal peak energy and HOMO-LUMO gap of gold nanowires...................... 58

Table 4.9. Longitudinal peak energy and HOMO-LUMO gap of small positively charged pentagon-shaped gold nanorods 58

Table 4.10. Longitudinal peak energy and HOMO-LUMO gap of positively charged star-shaped gold nanorods. 58

Table 4.11. Longitudinal peak energies and HOMO-LUMO gap of large pentagon-shaped gold nanorods. 59

Table 4.12. Energy, oscillator strength and transitions of the main A_2'' peaks of Au_{71}^{-3}. 62

Table 5.1. Excitation energies of α and β peaks of acenes, transitions involved, and their transition dipole moment contributions at the LB94/TZP level of theory. 72

Table 5.2. Transitions with B_{2u} symmetry for naphthalene at the LB94/TZP level of theory...... 76

Table 5.3. TDDFT wavelength of the α-band of acenes with various exchange-correlation functionals. 79

Table 5.4. TDDFT wavelength of the β-band of acenes with various exchange-correlation functionals. 79

Table 5.5. TDDFT wavelength of the p-band of acenes with various exchange-correlation functionals. 80

Table 5.6. Slope of the linear fits from Figure 4 (in nm/ring). 81

Table 5.7. Matrix elements H_{11} and H_{12} of the secular equation 5.2 in eV for acenes with various exchange-correlation functional and cc/pVTZ basis set. 83

Table 6.1. Eigenvectors of matrix (6.5). 89

Table 6.2. Eigenvectors of matrix (6.10). 91

Table 6.3. Eigenvectors of the CI matrix in case 3 where α_3=2.5 eV, α_1=6.0 eV and α_2=5.0 eV. All β values are equal to 0.5 eV. 95

Table 6.4. Eigenvectors of the CI matrix for case 3 where α_3=7.5 eV, α_1=6.0 eV and α_2=5.0 eV. All β values are equal to 0.5 eV. 96

Table 6.5. Excited states energies and oscillator strength for a system with α_1=5.0 eV, α_2=5.1 eV, α_3=5.2 eV, β_{12}=0.5 eV and different values of $\beta_{13}=\beta_{23}$ (case 7). 101

Table 7.1. Energy splitting (eV) of each set of orbitals of the $Au_{102}(SR)_{44}$ nanoparticle. 118

Table 7.2. Band gap energies (eV) of the $Au_{144}(SR)_{60}$ nanoparticle. 121

Table 7.3. Energy splitting (eV) of each set of orbitals of the $Au_{144}(SR)_{60}$ nanoparticle. 122

Table 7.4. Energy spread of each set of orbitals for the 3 nm nanoparticle. 125

Table 8.1. Longitudinal modes of naphthalene at the LB94/TZP level of theory.[273] 128

Table 8.2. Longitudinal (L) and transverse (T) peak energies, oscillator strength and transition densities of the nanowire Ag_6 at the LB94/DZ level of theory. Single-particle states and dipole moments contributing to each peak are also given. 129

Table 8.3. Comparison between TDDFT and CI excitation energies and oscillator strengths for the three excited states in Ag_6 resulting from the combination of the single-particle states $\Sigma_m \rightarrow \Pi_m$ (m=1, 2, 3). 130

Table 8.4. Two longitudinal peak energies, oscillator strength and transition densities of the nanorod Ag_{71}^{-3} at the LB94/DZ level of theory. 132

Table 8.5. Excited state energies, oscillator strength and transition densities of the tetrahedral Ag_{20} cluster at the LB94/TZP level of theory. 133

Table 8.6. Comparison between TDDFT and CI excitation energies and oscillator strengths for the excited states in the tetrahedral cluster $Ag_{20.}$ 134

Table 9.1. Relative energies and HOMO-LUMO gaps of the silver mono-substituted $Au_{24}Ag(SH)_{18}^-$ clusters (eV). 140

Table 9.2. $Au_{25}+n\text{Ag} \rightarrow Au_{25-n}\text{Ag} + n\text{Au}$ reaction energies per silver atom in eV at the Xα/TZP level of theory. 142

Table 9.3. Relative energies and HOMO-LUMO gaps of the silver bi-substituted $Au_{23}Ag_2(SH)_{18}^-$ cluster (eV). 145

Table 9.4. Superatom orbital splitting of the three $Au_{23}Ag_2(SH)_{18}^-$ isomers (eV) at the LB94/TZP level of theory. 146

Table 9.5. Relative energies and HOMO-LUMO gaps of the silver tetra-substituted $Au_{21}Ag_4(SH)_{18}^-$ cluster (eV). 148

Table 9.6. Relative energies and HOMO-LUMO gaps of the $Au_{19}Ag_6(SH)_{18}^-$ cluster (eV). 148

Table 9.7. Relative energies and HOMO-LUMO gaps of the $Au_{17}Ag_8(SH)_{18}^-$ cluster (eV). 149

Table 9.8. Relative energies and HOMO-LUMO gaps of the $Au_{15}Ag_{10}(SH)_{18}^-$ cluster (eV)..... 149

Table B.1. Longitudinal and transverse peak energies of negatively charged star-shaped silver nanorods. 211

Table B.2. Longitudinal and transverse peak energies of negatively charged large pentagon-shaped silver nanorods. 211

Table B.3. Energy, oscillator strength, and transitions involved in the main longitudinal peak of the small pentagon-shaped Au_{67}^{+1} nanorod. 212

Table D.1. Energies and oscillator strengths for varying values of α_1 (case 2). Case 1 is shown in red. 214

Table D.2. Values of T_1 and T_2 for the E_2 peak (case 2). 216

Table D.3. Values of T_1 and T_2 for the E_3 peak (case 2). 216

Table D.4. Eigenvectors of the CI matrix for case 2 where α_1=2.5 eV. 217

Table D.5. Eigenvectors of the CI matrix for case 2 where α_1=3.0 eV. 217

Table D.6. Eigenvectors of the CI matrix for case 2 where α_1=3.5 eV. 217

Table D.7. Eigenvectors of the CI matrix for case 2 where α_1=4.0 eV. 217

Table D.8. Eigenvectors of the CI matrix for case 2 where α_1=4.5 eV. 218

Table D.9. Eigenvectors of the CI matrix for case 2 where α_1=4.75 eV. 218

Table D.10. Eigenvectors of the CI matrix for case 2 where α_1=4.95 eV. 218

Table D.11. Eigenvectors of the CI matrix for case 2 where α_1=5.05 eV. 218

Table D.12. Eigenvectors of the CI matrix for case 2 where α_1=5.25 eV. 219

Table D.13. Eigenvectors of the CI matrix for case 2 where α_1=5.5 eV. 219

Table D.14. Eigenvectors of the CI matrix for case 2 where α_1=6.0 eV. 219

Table D.15. Eigenvectors of the CI matrix for case 2 where α_1=6.5 eV. 219

Table D.16. Eigenvectors of the CI matrix for case 2 where α_1=7 eV. 220

Table D.17. Eigenvectors of the CI matrix for case 2 where α_1=7.5 eV. 220

Table D.18. Energies and oscillator strengths for different values of α_3 (case 3). 220

Table D.19. Eigenvectors of the CI matrix for case 3 where α_3=2.5 eV. 221

Table D.20. Eigenvectors of the CI matrix for case 3 where α_3=3.0 eV. 221

Table D.21. Eigenvectors of the CI matrix for case 3 where α_3=3.5 eV. 221

Table D.22. Eigenvectors of the CI matrix for case 3 where α_3=4.0 eV. 221

Table D.23. Eigenvectors of the CI matrix for case 3 where α_3=4.5 eV. 222

Table D.24. Eigenvectors of the CI matrix for case 3 where α_3=4.75 eV. 222

Table D.25. Eigenvectors of the CI matrix for case 3 where α_3=4.95 eV. 222

Table D.26. Eigenvectors of the CI matrix for case 3 where α_3=5.05 eV. 222

Table D.27. Eigenvectors of the CI matrix for case 3 where α_3=5.25 eV. 223

Table D.28. Eigenvectors of the CI matrix for case 3 where α_3=5.5 eV. 223

Table D.29. Eigenvectors of the CI matrix for case 3 where α_3=6.0 eV. 223

Table D.30. Eigenvectors of the CI matrix for case 3 where α_3=6.5 eV. 223

Table D.31. Eigenvectors of the CI matrix for case 3 where α_3=7 eV. 224

Table D.32. Eigenvectors of the CI matrix for case 3 where α_3=7.5 eV. 224

Table D.33. Energies and oscillator strengths for varying values of β_{12} (case 4)....................... 224

Table D.34. Eigenvectors of the CI matrix for case 4 where β_{12}=0.25 eV. 225

Table D.35. Eigenvectors of the CI matrix for case 4 where β_{12}=0.3 eV. 225

Table D.36. Eigenvectors of the CI matrix for case 4 where β_{12}=0.35 eV. 225

Table D.37. Eigenvectors of the CI matrix for case 4 where β_{12}=0.40 eV. 225

Table D.38. Eigenvectors of the CI matrix for case 4 where β_{12}=0.45 eV. 226

Table D.39. Eigenvectors of the CI matrix for case 4 where β_{12}=0.475 eV. 226
Table D.40. Eigenvectors of the CI matrix for case 4 where β_{12}=0.495 eV. 226
Table D.41. Eigenvectors of the CI matrix for case 4 where β_{12}=0.505 eV. 226
Table D.42. Eigenvectors of the CI matrix for case 4 where β_{12}=0.525 eV. 227
Table D.43. Eigenvectors of the CI matrix for case 4 where β_{12}=0.55 eV. 227
Table D.44. Eigenvectors of the CI matrix for case 4 where β_{12}=0.60 eV. 227
Table D.45. Eigenvectors of the CI matrix for case 4 where β_{12}=0.65 eV. 227
Table D.46. Eigenvectors of the CI matrix for case 4 where β_{12}=0.70 eV. 228
Table D.47. Eigenvectors of the CI matrix for case 4 where β_{12}=0.75 eV. 228
Table D.48. Energies and oscillator strengths for varying values of β_{23} (case 5). 228
Table D.49. Eigenvectors of the CI matrix for case 5 where β_{23}=0.25 eV. 229
Table D.50. Eigenvectors of the CI matrix for case 5 where β_{23}=0.30 eV. 229
Table D.51. Eigenvectors of the CI matrix for case 5 where β_{23}=0.35 eV. 229
Table D.52. Eigenvectors of the CI matrix for case 5 where β_{23}=0.40 eV. 229
Table D.53. Eigenvectors of the CI matrix for case 5 where β_{23}=0.45 eV. 230
Table D.54. Eigenvectors of the CI matrix for case 5 where β_{23}=0.475 eV. 230
Table D.55. Eigenvectors of the CI matrix for case 5 where β_{23}=0.495 eV. 230
Table D.56. Eigenvectors of the CI matrix for case 5 where β_{23}=0.505 eV. 230
Table D.57. Eigenvectors of the CI matrix for case 5 where β_{23}=0.525 eV. 231
Table D.58. Eigenvectors of the CI matrix for case 5 where β_{23}=0.55 eV. 231
Table D.59. Eigenvectors of the CI matrix for case 5 where β_{23}=0.60 eV. 231
Table D.60. Eigenvectors of the CI matrix for case 5 where β_{23}=0.65 eV. 231
Table D.61. Eigenvectors of the CI matrix for case 5 where β_{23}=0.70 eV. 232
Table D.62. Eigenvectors of the CI matrix for case 5 where β_{23}=0.75 eV. 232
Table D.63. Energies and oscillator strengths for varying values of β (case 6). 232
Table D.64. Eigenvectors of the CI matrix for case 6 where β=0. 233
Table D.65. Eigenvectors of the CI matrix for case 6 where β=0.001 eV. 233
Table D.66. Eigenvectors of the CI matrix for case 6 where β=0.005 eV. 233
Table D.67. Eigenvectors of the CI matrix for case 6 where β=0.01 eV. 233
Table D.68. Eigenvectors of the CI matrix for case 6 where β=0.05 eV. 234
Table D.69. Eigenvectors of the CI matrix for case 6 where β=0.10 eV. 234

Table D.70. Eigenvectors of the CI matrix for case 6 where β=0.2 eV. 234

Table D.71. Eigenvectors of the CI matrix for case 6 where β=0.3 eV. 234

Table D.72. Eigenvectors of the CI matrix for case 6 where β=0.4 eV. 235

Table D.73. Eigenvectors of the CI matrix for case 6 where β=0.5 eV. 235

Table D.74. Eigenvectors of the CI matrix for case 6 where β=1.0 eV. 235

Table D.75. Eigenvectors of the CI matrix for case 6 where β=2.0 eV. 235

Table D.76. Eigenvectors of the CI matrix for case 7 where β_{13}= β_{23}=0. 236

Table D.77. Eigenvectors of the CI matrix for case 7 where β_{13}= β_{23}=0.001 eV. 236

Table D.78. Eigenvectors of the CI matrix for case 7 where β_{13}= β_{23}=0.005 eV. 236

Table D.79. Eigenvectors of the CI matrix for case 7 where β_{13}= β_{23}=0.01 eV. 236

Table D.80. Eigenvectors of the CI matrix for case 7 where β_{13}= β_{23}=0.05 eV. 237

Table D.81. Eigenvectors of the CI matrix for case 7 where β_{13}= β_{23}=0.1 eV. 237

Table F.1. $Au_{24}Ag(SH)_{18}^-$ bond lengths calculated at the Xα/TZP level of theory. 239

Table F.2. $Au_{23}Ag_2(SH)_{18}^-$ average bond lengths (in Å) calculated at the Xα/TZP level of theory. 239

Acknowledgements

I would first and foremost like to acknowledge my advisor, Pr. Christine Aikens, for her guidance through the past five years. My grad school research and academic experiences at Kansas State were so wonderful mostly because of her support. I would also like to acknowledge my committee members: Pr. Paul Smith, Pr. Kenneth Klabunde, Pr. Uwe Thumm, Pr. Bin Liu and Pr. James Edgar.

I would also like to thank my group members, past and present, for their support and friendship. I enjoyed working alongside them all. I could not have asked for a better work environment.

I would like to thank all my friends at Kansas State University and in the International Coordinating Council. I am so grateful I had the amazing opportunity to become friend with students from all over the world. My experience at Kansas State would not have been the same without them.

I would also like to thank my boyfriend Yosuke for being there for me through it all.

Finally, I would like to thank Mr. Brichet, my middle school and high school chemistry teacher, for sparking my interest in chemistry.

Dedication

To my boyfriend Yosuke. To my family.

Chapter 1 - Introduction

Plasmons in noble metal nanoparticles

For centuries, gold and silver metals have been considered highly valuable by many civilizations in all continents and used to make jewelry and currency. The reason for the high value of these noble metals is the fact that they are inert and as a result, resistive to degradation by harsh environments. However, when the size of these systems decreases down to the nanometer size regime, they display unique catalytic, electrochemical and optical properties that have attracted a lot of research interest over the past two decades. One of the fascinating aspects of gold and silver nanoparticles is their plasmonic properties.[1-7] Upon excitation with an electromagnetic wave of wavelength λ, these nanoparticles have the unique capability of locally enhancing the electric field at their surface.[8] This phenomenon is explained by the localized surface plasmon resonance (LSPR), which is the collective oscillation of the conduction electrons across the system.[9] The main plasmon mode is the dipolar mode, as shown in Figure 1-1. Higher order modes may occur in large nanoparticles (Radius~ λ) due to retardation effects.[10-12] In this thesis, I will consider systems where the dipole approximation is valid, which means that retardation effects are negligible (Diameter<<λ).

Figure 1-1. Collective electron oscillation under electromagnetic radiation in spherical noble metal nanoparticles.

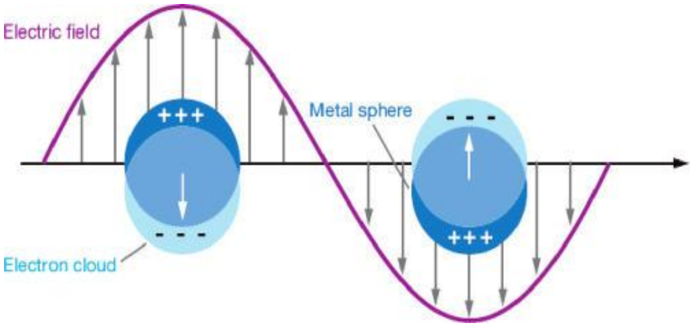

*Reproduced with permission of Annual Reviews from Ref[9](Copyright Annual Reviews 2007).

The surface plasmon resonance of noble metal nanoparticles makes them suitable for a wide variety of applications in fields such as energy conversion and storage,[13,14] sensing,[15-17], imaging,[18] nanoantennas,[19] and nanomedicine.[15,20] For instance, silver nanoparticles have the property to enhance the Raman signal of molecules in their vicinity and can be used for single-molecule detection via surface enhanced Raman spectroscopy (SERS).[21,22] On the other hand, gold nanoparticles are particularly well suited for biomedical applications due to their low toxicity.[20]

For spherical systems, the plasmon is manifested by a broad high-intensity peak in the absorption spectrum, usually in the UV-Vis.[10,23] The wavelength and intensity of the absorption peak can be modulated by modifying the particle size,[23-25] shape,[10,26] composition[27,28] and dielectric environment.[29,30] Nanorods and nanowires are among the most studied shapes because of the sensitivity of the wavelength of their plasmon mode to their aspect ratio (length /diameter). These elongated systems display two plasmon modes: a low-energy longitudinal mode, corresponding to photon absorption along the main axis of the system and a transverse mode, which corresponds to light absorption along the short axis of the system.[31-33] The longitudinal mode can shift down to the IR regime with increasing aspect ratio, which is particularly useful for biomedical applications such as cancer therapy since IR radiation can penetrate through tissues.[34-36] On the other hand, the wavelength of the transverse mode shows very little sensitivity to the particle's aspect ratio.

Theoretical modeling of plasmons in noble metal nanoparticles

Classical electromagnetic theory

The optical properties of silver and gold nanoparticles have been studied using classical electromagnetic theory.[30,37-40] In particular, Mie theory has proven successful in reproducing the plasmon extinction of spherical particles.[41,42] It was later extended by Gans for cylindrical particles.[43] In Mie theory, the particle is embedded in a dielectric medium and submitted to an electromagnetic field.[41] The Maxwell equations are then solved. Within the dipole approximation, the extinction cross-section of a spherical particle is given by:[10,39,44]

$$C = \frac{24\pi^2 R^3 \varepsilon_m^{3/2}}{\lambda} \frac{\varepsilon_2}{\left(\varepsilon_1 + 2\varepsilon_m\right)^2 + \varepsilon_2{}^2} \tag{1.1}$$

where R is the radius of the particle, ε_1 and ε_2 are the real and imaginary part of the dielectric function ε of the metal and ε_m is the dielectric constant of the surrounding medium. λ is the wavelength of the incident field. A plasmon occurs when ε_1=-2ε_m, assuming that ε_2 is small and weakly dependent on λ. The extinction cross-section is the sum of the absorption and scattering contributions. For particles smaller than about 20 nm, the main contribution to the extinction is the absorption and scattering is negligible.[45] The dielectric constant of the bulk metal is not a good value for small particles due to the electronic confinement. One common approach is to consider the Drude dielectric function, which applies for systems whose optical properties are only a function of the free conduction band electrons. The Drude dielectric function is given by:[39,46]

$$\varepsilon^{Drude}(\omega) = 1 - \frac{\omega_p^2}{\omega(\omega + i\gamma)} \tag{1.2}$$

where γ is the damping parameter, ω is the frequency of the incoming radiation and ω_p is the plasma frequency given by: $\omega_p = \sqrt{\frac{ne^2}{m_{eff} \cdot \varepsilon_0}}$. m_{eff} is the effective mass of the electrons, ε_0 is the permittivity, *e* is the electron charge and *n* is the density of free electrons. This model works well for alkali metals and reproduces the red-shift of the plasmon peak with decreasing cluster size (note that alkali clusters also have a plasmon but their instability makes them inadequate for practical applications).[47,48] This approach does not take into consideration the interband transitions (transitions out of the *d*-band) in noble metal nanoparticles, which result in a broader absorption spectra and a blue shift of the resonance frequency with decreasing cluster size.[49,50] Interband excitations were successfully included by expressing the dielectric function in terms of the sum of the free electron contribution (the Drude model) and the interband contribution.[51-53]

Analytical Mie theory cannot be easily applied to particles with complex shapes due to the difficulty in deriving an analytical cross-section for such systems. Numerical methods such as the finite-difference time domain (FDTD)[54] and the discrete dipole approximation (DDA),[55] which rely on the discrete mapping of space, can be used instead. These numerical methods have successfully modeled the plasmon of nanoparticles of various shapes.[32,37,38,56,57]

Classical electromagnetic theory does not account for quantum effects. Such effects may be very important for instance to describe the plasmon coupling with small molecules.[21,58,59] In addition, silver and gold clusters (< 2 nm) display molecular properties, as illustrated by their discrete absorption spectrum.[49,50] As a result, first principles calculations have been attempted and are discussed next.

First principle calculations on silver and gold nanoparticles

First principle calculations have been performed on a large variety of noble metal nanoparticles using the time-dependent local density approximation (TDLDA) with the Jellium model.[60-63] In this method, the nuclei are replaced with a single positive charge uniformly spread out. Plasmons of large systems can be modeled with this method due to the computational efficiency. However, ligand shells cannot be included with this method and structural effects cannot be determined since the nuclei are not explicitly considered.

Time-dependent density functional theory (TDDFT) with explicit nuclei has been used on a wide variety of clusters to investigate the effect of size and shape on the optical properties of the clusters.[50,64-72] The TDDFT evolution of the absorption spectrum of tetrahedral silver clusters with increasing size seems to converge to classical theory results, emphasizing the connection between molecular properties and plasmons.[64] Due to the high computational cost, systems with more than about 300 atoms cannot be modeled. With this method, the structural effects can be accounted for and information on electron dynamics can be obtained. In this section, we will discuss first principle calculations performed on 1) spherical ligand-protected gold clusters and 2) bare noble metal nanorods since these systems are analyzed in this thesis.

Spherical ligand-protected clusters

One important type of noble metal clusters is the thiol-protected gold clusters. Many have been synthesized and their structures characterized.[73-77] They are commonly composed of a metallic core surrounded by linear RS-Au(I)-SR and V-shaped RS-Au(I)-SR-Au(I)-SR “staple motifs”. Due to the ligands, these systems cannot be appropriately described with TDLDA and TDDFT with explicit nuclei needs to be used. The $Au_{25}(PET)_{18}^-$ (PET=phenylethylthiol) cluster is shown in Figure 1-2 as an example.

Figure 1-2. Structure of the thiol-protected $Au_{25}(SR)_{18}^-$ cluster.

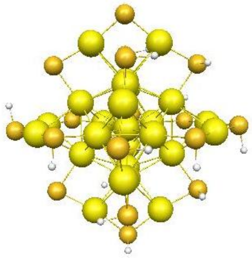

*The ligand R=PET has been replaced by R=H for clarity. Key: Yellow= gold, orange=sulfur and white=hydrogen. Coordinates from Ref[78].

The role of the staple motifs is to protect the reactive gold core and their arrangement was explained in terms of the "divide and protect model".[79] The DFT-calculated electronic structure of the $Au_{25}(SH)_{18}^-$ cluster is shown in Figure 1-3A. The frontier orbitals of these nanoparticles are commonly named "superatom orbitals"[80-82] and define the *sp*-band. They mainly result from linear combinations of the atomic gold valence *s* and *p* orbitals. The superatom orbitals look like the familiar *s, p, d* orbitals of the hydrogen atom but are delocalized over the metallic core (hence their name). They are labeled 1S, 1P, 1D,…These levels may be split due to the ligand field, as will be discussed in chapter 7. For a cluster with the stoichiometric formula $A_NX_ML_S^Z$, A corresponds to gold, X corresponds to electron-withdrawing ligands and L corresponds to Lewis ligands. Z corresponds to the total charge of the cluster. If the number of core electrons given by $n^*=N-M-Z$ is equal to a "magic number" (n^*=2, 8, 18, 34, 58…), the cluster tends to be stable.[80] These numbers correspond to a fully occupied superatomic electronic shell. For the $Au_{25}(SH)_{18}^-$ cluster, n^*=25-18+1=8, which corresponds to a full 1P shell. Below the *sp*-band is a large *d*-band. These orbitals mostly have atomic *d*-character but also contributions from the 3*p* orbitals of the sulfur ligands. They tend to be localized.

The absorption spectrum of the $Au_{25}(SH)_{18}^-$ cluster was calculated using TDDFT (Figure 1-3B). Discrete features were obtained, in agreement with experiment, and were interpreted in terms of the electronic structure of the cluster. Low energy excitations occur within the *sp*-band (1P→1D) and are labeled intraband whereas higher energy excitations between the *d*-band and the *sp*-band are called interband. Note that the absorption spectrum cannot be divided in terms of core and ligands contributions, showing that the thiol ligands represent an integral part of the cluster and greatly affect its electronic structure.[83,84]

Figure 1-3. A) Electronic structure and B) theoretical absorption spectrum of the $Au_{25}(SH)_{18}^{-}$ cluster.

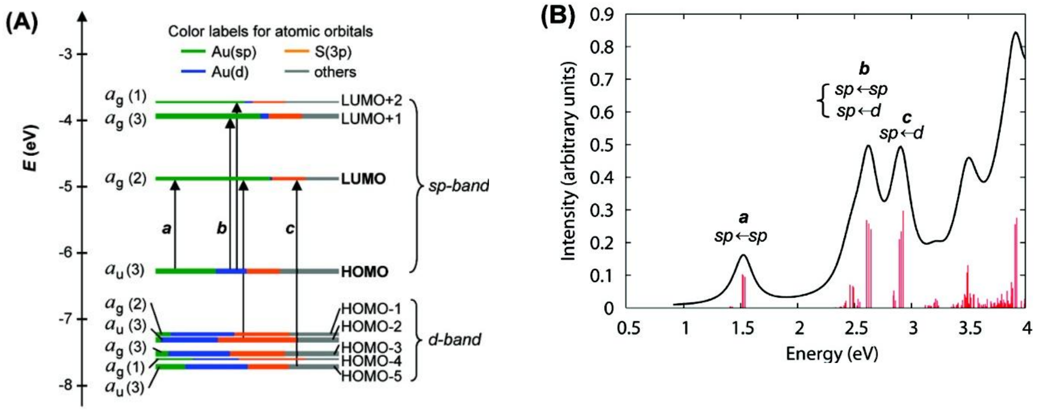

*Reprinted with permission from Ref [73]. Copyright 2008 American Chemical Society.

The transition from the discrete absorption spectrum of the small systems to the strong plasmon absorption of the large systems can be observed between 1.5 and 2 nm.[67] The $Au_{144}(SH)_{60}$ and $Au_{314}(SH)_{96}$ clusters are within that size range and have been studied using time-dependent density functional perturbation theory.[67] One broad absorption peak occurs at 540 nm for these systems. Transition densities for these systems show a collective dipole character. For the $Au_{144}(SH)_{60}$ cluster, the density is mostly within the core with a small amount at the outer surface of the particle. For the larger $Au_{314}(SH)_{96}$ cluster, the electron density is mostly focused on the outer surface, which is expected for the surface plasmon resonance. The authors showed that the ligands are responsible for the enhancement of the surface plasmon.[67] This also shows the importance of the ligand shell in the optical properties of these clusters.

Elongated noble metal clusters

The extinction spectra of noble metal nanorods display two main modes: the longitudinal mode, corresponding to excitations along the long axis of the system and the transverse mode, which corresponds to excitations along the short axis.[6,16,85] Both classical electromagnetic theory and first principle calculations have been performed to model the optical properties of silver and gold nanorods.[32,66,70] The electronic structure of silver nanorods with sizes between 13 and 67 atoms was analyzed using density functional theory.[70] The frontier orbitals of these systems are delocalized over the entire structure and have cylindrical symmetry.[70] They are labeled nL_m

where L= Σ, Π, Δ… and *n* and *m* are quantum numbers corresponding to the number of radial nodes plus one and the number of axial nodes plus one respectively. Like the superatom orbitals of the thiolate-protected clusters described above, they result from a linear combination of the singly occupied *s* orbitals of the silver atoms. The TDDFT absorption spectra of these nanorods display a strong low-energy longitudinal peak, corresponding to a superposition of Σ→Σ, Π→Π… transitions and a high energy transverse peak corresponding to a superposition of Σ→Π, Π→ Σ, Π→Δ… transitions.[66,70] The electronic confinement along the long axis of the rod decreases with increasing length but it remains constant along the short axis. As a result, the longitudinal peak shifts to the red while the transverse peak remains at nearly constant energy.[70] TDDFT calculations performed on cigar-like and hexagonal nanorods at the BP86/DZP level of theory show similar trends.[66] Few TDDFT calculations were performed on gold nanorods due to the higher computational cost. Liao *et al.* calculated the TDDFT absorption spectra of gold nanorods with up to 84 atoms and obtained very broad features due to relativistic effects.[66]

Objectives and overview of the thesis

Classical methods such as the discrete-dipole approximation (DDA),[55,86] finite-difference time domain (FDTD)[54,87] and Mie theory[41] can successfully describe the plasmon peak energy and intensity of noble metal nanoparticles.[37] However, these approaches do not capture quantum effects which may be important, for instance when describing the interaction of these particles with small molecules.[59,88,89] In addition, quantum effects play a critical role in very small systems (less than about 2 nm) as shown by the discrete features occurring in their absorption spectrum. A uniform description of the optical properties of noble metal particles of all sizes is necessary. The main objective of this thesis is to determine the origin of the plasmon resonance in noble metal nanoparticles and show that plasmons may occur at the molecular level. The second objective is to provide a uniform description of the optical properties of plasmonic systems. Silver and gold atoms have a similar electronic structure: a singly occupied valence *s* orbital and a fully occupied *d*-band. Due to relativistic effects, the gap between the *d* and *s* orbitals of silver is larger than for gold, which leads to differences in the optical behavior of silver and gold nanoparticles. The final objective of this thesis is to compare the optical properties of silver and gold nanoparticles and define the importance of relativistic effects.

Chapter 2 describes the theory and computational methods used in this research. In chapter 3 (Guidez, E. B.; Aikens, C. M. *Nanoscale* **2012**, *4*, 4190), the optical properties of both silver and gold nanowires (linear atomic chains) are analyzed. In chapter 4 (Guidez, E. B.; Aikens, C. M. *J. Phys. Chem. C* **2013**, *117*, 12325), I extend this study to systems with a larger diameter. Chapter 5 (Guidez, E. B.; Aikens, C. M. *J. Phys. Chem. C* **2013**, *117,* 21466) describes the plasmonic behavior of linear polycyclic hydrocarbons and the similarities with noble metal nanorods are discussed. A configuration interaction (CI) model to calculate plasmon peak energies and oscillator strengths is discussed in chapter 6. Chapter 7 (Guidez, E. B.; Aikens, C. M. *Phys. Chem. Chem. Phys.* **2012**, *14*, 4287) shows the development of a charge-perturbed particle-in-a-sphere model to determine the electronic structure of thiol-protected gold nanoparticles. In chapter 8, the CI method is applied to multiple silver clusters and the link between small clusters and large nanoparticles is discussed. Finally, the effect of silver doping on the optical properties of the $Au_{25}(SH)_{18}^-$ cluster is analyzed in chapter 9 (Guidez, E. B.; Mäkinen, V.; Häkkinen, H.; Aikens, C. M. *J. Phys. Chem. C* **2012**, *116*, 20617).

Chapter 2 - Theory and computational methods

Theory of quantum mechanics

The Schrödinger equation

Classical mechanics dictate that the evolution of a macroscopic system can be derived by solving Newton's equations of motion, provided we know the state of this system at an original time t_0. However, in the case of microscopic particles like electrons, the Heisenberg uncertainty principle dictates that their position and velocity cannot be determined simultaneously. The laws of classical mechanics therefore do not apply and quantum mechanics must be used. In quantum mechanics, all information about the system of interest is contained in a wavefunction Ψ , which depends on both the coordinates of the particles (noted $\boldsymbol{r}$) and on time t. The probability of finding a particle at a position between $\boldsymbol{r}$ and $\boldsymbol{r}+d\boldsymbol{r}$ at time t is given by the probability density ρ:

$$\rho(\boldsymbol{r},t) = \left|\Psi(\boldsymbol{r},t)\right|^2 d\boldsymbol{r} \tag{2.1}$$

The equation that describes the state of a quantum-mechanical system (such as an atom or a molecule) is the time-dependent Schrödinger equation (TDSE), which in atomic units reads:

$$i\frac{\partial\Psi(\boldsymbol{r},t)}{\partial t} = \hat{H}(\boldsymbol{r},t)\Psi(\boldsymbol{r},t) \tag{2.2}$$

where t is time and $i = \sqrt{-1}$. $\hat{H}$ is the Hamiltonian and it is defined in atomic units as:

$$\hat{H}(\boldsymbol{r},t) = -\sum_{i=1}^{N}\frac{1}{2m_i}\nabla_i^2 + \sum_{i=1}^{N}V(\boldsymbol{r}_i,t) + \sum_{i>j}^{N}\frac{Z_iZ_j}{r_{ij}} \tag{2.3}$$

The subscripts i and j refer to the quantum mechanical particles in the system. N is the total number of particles. m_i and Z_i correspond to the mass and charge of the particle i in atomic units respectively. The Laplacian operator ∇^2 refers to the second derivative with respect to the particle position. r_{ij} corresponds to the distance between particles i and j. The first term of the Hamiltonian represents the kinetic energy of the particles. The second term corresponds to the external potential acting on each particle i. The third term represents the coulomb interaction between particles i and j.

We now consider wavefunctions that can be written as a product of a time-dependent part and a position-dependent part such that:

$$\Psi(\boldsymbol{r},t) = f(t)\psi(\boldsymbol{r}) \tag{2.4}$$

where *f(t)* is a function of time only and $\psi(\boldsymbol{r})$ is a wavefunction that depends only on the position of the particles. $\psi(\boldsymbol{r})$ describes the states of a system where the probability density does not change with time. Such states are called stationary states.

If the system does not experience any time-dependent external forces, the time-dependence in the Hamiltonian disappears and one can derive the time-independent Schrödinger equation (TISE) which has the following form:

$$\hat{H}\psi(\boldsymbol{r}) = E\psi(\boldsymbol{r}) \tag{2.5}$$

where E is the energy of the system in its stationary state $\psi(\boldsymbol{r})$.

The Born-Oppenheimer approximation

In atomic units, the time-independent Hamiltonian $\hat{H}$ for a non-relativistic molecule or atom has the following form:

$$\hat{H} = -\sum_{i=1}^{N}\frac{1}{2}\nabla_i^2 - \sum_{A=1}^{M}\frac{1}{2M_A}\nabla_A^2 - \sum_{i=1}^{N}\sum_{A=1}^{M}\frac{Z_A}{r_{iA}} + \sum_{i=1}^{N}\sum_{j>i}^{N}\frac{1}{r_{ij}} + \sum_{A=1}^{M}\sum_{B>A}^{M}\frac{Z_A Z_B}{R_{AB}} \tag{2.6}$$

The subscripts *i* and *j* refer to the electrons whereas *A* and *B* refer to the nuclei. *N* and *M* represent the number of electrons and nuclei of the system respectively. M_A and Z_A are the mass and charge of nucleus *A* respectively. We note that in atomic units, the mass of the electron is equal to 1 and the charge of the electron is -1. r_{ij} corresponds to the distance between electrons *i* and *j*. r_{iA} refers to the distance between electron *i* and nucleus *A*. R_{AB} corresponds to the distance between nuclei *A* and *B*. The first and second terms of equation 2.6 correspond to the kinetic energy of the electrons and nuclei respectively. The third term corresponds to the coulomb attraction between electrons and nuclei whereas the last two terms represent the inter-electronic and inter-nuclear repulsion respectively.

Even the time-independent Schrödinger equation (eq. 2.5) is impossible to solve for large molecules of interest to chemists when using the full Hamiltonian (eq. 2.6). Approximations must therefore be made to render the calculations manageable. One of these approximations is to consider that the nuclei, being much heavier than the electrons, move slower. Consequently, electrons can be assumed to move in a field of fixed nuclei. The second term in eq. 2.6 can be neglected and the last term is a constant. The new Hamiltonian describing the electronic motion becomes:

$$\hat{H} = \hat{H}_{el} + V_{MM} \tag{2.7}$$

where $\hat{H}_{el}$ is the electronic Hamiltonian which is written as:

$$\hat{H}_{el} = -\sum_{i=1}^{N} \frac{1}{2} \nabla_i^2 - \sum_{i=1}^{N} \sum_{A=1}^{M} \frac{Z_A}{r_{iA}} + \sum_{i=1}^{N} \sum_{j>i}^{N} \frac{1}{r_{ij}} \tag{2.8}$$

and V_{MM} is the inter-nuclear repulsion term:

$$V_{MM} = \sum_{A=1}^{M} \sum_{B>A}^{M} \frac{Z_A Z_B}{R_{AB}} \tag{2.9}$$

Since V_{MM} is a constant for any set of nuclear coordinates, it can be omitted in the time-independent Schrödinger equation (eq. 2.5) which gives:

$$\hat{H}_{el} \psi_{el} = E_{el} \psi_{el} \tag{2.10}$$

This equation can be solved for many different possible sets of nuclear configurations. Therefore, the purely electronic energy E_{el} and the electronic wavefunction ψ_{el} depend parametrically on the nuclear coordinates. We can now add the internuclear-repulsion term defined in equation 2.9 to the purely electronic energy E_{el} to obtain the total electronic energy U:

$$U = E_{el} + V_{MM} \tag{2.11}$$

The time-independent Schrödinger equation (eq. 2.5) can also be solved for the nuclear motion:

$$\hat{H}_{nuc} \psi_{nuc} = E_{nuc} \psi_{nuc} \tag{2.12}$$

The nuclear Hamiltonian is:

$$\hat{H}_{nuc} = -\sum_{A=1}^{M} \frac{1}{2M_A} \nabla_A^2 + U(\{\boldsymbol{R}_A\}) \tag{2.13}$$

where the first term is the sum of the kinetic energies of the nuclei and the second term represents the average field of the electrons (eq. 2.11) for the set of nuclear coordinates $\{\boldsymbol{R}_A\}$ considered. The nuclear energy E_{nuc} includes electronic, vibrational, rotational and translational energies. The total molecular wavefunction using the Born-Oppenheimer approximation can be written as a product of the nuclear and electronic wavefunctions:

$$\psi = \psi_{el} \cdot \psi_{nuc} \tag{2.14}$$

Relativistic effects

When electrons move with a velocity comparable to the speed of light, it leads to an increase of their mass. Electrons in atomic *s* orbitals undergo a mass increase that is given by:

$$m = {m_0} \big/ {(1-(v/c))^{1/2}} \tag{2.15}$$

where m_0 is the rest mass of the electron, v is the velocity of the electron and c is the speed of light (c =137.04 a.u. = 300000 km/s). The velocity of a 1*s* electron in a hydrogen-like atom relative to the speed of light is approximately Z/*c*, where Z is the atomic number of the element and *c* is the speed of light in atomic units.[90] We can see that for high values of Z, the velocity of the electron represents a large portion of the speed of light. Therefore, the 1*s* electron mass substantially increases. The results of this mass increase on the properties of heavy metal compounds are referred to as scalar relativistic effects. The radial function of a hydrogen-like atomic 1*s* orbital is given by:

$$R(r)^{1s} = 2\left(\frac{Z}{a}\right)^{3/2} e^{-Zr/a} \tag{2.16}$$

where a is the Bohr radius defined in SI units as:

$$a = \frac{4\pi\varepsilon_0\hbar^2}{me^2} \tag{2.17}$$

where ε_0 is the permittivity of vacuum with a value of $8.8541878\cdot10^{-12}$ $C^2N^{-1}m^{-2}$, $\hbar = h/2\pi$ (h is the Plank constant equal to $6.626069\cdot10^{-34}$J·s), e is the elementary charge with a value of $1.6021765\cdot10^{-19}$C and m is the relativistic electron mass. For elements with a high Z, the mass of the 1*s* electron is significantly increased and the Bohr radius is reduced. As a result, the distance between the nucleus and the 1*s* electron will decrease. We note that for a non-relativistic 1*s* electron, the Bohr radius is equal to 1 a.u. since the electron mass is equal to its rest mass. In order to maintain orthogonality, the higher *s* orbitals (and to a lesser extent the *p* orbitals) must also shrink and therefore their energy will decrease. On the other hand, the *d* and *f* orbitals are more diffuse and become higher in energy due to the higher shielding of the inner *s* electrons.

Relativistic effects can strongly affect the geometries, optical properties, electrochemical properties and physical properties of heavy metal compounds.[90-94] Since this work focuses mainly on silver and gold nanoparticles, it is critical to take these effects into account.

Computational methods

Density functional theory (DFT)

DFT is one of the most widely used methods for ground state electronic calculations due to its high efficiency compared to correlation methods. A basic description of the method is given in this section. For more details, the reader is invited to consult some selected publications and texts.[95-98] DFT calculates the ground state energy E_0 and other ground state molecular properties as a function of the ground state electron density ρ_0. Unlike the wavefunction, which depends on $3N$ spatial coordinates and N spin coordinates (where N is the number of electrons), the ground state electron density is a function of only on three variables: the coordinates x, y and z. In DFT, all ground state properties of interest are calculated in principle as a function of the electron density only (and avoid wavefunctions), resulting in higher computational efficiency.

The Hohenberg-Kohn theorem

The ground state wavefunction of an N-electron molecule is an eigenfunction of the electronic Hamiltonian given in equation 2.8. We define the external potential $v(\boldsymbol{r}_i)$ acting on electron i for a real system as the potential generated by charges other than the electrons (aka the nuclei in the absence of additional potential):

$$v(\boldsymbol{r}_i) = -\sum_{A=1}^{M} \frac{Z_A}{r_{iA}} \tag{2.18}$$

The Hohenberg-Kohn theorem states that there is a one-to-one relationship between the ground state electron density ρ_0 and the sum of the external potentials acting on each electron (the nuclear attraction potential energy function $v(\boldsymbol{r})$).[99] A direct consequence of this relationship is that the ground state density determines the ground state energy E_0 and other ground state properties. E_0 is a functional of the ground state density ($E_0 = E[\rho_0]$). The ground state energy is given by the sum of the kinetic energy T, nuclear-electron attraction V_{Ne} and electron-electron repulsion V_{ee}:

$$E_0 = E[\rho_0] = \overline{T}[\rho_0] + \overline{V}_{Ne}[\rho_0] + \overline{V}_{ee}[\rho_0] \tag{2.19}$$

Each of these contributions is also a functional of the ground state electronic density. Overbars denote averages. The second term of this sum is known and given by:

$$V_{Ne} = \left\langle \Psi_0 \left| \sum_i v(\boldsymbol{r}_i) \right| \Psi_0 \right\rangle = \int \rho_0 v(\boldsymbol{r}) d\boldsymbol{r} \tag{2.20}$$

However, the dependence of the kinetic energy and electron-electron repulsion components on ρ_0 is not known.

The Kohn-Sham (KS) method

In order to evaluate the density of the interacting system, Kohn and Sham considered a fictitious system of N non interacting electrons that experience an external potential $v_s(\boldsymbol{r}_i)$ such that $\rho_s(\boldsymbol{r}) = \rho_0(\boldsymbol{r})$.[100] The subscript *s* denotes the non-interacting system. Since the electrons are not interacting, the electronic Hamiltonian for this fictitious system given in equation 2.8 becomes:

$$\hat{H}_s = \hat{h}^{KS} = -\sum_{i=1}^{N} \left(\frac{1}{2} \nabla_i^2 + v_s(\boldsymbol{r}_i) \right) = \sum_i^N \hat{h}_i^{KS} \tag{2.21}$$

where $\hat{h}_i^{KS} = -\frac{1}{2} \nabla_i^2 + v_s(\boldsymbol{r}_i)$ is the Kohn-Sham Hamiltonian for electron *i*. The ground state wavefunction of this non-interacting system can be written as a Slater determinant:

$$\Psi_{s,0} = |\chi_1 \chi_2 \cdots \chi_N\rangle \tag{2.22}$$

χ_i are the occupied Kohn-Sham spin-orbitals and can be written as a product of a spatial function ψ and a spin function σ:

$$\chi_i = \psi_i(\boldsymbol{r}_i)\sigma_i \tag{2.23}$$

The spin functions can only have two values: +1/2 and -1/2. For closed-shell systems, the electrons are paired in the spatial orbitals, one with spin +1/2 (α) and the other with spin -1/2 (β). In the restricted case (all electrons are paired), the ground state determinant has the form:

$$\Psi_{s,0} = |\psi_1^{\alpha} \psi_1^{\beta} \psi_2^{\alpha} \psi_2^{\beta} \ldots \psi_{N/2}^{\alpha} \psi_{N/2}^{\beta}\rangle \tag{2.24}$$

The orbitals ψ_i^{α} and ψ_i^{β} have α spin and β spin respectively. The spatial functions ψ_i are eigenfunctions of the Kohn-Sham Hamiltonian and are called the Kohn-Sham orbitals. The electron density can be derived from these orbitals by the relation:

$$\rho_0 = \rho_s = \sum_{i=1}^{N} f_i \left|\psi_i\right|^2 \tag{2.25}$$

f_i is the occupation number of the orbital (f_i=2 for a fully occupied orbital). According to the Hohenberg-Kohn variational theorem,[99] the true ground state density is the one that minimizes the ground state energy. Therefore, the Kohn-Sham orbitals can be optimized such that the resulting electron density minimizes the ground state energy. This optimization can be done by solving the KS equation (provided we have the appropriate potential $v_s\left(\boldsymbol{r}_i\right)$):

$$\hat{h}_i^{KS}\psi_i = \varepsilon_i \psi_i \tag{2.26}$$

where the eigenvalues ε_i correspond to the Kohn-Sham orbital energies. Now, we have to determine the external potential of this non-interacting system that would yield an electronic density equal to the density of the real system. We first write the two unknown components to the ground state energy in equation 2.19 in relation to this non-interacting system. For the kinetic energy we have:

$$\overline{T}\left[\rho_0\right] = -\frac{1}{2}\left\langle \Psi_{s,0} \middle| \sum_i \nabla_i^2 \middle| \Psi_{s,0} \right\rangle + \Delta\overline{T}\left[\rho_0\right] \tag{2.27}$$

where the first term of the sum represents the kinetic energy contribution to the ground state of the non-interacting system and the second term represents the kinetic energy difference between the real and non-interacting system. Using the Slater-Condon rules, we can rewrite eq. 2.27:

$$\overline{T}\left[\rho_0\right] = -\frac{1}{2}\sum_i \left\langle \psi_i(1) \middle| \nabla_1^2 \middle| \psi_i(1) \right\rangle + \Delta\overline{T}\left[\rho_0\right] \tag{2.28}$$

where (1) labels electron 1. For the electron-electron repulsion we have:

$$\overline{V}_{ee}\left[\rho_0\right] = \frac{1}{2}\iint \frac{\rho(\boldsymbol{r}_1)\rho(\boldsymbol{r}_2)}{r_{12}} d\boldsymbol{r}_1 d\boldsymbol{r}_2 + \Delta\overline{V}_{ee}\left[\rho_0\right] \tag{2.29}$$

where the first term of the sum represents the Coulomb interaction for a smeared out charge. r_{12} is the distance between coordinates $\boldsymbol{r}_1$ and $\boldsymbol{r}_2$. The term $\Delta\overline{V}_{ee}\left[\rho_0\right]$ is the difference in inter-electronic repulsion energy between the real system and the non-interacting system. The two unknown terms $\Delta\overline{V}_{ee}\left[\rho_0\right]$ and $\Delta\overline{T}\left[\rho_0\right]$ define the exchange-correlation energy functional:

$$E_{xc}\left[\rho_0\right]=\Delta\overline{T}\left[\rho_0\right]+\Delta\overline{V}_{ee}\left[\rho_0\right] \tag{2.30}$$

The external potential $v_s(\boldsymbol{r}_1)$ of the Kohn-Sham Hamiltonian in 2.21 that minimizes the ground state energy satisfies:

$$v_s(\boldsymbol{r}_1)=-\sum_{A=1}^{M}\frac{Z_A}{r_{1A}}+\int d^3r_1\frac{\rho(\boldsymbol{r}_2)}{r_{12}}+v_{xc}(1) \tag{2.31}$$

The first term is the external potential of the nuclei, the second term is the Hartree potential (electron-electron interaction) and the last term is the exchange-correlation potential given by:

$$v_{xc}(r)=\frac{\delta E_{xc}\left[\rho(r)\right]}{\delta\rho(r)} \tag{2.32}$$

This last term includes all many-body effects. Since the functional E_{xc} is unknown, various approximations have been developed. These approximations can be classified in Jacob's ladder, as shown in Table 2.1. The key to accuracy resides in the good approximation of the exchange-correlation functional. There is no single good functional. The functional to choose depends on the system and properties investigated.

In practice, the KS equations are solved self-consistently:

1) Take the KS orbitals $\psi_i^{(n)}$ (*n* is the step number. *n*=1 corresponds to the initial guess). Calculate $\rho^{(n)}$ from equation 2.25.
2) Construct the KS operator $\hat{h}_i^{KS(n)}$ using the potential given in equation 2.31.
3) Solve the KS equation 2.26 using the KS operator derived in step 2) to get new improved orbitals $\psi_i^{(n+1)}$.
4) Calculate $\rho^{(n+1)}$. If $E[\rho^{(n+1)}]-E[\rho^{(n)}]<\Delta$, where Δ is a preset convergence criterion, the calculation is converged. Otherwise, go back to step 1 where $\psi_i^{(n)}\rightarrow\psi_i^{(n+1)}$. Repeat until converged.

Table 2.1 Jacob's ladder

Functional category	Density dependence	Examples
Local Density Approximation (LDA)	ρ	VWN,[101] Xα[99,100]
Generalized-Gradient Appoximation (GGA)	ρ, ∇ρ	BP86,[102,103] PW91,[104] PBE[105]
Meta-GGA	ρ, ∇ρ, ∇^2ρ	TPSS,[106] M06-L[107]
Hybrid	ρ, ∇ρ, ∇^2ρ, exact Hartree-Fock exchange	B3LYP,[102,108] PBE0[109]

Construction of the molecular orbitals.

The molecular KS orbitals are usually expanded in linear combinations of atomic orbitals φ_r:

$$\psi_i^{KS} = \sum_{r=1}^{b} c_{ri}\varphi_r \tag{2.33}$$

The atomic orbitals φ_r are in turn expanded as a linear combination of Slater orbitals or Gaussian orbitals. The former is a function of $e^{-\xi r}$ where ζ is a coefficient representing the decay of the function. The latter is a function of $e^{-\xi r^2}$. The Slater orbitals describe more accurately the features of the molecular orbitals and fewer Slater orbitals are needed in the expansion of the atomic orbitals. The Amsterdam Density Functional (ADF)[110] program used in most of this research uses Slater orbitals. The reason Gaussian orbitals are often used is that the four-index integrals that have to be calculated can be expressed analytically as opposed to numerically with Slater functions. The number of Slater orbital used to model an atomic orbital represents the basis set. A double-zeta (DZ) basis set uses two Slater functions per atomic orbital. A triple-zeta (TZ) basis set uses three Slater functions, a quadruple zeta (QZ) basis set uses four Slater functions, and so forth. A larger basis set yields higher accuracy but also increases the computational cost. Additional features like polarization functions and diffuse functions may be added to the basis to account for orbital hybridization in polar bonds and loosely bound electrons (such as in anions, hydrogen bonds…) respectively. Polarization functions are labeled "nP" where n is the number of polarization functions (for instance TZP, QZ4P…) and diffuse functions are labeled with "-nD" where n is the number of diffuse functions (for instance QZ3P-2D). A more detailed description of basis sets can be found in Ref[111].

Relativistic effects: The zeroth order regular approximations (ZORA)

Relativistic effects are commonly integrated into the one-electron operator of the Hamiltonian in equation 2.8. The expression for the relativistic one-electron Hamiltonian was derived by Dirac:[112,113]

$$\hat{h}_D(i) = c\hat{\vec{\alpha}}_i \cdot \hat{\vec{p}}_i + \left(\hat{\beta}_i - \boldsymbol{I}_4\right)c^2 + \sum_A \frac{-Z_A}{r_{iA}} \tag{2.34}$$

$\hat{\vec{\alpha}} = \begin{pmatrix} \vec{0} & \hat{\vec{\sigma}} \\ \hat{\vec{\sigma}} & \vec{0} \end{pmatrix}$ and $\hat{\beta} = \begin{pmatrix} \boldsymbol{I_2} & \boldsymbol{0_2} \\ \boldsymbol{0_2} & \boldsymbol{-I_2} \end{pmatrix}$ are the 4X4 Dirac matrices where I_2 is the 2X2 identity matrix and $\hat{\vec{\sigma}}$ is the electron spin matrix. $\hat{\vec{p}}_i$ is the momentum operator for particle *i*.

The solution of the TISE for this Hamiltonian is a 4-electron spinor:

$$\psi^D = \begin{pmatrix} \psi^U \\ \psi^L \end{pmatrix} \tag{2.35}$$

U and *L* denote the upper and lower components of the Dirac wavefunction respectively. Each of these components has a α-spin component and a β-spin component. The upper and lower spinors are not linearly independent:

$$\psi^L = \left(\frac{1}{2c} k\boldsymbol{\sigma} \cdot \boldsymbol{p}\right)\psi^U \tag{2.36}$$

with $k = \left(1 - \frac{V-E}{2c^2}\right)$.

Only the upper spinor is needed to describe electronic states. However, the relation between the lower and upper components must be enforced as a constraint to avoid variational collapse.

In this work, relativistic effects are treated with the zeroth order regular approximation (ZORA).[114-116] In the regular approximation, the parameter *k* in the coupling between upper and lower component spinor is approximated using an expansion in a power series. ZORA corresponds to the approximation where the power series is cut to the zeroth order term. Since ZORA is variationally stable and computationally efficient, it is one of the preferred methods for relativistic calculations.

Time-dependent density functional theory (TDDFT)

When a system is submitted to an external perturbation, for instance an electromagnetic field, its electronic structure undergoes changes that depend on time. TDDFT allows the study of the evolution of the electron density in real time (RT-TDDFT). A robust linear response formalism (LR-TDDFT) was also developed to obtain useful excited states properties in the frequency domain such as excited state energies, oscillator strengths, gradients, etc... One great advantage of TDDFT compared to correlation methods is that it can simulate larger systems. One of the main limitations is the poor description of charge-transfer states. The basics of the method are given in this section but the reader is invited to consult selected references for more details.[117-120] First, I will state the Runge-Gross theorem, which is the foundation of the method. Then, I will state the time-dependent Kohn-Sham equations and finally, I will discuss the linear response formalism, which is used in the TDDFT calculations performed.

The Runge-Gross theorem

The Runge-Gross theorem is the foundation of TDDFT and can be viewed as the time-dependent analog of the Hohenberg-Kohn theorem. It states that there is a one-to-one mapping between the time-dependent external potential $v_{ext}(\boldsymbol{r},t)$ and the time-dependent electron density $\rho(\boldsymbol{r},t)$ up to a phase factor *C(t)*. This means that if two different time-dependent potentials $v_{ext}^{A}(\boldsymbol{r},t)$ and $v_{ext}^{B}(\boldsymbol{r},t)$ are applied on a system in its ground state at $t=t_0$ ($v_{ext}^{A}(\boldsymbol{r},t) \neq v_{ext}^{B}(\boldsymbol{r},t) + C(t)$), the two resulting time-dependent electron densities $\rho^{A}(\boldsymbol{r},t)$ and $\rho^{B}(\boldsymbol{r},t)$ will be different at any time $t_1>t_0$. Similar to the Hohenberg-Kohn theorem, this means the external potential can be expressed as functional of the electron density (there is a one-to-one correspondence) and all properties of the system can be obtained.

The time-dependent Kohn-Sham equations

Like we did for the time-independent scheme, we now define a non-interacting system with an electron density ρ_s equal to the electron density of the real system ρ. The non-interacting system is represented by a single determinant $\Psi(\mathbf{r},t)$. If for instance an electron is excited from an orbital ψ_N to an orbital ψ_{N+1} we have:

$$\Psi(\boldsymbol{r},t) = \left|\psi_1^{\alpha}(\boldsymbol{r},t)\psi_1^{\beta}(\boldsymbol{r},t)...\psi_N^{\alpha}(\boldsymbol{r},t)\psi_{N+1}^{\beta}(\boldsymbol{r},t)\right\rangle \tag{2.37}$$

The electron density can be calculated from the time-dependent Kohn-Sham orbitals $\psi_i(\boldsymbol{r},t)$:

$$\rho(\boldsymbol{r},t) = \rho_s(\boldsymbol{r},t) = \sum_i^N f_i \left|\psi_i(\boldsymbol{r},t)\right|^2 \tag{2.38}$$

f_i is the occupation number of the spatial orbital ψ_i. The time-dependent density can be obtained by solving the time-dependent Kohn-Sham (TDKS) equations until self-consistency is reached. The TDKS have the following form:

$$i\frac{\delta}{\delta t}\psi_i(\boldsymbol{r},t) = h^{KS}(\boldsymbol{r},t)\psi_i(\boldsymbol{r},t) \tag{2.39}$$

where

$$h^{KS}(\boldsymbol{r},t) = -\frac{1}{2}\nabla_i^2 + v_S[\rho](\boldsymbol{r},t) \tag{2.40}$$

The time-dependent potential of the non-interacting system can be written as a sum of three terms:

$$v_S[\rho](\boldsymbol{r},t) = v_{ext}[\rho](\boldsymbol{r},t) + v_{Hartree}[\rho](\boldsymbol{r},t) + v_{xc}[\rho](\boldsymbol{r},t) \tag{2.41}$$

The external potential v_{ext} includes the potential from the nuclei and the potential generated by for instance an external electromagnetic field.

The Hartree potential is written as:

$$v_{Hartree}(\boldsymbol{r}_1,t) = \int d^3r_1 \frac{\rho(\boldsymbol{r}_2,t)}{r_{12}} \tag{2.42}$$

The TDKS equations can be solved iteratively until self-consistent like in the static case. Two questions remain: 1) how do we define self-consistency? 2) What is the exchange-correlation potential v_{xc}? We first answer question 1). Contrary to static DFT, the density and energy are not conserved quantities and we cannot derive an equivalent to the Hohenberg-Kohn variational principle. Instead, we have to find the state that corresponds to a stationary point of the quantum mechanical action integral *A*, which is a functional of the density:

$$A[\rho] = \int_{t_0}^{t_1} dt \left\langle \Psi[\rho](\boldsymbol{r},t) \middle| i\frac{\delta}{\delta t} - \hat{H}(t) \middle| \Psi[\rho](\boldsymbol{r},t) \right\rangle \tag{2.43}$$

$\hat{H}$ is the Hamiltonian, which is written as a sum of the kinetic energy and electron-electron repulsion term:

$$\hat{H} = -\sum_{i=1}^{N} \frac{1}{2}\nabla_i^2 + \sum_{i=1}^{N}\sum_{j>i}^{N} \frac{1}{r_{ij}} \tag{2.44}$$

The exact density can be determined by solving the Euler equation:

$$\frac{\partial A[\rho]}{\partial \rho(\boldsymbol{r},t)} = 0 \tag{2.45}$$

The action integral can be rewritten in the following form:

$$A[\rho] = B_s[\rho] - \int_{t_0}^{t_1} dt \int d^3 r_1 \rho(\boldsymbol{r_1},t) v_{ext}(\boldsymbol{r},t) - \frac{1}{2}\int_{t_0}^{t_1} dt \int d^3 r_1 \int d^3 r_2 \frac{\rho(\boldsymbol{r_1},t)\rho(\boldsymbol{r_2},t)}{r_{12}} - A_{xc}[\rho] \tag{2.46}$$

B_s is the universal functional for the non-interacting system:

$$B_s[\rho] = \int_{t_0}^{t_1} dt \left\langle \Psi[\rho](\boldsymbol{r},t) \middle| i\frac{\delta}{\delta t} + \hat{T}(\boldsymbol{r}) \middle| \Psi[\rho](\boldsymbol{r},t) \right\rangle \tag{2.47}$$

where $\hat{T}$ is the time-independent kinetic energy operator. The first three terms of 2.46 can be readily evaluated. The fourth term of equation 2.46 is the exchange-correlation functional and it is unknown. This leads us to question 2: what is the exchange-correlation part of the potential? The exchange-correlation part of the potential can be expressed as:

$$v_{XC}(\boldsymbol{r},t) = \frac{\partial A_{xc}[\rho]}{\partial \rho(\boldsymbol{r},t)} \tag{2.48}$$

The first approximation for the action functional is the adiabatic approximation, where the time-dependent exchange-correlation functional is replaced by a time-independent one (eq. 2.32). This is a good approximation if the probability density changes slowly with time.

Time-dependent density function response theory (TD-DFRT)

The following section summarizes the formalisms used in TD-DFRT used in ADF and is based on Ref[121]. The derivation of properties like excitation energies and polarizabilities only require the linear density response of the system. The linear response of a system to a time-dependent electric field is given by:

$$\mu_i = \mu_i^{(0)} + \sum_j \alpha_{ij}(\omega) E_j(\omega) \tag{2.49}$$

where μ_i is the dipole moment in direction *i* at time *t* and $\mu_i^{(0)}$ is the dipole moment in direction *i* (*i*=*x*, *y*, *z*) at *t*=0 (molecule in the ground state). $\alpha_{ij}(\omega)$ is the linear dipole polarizability tensor, which has poles at the vertical excitation frequencies ω_i .

We need the first-order change in the time-dependent density of the spin *σ* electrons $\rho_\sigma^{(1)}$ in order to derive the polarizabilities. The first order time-dependent density in terms of KS orbitals in given by:

$$\rho_\sigma^{(1)}(\boldsymbol{r},\omega)=\sum_{i,a}\left[P_{ia}^{\sigma}(\omega)\psi_{a\sigma}(\boldsymbol{r})\psi_{i\sigma}(\boldsymbol{r})+P_{ai}^{\sigma}(\omega)\psi_{a\sigma}(\boldsymbol{r})\psi_{i\sigma}(\boldsymbol{r})\right] \tag{2.50}$$

The indices *i*, *j*, *k*… and *a*, *b*, *c*… denote occupied and unoccupied orbitals respectively. The indices *σ* and *τ* denote electron spins. *P* is the first order density matrix. Expanding the KS equations to first order of the applied field yields the following set of equations that can be solved to determine the density matrix elements:

$$\begin{gathered}\sum_{jb\tau}\left[\delta_{\sigma\tau}\delta_{ij}\delta_{ab}\left(\varepsilon_{a\sigma}-\varepsilon_{i\sigma}+\omega\right)+K_{ia\sigma,jb\tau}\right]P_{jb}^{\tau}+\sum_{jb\tau}K_{ia\sigma,jb\tau}P_{jb}^{\tau}=\left[\delta v_{ext}\right]_{ia\sigma}\\ \sum_{jb\tau}\left[\delta_{\sigma\tau}\delta_{ij}\delta_{ab}\left(\varepsilon_{a\sigma}-\varepsilon_{i\sigma}+\omega\right)+K_{ai\sigma,bj\tau}\right]P_{jb}^{\tau}+\sum_{jb\tau}K_{ai\sigma,jb\tau}P_{jb}^{\tau}=-\left[\delta v_{ext}\right]_{ai\sigma}\end{gathered} \tag{2.51}$$

where δ_{ij} is the Kronecker delta, ω is the frequency of the electromagnetic wave, and ε are KS orbital energies. The matrix elements of the external field $\left[\delta v_{ext}\right]_{ia\sigma}$ are given by:

$$\left[\delta v_{ext}\right]_{ia\sigma}=\left[\delta v_{ext}\right]_{ai\sigma}=\int d\boldsymbol{r}\psi_{i\sigma}(\boldsymbol{r})\delta\upsilon_{ext}(\boldsymbol{r})\psi_{a\sigma}(\boldsymbol{r}) \tag{2.52}$$

In the dipole case, the external potential can be written as:

$$\delta\upsilon_{ext}(\boldsymbol{r},\omega)=\sqrt{\frac{4\pi}{3}}Er\boldsymbol{\alpha}\cos(\omega t) \tag{2.53}$$

where *E* is the amplitude of the field and ***α*** is the polarization of the field (= *x*, *y*, *z*).
The matrix K is the coupling matrix and is defined as:

$$\begin{gathered}K_{ia\sigma,jb\tau}=\int d\boldsymbol{r}_1\int d\boldsymbol{r}_2\psi_{i\sigma}(\boldsymbol{r}_1)\psi_{a\sigma}(\boldsymbol{r}_1)\times\frac{1}{r_{12}}\psi_{j\sigma}(\boldsymbol{r}_2)\psi_{b\sigma}(\boldsymbol{r}_2)+\\ \int d\boldsymbol{r}_1\int d\boldsymbol{r}_2\psi_{i\sigma}(\boldsymbol{r}_1)\psi_{a\sigma}(\boldsymbol{r}_1)\times f_{xc}^{\sigma\tau}(\boldsymbol{r}_1,\boldsymbol{r}_2,\omega)\psi_{j\sigma}(\boldsymbol{r}_2)\psi_{b\sigma}(\boldsymbol{r}_2)\end{gathered} \tag{2.54}$$

The first term of the sum is the Hartree part and the second term is the exchange-correlation part. The *xc* kernel $f_{xc}^{\sigma\tau}$ is given by:

$$f_{xc}^{\sigma\tau}(\boldsymbol{r}_1,\boldsymbol{r}_2,t_1-t_2)=\frac{\delta v_{xc}(\boldsymbol{r}_1,t_1)}{\delta\rho_\tau(\boldsymbol{r}_2,t_2)} \tag{2.55}$$

If the adiabatic approximation is used and we choose real KS orbitals, we have $K_{ia\sigma,jb\tau}=K_{ia\sigma,bj\tau}$. Equation 2.51 can now be greatly simplified. The excitation energies ω_I and oscillator strengths f_I (I here labels the excited state number) can now be derived from a simple eigenvalue equation:

$$\Omega\boldsymbol{F}_I=\omega_I^2\boldsymbol{F}_I \tag{2.56}$$

where the matrix elements Ω are given by:

$$\Omega_{ia\sigma,jb\tau}=\delta_{\sigma\tau}\delta_{ij}\delta_{ab}\left(\varepsilon_a-\varepsilon_i\right)^2+2\sqrt{\left(\varepsilon_a-\varepsilon_i\right)}K_{ia\sigma,jb\tau}\sqrt{\left(\varepsilon_b-\varepsilon_j\right)} \tag{2.57}$$

The oscillator strength can be derived from the eigenvectors F_I:

$$f_I=\frac{2}{3}\left(\left|\vec{x}^\dagger S^{-1/2}\vec{F}_I\right|^2+\left|\vec{y}^\dagger S^{-1/2}\vec{F}_I\right|^2+\left|\vec{z}^\dagger S^{-1/2}\vec{F}_I\right|^2\right)/\left|\vec{F}_I\right|^2 \tag{2.58}$$

where $S_{ia\sigma,jb\tau}=\dfrac{\delta_{\sigma\tau}\delta_{ij}\delta_{ab}}{\left(f_{j\tau}-f_{b\tau}\right)\left(\varepsilon_{b\tau}-\varepsilon_{j\tau}\right)}$

If we assume that the products $\psi_{i\sigma}(\boldsymbol{r})\psi_{a\sigma}(\boldsymbol{r})$ are linearly independent and the ground state wavefunction is a single determinant (eq.2.24) we can expand the excited state wavefunction as a linear combination of singly excited configurations Ψ:

$$\Phi_I=\sum_{ia\sigma}^{f_{i\sigma}-f_{a\sigma}>0}\sqrt{\frac{\varepsilon_{a\sigma}-\varepsilon_{i\sigma}}{\omega_I}}F_{ia\sigma}^I\hat{a}_{i\sigma}^\dagger\hat{a}_{a\sigma}\Psi \tag{2.59}$$

where $\hat{a}^\dagger$ and $\hat{a}$ are the creation and annihilation operators respectively. Ψ represents singly excited wavefunctions defined in eq.2.37. $F_{ia\sigma}^I$ represents the contribution of the one-electron transition $\psi_{i\sigma}\rightarrow\psi_{a\sigma}$. We can now also express the oscillator strength (2.58) of each excited state as a combination of the elements $F_{ia\sigma}^I$ and therefore assign each single-particle transition a contribution to the total oscillator strength.

Configuration interaction

Configuration interaction (CI) is a quantum mechanical method used to determine the correlation energy of a system in its ground state and can also be used for excited states. The essence of the method is to diagonalize the N-electron Hamiltonian in a basis of N-electron Slater determinants. The CI wavefunction is given by:

$$\Psi = \sum_{i=1}^{N} A_i \Phi_i \tag{2.60}$$

where A_i are weighing coefficients and Φ_i are the Slater determinants. The Slater determinants can be the ground state determinant but also singly excited (CIS), doubly excited (CISD), triply excited (CIDST)… In order to determine the energy E and wavefunction Ψ of the state of interest, we solve the eigenvalue problem:

$$\begin{bmatrix} \langle \Phi_1 | \hat{H} | \Phi_1 \rangle & \langle \Phi_1 | \hat{H} | \Phi_2 \rangle & \cdots & \langle \Phi_1 | \hat{H} | \Phi_N \rangle \\ \langle \Phi_2 | \hat{H} | \Phi_1 \rangle & \langle \Phi_2 | \hat{H} | \Phi_2 \rangle & \cdots & \langle \Phi_2 | \hat{H} | \Phi_N \rangle \\ \vdots & \vdots & \ddots & \vdots \\ \langle \Phi_N | \hat{H} | \Phi_1 \rangle & \langle \Phi_N | \hat{H} | \Phi_2 \rangle & \cdots & \langle \Phi_N | \hat{H} | \Phi_N \rangle \end{bmatrix} \begin{bmatrix} A_1 \\ A_2 \\ \vdots \\ A_N \end{bmatrix} = E \begin{bmatrix} A_1 \\ A_2 \\ \vdots \\ A_N \end{bmatrix} \tag{2.61}$$

In principle, if we expand the wavefunction in an infinite basis and includ all possible excited determinants (singly, doubly, triply, quadruply…), the solution to the CI gives the exact wavefunction with the exact energy. Computationally, this is of course not possible and the level of accuracy obtained depends on the level of theory used. For commonly investigated systems (in the order of 10 atoms), it is difficult to go beyond CISD. Alternative methods have been developed to include triply excited configurations at a lower cost by including them perturbatively. This is called CISD(T). The CI method is not highly used due its high computational cost and the fact that it is not size consistent. However, it is one of the best to describe highly correlated systems.

Chapter 3 - Theoretical analysis of the optical excitation spectra of silver and gold nanowires

Guidez, E. B.; Aikens, C. M. *Nanoscale* **2012**, *4,* 4190
Reproduced by permission of The Royal Society of Chemistry

Abstract

The excitation spectra of linear atomic chains of silver and gold with various sizes have been calculated using time-dependent density functional theory. Silver chains show longitudinal and transverse peaks as well as a low-intensity *d*-band. The longitudinal peak, corresponding to the HOMO-LUMO transition (along the main axis of the chain), shifts linearly to the red as the length of the system increases, consistent with the particle-in-a-box model. The transverse peak remains at approximately constant energy for all systems studied and corresponds to $\Sigma_m \rightarrow \Pi_m$ transitions in the *xy* plane perpendicular to the chain. As the chain grows, transitions arising from *d* orbitals contribute to the transverse peak, which affects its oscillator strength. Contrary to silver, gold chains display a strong *d*-band that converges to a distinct pattern at a chain length of about twelve atoms. The transitions involved in the *d*-band originate from localized *d*-orbitals with a d_{z^2} character since they have the right symmetry to give transitions into the LUMO, LUMO+1... which have Σ symmetry. Transitions arising from these localized *d*-orbitals also affect the position of the longitudinal peak and generate a wide transverse band. Although the majority of the transitions involved in the transverse band have a $d\Sigma \rightarrow \Pi$ or $d\Pi \rightarrow \Sigma$ character, they are hidden by much stronger excitations of $d\Pi \rightarrow \Pi$ character in gold nanowires.

Introduction

Noble metal nanoparticles (e.g. Ag, Au) have been recently studied for applications in sensing,[122,123] catalysis[124] as well as the environmental[125] and biomedical fields.[34,36,126,127] One of the attractive properties of 10-100 nm noble metal nanoparticles is that they show a strong absorption peak in the visible-IR region that can be tuned by varying their size,[24] shape,[128,129] or chemical environment.[29] This is due to the concerted excitation of the conduction electrons in the presence of an electric field, or surface plasmon resonance (SPR).[51,52,130-132] As the nanoparticle size decreases (down to hundreds of atoms), molecular properties arise and the absorption spectrum becomes more complex. Quantum-mechanical calculations have been used to model the optical properties of noble metal clusters. In particular, time-dependent density functional theory (TDDFT) has been shown to provide insights regarding the origin of the discrete absorption spectra of noble metal clusters.[64,66,81,133,134] Molecular excitations obtained with TDDFT for small clusters show intense peaks analogous to the plasmon excitations of larger nanoparticles and correspond well with peaks described in the Mie theory framework or with other classical electrodynamics methods.[50,64] For example, tetrahedral Ag_{20} exhibits an intense peak that arises from a collective *sp* → *sp* intraband transition.[64]

Significant progress has been achieved in synthesizing gold and silver nanoparticles with a wide variety of shapes including spherical,[58] cylindrical,[135] decahedral,[136] icosahedral,[137] and triangular.[138] Cylindrical nanoparticles (nanorods and nanowires) are of particular interest since their optical properties are very sensitive to their aspect ratio.[131,139,140] Studies of linear atomic chains of alkali metals (Na, K) and noble metals (Ag, Au) showed two main plasmon resonances: a longitudinal mode along the main axis of the chain and two transverse modes perpendicular to that axis.[141,142] The energy and intensity of the longitudinal mode can be tuned by changing the length of the chain. The two transverse modes correspond to plasmon resonances at the end-atoms and inner atoms of the chain respectively. Therefore, the behavior of the electrons on the more exposed end-atoms is very distinct from the central atoms. The transverse plasmon resonance of gold nanowires was previously shown to strongly enhance two-photon absorption.[143] Both alkali metals and noble metals have a single electron in their valence shell. However, *d* electrons affect the plasmon resonance of the noble metal clusters, especially for gold due to relativistic effects.[53,66,144]

The aim of this work is to compare the absorption spectra of gold and silver nanowires (NWs), here defined as a linear chain of atoms, using time-dependent density functional theory and show how they are affected by the length of the nanowires. Orbitals involved in the main longitudinal and transverse excitations are discussed in detail for both silver and gold nanowires.

Computational details

All calculations in this work are performed with the Amsterdam Density Functional (ADF) package.[110] All the geometry optimizations are run using the generalized gradient approximation

(GGA) Becke-Perdew (BP86) exchange-correlation functional[102,103] and an all-electron double-zeta (DZ) basis set. Scalar relativistic effects are included with the zeroth-order regular approximation (ZORA).[115,116] In order to have closed-shell species, positively and negatively charged species are considered for nanowires with an odd number of atoms. Excitation spectra are calculated using time-dependent density functional theory (TDDFT) with the statistical average of orbital potentials (SAOP)[145] and LB94[146] model potentials. An all-electron double-zeta basis set is used for the SAOP calculations. With the LB94 potential, a frozen core is considered and the basis set used is DZ.4p for silver and DZ.4f for gold. The absorption spectra are convoluted with a Gaussian with a full width at half maximum of 0.2 eV. Orbitals are represented with a contour value of 0.02.

Results and discussion

Silver nanowires

The excitation spectra of silver nanowires are analyzed in this section. The spectra of the neutral silver nanowires are analyzed first at the SAOP/DZ and LB94/DZ levels of theory, followed by a comparison with the positively and negatively charged nanowires.

Neutral nanowires

The absorption spectra of silver nanowires Ag_n (n=2, 4, 8, 10, …, 20, and 40) show three distinct features: a sharp low-energy longitudinal peak, a low-intensity *d*-band and a transverse peak at about 6.3 eV (197 nm). The excitation spectrum of Ag_{20} is presented in Figure 3-1A.

Figure 3-1. Excitation spectra of A) Ag_{20} nanowire and B) Ag_{40} nanowire at the SAOP/DZ level of theory.

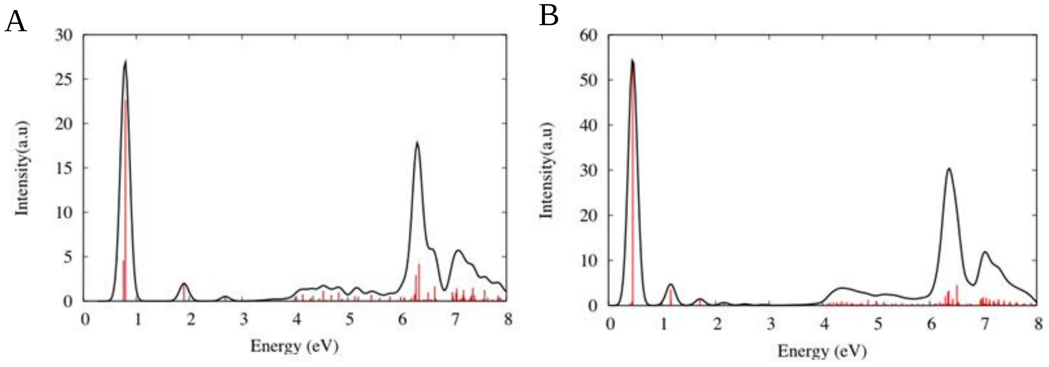

The rest of the spectra are shown in Appendix A. The longitudinal peak corresponds to the HOMO→LUMO transition (Σ→Σ). At the SAOP/DZ level of theory, this peak red shifts linearly from about 358 nm (3.46 eV) to 1562 nm (0.79 eV) as the length of the wire chain increases, as shown in Figure 3-2A.

Figure 3-2. Longitudinal and transverse peak wavelengths (nm) for A) neutral B) positively charged and C) negatively charged silver nanowires.

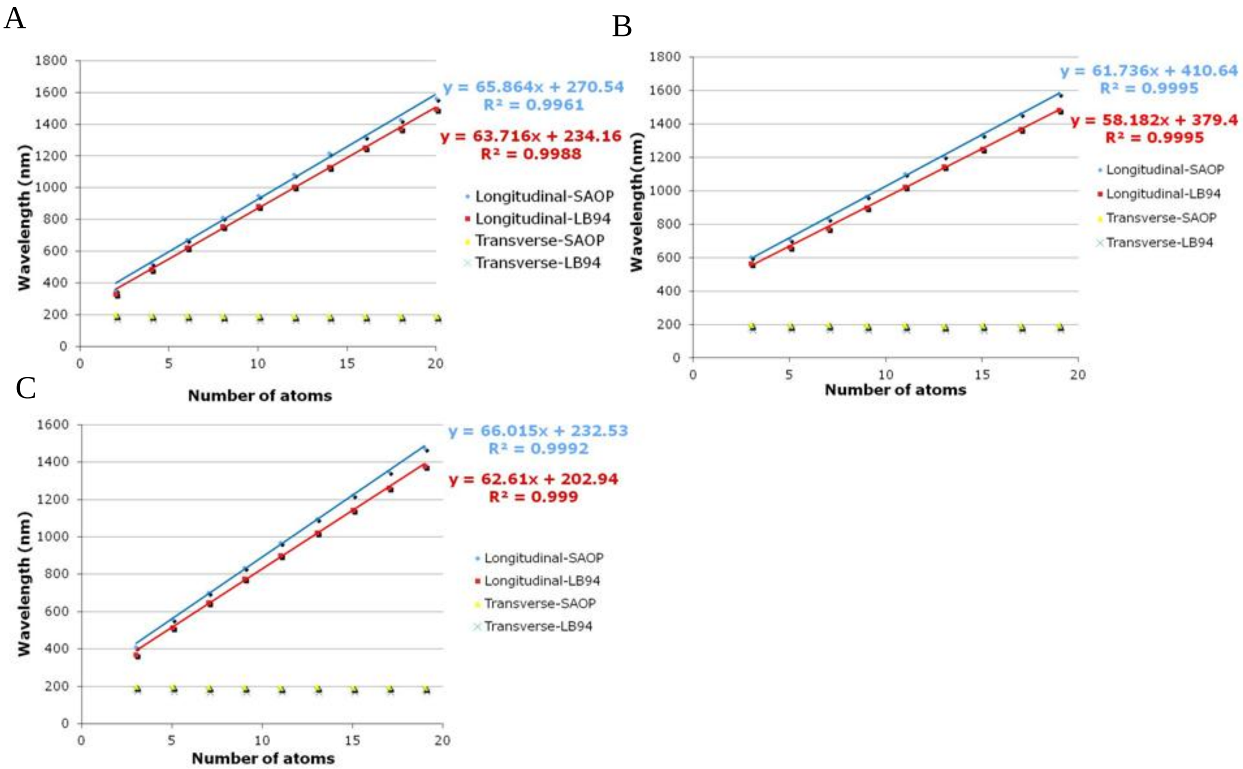

The linear shift of the longitudinal peak is in accordance with the particle-in-a-cylinder model, as previously discussed by Johnson and Aikens.[70] A similar linear relationship is observed at the LB94/DZ level of theory but with a slightly smaller magnitude (Figure 3-2A). Note that the transition energies tend to occur at higher wavelength with the exchange-correlation model LB94 than with SAOP as previously observed elsewhere.[64,70] An analogous red-shift of the longitudinal absorption peak with increasing aspect ratio is observed for noble metal nanowires synthesized experimentally.[32,147] As the aspect ratio increases, the energy of this peak tends to zero and its wavelength increases. Nanowires with very high aspect ratios can be transparent in the visible and near-IR regions.[147] In the linear atomic chains, the HOMO-LUMO gap will eventually approach zero which means that the system will become metallic as in the bulk material.

The HOMO and LUMO orbitals both have a strong delocalized *s* character as shown for Ag_6 in Figure 3-3. These delocalized orbitals originate from the linear combination of the singly occupied 5*s* electron of the silver atoms.

Figure 3-3. Kohn-Sham orbital energy diagram of Ag_6 at the BP86/DZ level of theory.

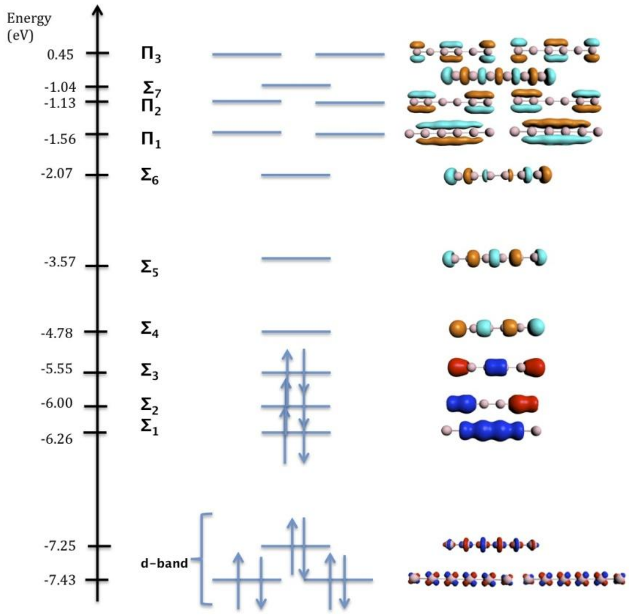
Energy (eV)
0.45
-1.04
-1.13
-1.56
-2.07
-3.57
-4.78
-5.55
-6.00
-6.26
-7.25
-7.43
Π_3
Σ_7
Π_2
Π_1
Σ_6
Σ_5
Σ_4
Σ_3
Σ_2
Σ_1
d-band

Since the 5*s* orbital of silver lies much higher in energy than the 4*d* orbitals, the HOMO-LUMO transitions are well defined and separated from the rest of spectrum (about 1.1 eV gap for Ag_{20}). We also note that the HOMO-LUMO transition starts splitting at a chain length of six atoms due to some contribution of the HOMO-2→LUMO transition, which is close in energy. As the nanowires grow longer, the splitting between the two peaks becomes smaller. The intensity of the longitudinal peak varies linearly with the length of the wire (and thus the number of electrons), as shown in Figure 3-4. The peak intensities tend to be somewhat higher at the LB94/DZ level of theory but follow the same trend.

Figure 3-4. Oscillator strength* of A) the longitudinal peak of silver nanowires with SAOP/DZ; B) the transverse peak of silver nanowires with SAOP/DZ; C) the longitudinal peak of silver nanowires with LB94/DZ; D) the transverse peak of silver nanowires with LB94/DZ.

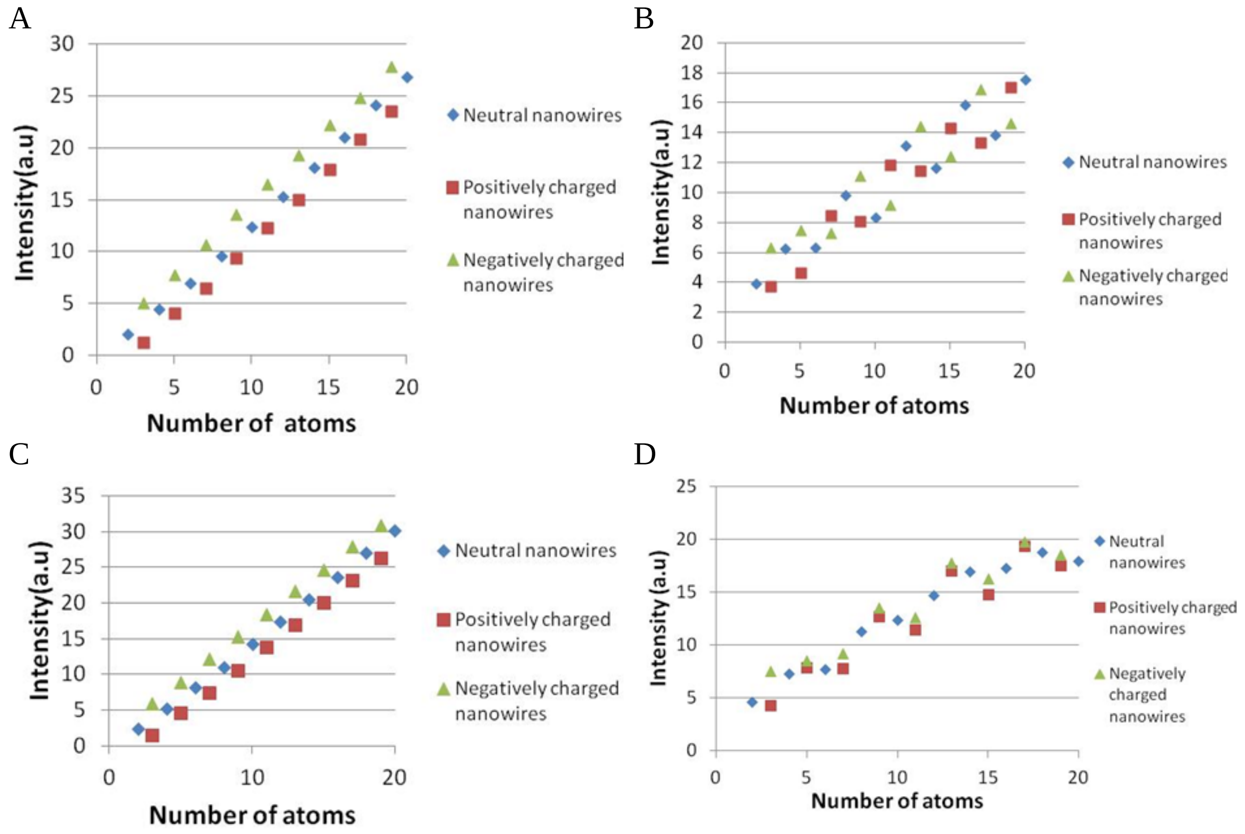

* The maximum intensity of the Gaussian convolution was considered.

In the nanowire case, the longitudinal peak corresponds to a single HOMO-LUMO excitation. On the other hand, the longitudinal peak of silver nanorods with a larger diameter arise from several transitions involving delocalized orbitals.[70] For example, for the pentagonal Ag$_{25}^{+1}$, the strong longitudinal peak appears at 3.40 eV and corresponds to a linear combination of three "single-particle transitions" (a term referring to an electronic transition between an occupied and an unoccupied orbital) of Π→Π (HOMO-1 → LUMO+4) and Σ→Σ (HOMO-2 → LUMO and HOMO-2 → LUMO+2) character.[70] The HOMO-LUMO transition is not allowed by symmetry.[70] The mixed transition at 3.40 eV arises when the *z*-components of the transition dipole moment combine in-phase; two weak peaks at 1.85 eV and 2.07 eV also arise from a linear combination of the same three single-particle transitions but have low oscillator strength and are not observable in the excitation spectrum because of a destructive interference of the transition dipole moments.[70] The coupling between those transitions and the mechanism by which they form a single peak is yet to be understood, but appears to be the key factor in connecting the excitations of smaller clusters with the plasmon resonance of larger nanoparticles. The longitudinal peak for the nanowires examined in this work corresponds mainly to a single excitation, leading to a very sharp single peak. The peak assigned as plasmon for larger systems involves more transitions leading to broadening of the peak, especially for systems with partially filled shells.[64,70] Thus, it appears that a plasmon may be understood as a combination of single-particle transitions that constructively interact; in addition, multiple peaks in the same energy region can contribute. It is also important to note that we can expect the electron density of these nanorods in the excited state to be delocalized on the surface similar to the surface plasmon resonance, as explained by Harb *et al* for spherical silver clusters.[50]

The next transition observed for the small nanowires Ag_n ($4 \leq n \leq 8$) corresponds to a transition out of the *d*-band. The energy between the start of the *d*-band and the HOMO-LUMO peak varies between 1.56 eV (Ag_4) and 1.73 eV (Ag_8). For the larger nanowires Ag_n ($10 \leq n \leq 20$), a second longitudinal peak appears below the *d*-band transitions. Its energy lies between 1.1 eV (Ag_{20}) and 1.6 eV (Ag_{10}) higher than the HOMO-LUMO peak. As the nanowires grow longer, energy gaps become smaller due to the increased number of interactions between the orbitals. Therefore, additional peaks appear and a greater number of *d*-band transitions are revealed. However, the intensities and energies of the *d*-band transitions remain constant, contrary to the main longitudinal peak. The *d*-orbitals are localized as shown in Figure 3-3. As a result, the energies and intensities of the transitions originating from these orbitals are not greatly affected by the size of the nanowires. The *d*-band also appears smaller as the nanowires grow longer since the intensity of the main longitudinal peak increases uniformly with the chain length. For very long nanowires, the *d*-band practically disappears as observed in the Ag_{40} case (Figure 3-1B) in which only the longitudinal and transverse peaks can be seen. This is in accordance with what is observed experimentally for silver nanorods with diameters in the several-tens of nanometers range.[148]

The transverse peak corresponds to transitions in the *xy* plane ($\Sigma_m \rightarrow \Pi_m$, where *m* is a quantum number). Since the diameter of the nanowires does not change, the energy of this peak remains relatively constant, only varying between 6.1 eV (204 nm) and 6.4 eV (195 nm) at the SAOP/DZ level of theory, as shown in Figure 3-2A. As discussed previously, transitions are shifted to smaller wavelengths with LB94/DZ and the energy of the transverse peak varies between 6.6 eV (186 nm) and 6.9 eV (178 nm). Table 3-1 shows the transitions involved in the main transverse peak at the SAOP/DZ level of theory. For Ag_n, the number of $\sum_m \rightarrow \prod_m$ transitions is $n/2$. Therefore, the longer the nanowires are, the higher the number of transitions that can contribute to the transverse peak. For instance, the transverse peak of the nanowire Ag_8 has contributions from $\sum_1 \rightarrow \prod_1$, $\sum_2 \rightarrow \prod_2$, $\sum_3 \rightarrow \prod_3$ and $\sum_4 \rightarrow \prod_4$. The dipole moment contributions for each transition add constructively. For $n \geq 10$, the trend continues but only the first few transitions are shown in the table. Additionally, we can see that the transverse peak has a large intensity (at least three times as large as the *d*-band). Although the intensity of the peak generally increases with length, it shows some oscillations as shown in Figure 3-4B. Note that this oscillatory behavior is a little different at the LB94/DZ level of theory (Figure 3-4D). These oscillations can be explained by some contributions of the *d*-band to the peak. In fact, starting at a length of six atoms, *d*-transitions start to mix with the $\sum_m \rightarrow \prod_m$ transverse transitions as shown in Table 3.1. Although the main contribution to the dipole moment originates from $\sum_m \rightarrow \prod_m$ transitions, the weights of the *d*-transitions that participate are large enough that the contribution to the peak intensity is non-negligible. However, the individual *d*-band contributions to the dipole moment are rather small.

Table 3.1. Transitions contributing to the high-intensity transverse peak in silver nanowires at the SAOP/DZ level of theory.

Ag$_n$	Energy (eV)	Transitions	Type of transition	Weight	Contribution to dipole moment
2	6.06	$10\sigma^{+}_{g}$(HOMO)$\rightarrow 6\pi_{u}$	$\Sigma_1\rightarrow\Pi_1$	0.9269	2.2276
4	6.17	$19\sigma^{+}_{u}$(HOMO)$\rightarrow 11\pi_{g}$	$\Sigma_2\rightarrow\Pi_2$	0.4742	-1.5740
		$19\sigma^{+}_{g}$(HOMO-1)$\rightarrow 11\pi_{u}$	$\Sigma_1\rightarrow\Pi_1$	0.3838	-1.4066
6	6.20	$13\pi_{u}\rightarrow 30\sigma^{+}_{g}$	d-band	0.4017	-0.1888
		$29\sigma^{+}_{g}$(HOMO)$\rightarrow 17\pi_{u}$	$\Sigma_3\rightarrow\Pi_3$	0.1873	0.9849
		$28\sigma^{+}_{u}$(HOMO-1)$\rightarrow 16\pi_{g}$	$\Sigma_2\rightarrow\Pi_2$	0.1340	0.8309
		$28\sigma^{+}_{g}$(HOMO-2)$\rightarrow 16\pi_{u}$	$\Sigma_1\rightarrow\Pi_1$	0.1071	0.7391
8	6.29	$37\sigma^{+}_{u}$(HOMO-2)$\rightarrow 22\pi_{g}$	$\Sigma_2\rightarrow\Pi_4$	0.2632	0.1029
		$38\sigma^{+}_{u}$(HOMO)$\rightarrow 22\pi_{g}$	$\Sigma_4\rightarrow\Pi_4$	0.1583	0.8980
		$37\sigma^{+}_{g}$(HOMO-3)$\rightarrow 21\pi_{u}$	$\Sigma_1\rightarrow\Pi_1$	0.1036	0.7217
		$37\sigma^{+}_{u}$(HOMO-2)$\rightarrow 21\pi_{g}$	$\Sigma_2\rightarrow\Pi_2$	0.0971	0.7008
		$38\sigma^{+}_{g}$(HOMO-1)$\rightarrow 22\pi_{u}$	$\Sigma_3\rightarrow\Pi_3$	0.0909	0.6796
10	6.25	$21\pi_{g}\rightarrow 49\sigma^{+}_{u}$	d-band	0.4215	-0.2309
		$22\pi_{g}\rightarrow 49\sigma^{+}_{u}$	d-band	0.1269	0.1588
		$48\sigma^{+}_{g}$(HOMO)$\rightarrow 28\pi_{u}$	$\Sigma_5\rightarrow\Pi_5$	0.1106	0.7517
		$47\sigma^{+}_{u}$(HOMO-1)$\rightarrow 27\pi_{g}$	$\Sigma_4\rightarrow\Pi_4$	0.0938	0.6919
12	6.26	$27\pi_{g}\rightarrow 59\sigma^{+}_{u}$	d-band	0.3018	0.0745
		$57\sigma^{+}_{g}$(HOMO-1)$\rightarrow 34\pi_{u}$	$\Sigma_5\rightarrow\Pi_7$	0.1418	0.1009
		$57\sigma^{+}_{u}$(HOMO)$\rightarrow 33\pi_{g}$	$\Sigma_6\rightarrow\Pi_6$	0.1061	-0.7348
		$57\sigma^{+}_{g}$(HOMO-1)$\rightarrow 33\pi_{u}$	$\Sigma_5\rightarrow\Pi_5$	0.0806	-0.6399
14	6.27	$30\pi_{u}\rightarrow 69\sigma^{+}_{g}$	d-band	0.4543	0.2564
		$67\sigma^{+}_{g}$(HOMO)$\rightarrow 40\pi_{u}$	$\Sigma_7\rightarrow\Pi_7$	0.0401	-0.4511
		$31\pi_{u}\rightarrow 69\sigma^{+}_{g}$	d-band	0.0896	-0.1321
		$66\sigma^{+}_{u}$(HOMO-1)$\rightarrow 39\pi_{g}$	$\Sigma_6\rightarrow\Pi_6$	0.0346	-0.4185
16	6.28	$36\pi_{u}\rightarrow 79\sigma^{+}_{g}$	d-band	0.3422	-0.0875
		$76\sigma^{+}_{u}$(HOMO)$\rightarrow 45\pi_{g}$	$\Sigma_8\rightarrow\Pi_8$	0.1085	-0.0582
		$76\sigma^{+}_{u}$(HOMO)$\rightarrow 44\pi_{g}$	$\Sigma_8\rightarrow\Pi_6$	0.0720	0.6037
		$76\sigma^{+}_{g}$(HOMO-1)$\rightarrow 44\pi_{u}$	$\Sigma_7\rightarrow\Pi_7$	0.0599	0.5499
18	6.28	$38\pi_{g}\rightarrow 88\sigma^{+}_{u}$	d-band	0.4372	-0.2608
		$39\pi_{g}\rightarrow 88\sigma^{+}_{u}$	d-band	0.1469	0.1669
		$86\sigma^{+}_{g}$(HOMO)$\rightarrow 50\pi_{u}$	$\Sigma_9\rightarrow\Pi_9$	0.0519	0.5125
		$85\sigma^{+}_{u}$(HOMO-1)$\rightarrow 49\pi_{g}$	$\Sigma_8\rightarrow\Pi_8$	0.0457	0.4804
20	6.34	$44\pi_{g}\rightarrow 98\sigma^{+}_{u}$	d-band	0.4078	-0.0984
		$49\pi_{g}\rightarrow 99\sigma^{+}_{u}$	d-band	0.0564	-0.0071
		$43\pi_{g}\rightarrow 98\sigma^{+}_{u}$	d-band	0.0553	0.1042
		$91\sigma^{+}_{g}\rightarrow 55\pi_{u}$	d-band	0.0490	0.0028
		$95\sigma^{+}_{u}$(HOMO)$\rightarrow 55\pi_{g}$	$\Sigma_{10}\rightarrow\Pi_{10}$	0.0376	-0.4333
		$95\sigma^{+}_{g}$(HOMO-1)$\rightarrow 55\pi_{u}$	$\Sigma_9\rightarrow\Pi_9$	0.0356	-0.4215

Positively and negatively charged nanowires

The absorption spectra of the positively charged silver nanowires Ag_n^+ (n=3, 5, 7, 9, …, 19) and their negatively charged counterparts Ag_n^- (n=3, 5, 7, 9, …, 19) share many similar features with the spectra of the neutral nanowires: they also have a longitudinal peak corresponding to the HOMO-LUMO transition, a low-intensity *d*-band, and a transverse peak that corresponds to one or more $\sum_m \rightarrow \prod_m$ transitions. We note that the HOMO-LUMO gap of the positively charged nanowires decreases much slower than the HOMO-LUMO gaps obtained for the neutral and negatively charged species. In fact, the slope of the absorption wavelength of the longitudinal peak is distinctively smaller for positively charged nanowires, as shown in Figure 3-2. Figures 3-4A and 3-4C shows that the more negatively charged the nanowires is, the larger the intensity of the longitudinal peak. This may be explained by the larger electron density for the negative species. On the other hand, the energy of the transverse peak is not very affected by the charge of the nanowires. The intensity of the transverse peak shows similar oscillations for the positively charged and negatively charged species as those encountered for the neutral species (Figure 3-4B and 3-4D). The energy and intensity of the *d*-based transitions are also not affected by the charge of the nanowires, which can be explained by the fact that the *d* orbitals are localized.

Gold nanowires

In this section, the absorption spectra of gold nanowires are analyzed and compared with their silver analogs. The absorption spectra of gold nanowires also exhibit longitudinal and transverse peaks as well as transitions arising from the *d*-band, as shown with Au_{20} in Figure 3-5A. The spectra of the neutral species are first discussed with an additional focus on the *d*-band, followed by a brief comparison with the positively charged and negatively charged species.

Figure 3-5. A) SAOP/DZ excitation spectrum of the Au_{20} nanowire. B) Subset of SAOP/DZ transverse excitation modes for the Au_{20} nanowire.

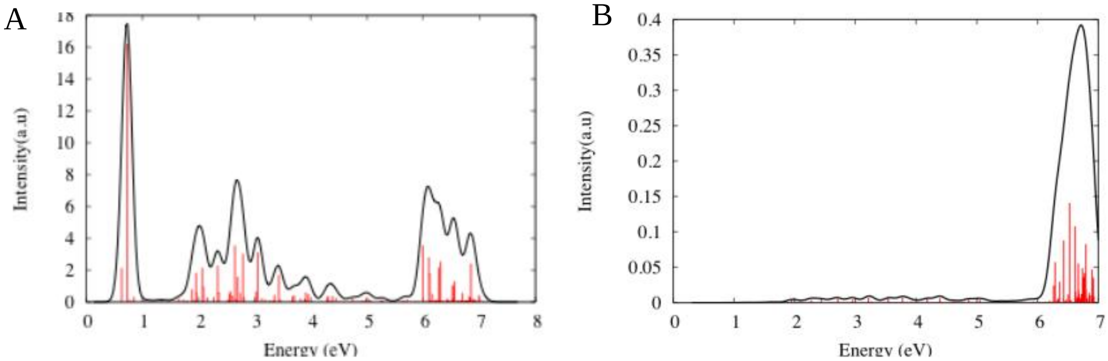

Neutral gold nanowires

Contrary to the silver case, transitions originating from the *d*-band are important for the gold nanowires since they highly affect the longitudinal and transverse peak energies and intensities. In fact, the 5*d* orbitals of the gold atom lie closer in energy to the 6*s* orbital than do the 4*d* orbitals of silver to the 5*s*. Figure 3-6A shows the wavelengths of the longitudinal peak for neutral gold nanowires. A red shift of the longitudinal peak is observed. A similar observation was found at the PW91/LANLDZ level of theory.[144] At the SAOP/DZ level of theory, a break in linearity occurs at ten atoms (eights atoms with LB94/DZ), which is the size where the longitudinal peak becomes distinguishable from the *d*-based transitions.

Figure 3-6. Wavelengths of main longitudinal peak for A) neutral B) positively charged and C) negatively charged gold nanowires.

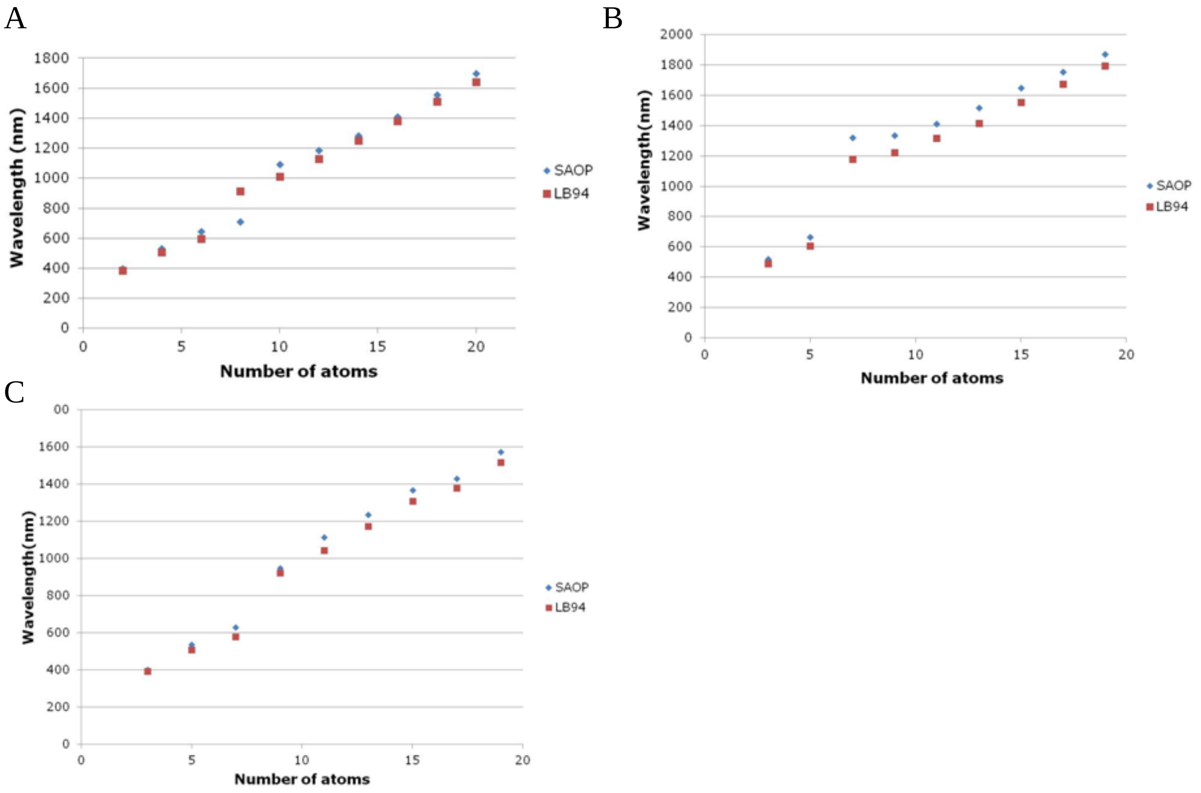

At that system length, the peak intensity becomes stronger than the intensity of the transitions originating from the *d*-band. The HOMO-LUMO transition couples with the *d*-based transitions because they have the same symmetry. As a result, a splitting of the longitudinal peak occurs. We can adjust for this effect by considering the weighted average of the transition dipole moment of the HOMO-LUMO transition from several excitation peaks. As shown in Figure 3-7A, the linear relationship between the wavelength of the HOMO-LUMO transition and the number of atoms in the chain is recovered. This shows that the longitudinal transitions of gold nanowires still follow the particle-in-a-cylinder model but the *d*-band splits the HOMO-LUMO peak. Since the *d*-band energy does not vary much with size whereas the energy of the longitudinal peak red shifts with length, the energy difference between the *d*-based transitions and the longitudinal peak increases as the nanowires grows from Au_{10} to Au_{20} and this difference reaches about 1 eV for Au_{20}. However, this energy difference is more than 1 eV smaller than the one discussed previously with the silver nanowires.

Figure 3-7. Weighted average of the HOMO-LUMO transition for A) neutral B) positively charged and C) negatively charged gold nanowires.

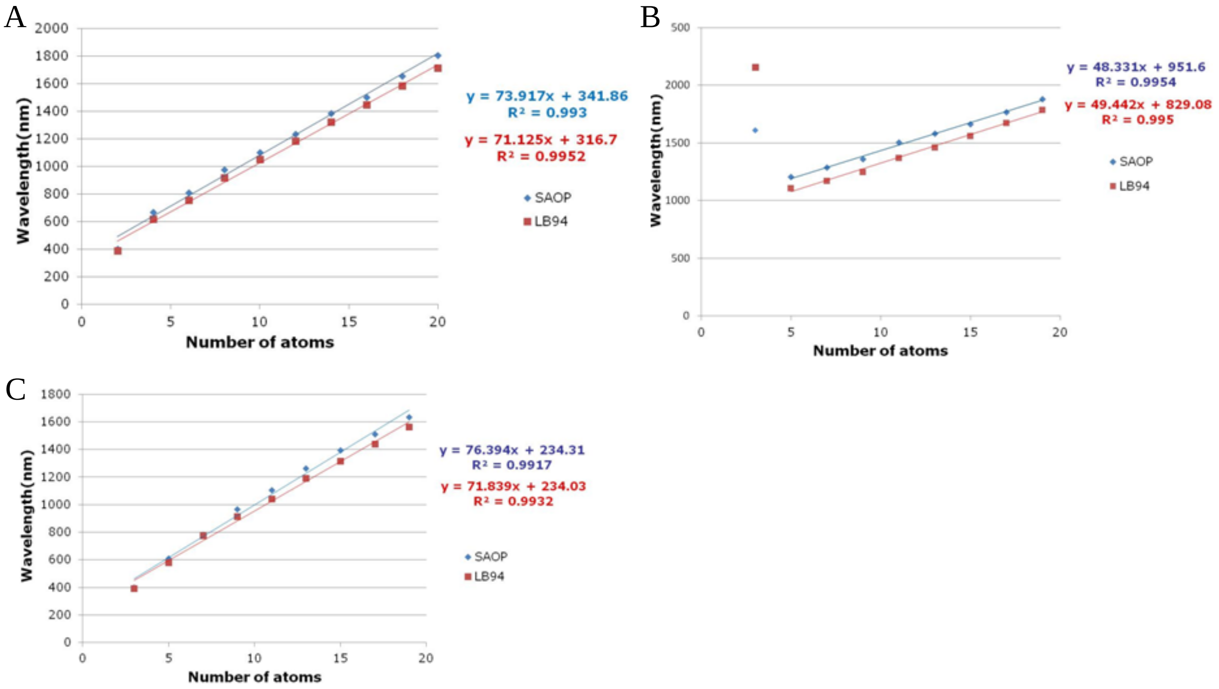

It should be noted that the *d*-band mixing is also reflected in the intensity of the longitudinal peak. As shown in Figure 3-8, the intensity of the longitudinal peak starts increasing linearly with chain length at 8-10 atoms. This corresponds to the size where the longitudinal peak starts to separate from the *d*-based transitions.

Figure 3-8. Oscillator strength of the longitudinal transition energy of gold nanowires with A) SAOP/DZ and B) LB94/DZ.

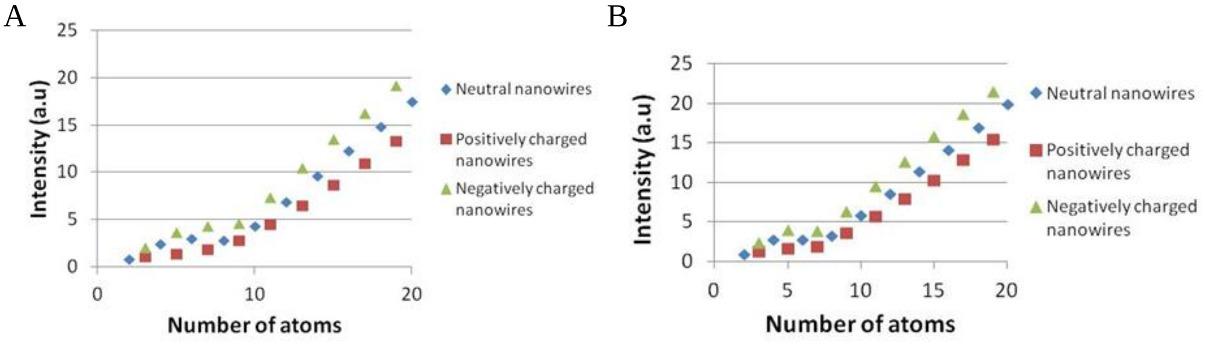

Contrary to the silver case, a transverse peak can only be distinguished in the two-atom chain. For the longer nanowires, a broad band begins at about 6 eV instead. This band shows a similar pattern for all the nanowires and starts converging at a system length of about twelve atoms. The high-intensity transitions involved are mainly d∏→∏ transitions, as shown in Table 3.2. These transitions arise from localized *d*-orbitals to delocalized *s*-based ∏ orbitals. Because of the symmetry of these transitions, they will be excited by *z*-polarized light.

Table 3.2. Transitions with the highest oscillator strength occurring between 6 and 7 eV for the Au_{20} nanowire.

Energy (eV)	Oscillator strength	Transition	Weight	Contribution to the dipole moment
5.99	0.76	$80\pi_g \rightarrow 81\pi_u$	0.9530	2.8721
6.10	0.60	$79\pi_g \rightarrow 81\pi_u$ $80\pi_u \rightarrow 81\pi_g$	0.5901 0.3476	-0.1782 -1.6479
6.28	0.46	$79\pi_u \rightarrow 81\pi_g$ $79\pi_g \rightarrow 82\pi_u$	0.5308 0.3315	0.1957 1.4809
6.31	0.54	$79\pi_g \rightarrow 82\pi_u$	0.4586	1.7373
6.85	0.52	$78\pi_g \rightarrow 83\pi_u$	0.6392	1.6190

Figure 3-5B displays only the transverse excitations of Au_{20}, which correspond to excitations across the short axis of the wire (*xy*-plane). Transverse peaks begin at a wavelength of about 6.3 eV and their oscillator strength is about ten times smaller than the d∏→∏ excitation. Those transverse modes are mainly d∑→∏ and d∏→∑ transitions and they all have high contributions to the dipole moments, although not quite as high as the d∏→∏ transitions (Table 3.3).

Table 3.3. d∑→∏ transitions involved in the transverse band of the Au_{20} nanowire at SAOP/DZ level of theory.

Energy (eV)	Oscillator strength	Transition	Weight	Contribution to the dipole moment
6.29	0.013	$129\sigma^+_g \rightarrow 81\pi_u$	0.2369	-1.0961
6.43	0.019	$130\sigma^+_g \rightarrow 82\pi_u$	0.5052	-1.4817
6.53	0.030	$130\sigma^+_u \rightarrow 82\pi_g$	0.4212	1.3255
6.62	0.023	$132\sigma^+_g \rightarrow 83\pi_u$	0.4002	1.1708
6.79	0.018	$131\sigma^+_u \rightarrow 83\pi_g$	0.4873	-0.7199

The d∑→∏ and d∏→∑ transitions are the majority in the 6-7 eV range but they are hidden by a few more intense d∏→∏ transitions described above. It should be noted that a band of transverse dipole excitation modes between 5 and 6 eV was previously observed at the PW91/LANL2DZ level of theory with a frozen orbital picture.[144] Moreover, we expect that the intensity of this transverse band would increase as the diameter of the system increases. An investigation of the effect of the diameter on the excitation spectra is currently underway.

Since the *d*-band is so important for gold species, it is discussed in more detail here. As the wire grows longer, the *d*-band forms a distinct pattern. In order to study this pattern, all the *d*-based transitions between the longitudinal peak and transverse band are plotted for the neutral nanowires with 12 to 20 atoms, as shown in Figure 3-9A. Two main transitions occur at about 2 and 2.8 eV. A series of transitions with lower oscillator strength occur between 3.5 and 5.5 eV. The transition energies shift slightly depending on the size of the nanowires but the overall pattern is apparent. A density of states diagram showing the *d* orbitals for gold nanowires with 12 to 20 atoms is also shown in Figure 3-9B. We note that the two figures are practically mirror images of one another. However, the density of states diagram is broader than the excitation spectrum. This can be explained by the fact that the density-of-states diagram includes all the *d* orbitals (i.e with d_{xy}, d_{xz}, d_{yz}, $d_{x^2-y^2}$ and d_{z^2} character). However, the transitions involved in the excitation spectrum originate from *d* orbitals with d_{z^2} character. In fact, they are the only *d* orbitals with the right symmetry to contribute to transitions into LUMO, LUMO+1, LUMO+2, LUMO+3 and LUMO+4 orbitals, which have ∑ character.

Figure 3-9. A) *d*-band of the neutral nanowires starting at a wire length of twelve atoms. B) Density of states of the *d* orbitals of gold nanowires. This data was plotted with SAOP/DZ.

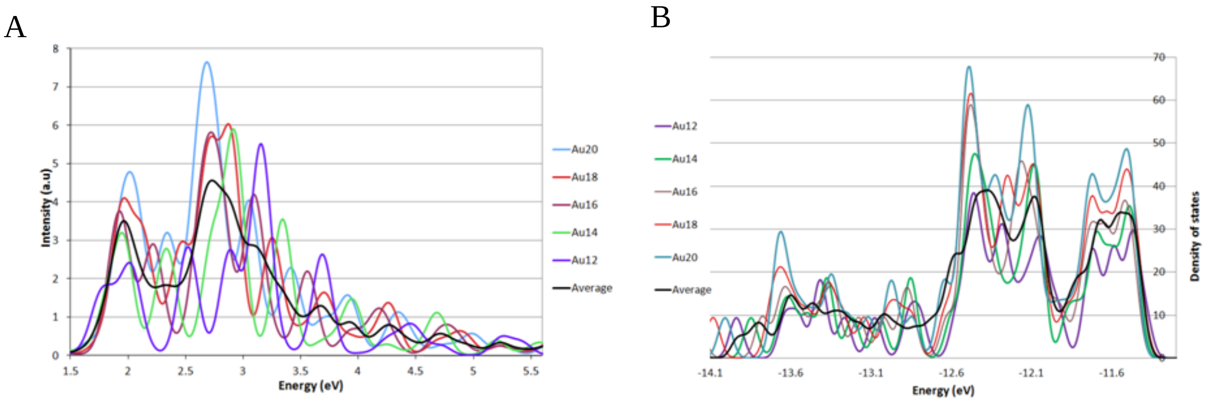

Positively and negatively charged nanowires

The positively charged and negatively charged gold nanowires display similar trends as the neutral ones. The wavelength of the longitudinal peak also shows a break in linearity at five atoms for the positively charged systems and at seven atoms for the negatively charged species, as shown in Figures 3-6B and 3-6C. In a similar manner as the neutral case, linearity is recovered by taking the weighted average of the HOMO-LUMO transition, as shown in Figures 3-7B and 3-7C. However, Au_3^+ does not fit the trend for the positively charged nanowires. In fact, the HOMO-LUMO transition for this system is at much lower energy. Similarly to the silver case, the wavelength of the HOMO-LUMO transition increases more rapidly with size for the neutral and negatively charged nanowires than for the positively charged nanowires. Also, similarly to the neutral case, the coupling between the HOMO-LUMO transition and the *d*-band is reflected in the intensity of the longitudinal peak. In fact, there is a bump in the peak intensity between three and seven atoms for the charged species (Figure 3-8). After that, the peak intensity varies linearly with the chain length, similarly to the silver case. The *d*-band pattern is also recovered for the positively charged and negatively charged species. Since these orbitals are fairly localized, this is expected. The transverse band at 6 eV also compares fairly well with the neutral species, which suggests that the transitions involved originate from similar orbitals as the neutral case.

Conclusions

The excitation spectra of linear chains of silver and gold have been studied for systems with lengths between two and twenty atoms. Neutral, positively charged, and negatively charged nanowires typically follow the same patterns. For silver, a series of delocalized Σ_m and Π_m orbitals formed from 5*s* orbitals lie near the HOMO-LUMO gap. Localized 4*d*-based orbitals are well separated in energy. The excitation spectra for both silver and gold exhibit a main longitudinal peak corresponding to the HOMO-LUMO excitation along the chain. This peak shifts to the red as the chain length increases. The shift is linear for silver, which is consistent with the particle-in-a-cylinder model. However, the *d*-band of the gold species affects the energy of this peak because of coupling due to symmetry; this can be treated by taking a weighted average of the transition dipole moment contributions for all peaks with some HOMO-LUMO contribution. Silver nanowires show a transverse peak with nearly constant energy that is formed from delocalized $\Sigma_m \rightarrow \Pi_m$ transitions whose transition dipole moments add in a constructive manner in analogy to the transverse plasmonic peak of larger nanoparticles. Transitions arising from the *d*-band also tend to contribute to this peak as the chain becomes longer. The gold species show a wide transverse band corresponding to $d\Sigma \rightarrow \Pi$ and $d\Pi \rightarrow \Sigma$ transitions. This band is mostly hidden by $d\Pi \rightarrow \Pi$ transitions with oscillator strength about ten times higher than the transverse excitations. Silver nanowires show a low-intensity *d*-band that essentially goes away for systems of longer length. On the other hand, the excitation spectra of the gold species show a strong *d*-band that converges to a specific pattern at a chain length of about twelve atoms. This *d*-band also affects the position of the main longitudinal peak.

Acknowledgements

This material is based upon work supported by the Air Force Office of Scientific Research under AFOSR Award No. FA9550-09-1-0451. C. M. A. also thanks the Alfred P. Sloan Foundation for a Sloan Research Fellowship (2011-2013) and the Camille and Henry Dreyfus Foundation for a Camille Dreyfus Teacher-Scholar Award (2011-2016).

Chapter 4 - Diameter-Dependence of the Excitation Spectra of Silver and Gold Nanorods

Reproduced with permission from:
Guidez, E. B.; Aikens, C. M. *J. Phys. Chem. C* **2013**, *117,* 12325.
Copyright 2013 American Chemical Society.

Abstract

An analysis of the excitation spectra of silver and gold nanorods with different cross-sections, lengths and diameters was performed using time-dependent density functional theory at the LB94/DZ level. Silver nanorods show a strong longitudinal peak, corresponding to excitations along the main axis (*z* axis) of the nanorods, and a smaller transverse peak, corresponding to excitations in the *xy* plane of the nanorods. For systems with a large cross-section (star-shaped and large pentagonal nanorods), the single transverse peak is split into a wide band. The orbitals involved in these transitions are delocalized cylindrical orbitals. Constructive addition of the dipole moments of these transitions is observed for the strong longitudinal and transverse peaks, which is likely at the origin of the surface plasmon resonance phenomenon. The wavelength of the longitudinal peak increases linearly with increasing length, crossing over the transverse peak or transverse band, which remains at nearly constant energy. The intensity of the longitudinal peak increases with increasing system length due to the increasing number of electrons being collectively excited. The energy of the longitudinal peak for systems of identical length also tends to increase as the diameter of the system increases, which can be correlated to a decreasing aspect ratio. Gold nanorods display more complex excitation spectra due to the presence of transitions originating from the *d*-band. Such transitions may also mix with cylindrical orbital-based transitions, especially for systems with low aspect ratios, splitting the longitudinal peak into several peaks of lower intensity. As the aspect ratio increases, the energy of the longitudinal peak decreases and its intensity increases. It then becomes separated from the *d*-band transitions which remain approximately constant in intensity and energy. Consequently, the amount of *d*-band coupling to the main cylindrical orbital-based excitations decreases, which leads to a strong isolated longitudinal peak similar to the silver case.

No strong transverse peak is observed for gold nanorods at this level of theory. Instead, the transverse excitations are hidden by the *d*-band transitions.

Introduction

Gold and silver nanoparticles show unique catalytic,[3,149,150] optical[151-156] and electrochemical[157] properties that can be used in the biomedical,[17,127,157-160] sensing[157,161-167] and imaging[15,165] fields. Possible biomedical applications include cancer diagnostics,[168,169] cancer therapy,[35,170,171] and tissue imaging.[172] Noble metal nanoparticles with sizes on the order of 10-100 nm display a strong peak in the excitation spectrum near the visible region that is due to their unique surface plasmon resonance (SPR).[157,164,173-176] This phenomenon is formally defined as a collective excitation of the electrons under the application of an electric field. The plasmon resonance can enhance the SERS signal of small molecules like HCN[177] and enhance the circular dichroism signal generated by chiral molecules.[163,178] In addition, when attached to a receptor, the localized surface plasmon resonance of gold nanoparticles can be spectrally tuned after binding of the receptor to the analyte.[179] The size,[32,167,174] shape,[71,174] and composition[180-182] of the nanoparticle as well as the dielectric constant[174] of the medium can help tune the SPR. Significant progress has been achieved in the synthesis of nanoparticles[183] and it is now possible to produce particles with a wide variety of shapes[184-186] and sizes[187-189] with a narrow size distribution.

Optical properties of noble metal nanorods have been intensively studied both experimentally[32,175,189-194] and theoretically.[32,70,174,193-197] The absorption spectra of gold and silver nanorods show one low-energy peak that corresponds to a superposition of transitions along the main axis of the system (longitudinal).[85,191] This peak shifts to lower energy, as explained by the particle-in-a-cylinder model,[198] and its intensity increases as the aspect ratio of the rod increases.[32,193] The absorption spectra also show a second peak at higher energy and of lower intensity, which corresponds to transitions across the short axis of the system (transverse).[85]

Gold and silver atoms have a single electron in their valence *s* orbital. Frontier orbitals of silver and gold nanoparticles are a linear combination of these *s* orbitals and are delocalized over the entire structure.[71,180,195,199-202] The main difference between the two types of nanoparticles is due to relativistic effects.[91,203-205] In silver systems, the *d*-band is much lower in energy than in the case of gold. Gold nanowires show a strong *d*-band compared to their silver counterparts, which affects the energies and intensities of the longitudinal and transverse peaks, leading to a more complex excitation spectrum.[144,206]

The objective of this work is to quantitatively determine how the absorption spectrum of silver and gold nanorods is affected by the shape and diameter of the system. In order to do that, four different systems are compared: nanowires[206] (linear atomic chains), nanorods with a pentagonal cross-section of two different diameters and nanorods with a star-shaped cross-section. These shapes are chosen because silver and gold nanorods are known to have a pentagonal structure.[189,207] In addition, the pentagonal and star-shaped structures are a subset of Marks decahedra, which form the cores of nanoclusters.[42,76]

Computational methods

All calculations in this work are performed with the Amsterdam Density Functional (ADF) program.[110] Geometry optimizations employ the generalized gradient approximation (GGA) Becke-Perdew exchange-correlation functional.[102,103] A double zeta Slater-type basis set with the frozen core approximation is used for all calculations. Scalar relativistic effects are included with the zeroth-order regular approximation (ZORA).[114-116] Multiple charge states leading to closed-shell electronic structures are considered in this work. Since some of the highest occupied orbitals are degenerate, this is taken into consideration when determining the available charge states. Most structures optimized with D_{5h} symmetry except for Au_{19}^{+1}, Au_{25}^{+1}, Au_{29}^{+3}, Au_{39}^{+1}, Ag_{39}^{+1}, Ag_{39}^{-1}, Ag_{29}^{-5} and Ag_{29}^{+3}, which utilized C_{5v} symmetry. These structures are local minima but may not be global minima for their respective sizes; as discussed in the introduction, these systems are of interest due to their symmetry and their relationship to experimental nanorods and nanoparticles. Excitation spectra are calculated using time-dependent density functional theory (TDDFT) with the asymptotically corrected LB94 model potential.[146] HOMO-LUMO gaps are also reported at the LB94/DZ level of theory. The absorption spectra are convoluted with a Gaussian with a full width at half maximum of 0.2 eV. All individual excitation spectra are available in Appendix B.

Results and discussion

Silver nanorods

In this section, silver nanorods with four different cross-sections are compared: the nanowires studied in Ref[195], the small pentagonal nanorods studied in Ref[70], the star-shaped nanorods and the large pentagonal nanorods calculated here. Figure 4-1 shows an end view and a side view for each of these systems as well as the length and radius considered. We note that for the silver and gold nanowires, the radii considered are 145 pm and 136 pm respectively, which correspond to their covalent radii. For each of these systems, several lengths are considered. Tables 4.1 to 4.4 show the systems considered and their aspect ratios. Since some of the highest occupied orbitals are degenerate, this is taken into consideration when determining the charge states of interest. The charges considered here all lead to closed-shell systems.

Figure 4-1. Side view and end view of A) Ag_9^{+1} nanowire B) Ag_{37}^{+1} small pentagon C) Ag_{73}^{+1} star-shaped silver nanorod and D) Ag_{55}^{+1} large pentagon-shaped nanorod. The length and radius considered for each system are noted L and R respectively.

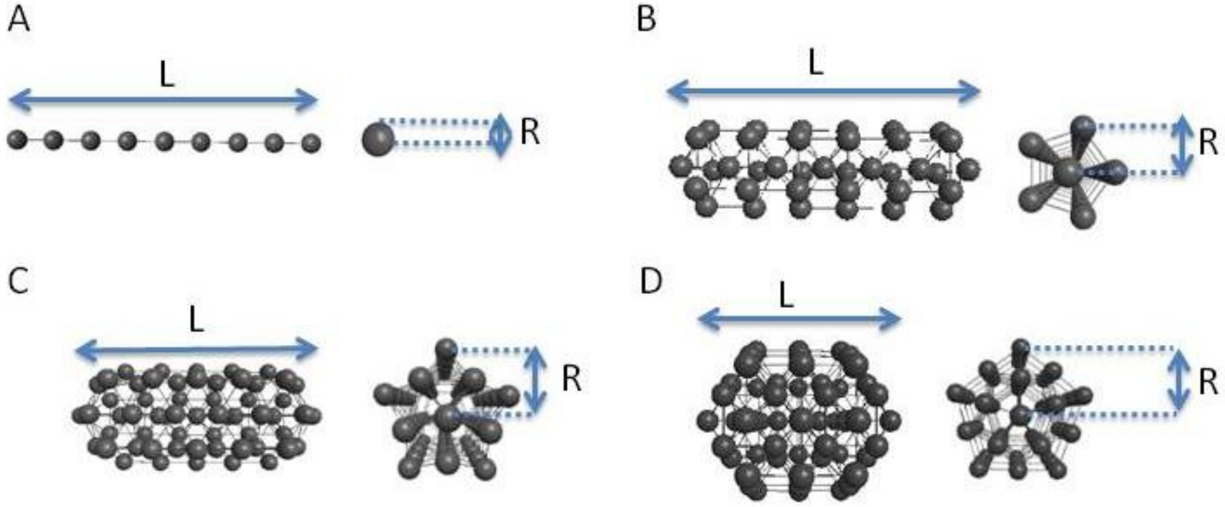

Table 4.1. Peak energies and HOMO-LUMO gaps of silver nanowires.

System	Aspect ratio (L/2R)	Longitudinal peak[a] (nm)	Transverse peak[a] (nm)	HOMO-LUMO gap (eV)
Ag_3^{+1}	1.84	565.63	181.16	0.90
Ag_7^{+1}	5.52	775.69	180.54	0.54
Ag_{11}^{+1}	9.19	1022.63	178.20	0.39
Ag_{15}^{+1}	12.85	1249.32	178.62	0.30
Ag_{19}^{+1}	16.52	1484.22	179.19	0.25

a. Ref[195]

Table 4.2. Peak energies and HOMO-LUMO gaps of small positively charged pentagon-shaped silver nanorods.

System	Aspect ratio (L/2R)	Longitudinal peak (nm)	Transverse peak (nm)	HOMO-LUMO gap (eV)
Ag_{19}^{+1}	1.62	305.88	261.02	0.24
Ag_{31}^{+1}	2.85	366.53	259.38	0.38
Ag_{43}^{+1}	3.94	434.97	256.70	0.35
Ag_{55}^{+1}	5.16	506.29	254.07	0.13
Ag_{67}^{+1}	6.24	560.82	254.07	0.22

Table 4.3. Peak energies and HOMO-LUMO gaps of positively charged star-shaped silver nanorods.

System	Aspect ratio (L/2R)	Longitudinal peak (nm)	Transverse peak 1 (nm)	Transverse peak 2 (nm)	HOMO-LUMO gap (eV)
Ag_{18}^{+4}	0.72	255.52	298.25	257.94	0.73
Ag_{29}^{+3}	1.12	285.03	290.81	259.02	0.29
Ag_{40}^{+2}	1.47	302.47	285.88	257.94	0.13
Ag_{51}^{+1}	1.82	317.85	283.26	255.81	0.18
Ag_{62}^{+2}	2.20	351.78	281.98	265.11	0.19
Ag_{73}^{+1}	2.58	375.19	279.44	260.10	0.018

Table 4.4. Peak energies and HOMO-LUMO gaps of large positively charged pentagon-shaped silver nanorods.

System	Aspect ratio (L/2R)	Longitudinal peak (nm)	Transverse peak 1 (nm)	Transverse peak 2 (nm)	HOMO-LUMO gap (eV)
Ag_{23}^{+1}	0.60	225.99	294.50	272.49	0.11
Ag_{39}^{+1}	0.89	261.75	279.87	263.80	0.58
Ag_{55}^{+1}	1.18	283.26	270.71	249.47	0.74
Ag_{71}^{+1}	1.49	302.05	273.09	255.11	0.14
Ag_{87}^{+1}	1.78	326.76	273.70	249.97	0.03

The HOMO-LUMO gaps of most silver systems are larger than 0.1 eV, as shown in Tables 4.1 to 4.4. The large star-shaped nanorod Ag_{73}^{+1} and the large pentagonal nanorod Ag_{87}^{+1} have HOMO-LUMO gaps of 0.018 eV and 0.03 eV respectively, which are comparable to kT (T=300K). However, other large systems such as Ag_{67}^{+1} have HOMO-LUMO gaps on the order of 0.22 eV. The HOMO-LUMO gaps for these systems do not monotonically decrease in this size regime, which is due to energy spacings between the orbitals that vary due to quantum confinement effects (more information about this is available in the SI of Ref [208]).

Figure 4-2. Excitation spectra of silver A) nanowires[195] B) small pentagonal nanorods[70] C) star-shaped nanorods and D) large pentagonal nanorods at the LB94/DZ level of theory.

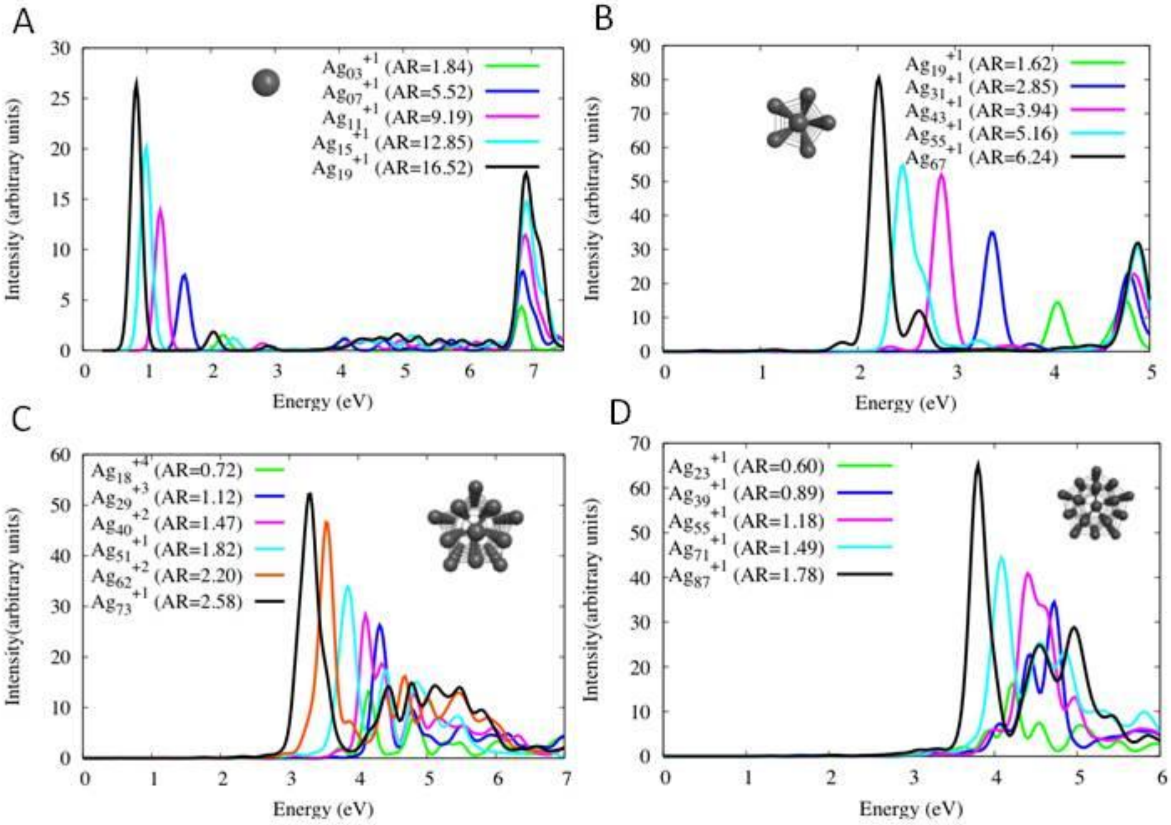

*The key shows the systems considered and their aspect ratios.

The absorption spectra of positively charged silver systems are narrow and show few strong peaks, as shown in Figure 4-2. The two main features of these spectra are the low-energy longitudinal peak, which shifts to the red and grows in intensity as the system becomes longer for a given radius, and the transverse peak, which does not shift or grow significantly. For nanowires and small pentagonal nanorods (Figures 4-2A and 4-2B respectively), these two peaks are far apart in the spectrum and can be easily identified. Tables 4.1 and 4.2 show the wavelength of the longitudinal and transverse peaks of these systems. The transverse peak is at 6.9 eV (180 nm) for the nanowires and at 4.8 eV (257 nm) for the small pentagonal nanorods. The longitudinal peak of the nanowires shifts from 2.19 eV (565.6 nm) to 0.84 eV (1484 nm) with increasing length. The longitudinal peak of the small pentagonal nanorods shifts from 4.05 eV

(305.9 nm) to 2.21 eV (560.8 nm). These trends are similar to what was previously observed at the SAOP/DZ level of theory.[70,195]

For the wider systems (star-shaped nanorods and large pentagonal-shaped nanorods), the transverse peak is strongly split, giving a transverse band between 4 and 6 eV. Four main peaks can be identified in the transverse band for the star-shaped nanorods. The first two strong peaks making up the band are given in Table 4.3 with the longitudinal peak. We can see that this band seems to slightly grow in intensity as the length of the system increases, due to an increasing density of states in the band. The longitudinal peak shifts from 4.86 eV (255.5 nm) to 3.31 eV (375.2 nm) with increasing length. It is lower in energy and has a higher intensity than the transverse band for systems with an aspect ratio larger than one as shown in Figure 4-2C and Table 4.3. As the aspect ratio decreases, the longitudinal peak becomes higher in energy and starts to overlap with the transverse band. Additionally, the intensity of the longitudinal peak is similar to the intensity of the transverse band for systems with a small aspect ratio, making the longitudinal peak less easily identifiable. For instance for Ag_{29}^{+3}, which has an aspect ratio of 1.12, the longitudinal peak at 4.35 eV (285.0 nm) overlaps the first peak making up the transverse band at 4.27 eV (290.8 nm). For Ag_{18}^{+4}, which has an aspect ratio smaller than one (0.72), the first transverse peak making up the transverse band is at 4.16 eV (298.3 nm), which is lower in energy than the longitudinal peak at 4.85 eV (255.5 nm). The longitudinal peak overlaps the second peak of the transverse band at 4.81 eV (257.9 nm).

Two main peaks are observed in the transverse band of the large pentagonal nanorods. The energies of these two peaks and the longitudinal peak are given in Table 4.4. The longitudinal peak shifts from 5.49 eV (226.0 nm) to 3.80 eV (326.8 nm) with increasing length. Like the star-shaped nanorods, the systems with a higher aspect ratio (Ag_{71}^{+1} and Ag_{87}^{+1}) show a strong identifiable longitudinal peak that is lower in energy than the transverse band. For instance, the longitudinal peak of Ag_{71}^{+1} occurs at 4.11 eV (302.1 nm) while the first peak of the transverse band appears at 4.54 eV (273.1 nm). For Ag_{55}^{+1}, which has an aspect ratio close to one (aspect ratio=1.18), the first transverse peak in the transverse band at 4.58 eV is close in energy to the longitudinal peak which is at 4.38 eV. Therefore, we only see one peak in the spectrum. Ag_{23}^{+1} has an aspect ratio of 0.60. The range of the transverse band for this system is from 4 to 5 eV, which is lower energy than the longitudinal peak at 5.49 eV since the aspect ratio is smaller than one.

The excitation spectra of negatively charged star-shaped and large pentagonal nanorods (Appendix B) show similar features and trends as their positively charged counterparts, which has been observed previously for negatively and positively charged nanowires.[195] The intensity of the main features tends to be higher for negatively charged systems due to the larger electron density, as explained previously for silver nanowires.[195] The negatively charged small pentagonal silver nanorods were not calculated but similar features are expected.

Analysis of the longitudinal peak

The longitudinal peaks for all the positively charged systems considered in Figure 4-2 are now analyzed in more detail. Longitudinal peaks have A_2'' symmetry for D_{5h} systems and A_2 symmetry for systems in which C_{5v} symmetry was applied. Transitions involved here take place along the length of the nanorods, as will be discussed in the next section. Figure 4-3 shows the wavelength of the longitudinal peak as a function of the number of core atoms. For all systems, the wavelength of the longitudinal peak increases linearly with the length of the rod. Such behavior was previously explained with the particle-in-a-cylinder model.[70] Despite the fact that the charge of the individual rods is not constant for the star-shaped systems, the linearity is very good, suggesting that the longitudinal peak energy is not significantly affected by the charge for these systems.

Figure 4-3. Longitudinal peak wavelengths of positively charged silver nanorods at the LB94/DZ level of theory.

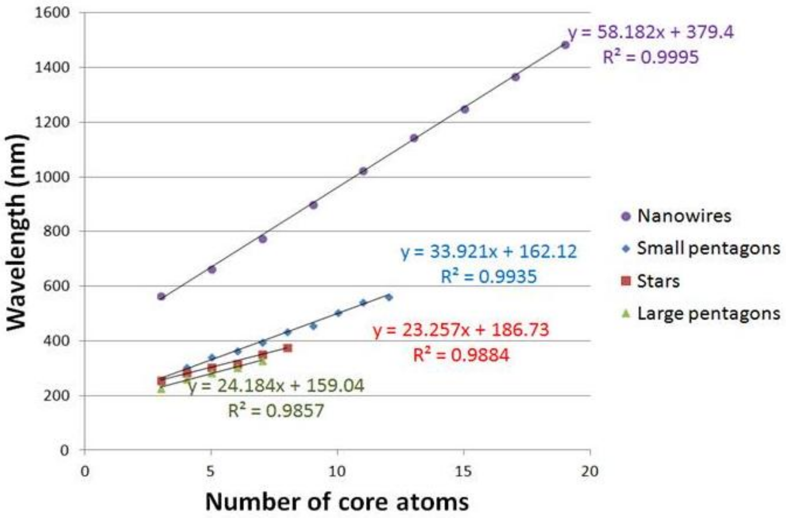

The wavelength of the longitudinal peak tends to decrease as the diameter of the system increases. This can be correlated to the fact that for a system with a given length, the aspect ratio decreases as the diameter increases. In addition, the slope of the line tends to decrease as the diameter of the system increases, meaning the red shift of the peak with increasing length becomes smaller as the diameter of the system increases. This is because the aspect ratio of a system with a larger radius increases slowly with increasing unit length compared to a system with a smaller radius. The change in wavelength of the longitudinal peak with increasing length is slightly smaller for star-shaped than for the large pentagon-shaped nanorods, although the large pentagons have a larger radius than the stars. This observation may be explained by the different shape of the two systems. Figure B-6 shows the energy of the longitudinal peak as the function of the number of core atoms for positively and negatively charged star-shaped and large pentagonal nanorods. The positively charged systems considered are the same as in Figure 4-2. The negatively charged systems considered, along with their HOMO-LUMO gap, longitudinal peak energy and transverse peak energy are shown in Table B1 and B2 of appendix B for the star-shaped nanorods and large pentagonal nanorods, respectively. The positively and negatively charged systems exhibit a very similar behavior and the position of the longitudinal peak does not significantly vary for the different charges. As mentioned above, this data also supports the fact that the charge does not significantly affect the excitation spectra for silver nanorods. The HOMO-LUMO gaps for the negatively charged systems are mostly larger than 0.1 eV, like the positively charged systems. The main exceptions are Ag_{39}^{-5} and Ag_{55}^{-3}, which have HOMO-LUMO gaps of 0.02 and 0.04 eV, respectively. On the other hand, the positively charged systems Ag_{39}^{+1} and Ag_{55}^{+1} have much higher HOMO-LUMO gaps of 0.58 and 0.74 eV, respectively.

Analysis of the transverse peak

Transverse peaks have E_1’symmetry for D_{5h} systems and E_1 symmetry for C_{5v} systems. As mentioned above, the nanowires and small pentagonal nanorods display a strong, identifiable transverse peak at 6.9 eV and 4.8 eV respectively. On the other hand, the transverse peak of the star-shaped rods and large pentagonal rods is split into a broad band between about 4 and 6 eV. We see that the transverse peak of the nanowires has a much shorter wavelength (higher energy) than the transverse peak of wider systems. However, the strong splitting of the transverse peak for the star-shaped and large pentagonal nanorods makes it difficult to derive a more quantitative relationship for the relationship between diameter and transverse peak wavelength.

Analysis of the Ag_{71}^{-3} spectrum

The excitation spectrum of the large pentagonal nanorod Ag_{71}^{-3} shown in Figure 4-4A is described in detail here.

Figure 4-4. Excitation spectra of A) Ag_{71}^{-3} and B) Au_{71}^{-3} at the LB94/DZ level of theory.

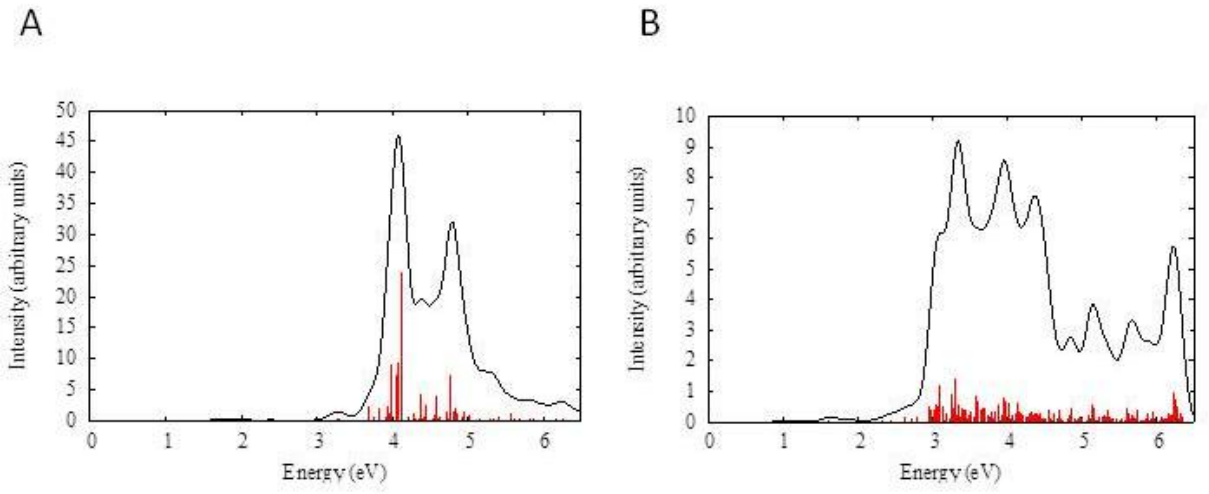

This system is chosen since it is the longest system with a large pentagonal cross-section whose gold counterpart was also obtained (Figure 4-4B). One intense sharp feature, the longitudinal peak, is observed at about 4 eV. This main feature is comprised of four peaks with energies varying between 3.98 and 4.12 eV. These four high-intensity peaks are of A_2'' symmetry, describing transitions along the main axis of the nanorod. The energy, oscillator strength and transitions involved are displayed in Table 4.5. Most of the orbitals involved in these transitions are very delocalized and located near the HOMO-LUMO gap, as shown in Figure 4-5. Due to the cylindrical symmetry of these system, these orbitals can be described with upper case Greek letters Σ, Π, Δ, Φ, Γ, H, …, and correspond to linear combinations of the valence *s* orbitals of the silver atoms. The subscript corresponds to the number of axial nodes plus one. The number before the upper case Greek letter corresponds to the number of radial nodes plus one. For instance, the LUMO+2 is a Π–like orbital with two axial nodes and one radial node giving the notation $2\Pi_3$. The transitions with the highest dipole moments involved in these four longitudinal peaks are $\Sigma_m \rightarrow \Sigma_{m+1}$, $\Pi_m \rightarrow \Pi_{m+1}$, $\Delta_m \rightarrow \Delta_{m+1}$, etc.

Figure 4-5. Kohn-Sham orbitals involved in the high intensity transitions for Ag_{71}^{-3} at the LB94/DZ level of theory. Contour value=0.01.

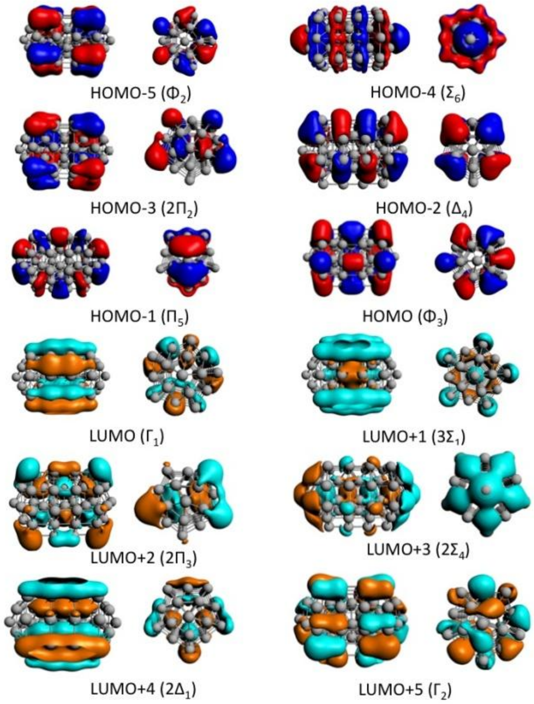

Table 4.5. Energy, oscillator strength and transitions of the main A_2'' peaks of Ag_{71}^{-3}.

Peak number	Energy (eV)	Intensity (a.u)	Transitions	z-component of transition dipole moment (a.u.)	Weight
1	3.9826	1.9463	Δ_4 (HOMO-2) → Φ_5 (LUMO+31)	-0.4687	0.3678
			Σ_6 (HOMO-4) → Σ_7 (LUMO+6)	0.8446	0.0182
			Δ_4 (HOMO-2) → Δ_5 (LUMO+11)	1.2746	0.0278
			$2\Sigma_3$ (HOMO-6) → $2\Sigma_4$ (LUMO+3)	0.5793	0.0122
			Π_5 (HOMO-1) → Π_6 (LUMO+7)	1.0255	0.0201
			Φ_3 (HOMO) → Φ_4 (LUMO+9)	0.8015	0.0179
2	4.0435	1.6048	Δ_4 (HOMO-2) → Φ_5 (LUMO+31)	-0.4747	0.383
			Φ_2 (HOMO-5)→$2\Phi_1$ (LUMO+23)	-0.0918	0.3249
			Σ_6 (HOMO-4) → Σ_7 (LUMO+6)	-0.6387	0.0106
			Δ_4 (HOMO-2) → Δ_5 (LUMO+11)	-0.9434	0.0155
			$2\Sigma_3$ (HOMO-6) → $2\Sigma_4$ (LUMO+3)	-0.4565	0.0077
			Π_5 (HOMO-1) → Π_6 (LUMO+7)	-0.7803	0.0118
			Φ_3 (HOMO) → Φ_4 (LUMO+9)	-0.5601	0.0089
			$2\Pi_2$ (HOMO-3)→ $2\Pi_3$ (LUMO+2)	-0.4491	0.007
3	4.0784	2.0185	Σ_6 (HOMO-4) → $3\Sigma_3$ (LUMO+26)	-0.0938	0.2189
			Φ_2 (HOMO-5) →$2\Phi_1$(LUMO+23)	-0.0992	0.3833
			Σ_6 (HOMO-4) → Σ_7 (LUMO+6)	0.9078	0.0216
			Δ_4 (HOMO-2) → Δ_5 (LUMO+11)	1.3674	0.0327
			$2\Sigma_3$ (HOMO-6) → $2\Sigma_4$ (LUMO+3)	0.5941	0.0132
			Π_5 (HOMO-1) → Π_6 (LUMO+7)	1.1183	0.0244
4	4.1268	5.1423	Σ_6 (HOMO-4) → $3\Sigma_3$ (LUMO+26)	0.1353	0.4609
			Σ_6 (HOMO-4) → Σ_7 (LUMO+6)	1.1479	0.0349
			Δ_4 (HOMO-2) → Δ_5 (LUMO+11)	1.8721	0.0621
			$2\Sigma_3$ (HOMO-6) → $2\Sigma_4$ (LUMO+3)	0.8478	0.0271
			Π_5 (HOMO-1) → Π_6 (LUMO+7)	1.5081	0.045
			Φ_3 (HOMO) → Φ_4 (LUMO+9)	1.0964	0.0347
			$2\Pi_2$ (HOMO-3) → $2\Pi_3$(LUMO+2)	0.8278	0.0242

For these four strong longitudinal peaks, the transitions with high dipole moments add up constructively, as shown in Table 4.5. This constructive addition of one-electron transitions leads to the sharp high intensity band observed in the excitation spectra and can be correlated to the plasmon resonance, which is described as a collective oscillation of the electrons in response to an electric field. Several other peaks at lower energy arise from the same transitions, as shown in Table 4.6. However, their dipole moments add up in a destructive manner, giving peaks of very low intensity. Similar trends were observed for silver nanowires[195] and small pentagonal nanorods,[70] as well as tetrahedral,[209] octahedral,[71] and icosahedral[71] silver clusters.

Table 4.6. Energy, oscillator strength and transitions of the low intensity A_2’’ peaks involving the same transitions as the main A_2’’ peaks for Ag_{71}^{-3}.

Peak number	Energy (eV)	Intensity (a.u)	Transitions	z-component of transition dipole moment (a.u.)	Weight
1'	1.3505	0.00787	Σ_6 (HOMO-4) → Σ_7 (LUMO+6)	-0.1652	0.0002
			Δ_4 (HOMO-2) → Δ_5 (LUMO+11)	0.316	0.0006
			$2\Sigma_3$ (HOMO-6) → $2\Sigma_4$ (LUMO+3)	0.5052	0.0032
			Π_5 (HOMO-1) → Π_6 (LUMO+7)	2.1431	0.0297
			Φ_3 (HOMO) → Φ_4 (LUMO+9)	2.6221	0.0649
			$2\Pi_2$ (HOMO-3) → $2\Pi_3$ (LUMO+2)	-7.8803	0.7165
			Φ_3 (HOMO) → $2\Delta_2$ (LUMO+10)	1.1095	0.0522
2'	1.4565	0.00294	Σ_6 (HOMO-4) → Σ_7 (LUMO+6)	2.0691	0.04
			Δ_4 (HOMO-2) → Δ_5 (LUMO+11)	1.3857	0.012
			$2\Sigma_3$ (HOMO-5) → $2\Sigma_4$ (LUMO+3)	0.5556	0.0041
			Π_5 (HOMO-1) → Π_6 (LUMO+7)	-9.3167	0.6058
			Φ_3 (HOMO) → Φ_4 (LUMO+9)	5.4624	0.304
3'	1.6538	0.03393	Σ_6 (HOMO-4) → Σ_7 (LUMO+6)	-2.3424	0.0582
			Δ_4 (HOMO-2) → Δ_5 (LUMO+11)	-5.7698	0.2364
			$2\Sigma_3$ (HOMO-5) → $2\Sigma_4$ (LUMO+3)	-2.754	0.1148
			Π_5 (HOMO-1) → Π_6 (LUMO+7)	2.745	0.0597
			Φ_3 (HOMO) → Φ_4 (LUMO+9)	4.9901	0.288
			$2\Pi_2$ (HOMO-3) → $2\Pi_3$ (LUMO+2)	2.4314	0.0835
4'	1.8546	0.00245	Σ_6 (HOMO-4) → Σ_7 (LUMO+6)	1.3719	0.0224
			Δ_4 (HOMO-2) → Δ_5 (LUMO+11)	3.9595	0.1248
			$2\Sigma_3$ (HOMO-5) → $2\Sigma_4$ (LUMO+3)	-5.1325	0.447
			$2\Pi_2$ (HOMO-3) → $2\Pi_3$ (LUMO+2)	-0.3946	0.0025
5'	1.8905	9.03E-04	Σ_6 (HOMO-4) → Σ_7 (LUMO+6)	7.4579	0.6743
			Δ_4 (HOMO-2) → Δ_5 (LUMO+11)	-5.4239	0.2388
			$2\Sigma_3$ (HOMO-5) → $2\Sigma_4$ (LUMO+3)	-1.1173	0.0216
			$2\Pi_2$ (HOMO-3) → $2\Pi_3$ (LUMO+2)	-0.4078	0.0027
			Φ_3 (HOMO) → Φ_4 (LUMO+9)	-0.9412	0.0117
			Π_5 (HOMO-1) → Π_6 (LUMO+7)	0.4744	0.002

Three transverse peaks are observed between 4.37 and 4.78 eV, as shown in Table 4.7. Their intensities are lower than the longitudinal ones because they have lower transition dipole moments. Contrary to the longitudinal case, we get the following transitions: Σ→Π, Π→Σ, Φ→Γ as well as Π→Φ or Π→H. For the nanowires, the main transitions involved in the transverse peak are of the type $\Sigma_m \to \Pi_m$.[195] For the small pentagonal nanorods, the transverse excitations are mainly of the type $\Sigma_m \to \Pi_m$, $\Pi_m \to \Sigma_m$, $\Pi_m \to \Delta_m$ etc., where the change in the azimuthal quantum number is ±1.[70] For the wider systems, we get more flexibility due to the fact that the cross-section is not spherical and due to the higher number of states available. For instance, we see some $2\Pi_1 \to H_1$ and $\Phi_3 \to 3\Pi_3$ transitions, where the changes in the azimuthal quantum number are +4 and -2 respectively. The quantum numbers *m* and *n* may also change. Nevertheless, we still see some $\Phi_m \to \Gamma_m$ transitions, which have a higher transition dipole moment than the others. We note that the unoccupied orbitals involved here are much higher above the LUMO than for the longitudinal case, which contributes to the higher energy of the transverse peak compared to the longitudinal peak. The excitations involved in peak 3 at 4.78 eV show a constructive interference of the transition dipole moments and the peak is therefore more intense than the other two where there is some destructive interference.

Table 4.7. Energy, oscillator strength and transitions of the main E_1' peaks of Ag_{71}^{-3}.

Peak number	Energy (eV)	Intensity (a.u)	Transitions	x-component of transition dipole moment (a.u.)	Weight
1	4.37	0.9199	Φ_1 (HOMO-10) → $3\Pi_1$ (LUMO+19)	-0.2474	0.3646
			$2\Pi_1$ (HOMO-7) → $3\Sigma_1$ (LUMO+1)	0.2936	0.0059
			$2\Pi_2$ (HOMO-3) → $3\Sigma_2$ (LUMO+8)	0.256	0.0046
			$2\Sigma_3$ (HOMO-6) → Π_7 (LUMO+25)	0.1024	0.0223
2	4.58	0.8743	Π_5 (HOMO-1) →H_3 (LUMO+35)	0.2982	0.3445
			Φ_3 (HOMO) → $3\Pi_3$ (LUMO+37)	0.1667	0.2092
			Φ_1 (HOMO-10) → Γ_1 (LUMO)	-0.4572	0.0084
			$2\Pi_1$ (HOMO-7) → H_1 (LUMO+21)	-0.1287	0.0063
3	4.78	1.5949	$2\Pi_1$ (HOMO-7) → H_1 (LUMO+21)	-0.172	0.0118
			$2\Pi_2$ (HOMO-3) → H_2 (LUMO+29)	-0.1483	0.01
			Φ_1 (HOMO-10) → Γ_1 (LUMO)	-0.5507	0.0128
			Φ_3 (HOMO) → Γ_3 (LUMO+12)	-0.2411	0.0051

Gold nanorods

The gold equivalents of the small pentagonal nanorods, star-shaped nanorods and the large pentagonal nanorods are modeled. The charge of the systems is usually the same as their silver counterpart except for the star-shaped Au_{51}^{+3} and Au_{73}^{+3} and the large pentagonal Au_{71}^{-3}. These systems do not have a +1 charge contrary to their silver equivalent studied in the previous section because a closed-shell occupation was not obtained for the singly positively charged system. Figure 4-6 shows the absorption spectra of the gold nanowires,[195] small pentagonal nanorods, star-shaped nanorods and large pentagonal nanorods examined in this work. Tables 4.8 to 4.11 show the HOMO-LUMO gaps and longitudinal peak energies of the systems considered in Figure 4-6.

Figure 4-6. Excitation spectra of gold A) nanowires[195] B) small pentagonal nanorods C) star-shaped nanorods and D) large pentagonal nanorods at the LB94/DZ level of theory.

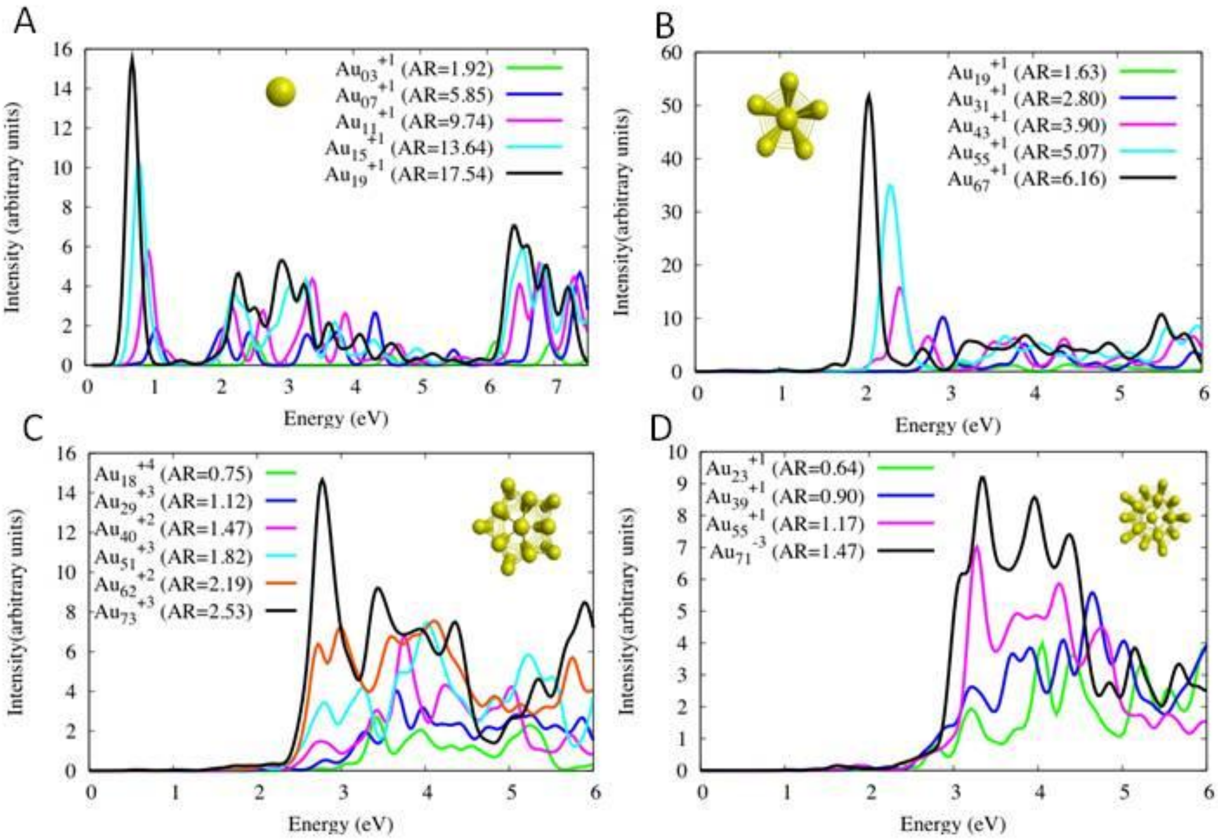

*The key shows the system considered and their aspect ratio.

Table 4.8. Longitudinal peak energy and HOMO-LUMO gap of gold nanowires.

System	Aspect ratio (L/2R)	Longitudinal peak (nm)[a]	HOMO-LUMO gap (eV)
Au_3^{+1}	1.92	489.55	0.38
Au_7^{+1}	5.85	1177.77	0.35
Au_{11}^{+1}	9.74	1315.58	0.27
Au_{15}^{+1}	13.64	1553.74	0.22
Au_{19}^{+1}	17.54	1795.49	0.18

a) Ref [195]

Table 4.9. Longitudinal peak energy and HOMO-LUMO gap of small positively charged pentagon-shaped gold nanorods .

System	Aspect ratio (L/2R)	Longitudinal peak (nm)	HOMO-LUMO gap (eV)
Au_{19}^{+1}	1.63	390.27	0.24
Au_{31}^{+1}	2.80	424.21	0.32
Au_{43}^{+1}	3.90	511.40	0.30
Au_{55}^{+1}	5.07	545.11	0.13
Au_{67}^{+1}	6.16	598.55	0.03

Table 4.10. Longitudinal peak energy and HOMO-LUMO gap of positively charged star-shaped gold nanorods.

System	Aspect ratio (L/2R)	Longitudinal peak (nm)	HOMO-LUMO gap (eV)
Au_{18}^{+4}	0.75	328.91	0.83
Au_{29}^{+3}	1.12	340.10	0.34
Au_{40}^{+2}	1.47	436.59	0.16
Au_{51}^{+3}	1.82	438.31	0.04
Au_{62}^{+2}	2.19	457.51	0.01
Au_{73}^{+3}	2.53	450.65	0.19

Table 4.11. Longitudinal peak energies and HOMO-LUMO gap of large pentagon-shaped gold nanorods.

System	Aspect ratio (L/2R)	Longitudinal peak (nm)	HOMO-LUMO gap (eV)
Au_{23}^{+1}	0.64	235.51	0.18
Au_{39}^{+1}	0.90	298.02	0.43
Au_{55}^{+1}	1.17	379.20	0.78
Au_{71}^{-3}	1.47	397.21	0.34

The HOMO-LUMO gaps of gold systems are generally larger than 0.2 eV and can be as high as 0.83 eV. The star-shaped nanorod Au_{40}^{+2} has a HOMO-LUMO gap of 0.16 eV at the LB94/DZ level of theory and 0.17 eV at the BP86/DZ level of theory, which is 0.1 eV smaller than the more compact Au_{40} nanorod studied by Liu et al.[210] This emphasizes the fact that the HOMO-LUMO gaps do not correlate with the number of atoms in the system. On the other hand, the small pentagonal nanorod Au_{67}^{+1}, and the star-shaped nanorods Au_{51}^{+3} and Au_{62}^{+2} have very small HOMO-LUMO gaps (smaller than 0.04 eV). Excitation spectra for gold nanorods are much broader and exhibit a multitude of transitions out of the *d*-band compared to their silver counterparts. Transitions out of the *d*-band occur in gold systems because of relativistic effects: the heavy nuclei of gold atoms induce a contraction of the valence *s* electrons, which brings the valence *s* orbitals close to the *d*-band.[91,203,204] The effect of the *d*-band was previously studied in detail for gold nanowires.[141,142,195] The longitudinal peak is less obvious than for the silver case for systems with a low aspect ratio since the transitions originating from the *d*-band have a similar intensity. As the aspect ratio increases, the longitudinal peak becomes stronger and shifts to the red, making it more easily identifiable. Systems with an aspect ratio larger than 2.80 for the small pentagon-shaped nanorods and 2.19 for the star-shaped nanorods show a strong, distinguishable longitudinal peak. We note that for the large pentagons, the longest system that could be studied at this level of theory has a 1.47 aspect ratio and therefore the main longitudinal peak is difficult to identify. For systems with very high aspect ratio, only the main longitudinal peak is strong and the *d*-band seems to disappear since these transitions have a constant intensity. However, we cannot see any strong transverse peak for these gold systems at this level of theory, which is in contradiction with experiment.[32,175] The transverse peaks are weak and blend in with the *d*-band, similar to what was observed with gold nanowires.[195] More investigations need to be performed on these gold nanorods and new computational methods need to be developed to provide a better description of their plasmonic properties.

Figure 4-7. Longitudinal peak wavelengths of positively charged gold nanorods.

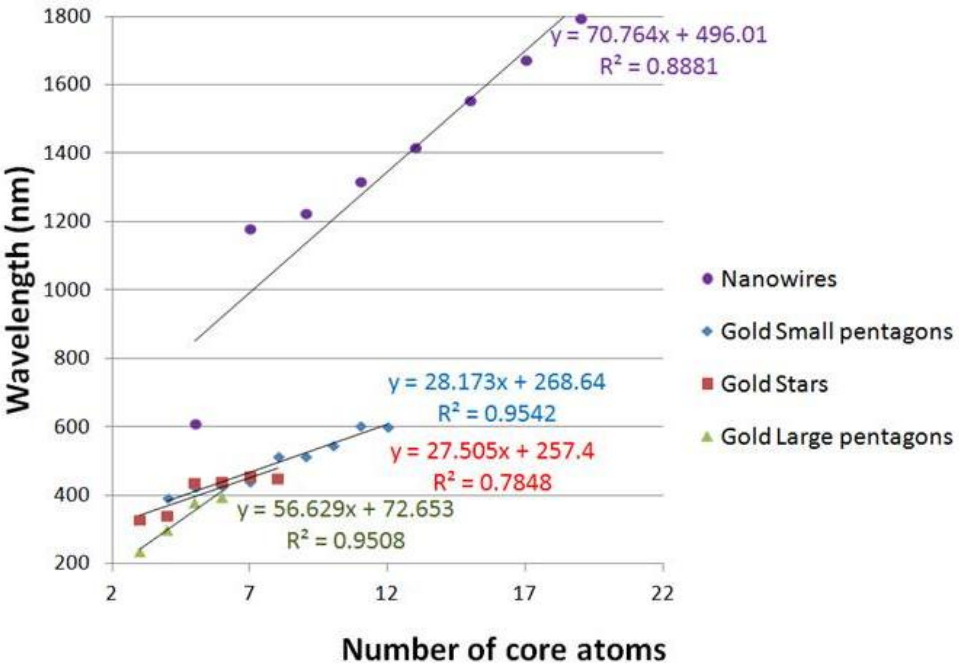

The wavelength of the longitudinal peak of positively charged gold nanorods as a function of the number of core atoms is shown in Figure 4-7. Longitudinal peak energies, HOMO-LUMO gaps and aspect ratios of these systems are presented in Tables 4.8 to 4.11. The data for the nanowires is from Ref[195]. All nanowires considered have a +1 charge. We note that just like in the silver case, the charges of the star-shaped nanorods considered vary. All the other systems considered have a +1 charge except for the large-pentagon Au_{71}^{-3}. The excitation spectrum of the positively charged Au_{71}^{+1} system could not be obtained. The relationship between the peak wavelength and number of core atoms is not as linear as the silver case. This was explained for the nanowires by the coupling of *d*-band transitions with the main HOMO-LUMO transition, which splits the HOMO-LUMO (longitudinal) peak and affects the peak energy.[195] The linearity was recovered by taking the weighted average of the energy of the HOMO-LUMO transition. A similar effect is observed for the larger systems. In fact, excitations from the *d*-band contribute to the main longitudinal peak for systems with a low aspect ratio, splitting the longitudinal peak. As the nanorods grow longer, the contributions from the excitations out of the *d*-band decrease and the main longitudinal peak grows stronger, just as it does for the silver case. This will be discussed in more detail in the next section. Similar to the silver case, we can see that the energy of the longitudinal peak tends to increase as the diameter of the system increases. However, the longitudinal peaks of star-shaped and small pentagon-shaped nanorods of similar length have similar energies. This discrepancy may be due to the different shapes of the two systems and also possibly to the contributions of the *d*-band.

Analysis of the Au_{71}^{-3} nanorod

The spectrum of Au_{71}^{-3} is much broader than its silver counterpart, as shown in Figure 4-4B. Nevertheless, a few peaks are slightly more intense than the rest and are analyzed in more detail in this section. Five peaks of A_2'' symmetry with oscillator strength between 0.11 and 0.31 appear at low energy between 2.96 and 3.58 eV (Table 4.12). We note that the contributions of the transition dipole moments are not as high as the silver case. In addition, there is also more destructive addition of the transition dipole moments. Many transitions are of $\Sigma_m \rightarrow \Sigma_{m+1}$, $\Pi_m \rightarrow \Pi_{m+1}$ or $\Delta_m \rightarrow \Delta_{m+1}$ character, involving delocalized orbitals around the HOMO-LUMO gap that are shown in Figure 4-8. We note that these orbitals have a small amount of *d*-character mixed in. We also see some excitations like $\Phi_1 \rightarrow \Phi_4$ or $2\Sigma_3 \rightarrow \Sigma_8$, where the azimuthal quantum number does not change but Δm is larger than 1 and Δn is larger than zero. Peaks 1 through 4 display some common excitations, suggesting some splitting has occurred. These longitudinal peaks also display high contributions from transitions out of localized *d*-band orbitals, which are closer in energy to the delocalized cylindrical orbitals than in the silver case, again due to relativistic effects.[91,203] Peak number 5 is comprised only of transitions from the *d*-band and its intensity is slightly higher than peak 1 which only has contributions from delocalized orbitals. In fact, we can see that *d*-band transitions have a similar dipole moment to the delocalized orbital-based transitions or even higher. Two of these *d*-band orbitals are also shown in Figure 4-8.

Table 4.12. Energy, oscillator strength and transitions of the main A_2'' peaks of Au_{71}^{-3}.

Peak number	Energy (eV)	Intensity (au)	Transition	z-contribution of transition dipole moment (a.u.)	Weight
1	2.96	0.114	Σ_6 (HOMO-4) → $3\Sigma_3$ (LUMO+16)	0.3802	0.6639
			Φ_1 (HOMO-10) → Φ_4 (LUMO+9)	0.2062	0.1206
			Σ_6 (HOMO-4) → Σ_7 (LUMO+6)	-0.4679	0.0051
			Σ_5 (HOMO-11) → $2\Sigma_4$ (LUMO+5)	-0.2744	0.0296
			Π_5 (HOMO-1) → $3\Pi_4$ (LUMO+23)	0.2121	0.0101
			Π_5 (HOMO-1) → $2\Pi_4$ (LUMO+18)	-0.1668	0.0099
2	3.1	0.265	d-orbital→ Γ_1 (LUMO)	0.308	0.2794
			$2\Sigma_3$ (HOMO-5) → Σ_8 (LUMO+15)	-0.2033	0.1391
			Π_5 (HOMO-1) → $3\Pi_4$ (LUMO+23)	-0.8633	0.1744
			Σ_6 (HOMO-4) → Σ_7 (LUMO+6)	0.6281	0.0097
			$2\Sigma_3$ (HOMO-5) → $2\Sigma_4$ (LUMO+5)	0.5101	0.0082
			Δ_4 (HOMO-2) →Δ_5 (LUMO+10)	1.0967	0.0171
			Π_5 (HOMO-1) → Π_6 (LUMO+8)	0.4603	0.0062
3	3.25	0.1944	d-orbital → Γ_1 (LUMO)	0.25	0.2926
			Π_5 (HOMO-1) → $3\Pi_4$ (LUMO+23)	-0.6312	0.0978
			$2\Sigma_3$ (HOMO-5) → $2\Sigma_4$ (LUMO+5)	-0.4253	0.006
			Δ_4 (HOMO-2) → Δ_5 (LUMO+10)	-0.8805	0.0116
4	3.29	0.3057	d-orbital → $3\Sigma_1$ (LUMO+1)	-1.0268	0.4271
			d-orbital → Γ_2 (LUMO+2)	0.317	0.1318
			d-orbital → Γ_1 (LUMO)	0.1291	0.079
			d-orbital → $2\Delta_1$ (LUMO+3)	0.239	0.0694
			Π_5 (HOMO-1) → $3\Pi_4$ (LUMO+23)	0.3999	0.0398
			Σ_6 (HOMO-4) → Σ_7 (LUMO+6)	0.456	0.0054
5	3.58	0.1814	d-orbital → Σ_7 (LUMO+6)	0.173	0.1942
			d-orbital → $2\Delta_1$ (LUMO+3)	0.7514	0.1872
			d-orbital → $2\Delta_1$ (LUMO+3)	-0.2858	0.1661
			d-orbital → Φ_4 (LUMO+9)	-0.2683	0.067

Figure 4-8. Kohn-Sham orbitals involved in the high intensity transitions for Au_{71}^{-3} at the LB94/DZ level of theory. Contour value= 0.01.

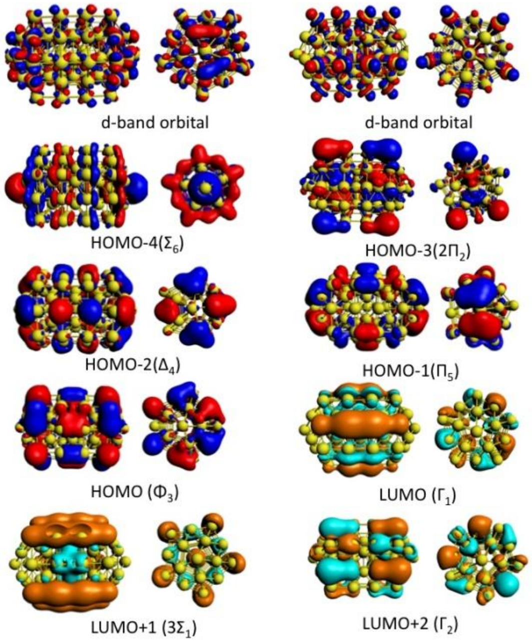

For systems with a low aspect ratio like this one, excitations out of the *d*-band tend to mix with transitions from the delocalized orbitals and split the longitudinal peak into peaks of lower intensity, making it less identifiable. For systems with a high aspect ratio such as the small pentagon-shaped nanorod Au_{67}^{+1}, there is no contribution of the *d*-band to the longitudinal peak. The transitions from the cylindrical orbitals have a high dipole moment and add up constructively, leading to a strong, easily identifiable longitudinal peak similar to the silver case. The transitions involved in the main longitudinal peak of Au_{67}^{+1} are mainly $\Sigma_m \rightarrow \Sigma_{m+1}$, $\Pi_m \rightarrow \Pi_{m+1}$ and $\Delta_m \rightarrow \Delta_{m+1}$ also like in the silver case. We note that the longitudinal peak has a contribution from the $\Sigma_{11} \rightarrow 2\Sigma_4$ transition, which involves Δn=1 and Δm=-7. All these transitions are summarized in Table B3 of Appendix B and pictures of the orbitals involved are shown in Figure B7 of Appendix B. It should be noted that the cylindrical orbitals also have a small amount of *d* character mixed in contrary to the silver case.

Conclusions

Silver and gold nanorods with different lengths and diameters were analyzed in this work. The excitation spectrum of silver nanorods shows two main strong peaks: a longitudinal peak corresponding to transitions along the main (*z*) axis of the nanorods and a transverse peak, corresponding to transitions in the *xy* plane of the nanorod. The longitudinal peak increases in intensity and shifts to lower energy as the length of the system increases. The dipole moments of the single electron excitations involved in this main peak add up constructively, which can be related to the surface plasmon resonance of noble metal nanoparticles. The increasing intensity of this peak may be explained by the increasing number of one-electron excitations adding constructively. The transitions involved are of $\Sigma \rightarrow \Sigma$, $\Pi \rightarrow \Pi$, $\Delta \rightarrow \Delta$, etc. character where the upper case Greek letter is a label for the cylindrical orbitals. For a system with a given length, the energy of the longitudinal peak increases as the diameter increases, due to the decreasing aspect ratio. The red shift of the longitudinal peak with increasing length becomes smaller as the diameter of the system increases, which correlates with the smaller increase of the aspect ratio for each added unit length to the system. The transverse peak is narrow and well separated from the longitudinal peak for systems with a small diameter such as nanowires and small pentagonal nanorods. For the star-shaped and large pentagonal nanorods, the transverse peak is split into a broad band. The transverse peak or band stays at nearly constant energy and intensity for each system of a given radius. The transitions involved are of $\Sigma \rightarrow \Pi$, $\Phi \rightarrow \Gamma$, etc. character for the nanowires and small pentagonal nanorods, but additional transitions such as $\Pi \rightarrow \mathrm{H}$ also occur for the wider systems. The transition dipole moments have a smaller magnitude than for the longitudinal peak. For systems with an aspect ratio smaller than one, the longitudinal peak is higher in energy than the transverse peak; as the aspect ratio increases, these two peaks cross in the excitation spectrum so that the longitudinal peak becomes the lowest in energy. Gold nanorods show a much wider excitation spectrum due to the high density of transitions originating from the *d*-band. The longitudinal peak shifts to lower energy and increases in intensity with increasing length, like in the silver case. However, the longitudinal peak of systems with a low aspect ratio shows strong contributions from transitions originating from the *d*-band in addition to the transitions originating from delocalized cylindrical orbitals. The amount of *d*-band mixing decreases as the aspect ratio increases and the longitudinal peak shifts away from the *d*-band. At the LB94/DZ level of theory, the transverse peaks are hidden in the *d*-band. While the LB94 functional usually works well for gold and silver systems, no strong transverse peak is shown for the gold nanorods studied here, which contradicts experiment.

Acknowledgements

This material is based upon work supported by the Air Force Office of Scientific Research under AFOSR Award No. FA9550-09-1-0451. C.M.A. also thanks the Alfred P. Sloan Foundation for a Sloan Research Fellowship (2011–2013) and the Camille and Henry Dreyfus Foundation for a Camille Dreyfus Teacher-Scholar Award (2011–2016). This work used the Extreme Science and Engineering Discovery Environment (XSEDE), which is supported by National Science Foundation grant number OCI-1053575.

Chapter 5 - Origin and TDDFT Benchmarking of the Plasmon Resonance in Acenes

Reproduced with permission from:
Guidez, E. B.; Aikens, C. M. *J. Phys. Chem. C* **2013**, *117,* 21466.
Copyright 2013 American Chemical Society.

Abstract

The origin of plasmon resonance in acenes is described by analyzing the excitation spectrum of naphthalene in terms of configuration interaction. The strong longitudinal β-peak in the UV region of the spectrum results from a constructive interaction of the transition dipole moments of two degenerate configurations V_1 and V_2. V_1 corresponds to the excitation of an electron from the HOMO to the LUMO+1. V_2 corresponds to the excitation of an electron from the HOMO-1 to the LUMO. The weak longitudinal α-peak in the visible results from a destructive interaction of the dipole moments of the same two configurations. Previous TDDFT calculations showed a similar behavior for silver and gold nanoparticles but often with more than two interacting configurations. The plasmon occurs at the frequency where all configurations interact constructively. The β-peak of acenes can therefore be identified as the plasmon peak. The natural transition orbitals involved in the α- and β- peaks of naphthalene have identical shapes, which reflects the fact that the transitions involved in these two peaks are similar, but they may have opposite phases. An analysis of the transition density of the β-peak of naphthalene reveals that the electron density moves from one side of the molecule to the other upon excitation, as expected for a dipolar plasmon. The plasmonic character of the β-peak is compared to the single-particle transition character of the transverse p-band. Several exchange-correlation functionals have been benchmarked. Hybrid functionals give the best description of the β-peak and the α-peak. The couplings between the two interacting configurations at all levels of theory are similar to experimental values. On the other hand, long-range corrected functionals give the most accurate energies for the transverse p-band.

Introduction

Polycyclic aromatic hydrocarbons have been studied for almost a century due to their environmental impact and their role as carcinogens.[211,212] Linear polycyclic aromatic hydrocarbons, or acenes (Figure 5-1), have recently attracted more attention due to their potential use as semi-conducting materials such as field-effect transistors.[213-218]

Figure 5-1. Linear polycyclic aromatic hydrocarbons (acenes).

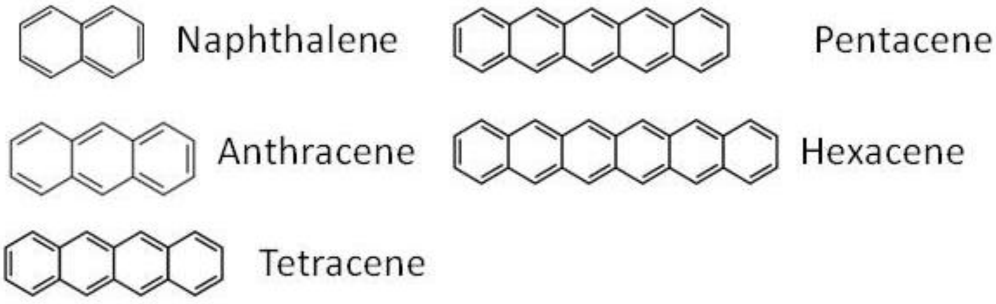

Acenes with up to five fused aromatic rings can be easily synthesized with a procedure readily available in the literature.[211] However, the synthesis of longer acenes is more difficult due to their increasing instability in solution as the number of rings increases.[219-221] Octacene and nonacene were synthesized in a cryogenic argon matrix in 2010.[222] Computational methods are therefore necessary to study the electronic structure of acenes in the ground state[223-225] and excited state.[226-228] Despite their long history, the electronic properties of acenes are still subject to some controversy. For instance, Houk et al. predicted a singlet ground state for acenes shorter than nonacene and a triplet ground state for acenes longer than nonacene using density functional theory[229] while Bendikov et al. predicted a singlet ground state with a strong diradical nature for acenes larger than hexacene.[230] Chan et al. showed than the polyradical character increases with increasing number of rings.[231]

The excitation spectra of acenes show three main features: the β-band, α-band and p-band.[211,232] The α- and β-bands are comprised of two transitions polarized along the long axis of the system (HOMO→LUMO+1 and HOMO-1→LUMO) and have B_{3u} symmetry.[233] The p-band corresponds to transitions polarized along the short axis of the system (B_{2u} symmetry), where the main component is the HOMO-LUMO transition.[211,234] The α- and p-bands are also known as the $1L_b$ and $1L_a$ states, respectively. The β-band is in the UV region of the spectrum and has a very large oscillator strength while the p-band and α-band are in the visible and are very weak.[211] All three bands shift to lower energy as the number of rings increases.[211,235] However, the shift of the p-band is larger than the shift of the α-band and consequently the two peaks cross. The α-band of naphthalene is lower in energy than the p-band whereas the α-band is higher in energy than the p-band for anthracene and longer acenes.[211] Several models involving configuration interaction have been used to describe the excited states of acenes. These methods include configuration interaction calculations using the free-electron approach,[234,236] as well as configuration interaction using a linear combination of atomic orbitals approximation with neglect of differential overlap between atomic orbitals.[237] More recently, Sony and Shukula used the Pariser-Parr-Pople (PPP) Hamiltonian in conjunction with the configuration interaction method to reproduce the excitation spectrum of acenes.[233] Time-dependent density functional theory has also been used to calculate the excited states of acenes. But in 2003, Grimme and Parac determined that standard GGAs and hybrid functionals used in time-dependent functional theory calculations tend to strongly underestimate the energy of the p-band with increasing acene length, which is why these standard functionals do not give the correct ordering between the α-band and p-band.[228] In the last three years, Wong and Hseih and Herbert et al. employed several long-range corrected exchange-correlation functionals to obtain the correct ordering between the α and p-bands for all acenes.[238,239] Later, Ziegler et al performed an all-order constricted variational density functional theory calculation and obtained excitation energies for the α-and p-bands in good agreement with experiment.[240]

Several experiments have suggested that carbon nanotubes and graphene exhibit a plasmonic behavior.[241-245] Since acenes are building blocks of these systems, it is important to understand their properties. Recently, Manjavacas et al. showed that polycyclic aromatic hydrocarbons exhibit plasmons that are highly dependent on the charge of the molecule.[246] Plasmons, defined as a collective oscillation of electrons under an electromagnetic field, have previously been widely studied in noble metal nanoparticles.[2,64,71,151,192,209,247,248] The occurrence of plasmons in organic molecules opens many doors for plasmonic devices and an understanding of the origin of this phenomenon is essential in order to enhance its applications.

The majority of the theoretical studies of acenes in their excited states focus on the α- and p-band since they lie in the visible region.[228,240,249,250] However, very few studies focus on the β-peak which shows strong resonance. The goal of this study is to show that the β-peak is plasmonic and to theoretically derive the origin of this plasmon in naphthalene (i.e. acene with two fused benzene rings) using configuration interaction. We will also briefly compare the plasmonic character of the β-band with the single-particle excitation character of the p-band. Finally, we will benchmark exchange-correlation functionals for the plasmonic β-peak for the acene series up to hexacene.

Computational methods

The Q-Chem software was used to perform time-dependent density functional theory (TDDFT) calculations on acenes.[251] The acenes studied are naphthalene (two fused aromatic rings) up to hexacene (six fused aromatic rings). The geometries used to perform the TDDFT calculations were the ones optimized at the B3LYP/6-31G* level by Richard and Herbert.[239] The exchange-correlation functionals used for the TDDFT calculations are the GGAs BP86[102,103] and BLYP,[102,108] the hybrid functionals PBE0[105] and B3LYP,[102,108] and the asymptotically corrected functional LB94,[146] as well as three long-range corrected functionals ωPBEh,[252] μBLYP[239] and CAM-B3LYP.[253] For ωPBEh, we use the same parameters as Herbert et al as they were found to give accurate energies for the α and p-bands of acenes.[239] For μBLYP, we use a Coulomb parameter μ=0.17 a_0^{-1} which was also used by Herbert on acenes[239] and by Wong on Courmarin dyes.[254] For CAM-B3LYP, the original parameters by Yanai et al. are used.[253] A cc-pVTZ[255] basis set was used for all these calculations. Natural Transition Orbitals (NTOs) were also obtained using Q-Chem[256] and visualized using MacMolPlot.[257] The Amsterdam Density Functional package (ADF)[110] was used to perform TDDFT calculations at the asymptotically corrected SAOP[145]/TZP, LB94/TZP and LB94/QZ4P levels of theory. The transition densities were calculated with ADF using the excitations at the LB94/TZP level of theory and visualized using VMD.[258]

Results and discussion

Theoretical explanation of plasmon resonance in acenes

In this section, we will derive the plasmon resonance of naphthalene using a configuration interaction approach. The single-electron excitations making up the longitudinal α- and β-peaks are HOMO→LUMO+1 and HOMO-1→LUMO.[233] Only singly excited configurations are considered in this derivation. Both transitions have B_{3u} symmetry. In the neglect of differential overlap model, these transitions are exactly degenerate. We note that this configuration interaction approach was previously performed by Pariser,[237] but we expand on the important steps here to make a link to the origin of the plasmon effect. The excited state wavefunctions for the α- and β- peaks are given by the configuration interaction expression:

$$\Psi_{ex} = A_1 V_1 + A_2 V_2 \tag{5.1}$$

where V_1 and V_2 designate the singly excited determinantal configuration functions where an electron is excited from the HOMO to the LUMO+1 and from the HOMO-1 to the LUMO respectively.

The configuration interaction secular equations that must be solved are:

$$\begin{vmatrix} \mathrm{H}_{11} - \mathrm{E} & \mathrm{H}_{12} \\ \mathrm{H}_{21} & \mathrm{H}_{22} - \mathrm{E} \end{vmatrix} = 0 \tag{5.2}$$

$$\begin{bmatrix} \mathrm{H}_{11} - \mathrm{E} & \mathrm{H}_{12} \\ \mathrm{H}_{21} & \mathrm{H}_{22} - \mathrm{E} \end{bmatrix} \begin{bmatrix} \mathrm{A}_1 \\ \mathrm{A}_2 \end{bmatrix} = 0 \tag{5.3}$$

where the matrix elements H_{ij} are defined by $\mathrm{H}_{ij} = \int \mathrm{V}_i^* \left(\mathbf{H}_{ij}^{\mathrm{core}} + \frac{1}{2} \sum_{pq} \frac{e^2}{r_{pq}} \right) \mathrm{V}_j \mathrm{d}\upsilon$ and p and q designate the atomic p_π-orbitals. The neglect of differential overlap is used to simplify the Coulomb integrals. In addition to the neglect of differential overlap and the neglect of multiply excited configurations, only nearest neighbor resonance interactions were considered for the calculation of the coupling elements $\mathbf{H}_{ij}^{\mathrm{core}}$. Penetration integrals are constant or neglected for the core integrals $\mathbf{H}_{ii}^{\mathrm{core}}$.[237] Using these approximations, the configurations V_1 and V_2 are degenerate and we have $H_{11}=H_{22}$ and $H_{12}=H_{21}$.[237] The numerical values calculated from the configurational secular equations for H_{11}, H_{12}, H_{12} and H_{22} are:[237]

$$H_{11}=H_{22}=5.17 \text{ eV}$$

$$H_{12}= H_{21}=0.93 \text{ eV}$$

By solving equation 5.2, two excitation energies arise that correspond to the α and β peaks: $E^{\alpha} =H_{11}-H_{12}=4.24$ eV and $E^{\beta} =H_{11}+H_{12}=6.10$ eV. Now solving for the coefficients A_1 and A_2 yields $A_1 = -A_2$ for E^{α} and $A_1 = A_2$ for E^{β}. Therefore we get excited state wavefunctions for the α and β peaks; after normalizing coefficients A_1 and A_2, these wavefunctions are:

$$\Psi^{\alpha} = \frac{1}{\sqrt{2}}\mathrm{A}_1 - \frac{1}{\sqrt{2}}\mathrm{A}_2 \tag{5.4}$$

$$\Psi^{\beta} = \frac{1}{\sqrt{2}}\mathrm{A}_1 + \frac{1}{\sqrt{2}}\mathrm{A}_2 \tag{5.5}$$

Now, we can calculate the dipole moment of electronic transitions from the ground state to these two excited states. The transition dipole moments are directly related to the oscillator strength of the peaks observed in the excitation spectrum. The transition dipole moment between the ground state and an excited state is given by:

$$\mathbf{M}_{0\mathrm{ex}} = \int \Psi_0^{*}\mathbf{M}\Psi_{\mathrm{ex}}\,\mathrm{d}\upsilon \tag{5.6}$$

with

$$\mathbf{M} = \sum_{\mathrm{t}} \mathrm{e_t}\mathbf{r}_{\mathrm{t}} \tag{5.7}$$

where e_t and r_t are the charge and position of the t^{th} particle. Also, since the α and β excitations take place along the *z*-axis (long axis) of the molecule, we can simplify **M** by considering only the *z*-component of the transition which gives us:

$$\mathbf{M} = \sum_{\mathrm{t}} \mathrm{e_t z_t} \tag{5.8}$$

The transition dipole moment to the α state is given by:

$$\begin{aligned}\mathbf{M}_{0\alpha} &= \int \Psi_0^{*}\mathbf{M}\Psi_{\alpha}\,\mathrm{d}\upsilon = \int \mathrm{V}_0^{*}\sum_{\mathrm{t}}\mathrm{e_t z_t}\left[\frac{1}{\sqrt{2}}\mathrm{V}_1 - \frac{1}{\sqrt{2}}\mathrm{V}_2\right]\mathrm{d}\upsilon \\ &= \frac{1}{\sqrt{2}}\int \mathrm{V}_0^{*}\sum_{\mathrm{t}}\mathrm{e_t z_t V_1}\,\mathrm{d}\upsilon - \frac{1}{\sqrt{2}}\int \mathrm{V}_0^{*}\sum_{\mathrm{t}}\mathrm{e_t z_t V_2}\,\mathrm{d}\upsilon = \frac{1}{\sqrt{2}}(\mathrm{m}_1 - \mathrm{m}_2) \approx 0\end{aligned} \tag{5.9}$$

where $m_1 = [\emptyset_{HOMO}|\boldsymbol{M}|\emptyset_{LUMO+1}]$ and $m_2 = [\emptyset_{HOMO-1}|\boldsymbol{M}|\emptyset_{LUMO}]$. Using the approximations mentioned above, m_1=m_2 and equation 5.9 is exactly equal to zero. The transition dipole moment to the β state is given by:

$$
\begin{aligned}
\mathbf{M}_{0\beta} &= \int \Psi_0^{*}\mathbf{M}\Psi_{\beta}\,d\upsilon = \int V_0^{*}\sum_{t} e_t z_t \left[\frac{1}{\sqrt{2}}V_1 + \frac{1}{\sqrt{2}}V_2\right] d\upsilon \\
&= \frac{1}{\sqrt{2}}\int V_0^{*}\sum_{t} e_t z_t V_1 d\upsilon + \frac{1}{\sqrt{2}}\int V_0^{*}\sum_{t} e_t z_t V_2 d\upsilon = \frac{1}{\sqrt{2}}\left(m_1 + m_2\right) \approx \sqrt{2}m_1
\end{aligned}
\tag{5.10}
$$

How does this relate to the plasmon resonance? We see that the transitions involved in the α- and β-bands are identical but interact constructively in one case, giving the high-energy β-band, and destructively in the other, giving the low-intensity α-band. The TDDFT calculations performed for acenes from naphthalene to hexacene at the LB94/TZP level also display this behavior, as shown in Table 5.1.

Table 5.1. Excitation energies of α and β peaks of acenes, transitions involved, and their transition dipole moment contributions at the LB94/TZP level of theory.

Acene	Peak energy (eV)	Oscillator strength (a.u.)	Transitions	Weight	Transition dipole moment contribution (a.u.)
2	4.09 (α-peak)	0.000032	HOMO-1→ LUMO	0.5027	2.2022
			HOMO→ LUMO+1	0.4967	-2.1736
	5.60 (β-peak)	1.107	HOMO-1→ LUMO	0.4734	-1.8247
			HOMO→ LUMO+1	0.4811	-1.8267
3	3.50 (α-peak)	0.00052	HOMO-1→ LUMO	0.5166	2.8333
			HOMO→ LUMO+1	0.4830	-2.7312
	4.82 (β-peak)	1.678	HOMO-1→ LUMO	0.4597	-2.2764
			HOMO→ LUMO+1	0.4944	-2.3536
4	3.12 (α-peak)	0.0017	HOMO-1→ LUMO	0.5295	3.3752
			HOMO→ LUMO+1	0.4701	-3.1848
	4.26 (β-peak)	2.152	HOMO-1→ LUMO	0.4441	-2.6426
			HOMO→ LUMO+1	0.5042	-2.8198
5	2.86 (α-peak)	0.0042	HOMO-1→ LUMO	0.5426	-3.8516
			HOMO→ LUMO+1	0.4569	3.5533
	3.85 (β-peak)	2.508	HOMO-1→ LUMO	0.4257	2.9407
			HOMO→ LUMO+1	0.5111	3.2396
6	2.67 (α-peak)	0.0083	HOMO-1→ LUMO	0.5563	4.2759
			HOMO→ LUMO+1	0.4431	-3.8489
	3.52 (β-peak)	2.742	HOMO-1→ LUMO	0.4047	-3.1773
			HOMO→ LUMO+1	0.5163	-3.6193

In fact, Table 5.1 shows that the HOMO→LUMO+1 and HOMO-1→LUMO both contribute essentially equally to the β- and α-peaks. The transition dipole moments have similar amplitudes but opposite signs for the α-peak, which explains why this peak is weak. On the other hand, the transition dipole moments have the same sign (and again similar amplitudes) for the β-peak, leading to a strong peak. Both transitions have similar weights for both the α-peak and the β-peak. We note that the theoretical derivation described above yields a zero oscillator strength for the α-peak but this peak is observed both experimentally and with TDDFT. This is because, as mentioned above, the theoretical derivation used some approximations like the neglect of differential overlap that do not exactly apply in a real system. In a real system H_{11} is not exactly equal to H_{22}, which will affect not only the energies of the α- and β- peaks but also their oscillator strengths. Thus, the oscillator strength of the α-peak is not exactly equal to zero although it remains small. This constructive versus destructive addition of the transition dipole moments giving the β- and α-peak in acenes also occurs in noble-metal nanoparticles as shown by several TDDFT calculations.[64,70,71,195,209] In the case of the acenes studied here, only two configurations interact, but many configurations may interact for silver and gold nanoparticles. The higher the number of interacting configurations, the more excitation peaks are obtained. For instance if four configurations interact, four peaks are obtained. At a specific frequency all of these configurations interact constructively, leading to the strong peak (the plasmon peak) observed in the excitation spectrum of these systems. Therefore, the β-band in acenes can be identified as a plasmon band in which only two configurations contribute. It is worth pointing out that the intensity and the wavelength of the β-peak (the plasmon peak) increase with increasing number of rings the same way the intensity and the wavelength of the longitudinal plasmon peak in noble metal nanorods do with increasing length.[55,56] In the hypothetical example with four interacting configurations, the other three peaks, resulting from a destructive interaction of the dipole moments of these configurations, are weaker but their oscillator strengths may vary from one another depending on the total resulting dipole moment. These peaks are analogs of the α-peak observed in acenes.

Natural transition orbitals (NTOs) calculated for both the α and β peaks of naphthalene at the LB94/cc-pVTZ and ωPBEh/cc-pTZV levels of theory are shown in Figure 5-2 and Figure C-1 of Appendix C, respectively. NTOs are used to express an excitation in terms of a single electron-hole pair of orbitals. The “hole” represents the orbital where the electron density is excited from and the “electron” represents the orbital the electron density is excited to.[256]

Figure 5-2. Natural transition orbitals involved in the α and β-peak at the LB94/cc-pVTZ level of theory.

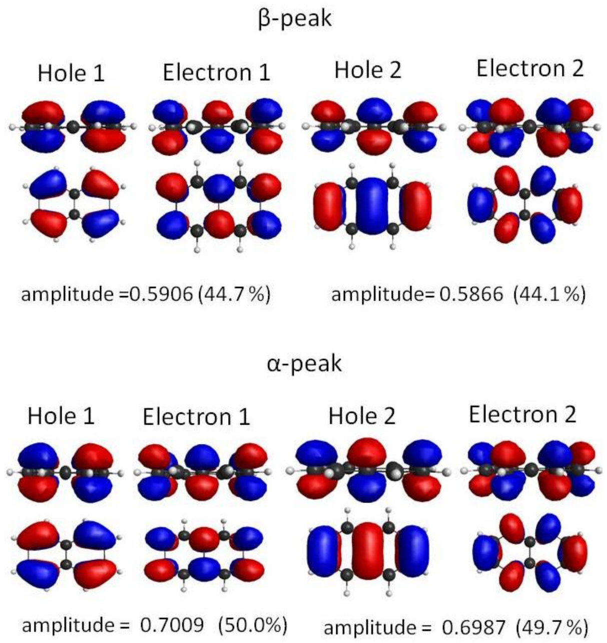
β-peak
Hole 1
Electron 1
Hole 2
Electron 2
amplitude =0.5906 (44.7 %)
amplitude= 0.5866 (44.1 %)
α-peak
Hole 1
Electron 1
Hole 2
Electron 2
amplitude = 0.7009 (50.0%)
amplitude = 0.6987 (49.7 %)

*An edge view and a face view of each orbital are presented.

At both the LB94 and ωPBEh levels, a single pair could not be obtained but two pairs of delocalized orbitals with approximately equal amplitude were obtained. We can see that the two orbital pairs involved are the same for both the α- and β-peaks. This again results from the fact that the two single-electron configurations involved in both peaks are the same but may interact constructively or destructively. We also note that the orbitals are the same at both levels of theory examined here. At the LB94/cc-pVTZ level of theory, we can see that the two holes of the α-peak have the opposite phase as the two holes of the β-peak. In addition, electron 1 of the β-peak has the opposite phase as electron 1 of the α-peak. Electron 2 of the α-peak and electron 2 of the β-peak are in phase. At the ωPBEh/cc-pVTZ level of theory, only hole 1 of the α-peak has the opposite phase as hole 2 of the β-peak. All other NTO pairs are in phase. It is likely that this behavior is related to the fact that the wavefunctions describing the α- and β-peaks differ by a negative sign (equations 5.4 and 5.5). The holes are the eigenvectors that diagonalize the matrix $\mathbf{T}\mathbf{T}^{\dagger}$ and the electrons are the eigenvectors that diagonalize the matrix $\mathbf{T}^{\dagger}\mathbf{T}$ where $\mathbf{T}$ is the transition density matrix defined by:[118]

$$\mathbf{T}_{ia} = \langle \phi_i | \hat{T}(r) | \phi_a \rangle \tag{5.11}$$

with

$$T(r) = N\int \left| \Psi^{ex}(r_1,r_2,\ldots,r_n) \right\rangle \left\langle \Psi_0(r_1,r_2,\ldots,r_n) \right| dr_2 \ldots dr_n \tag{5.12}$$

The indices *i* and *a* define occupied and unoccupied orbitals respectively. Ψ^{ex} corresponds to the excited state (here α or β) and Ψ_0 labels the ground state.

The transition densities corresponding to the α- and β-peaks of naphthalene are plotted in Figure 5-3.

Figure 5-3. Edge view and side view of the transition densities for the α- and β-peaks of naphthalene.

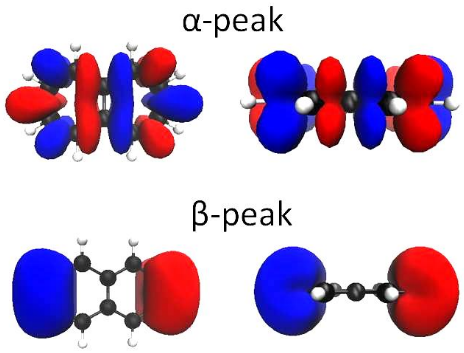

*In blue is the region of the molecule where the electron density decreases. In red is the region of the molecule where the electron density increases. |Isovalue (α–peak)|=0.005. |Isovalue ((β–peak)|=0.05.

For the β-peak (the plasmon peak), we can see that upon excitation, the electron density moves from one end of the molecule (blue region) to the other (red region). This is what we expect for this dipolar plasmonic excitation, where the valence electrons are coherently excited.[259] For the α-peak, we can see that the region of the naphthalene molecule where the electron density is depleted upon excitation is not concentrated at the ends of the molecule, but is spread throughout the ring system. The same observation can be made for the part of the molecule where the electron density accumulates upon excitation. We note that the amplitude of the isovalue used to plot the β-peak transition density is ten times larger than for the α-peak. This choice was made in order to be able to visualize the transition density of the α-peak. This indicates that the α-peak involved a much smaller charge redistribution upon excitation than the β-peak. In summary, we can see that the plasmon peak involves a high charge redistribution from one end of the naphthalene molecule to the other, which results from the constructive addition of the transition dipole moments of the HOMO-1→LUMO and HOMO→LUMO+1 excitations. On the other hand, the α-peak involves a small rearrangement of the electron density upon excitation due to the destructive addition of the dipole moments of the HOMO-1→LUMO and HOMO→LUMO+1 transitions.

Single-particle versus plasmonic character of the p-band

We have demonstrated above that the β-band and α-band result from the interaction between the HOMO→LUMO+1 and HOMO-1→LUMO configurations which have the same symmetry and similar energies. The dipole moments of these two transitions have similar amplitudes but interact constructively in one case, which yields the high-intensity β-band in the UV, and destructively in the other, yielding the low-intensity α-band in the visible. We now briefly focus on the p-band, which involves transitions perpendicular to the main axis of the system. Like the α-band, the p-band is in the visible and has low oscillator strength. It also shifts to lower energy with increasing system length.[233,239] It is known that the HOMO→LUMO transition, which has B_{2u} symmetry, is the main component of the p-band.[233] Table 5.2 shows the transitions contributing to the p-band in naphthalene at the LB94/TZP level of theory.

Table 5.2. Transitions with B_{2u} symmetry for naphthalene at the LB94/TZP level of theory.

Energy (eV)	Oscillator strength(a.u.)	Transitions	Weight	Transition dipole moment (a.u.)
3.99 (p-band)	0.0416	HOMO→LUMO	0.9173	-1.8247
		HOMO-2→LUMO+2	0.0413	0.5384
		HOMO-1→LUMO+1	0.0311	0.3996
5.75	0.129	HOMO-1→LUMO+1	0.8877	1.7760
		HOMO-2→LUMO+2	0.0673	-0.5720
		HOMO→LUMO	0.0145	0.1909
7.38	0.503	HOMO-2→LUMO+2	0.8602	-1.8060
		HOMO→LUMO	0.0494	-0.3111
		HOMO-1→LUMO+1	0.0485	-0.3663

The HOMO→LUMO transition indeed has a very high dipole moment but two other transitions are also involved in the p-band: HOMO-1→LUMO+1 and HOMO-2→LUMO+2. These two transitions of course also have B_{2u} symmetry. They have a smaller dipole moment and a lower weight than the HOMO→LUMO transition. Two other peaks in the excitation spectrum are comprised of these three transitions, as shown in Table 5.2. For the peak at 5.75 eV and the p-band at 3.99 eV, the dipole moments of these transitions interact destructively with the dipole moment of the HOMO→LUMO. These peaks therefore have moderately low oscillator strength. Even so, the p-band is observed experimentally.[211] The peak at 5.75 eV is very close in energy to the strong β-band and therefore cannot be easily resolved experimentally. For the higher energy peak at 7.38 eV, the dipole moments of the three transitions interact constructively and this peak has a higher oscillator strength than the other two. However, it is at such a high energy that it is not observed experimentally. This behavior is what we expect for three interacting transitions: two low-energy and low-intensity peaks resulting from the destructive addition of the three transition dipole moments and one high-energy peak resulting from the constructive addition of the three transition dipole moments. Does this mean that this high energy peak is plasmonic? By looking at the weights and dipole moments of the transitions involved in these peaks, it is obvious than one transition strongly dominates the other two. For the p-band, the HOMO→LUMO transition dominates with a weight of 0.9173 and a dipole moment of -1.8247 a.u. On the other hand, the HOMO-1→LUMO+1 and HOMO-2→LUMO+2 transitions have much lower weights (0.0413 a.u. and 0.0311 a.u. respectively) and lower dipole moments (0.5384 and 0.3996 a.u. respectively). In a similar way, we can see that for the second peak at 5.75 eV, the HOMO-1→LUMO+1 transition dominates and for the peak at 7.38 eV, the HOMO-2→LUMO+2 transition dominates. This behavior can be explained by the fact that these three transitions have very different energies and therefore do not mix as efficiently as the transitions involved in the α and β-bands. These transverse peaks are therefore best described as single-particle excitations. However, there is a small amount of plasmonic character mixed in, which makes the peak at 7.38 eV peak gain some oscillator strength.

Benchmarking of exchange-correlation functionals

The β-band is the strongest excitation peak and was shown in the first section to have plasmonic character. However, most previous theoretical studies on acenes have focused on the α- and p-bands since they lie in the visible region.[238,239] Therefore, benchmarking of a variety of DFT exchange-correlation functionals is performed for the β-peak.

Several GGAs, hybrid and long-range corrected exchange-correlation functionals were used to calculate the excitation energies and oscillator strengths of acenes with two to six rings. The wavelength of the α-, β- and p-bands obtained as well as experimental values are shown in Figures 5-4A to 5-4C. Tables 5.3 to 5.5 show the excitation energy values calculated with different functionals for all three bands as well as the Mean Absolute Error (MAE) calculated in comparison with experiment.

Figure 5-4. A) β-band B) p-band and C) α-band excitation energies of acenes with two to six rings at various levels of theory.

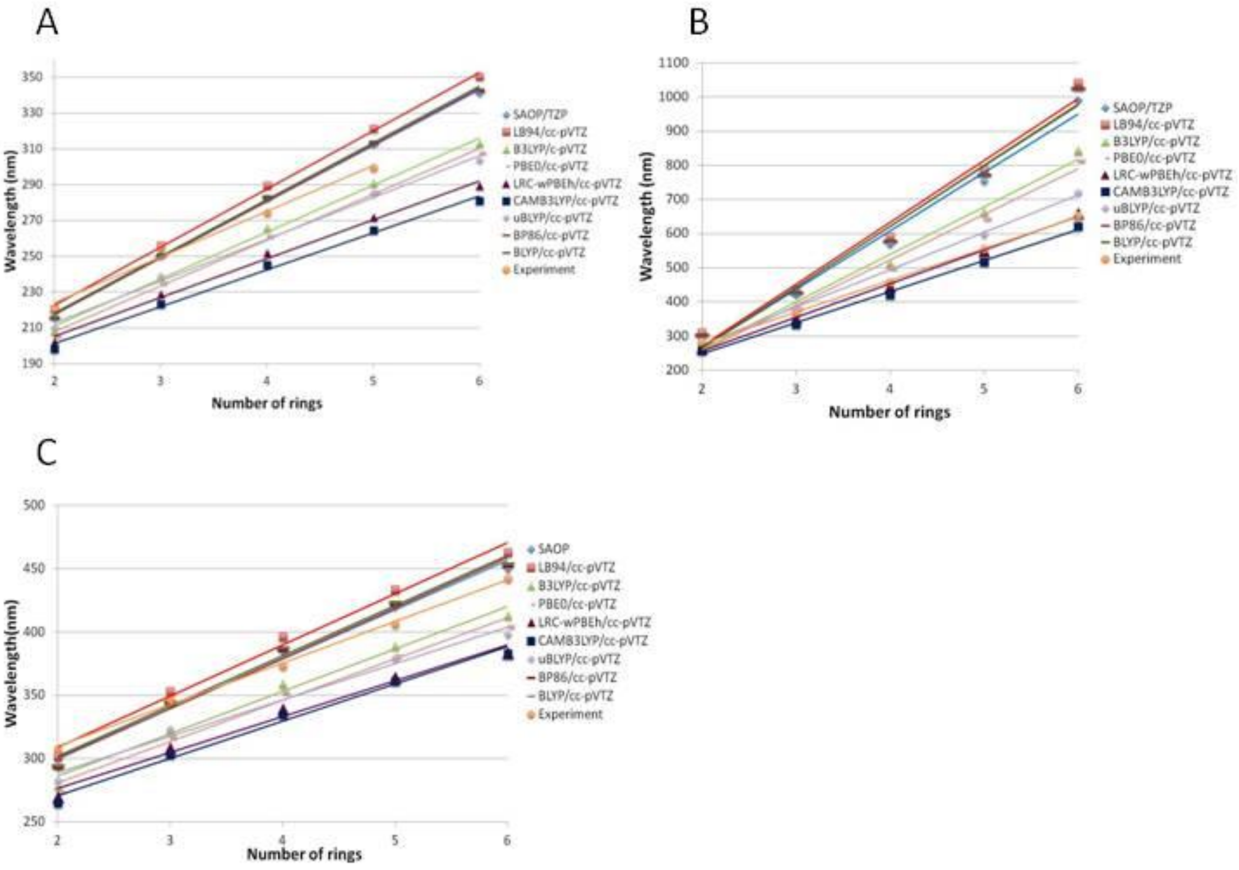

*Due to convergence issues, the excitation energies of tetracene at the μBLYP/cc-pVTZ level of theory could not be obtained. Experimental data is obtained from Ref[235].

Table 5.3. TDDFT wavelength of the α-band of acenes with various exchange-correlation functionals.

Number of rings	2	3	4	5	6	MAE (nm)
SAOP/TZP	293.87	343.47	385.35	420.69	450.49	10.28
LB94/cc-pVTZ	301.58	353.15	396.57	433.81	463.42	16.60
LB94/TZP	303.43	354.70	397.73	433.07	464.01	16.74
LB94/QZ4P	302.86	354.52	398.00	434.48	465.06	17.36
B3LYP/cc-pVTZ	279.17	323.21	359.66	389.50	413.58	22.52
PBE0/cc-pTZV	274.28	317.10	352.45	381.48	404.95	29.49
ωPBEh/cc-pVTZ	269.82	308.48	339.45	364.16	383.73	42.41
CAM-B3LYP/cc-pVTZ	264.91	303.21	335.02	361.41	383.15	46.00
μBLYP/cc-pVTZ	282.91	323.64	NA[a]	379.82	398.68	29.80[c]
BP86/cc-pVTZ	292.97	343.36	385.94	421.92	452.18	11.18
BLYP/cc-pVTZ	294.77	345.25	387.94	423.95	454.25	11.66
Experiment[b]	307.65	347.29	373.45	406.51	442.80	

a. Data could not be obtained due to convergence issues.
b. Data from Ref[235]
c. MAE calculated with four systems (tetracene omitted)

Table 5.4. TDDFT wavelength of the β-band of acenes with various exchange-correlation functionals.

Number of rings	2	3	4	5	6	MAE[c] (nm)
SAOP/TZP	215.96	250.53	282.48	312.72	341.35	7.66
LB94/cc-pVTZ	220.31	256.26	289.66	321.29	350.40	9.65
LB94/TZP	221.23	257.30	290.71	322.33	352.20	10.52
LB94/QZ4P	222.67	258.47	291.71	323.18	353.00	11.63
B3LYP/cc-pVTZ	208.27	238.48	266.09	291.19	313.21	11.37
PBE0/cc-pTZV	205.35	235.13	261.24	286.01	307.71	15.44
ωPBEh/cc-pVTZ	202.20	228.80	251.82	271.85	289.24	23.71
CAM-B3LYP/cc-pVTZ	198.28	223.41	245.28	264.41	281.11	29.53
μBLYP/cc-pVTZ	210.19	238.93	NA[a]	285.21	303.86	13.63[d]
BP86/cc-pVTZ	215.44	250.36	282.60	313.15	342.11	7.97
BLYP/cc-pVTZ	216.22	251.14	283.48	314.16	343.28	8.06
Experiment[b]	220.61	255.11	274.30	299.48	NA	

a. Data could not be obtained due to convergence issues.
b. Data from Ref[235]
c. Hexacene omitted for MAE calculation since no experimental data is available for the β peak
d. MAE calculated with three systems (tetracene and hexacene omitted).

Table 5.5. TDDFT wavelength of the p-band of acenes with various exchange-correlation functionals.

Number of rings	2	3	4	5	6	MAE (nm)
SAOP/TZP	302.80	422.38	569.32	754.34	992.29	145.04
LB94/cc-pVTZ	310.83	436.09	590.85	786.85	1040.92	169.92
LB94/TZP	311.10	434.71	586.61	777.61	1022.99	163.42
LB94/QZ4P	312.25	437.55	592.31	788.08	1041.55	171.16
B3LYP/cc-pVTZ	285.09	389.37	514.22	664.15	844.29	76.24
PBE0/cc-pTZV	279.03	379.88	500.02	643.31	813.60	61.60
ωPBEh/cc-pVTZ	265.91	350.65	445.27	548.70	659.03	11.87
CAM-B3LYP/cc-pVTZ	257.49	334.48	421.21	517.29	621.79	32.73
μBLYP/cc-pVTZ	283.08	378.12	NA[a]	598.18	720.34	30.32
BP86/cc-pVTZ	304.06	426.44	578.55	772.34	1025.76	158.25
BLYP/cc-pVTZ	305.63	427.86	579.42	771.91	1022.55	158.29
Experiment[b]	283.07	366.82	457.51	555.98	652.55	

a. Data could not be obtained due to convergence issues.
b. Data from Ref[235]
c. MAE calculated with four systems (tetracene omitted).

All three peaks display a linear increase of their wavelength with increasing length. The longitudinal peak of noble metal nanorods exhibit a similar behavior which was explained by the particle-in-a-cylinder model.[70] The α- and β-peaks show similar trends, which is not surprising since they are comprised of the same one-electron transitions.

We now compare the excitation energies obtained for the α- and β-peaks with the different functionals. GGAs (BP86 and BLYP) and asymptotically corrected functionals (LB94 and SAOP) give α- and β-peak wavelengths that are very close to experiment for small systems (naphthalene and anthracene). However, the error increases with increasing length and the peak wavelengths tend to be highly overestimated for the longest systems. We note that the energies calculated at the LB94/cc-pVTZ level of theory with Q-Chem and the energies calculated at the LB94/TZP with ADF are very similar, as shown in Tables 5.3 and 5.4. Also, the energy values calculated at the LB94/QZ4P level of theory are very similar to the LB94/TZP values, which suggests that there is almost no basis set dependence on the energies of the α- and β-peaks. Hybrid functionals (B3LYP and PBE0) tend to underestimate the α- and β-peak wavelengths but the difference between theory and experiment remains nearly constant with increasing system length. This is shown by the fact that the slope of the linear fit for these functional is nearly equal to the slope of the linear fit for experimental data (Table 5.6). B3LYP shows mean absolute errors of 11.37 nm and 22.52 nm in comparison with experiment for the β- and α- peaks respectively. The MAE values are slightly larger for the hybrid functionals than for the asymptotically corrected functional and GGAs but hybrid functionals give a better description of the α- and β-peak energies with increasing size. The long-range corrected functionals ωPBEh and CAM-B3LYP tend to underestimate the wavelength of the α- and β-peaks. This underestimation tends to become larger with increasing system size, as shown by the fact that the slope of the linear fit for these functional is smaller than the slope of the linear fit for the experimental data (Table 5.6).

Table 5.6. Slope of the linear fits from Figure 4 (in nm/ring).

Functional	α-band	β-band	p-band
SAOP/TZP	39.05	31.30	171.09
LB94/cc-pVTZ	40.44	32.52	181.09
BP86/cc-pVTZ	39.70	31.61	178.93
BLYP/cc-pVTZ	39.77	31.72	177.79
B3LYP/cc-pVTZ	33.51	26.26	139.32
PBE0/cc-pTZV	32.57	25.56	133.26
ωPBEh/cc-pVTZ	28.35	21.71	98.43
CAM-B3LYP/cc-pVTZ	29.47	20.67	91.14
μBLYP/cc-pVTZ	28.77	23.36	109.46
Experiment[a]	32.95	25.58	92.81

a. Data from Ref[235]

These long-range corrected functionals display the largest MAE values: 23.71 and 29.53 nm for ωPBEh and CAM-B3LYP respectively. The long-range corrected functional μBLYP, which does not contain any Hartree-Fock exchange contrary to the other two, gives peak wavelengths close to the ones obtained with hybrid functionals and also a similar MAE value. But like the other long-range corrected functionals studied here, the error increases with increasing system length.

We now briefly look at the p-band. GGAs and asymptotically corrected functionals tend to strongly overestimate the wavelength of the p-band and the overestimation strongly increases with system size, as also observed previously by Grimme.[228] This is illustrated by MAE values larger than 145 nm. We can make a similar observation for hybrid functionals, although the error does not increase as fast as for the GGAs and asymptotically corrected functionals, which is shown by smaller MAE values (61.60 and 76.24 nm for PBE0 and B3LYP respectively). We note that similar to the longitudinal peaks, the energies calculated at the LB94/cc-pVTZ level of theory with Q-Chem and the energies calculated at the LB94/TZP with ADF for the p-band are very similar, as shown in Table 5.5. However, the difference between the energy values calculated at the LB94/QZ4P level of theory and the values calculated at the LB94/TZP level of theory tends to increase with increasing size. The p-band energies therefore exhibit some basis set dependence. Long-range corrected functionals give an improved description of the p-band but not the α-band or β-band. The wavelengths for the long-range corrected functional ωPBEh and the experimental data nearly overlap each other. The MAE is 11.87 nm, which is smaller than all other functionals. It is also known that the ωPBEh functional gives the correct ordering between the α and β peak for all acenes.[239] CAM-B3LYP tends to underestimate the p-band wavelength but the difference between theory and experiment is approximately constant with increasing size, as shown by the slope of the linear fit which is similar to the slope of the linear fit of the experimental data. The long-range corrected functional μBLYP overestimates the p-band wavelength and the overestimation gets larger as the system size increases. The MAE values for CAM-B3LYP and μBLYP (32.73 and 30.32 nm respectively) are twice as large as the MAE calculated for ωPBEh (11.87 nm). Overall, hybrid functionals provide the best energies of the α- and β-bands whereas the long-range corrected functional ωPBEh provides the best energies for the p-band.

The matrix elements H_{mn} were calculated at the BP86, B3LYP, LB94, and ωPBEh levels of theory and for the experimental data using the expressions for E^{α} and E^{β} reported above: $E^{\alpha} = H_{11} - H_{12}$ and $E^{\beta} = H_{11} + H_{12}$. The values of $H_{11} = H_{22} = ½(E^{\alpha} + E^{\beta})$ and $H_{12} = H_{21} = ½(E^{\beta} - E^{\alpha})$ are reported in Table 5.7.

Table 5.7. Matrix elements H_{11} and H_{12} of the secular equation 5.2 in eV for acenes with various exchange-correlation functional and cc/pVTZ basis set.

	LB94		B3LYP		BP86		ωPBEh		Experiment[a]	
Number of rings	H_{11}	H_{12}	H_{11}	H_{12}	H_{11}	H_{12}	H_{11}	H_{12}	H_{11}	H_{12}
2	4.87	0.76	5.20	0.76	4.99	0.76	5.36	0.77	4.83	0.80
3	4.17	0.66	4.52	0.68	4.28	0.67	4.72	0.70	4.22	0.65
4	3.70	0.58	4.05	0.61	3.80	0.59	4.29	0.64	3.92	0.60
5	3.36	0.50	3.72	0.54	3.45	0.51	3.98	0.58	3.60	0.55
6	3.11	0.43	3.48	0.48	3.18	0.44	3.76	0.53	NA	NA

a. Experimental values calculated from the α and β bands in Ref[235]

Both H_{11} and H_{12} values decrease with increasing system size. This is in accordance with the decreasing orbital energy gaps with increasing length. The relative amount of coupling (H_{12}/H_{11}) seems to remain constant with increasing size. We see that the coupling matrix elements H_{12} are similar at all levels of theory, which suggests that the amount of coupling between the two configurations V_1 and V_2 does not vary significantly between different levels of theory. On the other hand, the matrix elements H_{11} can fluctuate between different levels of theory. The energies of the configurations V_1 and V_2 are therefore affected by the level of theory used. The asymptotically corrected LB94 functional gives accurate values of H_{11} for naphthalene and anthracene compared to experiment (the difference is 0.04 eV) but the error strongly increases with increasing system length (the difference is 0.24 eV for pentacene). The hybrid B3LYP functional gives a large difference with experiment for the H_{11} value but the error seems to decrease with increasing system length (from 0.37 eV for naphthalene to 0.13 eV for hexacene). A similar observation can be made for the long-range corrected ωPBEh functional, where the difference between theory and experiment is 0.54 eV for naphthalene down to 0.39 eV for hexacene.

Conclusions

This work presents a TDDFT analysis of the excitation spectrum of acenes and shows the origin of their plasmon resonance. The interaction between the quasi-degenerate HOMO→LUMO+1 and HOMO-1→LUMO transitions yields two peaks in the excitation spectrum: the β-peak and the α-peak. We have shown that the β-peak, which has a high energy and high intensity, originates from a constructive interaction of the two transition dipole moments and can be identified as a plasmon peak. The low-energy α-peak originates from a destructive interaction between the two transition dipole moments and is therefore weak. The configuration interaction singles analysis with the neglect of differential overlap approximation performed by Pariser[237] reproduces these features. We note that silver and gold nanoparticles, which are known to exhibit plasmon resonances, display a similar configuration interaction behavior to that described here although more than two transitions may interact. The frequency where the dipole moments of all the transitions involved interact constructively is the plasmon resonance. The natural transition orbitals were calculated for naphthalene and we saw that two electron-hole pairs of similar amplitudes were needed to describe the α- and β-peaks. The NTOs involved in both the α- and β-peaks are identical but may have opposite phases. An analysis of the transition densities shows a strong charge redistribution where electron density moves from one side of the molecule to the other upon excitation for the β-peak (plasmon peak). On the other hand, the α-peak involves much less charge redistribution upon excitation. In contrast to the plasmonic character of the longitudinal β-band, we show that the transverse p-band can be best described as a single-particle transition. Since very few theoretical studies have previously examined the β-peak, a benchmarking of several functionals was performed. Hybrid functionals give the best description of the α- and β-peaks but highly overestimate the p-band for long systems. The long-range corrected functional ωPBEh gives an accurate energy for the p-band but does not provide good excitation energies for the α- and β-peaks. The couplings between the two interacting configurations HOMO-1→LUMO and HOMO→LUMO+1 are similar to experiment regardless of the functional considered.

The occurrence of plasmon resonances in organic systems is very important as they can be used to make lighter optic devices compared to metallic nanoparticles. While our analysis focuses only on acenes, a wide variety of polycyclic aromatic hydrocarbons may display plasmon resonances.[246] Like noble metal nanoparticles, the plasmon resonances in these systems can be tuned for applications of interest.

Acknowledgements

This material is based on work supported by the National Science Foundation under grant no. EPS-0903806. The authors also thank Kansas State University for funding this work.

C.M.A. is grateful to the Alfred P. Sloan Foundation for a Sloan Research Fellowship (2011-2013) and the Camille and Henry Dreyfus Foundation for a Camille Dreyfus Teacher-Scholar Award (2011-2016). The computing for this project was performed on the Beocat Research Cluster at Kansas State University, which is funded in part by NSF grants CNS-1006860, EPS-1006860, and EPS-0919443.

Chapter 6 - Plasmon Resonance Analysis with Configuration Interaction

Abstract

Plasmon resonances are described using configuration interaction (CI). A fictitious system of three interacting configurations is considered, which yields three excited states. Excited states energies and oscillator strengths are derived from the eigenvalues and eigenvectors of the CI matrix, where the diagonal elements α_i (i=1,2,3) correspond to the interacting one-electron transition energies and the off-diagonal elements β_{ij} correspond to the coupling between these configurations. The plasmonic state is easily identified by its higher energy and much larger oscillator strength. This high oscillator strength is due to a constructive addition of the eigenvectors contributing to this state. The maximum oscillator strength enhancement of the plasmon peak is equal to the number of configurations in the CI matrix (three here), which occurs in the ideal case where all α elements are equal and all β elements are equal. When the transitions involved in the CI have different energies (different α values), the oscillator strength of the plasmon peak becomes smaller and its energy is shifted in comparison to the ideal case. Increasing all the coupling values from 0 up to the point where the coupling is similar in magnitude to the difference in α values leads to a rapid rise of the plasmon peak oscillator strength whereas its energy slightly blue-shifts. A further increase of the coupling values does not affect the oscillator strength of the plasmon peak, which remains near its maximum enhancement value, but drastically affects its energy, which rapidly rises. The plasmonic behavior of noble metal model systems is successfully described using configuration interaction.

Introduction

The plasmon resonance is defined classically as a collective oscillation of the conduction electrons of a system upon irradiation with light at a specific frequency. The plasmonic behavior of sodium clusters has been studied for several decades.[47,48,260-264] This phenomenon has also been intensively investigated in noble metal nanoparticles both theoretically[30,40,59,64,68,88,265-267] and experimentally[4,6,25,33,40,267-271] for applications in imaging,[15,16,165,271] sensing,[15-17,165,179,271], cancer therapy[6,170,171,271] and light harvesting devices.[19,248,272] More recently, polycyclic aromatic hydrocarbons[246,273] and graphene[243,274,275] have been described as plasmonic as well, which indicates that plasmons are not limited to metallic nanoparticles and opens additional doors for applications.[274,276]

Identification of plasmon modes is of course very important for the design of plasmonic materials. However, one question that still remains unanswered is: what is the quantum mechanical origin of these plasmons? One recent time-dependent density functional theory (TDDFT) study performed by Jacob et al. describes plasmon resonances as zero modes of the dielectric function ε, which depends on the coulomb kernel.[259] Plasmon modes can therefore be distinguished from single-particle transitions by scaling the electron-electron interaction. As a complementary interpretation, other studies suggest that plasmon resonances can be described as a constructive interaction of multiple one-electron transition dipole moments.[70,71,195,273,277] One-electron transitions may interact if they have the same symmetry and if they are close in energy. Using a configuration interaction approach, the energy and relative oscillator strength of the resulting peaks in the absorption spectrum can be determined.[237,273] The constructive interaction of the individual transitions leads to a strong, high-energy peak in the absorption spectrum (the plasmon peak). This is observed for several systems such as silver and gold nanoparticles[70,195,277] as well as polycyclic aromatic hydrocarbons.[237,273] For instance, two one-electron excitations with B_{3u} symmetry are involved in the longitudinal plasmon mode of acenes.[237,273] The constructive interaction between these two transition dipole moments yields a strong peak in the UV region called the β-peak (the plasmon peak) whereas the destructive addition of these two transition dipole moments yields the weak α-peak in the visible region.[273] More than two interacting configurations may be involved for noble metal nanoparticles, which leads to several peaks in their absorption spectrum with low intensity in addition to the higher-energy plasmon peak. For instance, TDDFT calculations show that the linear atomic chain Ag_6 has a strong transverse plasmon peak at 6.20 eV at the SAOP/DZ level of theory.[195] This peak arises from a constructive addition of the dipole moments of three single-particle transitions between delocalized cylindrical orbitals: $\Sigma_1 \rightarrow \Pi_1$, $\Sigma_2 \rightarrow \Pi_2$ and $\Sigma_3 \rightarrow \Pi_3$.[195] Two peaks in the spectrum located at 5.18 and 5.29 eV are composed of the same transitions, but they have low oscillator strength since their transition dipole moments add destructively.

The objective of this work is to determine how the relative energy between different transitions and the degree of coupling between these transitions affects the excitation spectrum of a plasmonic system. In order to do that, a fictitious system with three interacting transitions is considered. We will only consider dipolar plasmon modes. The eigenvalues of the secular matrix, corresponding to the energies of the peaks in the absorption spectrum, are calculated. The eigenvectors of this matrix are also solved to determine the oscillator strength of each peak.

Methods

We consider a plasmonic system with three interacting configurations such as the Ag_6 nanowire described above. V_i (i=1,2,3) defines the singly excited singlet determinantal function for each configuration.[237] The three excited state wavefunctions resulting from the interaction between these three configurations can be written in the form:

$$\Psi^{ex} = A_1V_1 + A_2V_2 + A_3V_3 \tag{6.1}$$

where the coefficients A_1, A_2 and A_3 are eigenvectors of the 3X3 configuration interaction (CI) secular matrix:

$$\begin{bmatrix} \alpha_1 & \beta_{12} & \beta_{13} \\ \beta_{21} & \alpha_2 & \beta_{23} \\ \beta_{31} & \beta_{32} & \alpha_3 \end{bmatrix} \tag{6.2}$$

The matrix elements β_{ij} correspond to the coupling between transitions i and j:[237]

$$\beta_{ij} = \int V_i^* \mathbf{H} V_j d\upsilon, \tag{6.3}$$

where V_i and V_j correspond to the singly excited determinantal configuration functions for transitions i and j respectively and **H** is the Hamiltonian. In this case, we consider $V_i^* = V_i$ and therefore $\beta_{ij}= \beta_{ji}$. The diagonal matrix elements α_i are defined as:[237]

$$\alpha_i = \int V_i^* \mathbf{H} V_i d\upsilon. \tag{6.4}$$

These values may be approximated in a Koopman-like approach by an orbital energy difference of the two singly occupied orbitals that represent the singly excited determinant V_i. The eigenvalues E_1, E_2 and E_3 of the CI matrix are the excited state energies. The eigenvectors corresponding to each eigenvalue can be used to construct the excited state wavefunctions, as shown in equation 6.1. All eigenvalues and eigenvectors of the CI matrix are calculated for different values of α_i and β_{ij} using Matlab 7.0.1.

If it is assumed that the transition moments between the ground and excited configurations are equal, which is a reasonable first approximation for these systems,[237,273] the sum of the eigenvectors for each eigenvalue is proportional to the transition dipole moment between the ground and excited state $\langle \Psi^0 | \hat{\mu} | \Psi^{ex} \rangle$ where $\hat{\mu}$ is the transition dipole operator and Ψ^0 is the ground state Slater determinant. Since the oscillator strength of the peak in the absorption spectrum is proportional to $\langle \Psi^0 | \hat{\mu} | \Psi^{ex} \rangle^2$, the value $|A_1+A_2+A_3|^2$ is the oscillator strength enhancement due to CI and will be referred to as "oscillator strength" for the remainder of this paper.

Results and discussion

Case 1: Ideal case.

Let us first consider the special case where all values of α and all values of β are equal. This yields the matrix:

$$\begin{bmatrix} \alpha & \beta & \beta \\ \beta & \alpha & \beta \\ \beta & \beta & \alpha \end{bmatrix} \tag{6.5}$$

This matrix is a special case of a Toeplitz matrix and of a circulant matrix, which have been studied for applications in various mathematical, physical and chemical problems.[278-281] The eigenvalues of this matrix are $E_1=\alpha-\beta$; $E_2=\alpha-\beta$; $E_3=\alpha+2\beta$. For these systems, we assume that β is positive, so E_3 is the highest energy eigenvalue. For higher *n*-dimensional matrices with a similar form, the lowest (*n*-1) states are degenerate with eigenvalue $\alpha-\beta$, and the highest state has energy $\alpha+(n-1)\beta$. For E_1 and E_2, the requirement for the eigenvectors is that $(A_1+A_2+A_3)=0$. For E_3, $A_1=A_2=A_3$. One set of normalized eigenvectors is reported in Table 6.1.

Table 6.1. Eigenvectors of matrix (6.5).

	$E_1=\alpha-\beta$	$E_2=\alpha-\beta$	$E_3=\alpha+2\beta$
A_1	$-1/\sqrt{2}$	$-1/\sqrt{2}$	$1/\sqrt{3}$
A_2	$1/\sqrt{2}$	0	$1/\sqrt{3}$
A_3	0	$1/\sqrt{2}$	$1/\sqrt{3}$
$\|A_1+A_2+A_3\|^2$	0	0	3.0000

For the two lowest eigenvalues E_1 and E_2, which are degenerate, the eigenvectors interact destructively and the oscillator strength of these two states is 0. For the third eigenvalue E_3, the eigenvectors interact constructively, yielding an oscillator strength value of 3. This state is the plasmon and the wavefunction has the form:

$$\Psi^{ex} = \frac{1}{\sqrt{3}}V_1 + \frac{1}{\sqrt{3}}V_2 + \frac{1}{\sqrt{3}}V_3. \tag{6.6}$$

The oscillator strength of this excited state can be written as:

$$\langle \Psi^0 | \hat{\mu} | \Psi^{ex} \rangle^2 = \left[\frac{1}{\sqrt{3}} \left[\langle \Psi^0 | \hat{\mu} | V_1 \rangle + \langle \Psi^0 | \hat{\mu} | V_2 \rangle + \langle \Psi^0 | \hat{\mu} | V_3 \rangle \right] \right]^2 . \tag{6.7}$$

As mentioned in the methods section, we use the assumption that the transition moments between the ground state and all excited configurations are equal:

$$\langle \Psi^0 | \hat{\mu} | V_1 \rangle = \langle \Psi^0 | \hat{\mu} | V_2 \rangle = \langle \Psi^0 | \hat{\mu} | V_3 \rangle. \tag{6.8}$$

Therefore we have:

$$\langle \Psi^0 | \hat{\mu} | \Psi^{ex} \rangle^2 = \left[\frac{1}{\sqrt{3}} \left[3 \times \langle \Psi^0 | \hat{\mu} | V_1 \rangle \right] \right]^2 = 3 \times \langle \Psi^0 | \hat{\mu} | V_1 \rangle^2 . \tag{6.9}$$

The oscillator strength enhancement of the plasmonic state due to CI is therefore a factor of 3. For *n*-dimensional matrices similar to this one, it can be shown that the enhancement due to CI is a factor of *n*, which is the number of transitions involved in the CI.

A similar behavior has been observed for silver and gold nanoparticles: one high-energy, high-intensity peak (plasmon) results from the constructive addition of the single-particle transitions and multiple low energy weaker peaks result from the destructive addition of the same transitions.[70,71,195,277] For real systems such as these noble metal nanoparticles, all values of α and β are not identical and deviations from this ideal case occur. A simple analytical solution for matrices with different values of α ($\alpha_1 \neq \alpha_2 \neq \alpha_3$) and β ($\beta_{12} \neq \beta_{23} \neq \beta_{13}$) cannot be obtained, although analytical solutions with different values of α with constant β ($\beta_{12} = \beta_{23} = \beta_{13}$) are possible. Therefore, in order to analyze the effect of varying the values of α and β on the absorption spectrum, we will give α and β numerical values that we will vary in a systematic fashion. First, we consider a matrix like (eq. 6.5) above but we set $\alpha_1 = \alpha_2 = \alpha_3 = 5$ eV and $\beta_{12} = \beta_{13} = \beta_{23} =$ 0.5 eV:

$$\begin{bmatrix} 5 & 0.5 & 0.5 \\ 0.5 & 5 & 0.5 \\ 0.5 & 0.5 & 5 \end{bmatrix} \tag{6.10}$$

The chosen values for α and β are similar to those obtained in the configuration interaction treatment of acenes.[237] The eigenvalues of this matrix are E_1= 4.5 eV, E_2= 4.5 eV and E_3= 6.0 eV, corresponding to α-β for E_1 and E_2 and α+2β for E_3, as expected. The rows and columns of the eigenvector matrix are orthogonal. As derived analytically, the oscillator strength is 0 for E_1 and E_2. The peak at E_3 has an oscillator strength of 3.0000, as expected (Table 6.2).

Table 6.2. Eigenvectors of matrix (6.10).

	E_1= 4.5 eV	E_2= 4.5 eV	E_3= 6.0 eV
A_1	0.1201	0.8076	0.5774
A_2	0.6394	-0.5078	0.5774
A_3	-0.7595	-0.2998	0.5774
$\|A_1+A_2+A_3\|^2$	0	0	3.0000

Case 2: Vary α_1 only.

We now consider the case where one of the values of α is different from the others. We still consider all values of β to be the same. The resulting matrix is:

$$\begin{bmatrix} \alpha_1 & \beta & \beta \\ \beta & \alpha & \beta \\ \beta & \beta & \alpha \end{bmatrix} \tag{6.11}$$

where $\alpha_1=\alpha+\varepsilon$. ε can be a positive or negative number. The eigenvalues for such a system are:

$$E_1=\alpha-\beta,\ E_2=\alpha+\frac{1}{2}(\varepsilon+\beta)-\frac{1}{2}\sqrt{9\beta^2-2\beta\varepsilon+\varepsilon^2} \text{ and } E_3=\alpha+\frac{1}{2}(\varepsilon+\beta)+\frac{1}{2}\sqrt{9\beta^2-2\beta\varepsilon+\varepsilon^2}$$

.[281] We see that E_1 does not depend on ε and its value therefore remains constant. On the other hand, E_2 and E_3 both depend on ε.

We now analyze the peak oscillator strengths by considering numerical values for ε of ±0.05, ±0.25, ±0.5, ±1.0, ±1.5, ±2.0 and ±2.5 eV. This corresponds to changes in α_1 by ±1, ±5, ±10, ±20, ±30, ±40 and ±50% of the value used in case 1 (5 eV). All other matrix elements remain the same as in case 1 (β=0.5 eV and α_2= α_3= 5 eV). The resulting matrix is:

$$\begin{bmatrix} \alpha_1 & 0.5 & 0.5 \\ 0.5 & 5 & 0.5 \\ 0.5 & 0.5 & 5 \end{bmatrix} \tag{6.12}$$

where α_1= 2.5, 3.0, 3.5, 4.0, 4.5, 4.75, 4.95, 5.05, 5.25, 5.5, 6.0, 6.5, 7.0 and 7.5 eV. The peak energies E_i (i=1, 2, 3) and oscillator strengths S_i (i=1, 2, 3) are shown in Figure 6-1A and 6-1B respectively.

Figure 6-1. A) Peak energies and B) oscillator strengths for different values of α_1 (case 2).

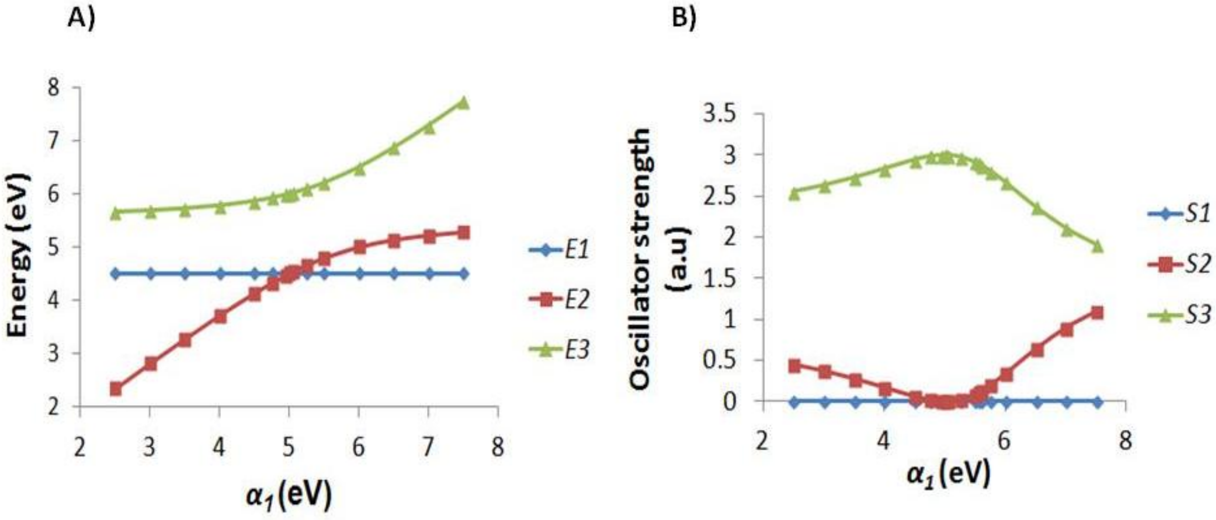

The computed values of the energies and oscillator strengths are reported in Table D-1 of Appendix D. Just as in the ideal case, the high-energy excited state E_3 with high oscillator strength corresponds to the plasmon. We can see that the degeneracy between E_1 and E_2 is lifted when α_1 shifts away from the 5 eV value of case 1. This can be explained by the ε-dependence of E_2. For ε=0, E_2=E_1= 4.5 eV, which corresponds to the ideal case discussed above. E_1 remains at 4.5 eV (α-β) and does not depend on ε, as derived analytically, and its oscillator strength remains 0. We note that E_1 is larger than E_2 when α_1< 5eV and smaller than E_2 when α_1> 5eV. This is because these excited states are labeled to correspond to the analytical results and not by increasing energies. E_2 quickly rises when α_1 increases from 2.5 to 5.5 eV and then slowly stabilizes for higher values of $\alpha_{1.}$ On the other hand, E_3 slowly increases when α_1 shifts from 2.5 to 5.5 eV and quickly rises when α_1 is larger than 5.5 eV. A more detailed discussion on the origin of this behavior is given in the discussion of the analytical solution in Appendix D. For values of α_1 smaller than 5.5 eV ($\varepsilon < \beta$), ε contributes mainly to the energy of the E_2 state. When

α_1 becomes larger than 5.5 eV ($\varepsilon > \beta$), E_3 takes advantage of the increasing ε value to raise its energy. The oscillator strength S_2 of E_2 grows as the value of α_1 changes from the 5 eV resonance value where $\alpha_1 = \alpha_2 = \alpha_3$ (the ideal case 1). On the other hand, the oscillator strength S_3 of the plasmon peak reaches a maximum for this value of α_1. S_3 therefore "borrows" less oscillator strength from S_2 when $\alpha_1 \neq \alpha$. We note that S_3 always has a larger value than S_2 in the α_1 range considered. The eigenvectors of all the matrices studied are reported in Appendix D (Tables D.4-D.17). The coefficients A_i contributing to the plasmon peak (with energy E_3) all have the same sign. The constructive interaction of the individual transitions making the plasmon therefore remains. We see that for E_1, $A_1 = 0$, $A_2 = 1/\sqrt{2}$ and $A_3 = -1/\sqrt{2}$ regardless of the value of α_1. This reflects that only transitions 2 and 3 contribute to that peak and their contributions remain constant. This is not surprising since $\alpha_2 = \alpha_3 = 5$ eV and all coupling constants are equal for all values of α_1. For E_2 and E_3, the contributions of transitions 2 and 3 are identical regardless of the value of α_1 ($A_2 = A_3$). As α_1 becomes larger, the contributions of transitions 2 and 3 increase for E_2 and decrease for E_3. On the other hand, $|A_1|$ increases for E_3 and decreases for E_2. This shows the growing contribution of transition 1 to E_3 as α_1 becomes larger. For $\alpha_1 >> \alpha$, it would be reasonable to expect that only transition one will contribute to the peak at energy E_3. E_3 will then be labeled as a single-electron transition and no longer be a plasmon. Only transitions two and three will mix efficiently and a high-intensity plasmon peak at 5.5 eV will result from the constructive interaction of these two transitions. Another peak with zero oscillator strength will occur at 4.5 eV. This illustrates why the configurations in the CI must be close in energy to create a plasmon. Overall, changing one of the values of α not only lifts the degeneracy between E_1 and E_2, but it also increases the oscillator strength of the peak at energy E_2, which would make it observable in the absorption spectrum. The increase in oscillator strength for E_2 also leads to a decrease in oscillator strength for E_3, which is the plasmon peak. The plasmon peak is therefore stronger when all the contributing transitions have identical values of α. The closer in energy the one-electron transitions involved in the plasmon are, the stronger the plasmon peak will be (up to its ideal value). In noble metal particles with a common diameter (2-100 nm), a high density of states is available and many allowed transitions with similar symmetry have very similar energies.[282] The strong plasmon peak commonly observed experimentally[6] can thus result from the interaction between these transitions. The low-intensity peaks associated with the same transitions also occur but are usually too small to be observed experimentally.

Case 3: Vary α_1 and α_3.

We now analyze the effect on the absorption spectrum of changing both α_1 and α_3. In this case, we change α_1 by 20% and α_3 by ±1, ±5, ±10, ±20, ±30, ±40 and ±50% of the value used in case 1 (5 eV). All other matrix elements remain the same as in case 1. The resulting CI matrix is:

$$\begin{bmatrix} \alpha_1 & 0.5 & 0.5 \\ 0.5 & 5 & 0.5 \\ 0.5 & 0.5 & \alpha_3 \end{bmatrix} \tag{6.13}$$

where α_1= 6.0 eV and α_3= 2.5, 3.0, 3.5, 4.0, 4.5, 4.75, 4.95, 5.05, 5.25, 5.5, 6.0, 6.5, 7.0 and 7.5 eV. The peak energies and oscillator strengths are reported in Figure 6-2A and 6-2B respectively.

Figure 6-2. A) Peak energies and B) oscillator strengths for different values of α_3 (case 3). (α_1=6.0 eV).

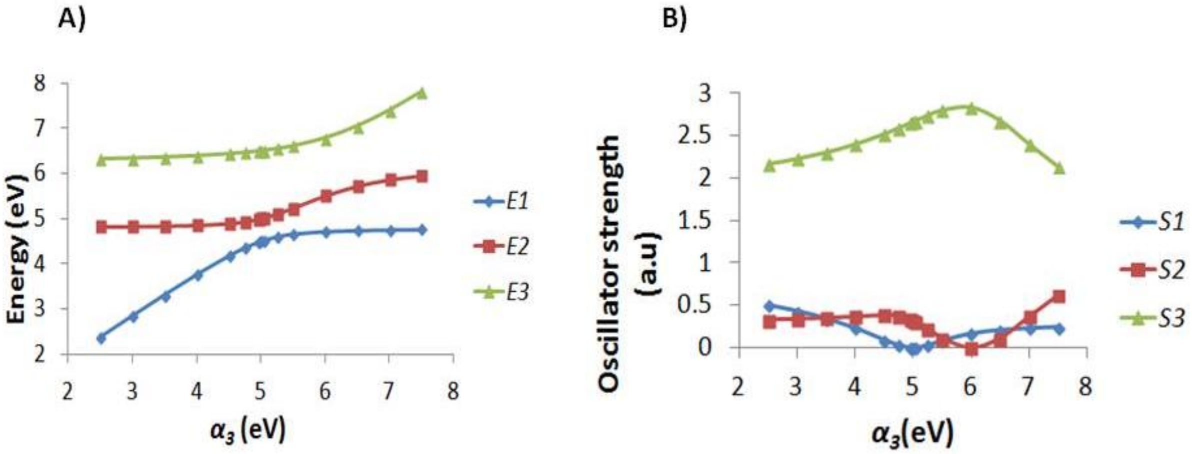

Table D.18 of Appendix D displays all energies and oscillator strengths of the three peaks. When all three values of α are different, all three peaks have non-zero oscillator strength. All three peak energies tend to increase with increasing value of α_3, which makes sense since the total energy $\alpha_1+\alpha_2+\alpha_3$ increases. Again, the peak at E_3 has higher energy and oscillator strength than the other two and corresponds to the plasmon peak. E_1 and E_3 behave in a similar way as E_2 and E_3 in case 2. The energy of the plasmon peak E_3 slowly blue shifts until α_3 reaches a value of approximately 5.0 eV and then grows much more rapidly. On the other hand, E_1 quickly rises until α_3 reaches a value of about 5.0 eV and then increases very slowly. When α_3 is between 2.5 and 5.0 eV, α_3 contributes mainly to E_1 and does not contribute significantly to E_2 or E_3 as these two values remain nearly constant. When α_3 shifts between 5.0 and 7.5 eV, it contributes mainly to the plasmon peak energy E_3, as shown by the rapid increase of E_3. It no longer contributes as meaningfully to E_1 since E_1 remains nearly constant for these values of α_3. We can see that E_2 increases slightly as well but seems to stabilize when α_3 becomes larger than 7 eV. This indicates that the contribution of α_3 to this state becomes larger when α_3 increases from about 5 to 7 eV and then remains nearly constant.

The eigenvectors A_1, A_2 and A_3 are shown in Tables D.19 to D.32 of Appendix D. When α_3 becomes very small (2.5 eV) or very large (7.5 eV), we can see that one transition dominates over the others for each peak. For instance, for α_3=2.5 eV, transition 3 dominates for the peak at energy E_1, as shown by the large value of A_3=0.9800 compared to the small values of A_1 and A_2 of -0.1120 and -0.1643, respectively (Table 6.3).

Table 6.3. Eigenvectors of the CI matrix in case 3 where α_3=2.5 eV, α_1=6.0 eV and α_2=5.0 eV. All β values are equal to 0.5 eV.

	E_1= 2.3590 eV	E_2= 4.8207 eV	E_3= 6.3202 eV
A_1	-0.1120	-0.4248	-0.8983
A_2	-0.1643	0.8995	-0.4048
A_3	0.9800	0.1023	-0.1706
$\lvert A_1+A_2+A_3\rvert^2$	0.4952	0. 3329	2.1718

We note that A_3 is very small for both E_2 and E_3, which suggests that transition 3 contributes very little to the peaks at E_2 and E_3. At α_3=7.5 eV, transition 3 dominates for the plasmon peak at energy E_3 (Table 6.4).

Table 6.4. Eigenvectors of the CI matrix for case 3 where α_3=7.5 eV, α_1=6.0 eV and α_2=5.0 eV. All β values are equal to 0.5 eV.

	E_1= 4.7629 eV	E_2= 5.9437 eV	E_3= 7.7934 eV
A_1	0.3339	0.8871	0.3188
A_2	-0.9362	0.2726	0.2220
A_3	0.1100	-0.3726	0.9215
$\lvert A_1+A_2+A_3\rvert^2$	0.2423	0.6195	2.1380

This is consistent with the fact that α_3 contributes mostly to the peak at energy E_1 when it is small but contributes mainly to the plasmon peak energy when it is large. These results confirm that as the value of α_3 increasingly differs from the other α values, the mixing between transition 3 and the other two becomes smaller. In other words, the further apart in energy the contributing transitions are, the less efficiently they will mix.

When α_3 becomes close to the other values of α (which occurs around 5.0 and 6.0 eV), it contributes to all three excited states due to the strong coupling that occurs. The oscillator strength of the plasmon peak tends to grow as α_3 gets closer to the value of α_1 (6.0 eV). When α_1 and α_3 are equal (transitions 1 and 3 are in resonance), the oscillator strength of the plasmon peak reaches a maximum. This maximum is less than the 3.0 value of the ideal case since all α values are not in resonance. On the other hand, the oscillator strength S_2 of the peak at energy E_2 reaches its minimum value of 0 when $\alpha_1 = \alpha_3$. We note that when α_3=5.0, we have $\alpha_2 = \alpha_3$ and the oscillator strength of peak 1 reaches its minimum value of 0. In that case, transitions 2 and 3 are in resonance.

Case 4: Vary β_{12} only.

We now investigate how changing the coupling values β affects the absorption spectrum of the system. First, only the coupling between transitions 1 and 2 is changed. The CI matrix studied in this section is:

$$\begin{bmatrix} 5 & \beta_{12} & 0.5 \\ \beta_{12} & 5 & 0.5 \\ 0.5 & 0.5 & 5 \end{bmatrix} \tag{6.14}$$

The values of β_{12} considered are varied by ±1, ±5, ±10, ±20, ±30, ±40 and ±50% of the value used in case 1 (0.5 eV), which gives β_{12}= 0.25, 0.30, 0.35, 0.40, 0.45, 0.475, 0.495, 0.505, 0.525, 0.55, 0.60, 0.65, 0.70 and 0.75 eV. The peak energies and oscillator strengths are reported in Figure 6-3 and in Table D.33 of Appendix D. The eigenvectors for each matrix studied in this section are reported in Tables D.34 to D.47 of the supporting information.

Figure 6-3. A) Peak energies and B) oscillator strengths for different values of β_{12} (case 4).

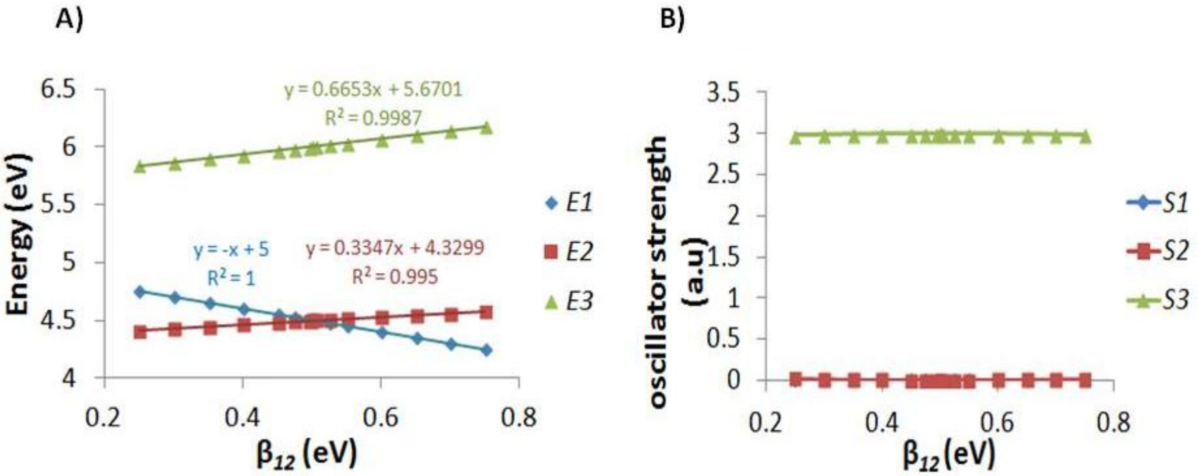

The state E_3 has the highest energy as well as the highest oscillator strength due to a constructive addition of its eigenvectors. Like in the previous cases, this state is the plasmon. One of the three excited states has $A_1 = -A_2 = 1/\sqrt{2}$ and A_3= 0 for all values of β_{12} (except in the ideal case where β_{12}=0.5 eV, due to the normalization of the eigenvectors). This state is labeled with energy E_1 and it has zero oscillator strength. It crosses with E_2 at β_{12}= 0.5 eV. The amplitude of the variation of the peak energies is very small (less than 0.5 eV), due to the fact that the values of β considered are only approximately 10% of the values of α. We can see that the energies of states 2 and 3 increase linearly with increasing β_{12} whereas the energy of state 1 decreases linearly. E_2 and E_3 use the intensifying coupling between transitions 1 and 2 to increase their energy, which results in a decrease of E_1. The decrease in E_1 (indicated by the slope of the linear fit of E_1 as a function of β_{12}) is equal to the increase of E_2 plus the increase of E_3. The oscillator strengths of the three excited states are nearly identical to those obtained for the ideal case regardless of the value of β_{12}. The plasmon state oscillator strength grows as β_{12} approaches the 0.5 eV value of the ideal case. However, the change is so small that the oscillator strength appears constant. The oscillator strength of state 2 slightly increases as the value of β_{12} differs more from the original

0.5 eV value but it remains so small that it is essentially zero. We can also see that $A_1 = A_2$ for the eigenvalues E_2 and E_3 regardless of the β_{12} value, reflecting the identical contributions of transitions 1 and 2. As β_{12} increases, we see that $|A_1|$ and $|A_2|$ decrease whereas $|A_3|$ increases for E_2 and vice versa for E_3.

Case 5: Vary β_{12} and β_{23}.

We now consider a matrix where all coupling elements are different. The CI matrix studied in this section is:

$$\begin{bmatrix} 5 & \beta_{12} & 0.5 \\ \beta_{12} & 5 & \beta_{23} \\ 0.5 & \beta_{23} & 5 \end{bmatrix} \tag{6.15}$$

In this case, β_{12}= 0.6 eV and the values of β_{23} considered are varied by ±1, ±5, ±10, ±20, ±30, ±40 and ±50% of the value used in case 1 (0.5 eV), which gives β_{23}= 0.25, 0.30, 0.35, 0.40, 0.45, 0.475, 0.495, 0.505, 0.525, 0.55, 0.60, 0.65, 0.70 and 0.75 eV. The peak energies and oscillator strengths are reported in Figure 6-4 and in Table D.48 of Appendix D.

Figure 6-4. A) Peak energies and B) oscillator strengths for different values of β_{23} (case 5). (β_{12}=0.6 eV)

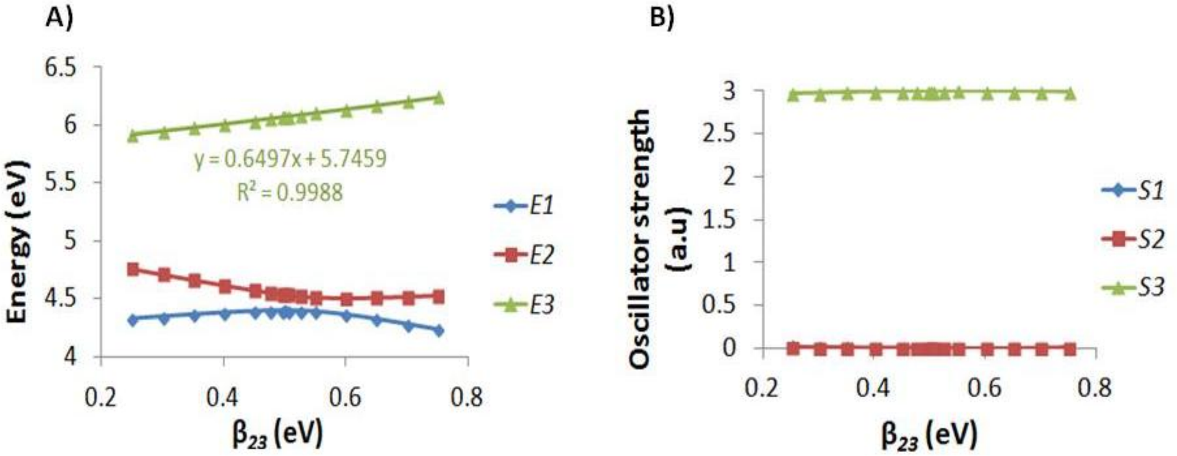

Again, we can see that the plasmon peak (peak 3), which corresponds to a constructive addition of the eigenvectors A_1, A_2 and A_3, has a much higher energy and oscillator strength than the other two. Its energy increases linearly with increasing value of β_{23}. Like in the previous case, the oscillator strength of all three peaks is nearly equal to the values obtained in the ideal case: 3 for the plasmon and 0 for the other two. There is a slight growth of the plasmon peak oscillator strength up to β_{23}=0.55 eV and then a slight decrease. The change is again so small that the plasmon peak oscillator strength appears to remain constant. Its maximum value of 2.9981 is slightly less than 3 since all these transitions do not couple equally. Peaks 1 and 2 both have very low oscillator strength. From β_{23}=0.25 to 0.5 eV, E_1 becomes larger. From β_{23}=0.5 to 0.75 eV, E_1 decreases. The opposite behavior is observed for E_2. From β_{23}=0.25 to 0.6 eV, E_2 becomes smaller. From β_{23}=0.6 to 0.75 eV, E_2 increases. Therefore, the plasmon peak of energy E_3 and the peak of energy E_1 use the ascending value of β_{23} up to the 0.5 eV (which is equal to β_{13}) to increase their energy in a similar way as in the previous case. This results in a drop of the E_2 energy. On the other hand, when β_{23} reaches 0.6 eV (value of β_{12}), E_2 takes advantage of the large coupling value to increase its energy, which leads to a decreasing value of E_1. E_1 reaches a maximum at β_{23}=0.5 eV where $\beta_{23}=\beta_{13}$, and S_1 attains its minimum value of zero. E_2 reaches a minimum at β_{23}=0.6 eV where $\beta_{23}=\beta_{12}$, and S_2 attains its minimum value of zero. The eigenvectors associated with each eigenvalue are displayed in Appendix D (Tables D.49-D.62). We can see that as β_{23} increases, A_1 decreases for the plasmon peak whereas A_2 and A_3 increase; overall, $|A_1+A_2+A_3|^2$ (the oscillator strength) remains nearly constant.

Case 6: Varying the β/α ratio.

We now consider a system where all three values of α are different and all coupling elements are identical, as in case 3. The values of α considered (α_1=5.0 eV, α_2=5.1 eV and α_3=5.2 eV) are similar to the values obtained for the nanowire Ag_6.[195] This time, we investigate the effect of increasing all three coupling values from 0 to 2.0 eV on the peak energies and oscillator strength. The CI matrix considered is:

$$\begin{bmatrix} 5.0 & \beta & \beta \\ \beta & 5.1 & \beta \\ \beta & \beta & 5.2 \end{bmatrix} \tag{6.16}$$

The values of β considered are: β=0, 0.001, 0.005, 0.01, 0.05, 0.1, 0.2, 0.3, 0.4, 0.5, 1.0 and 2.0 eV. Figure 6-5 shows the excited state energies and oscillator strengths as a function of the coupling. Table D.63 of the Appendix D gives the numerical values.

Figure 6-5. A) Peak energies and B) oscillator strengths for different values of $\beta=\beta_{12}=\beta_{13}=\beta_{23}$ and α_1=5.0 eV, α_2=5.1 eV, α_3=5.2 eV (case 6). Inset in A is an enlarged version of the region in the black square.

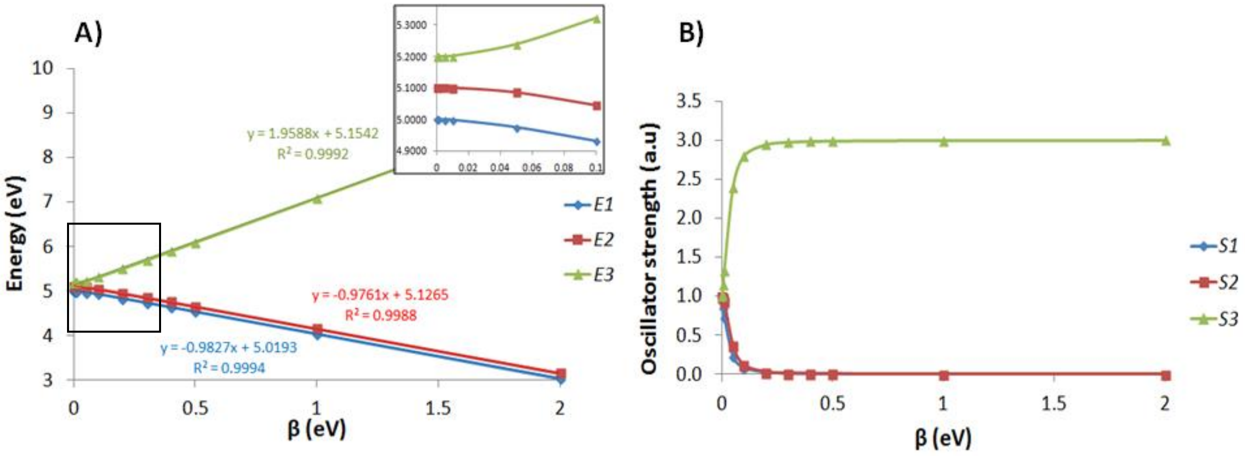

For β=0 (no coupling), the three excited states energies are equal to α_1, α_2 and α_3 and their oscillator strength is equal to 1. These states are therefore qualified as single particle transitions and there is no plasmon. When β>0, the eigenvectors add constructively for the highest energy peak E_3 and destructively for the other two peaks (Tables D.64 to D.75 of Appendix D). The energy of E_3 rises linearly as the coupling grows whereas the energy of the other two states decreases; the slope for the change in energy of E_3 is twice that of the other two states. For $\beta \leq 0.1$ eV, the peak energies do not differ significantly from the α values (e.g. less than 0.1 eV, Figure 6-5A inset). In that range, the oscillator strength of the highest energy peak rapidly increases and the oscillator strength of the other two peaks rapidly decreases (Figure 6-5B). As the coupling grows larger, the oscillator strength rapidly converges to a value close to 3 for the highest energy peak (now the plasmon peak), and 0 for the other two peaks. When β reaches a value close to the difference in energy of the α values (β=0.1-0.2 eV), the oscillator strength of the plasmon peak is already in the 2.80-2.95 range. We note that since the three transitions do not have the same energy, the plasmon peak oscillator strength will never identically reach the maximum value of 3, but strong coupling values do lead to oscillator strengths of essentially 3. Overall, the oscillator strength is highly sensitive to small coupling values and rapidly converges to its maximum (or minimum) value whereas the excited state energies are only significantly affected by large coupling values.

Case 7: Mixed-coupling systems.

In real systems, some transitions with similar α values may couple strongly while others couple weakly. For example, noble metal nanoparticles (especially gold) may have interband (i.e. excitations from the *d*-band into the *sp*-band) transitions that can mix with *sp*-band transitions of similar energy and affect the plasmon peak energy and oscillator strength. However, these interband excitations typically have significantly smaller dipole moments. We postulate that the coupling values between interband and *sp*-band transitions are smaller than the coupling values between *sp*-band transitions. In order to model this, we consider a matrix similar to the one in case F. Transitions 1 and 2 will be considered to be *sp*-band and we give them a large coupling value of β_{12}=0.5 eV. Transition 3 will be considered to be interband and the coupling values between this transition and the other two are identical but smaller than the coupling between the two *sp*-band transitions: $\beta=\beta_{13}=\beta_{23}<\beta_{12}$. The resulting CI matrix is:

$$\begin{bmatrix} 5.0 & 0.5 & \beta \\ 0.5 & 5.1 & \beta \\ \beta & \beta & 5.2 \end{bmatrix} \tag{6.17}$$

The values of β considered are β=0, 0.001, 0.005, 0.01, 0.05 and 0.1 eV. Peak energies and oscillator strengths are given in Table 6.5.

Table 6.5. Excited states energies and oscillator strengths for a system with α_1=5.0 eV, α_2=5.1 eV, α_3=5.2 eV, β_{12}=0.5 eV and different values of $\beta_{13}=\beta_{23}$ (case 7).

$\beta_{13}=\beta_{23}$(eV)	E_1 (eV)	S_1 (a.u.)	E_2 (eV)	S_2 (a.u.)	E_3 (eV)	S_3 (a.u.)
0.0000	4.5475	0.0050	5.2000	1.0000	5.5525	1.9952
0.0010	4.5475	0.0050	5.2000	0.9888	5.5525	2.0062
0.0050	4.5475	0.0049	5.1999	0.9440	5.5526	2.0512
0.0100	4.5475	0.0048	5.1994	0.8889	5.5531	2.1063
0.0500	4.5475	0.0043	5.1864	0.5108	5.5661	2.4847
0.1000	4.5474	0.0038	5.1505	0.2267	5.6021	2.7696

The first excited state remains at nearly constant energy with a low oscillator strength, which reflects the fact that within this range of coupling values, this state arises from the destructive combination of the two *sp*-band excitations. This is confirmed by the fact that A_1 and A_2 are much larger than A_3 for this state (Tables D.76 to D.81 of Appendix D). As in all the other cases, the high energy state E_3 is the plasmon, as reflected by the constructive addition of its eigenvectors; however, it should be noted that for small values of β, it is only a constructive combination of the two *sp*-band states and its oscillator strength is approximately 2. E_2 becomes slightly smaller and E_3 becomes slightly larger with increasing β. The energy change is small (less than 0.05 eV) but still observable. This in accordance with the observations made in case 6. The mixing of the interband transition therefore only has a small effect on the excited states energies. We can see that S_2 drastically decreases and S_3 drastically increases as β grows, again in accordance with previous observations (case 6). As a result, a small interband mixing can highly affect the oscillator strength of the plasmon peak. One must note that several interband transitions may occur in real gold clusters due to the higher density of states of these transitions. When a large proportion of interband excitations mix with the *sp*-band excitations, it is reasonable to expect more significant energy variations of the excited states. This has previously been observed in gold nanorods.[195,277] For accurate predictions of oscillator strengths, the difference in the transition dipole moment between the *sp*-band and interband transitions must also be considered.

Conclusions

In summary, we used configuration interaction to study plasmonic systems with three contributing transitions. The diagonal elements of the CI matrix correspond to the energy of each contributing transition whereas the off-diagonal elements correspond to the couplings between the transitions. In the ideal case where all the diagonal elements α are equal and all the off-diagonal elements β are equal, two degenerate low-energy peaks with zero oscillator strength occur as well as one high-energy peak with large oscillator strength. The latter arises from a constructive addition of the eigenvectors and is identified as the plasmon peak. On the other hand, the former two peaks result from a destructive addition of the eigenvectors. The same qualitative behavior is observed in TDDFT calculations on silver and gold nanoparticles where multiple configurations mix to yield a high-energy, high-intensity plasmon peak and multiple low-energy low-intensity peaks.[195] In these real systems, all values of α and β are not equal. This leads to deviations from the ideal case. We therefore considered systematic variations from the ideal case.

As we change one (or two) of the α values, the degeneracy between the two low-energy peaks is lifted and one (or two) low energy peak(s) gain(s) some oscillator strength. The α values can be related to the single-electron transition energies. As these energies increasingly vary from each other (i.e. their energies diverge from the ideal case), the mixing between the transitions becomes smaller. Therefore, the plasmon peak oscillator strength decreases and the oscillator strength of the other two peaks increases as we deviate from the ideal case. Changing one or two of the coupling constants within a 50% range has a small effect on peak energies and oscillator strength. If the coupling between two transitions becomes larger, the plasmon peak energy increases in a linear fashion. Its oscillator strength remains nearly constant with a value slightly smaller than its maximum value of 3. The other two peaks have nearly zero oscillator strength. The maximum oscillator strength enhancement due to CI is equal to the number of configurations involved (3 in the cases considered here) and occurs only in the ideal case where all transitions have identical energies and couplings.

We then considered a system with three different values of α and identical values of β that were varied in a systematic fashion. When the coupling elements increase up to approximately the difference in α values, the oscillator strength of the plasmon peak rapidly increases to a value near its maximum enhancement. However, its energy remains near the highest energy configuration. For higher coupling values, we get a high increase of the plasmon peak energy but its oscillator strength remains near the maximum value of 3. We also modeled a system similar to a real nanoparticle by considering two *sp*-band excitations and one interband excitation in the CI matrix. The interband character is modeled by taking a small coupling value between this transition and the two *sp*-band transitions. We found that the excited states energies are not as affected as the oscillator strength. However, we suggest that multiple interband transitions in the CI matrix (as would be expected in gold nanoparticles) might lead to larger variations in the excited state energies (including the plasmon), due to a highly split spectrum. Overall, we show that configuration interaction is a useful concept for understanding the coupling of single-particle transitions into a strong plasmon peak.

Acknowledgements

This material is based on work supported by the National Science Foundation under grant no. EPS-0903806. The authors also thank Kansas State University for funding this work. C.M.A. is grateful to the Alfred P. Sloan Foundation for a Sloan Research Fellowship (2011-

2013) and the Camille and Henry Dreyfus Foundation for a Camille Dreyfus Teacher-Scholar Award (2011-2016).

Chapter 7 - Development of a charge-perturbed particle-in-a-sphere model for nanoparticle electronic structure

Guidez, E. B.; Aikens, C. M. *Phys. Chem. Chem. Phys.* **2012**, *14*, 4287.
Reproduced by permission of the PCCP Owner Societies

Abstract

The complex surface structure of gold-thiolate nanoparticles is known to affect the calculated density functional theory (DFT) excitation spectra. However, as the nanoparticle size increases, it becomes impractical to calculate the excitation spectrum using DFT. In this study, a new method is developed to determine the energy levels of the thiolate-protected gold nanoparticles $[Au_{25}(SR)_{18}]^-$, $Au_{102}(SR)_{44}$ and $Au_{144}(SR)_{60}$. A 3 nm thiolate-protected nanoparticle is also modeled. The particle-in-a-sphere model is used to represent the core while the ligands are treated as point charge perturbations. The electronic structures obtained with this model are qualitatively similar to DFT results. The symmetry of the arrangement of the perturbations around the core plays a major role in determining the splitting of the orbitals. The radius chosen to represent the core also affects the orbital splitting. Increasing the number of perturbations around the core shifts the orbitals to higher energies but does not significantly change the band gaps and orbital splitting as long as the symmetrical arrangement of the perturbations is conserved. This model can be applied to any gold nanoparticle with a spherical core, regardless of its size or the nature of the ligands, at very low computational cost.

Introduction

In the past decade, many thiolate-protected gold nanoparticles (NPs) of various sizes have been synthesized[76,283-289] and studied for possible applications in areas such as biology,[290,291] catalysis[292] or biosensing.[293] Nanoparticles with tens to a few thousands of atoms are of particular interest since their properties lie between those of molecules and bulk materials. The structure, luminescence, and magnetic properties of several stable clusters such as $Au_{25}(SR)_{18}^{0/-1}$, $Au_{38}(SR)_{24}$, $Au_{102}(SR)_{44}$ and $Au_{144}(SR)_{60}$ have been intensively studied.[78,294-301] Gold nanoparticles show complex absorption spectra, which is due both to interband transitions and geometric effects on electronic structure. Density functional theory (DFT) calculations on such systems can be expensive or unachievable for the larger sized nanoparticles. Therefore, the need for a simpler model arises in order to determine the electronic structure of these nanoparticles. This work focuses on nanoparticles with spherical shape. The inherent stability of spherical gold nanoparticles was recently explained by the superatom model: spherical systems with a "magic number" (*n*=2, 8, 18, 34, 58...) of core electrons tend to be particularly stable.[80]

The magic numbers correspond to shell-filling numbers for particles in a spherical potential.[260] Orbitals near the HOMO-LUMO gap in gold nanoparticles have characteristics of S, P, D, etc. superatomic orbitals, which are delocalized throughout the nanoparticle core.[80,81,83]

A charge-perturbed particle-in-a-box model was effectively used by Goldsmith et al.[302] to explain the optical activity of several gold clusters such as $Au_{28}(SG)_{16}$. The gold core was modeled with non-interacting electrons confined to a cubic box and the ligands were described as perturbations using point charges. In this work, a similar method is used to predict the electronic structure of several thiolate-protected spherical gold NPs: the core is modeled as a spherical well and point charges representing the ligands act as perturbations. The spherical systems investigated in this work are $Au_{25}(SR)_{18}^-$, $Au_{102}(SR)_{44}$, $Au_{144}(SR)_{60}$ and a 3 nm nanoparticle with uniformly dispersed S-Au-S perturbations.

Method

A particle-in-a-sphere (PIS) model is used in this work to represent the spherical core of the nanoparticles. We consider a single unpaired electron in the core to be trapped in a spherical potential: V=0 inside the sphere and V=∞ outside the sphere. The PIS zeroth order wave functions have the following form:

$$\Psi_{n,l,m}(\theta,\phi,r) = Y_m^l(\theta,\phi)\, j_{n,l}(r) \tag{7.1}$$

where $Y_m^l(\theta,\phi)$ are the normalized spherical harmonics with quantum number *l* and *m* such that *l*=0,1,2…where *l*=0 corresponds to an S orbital, *l*=1 is a P orbital, *l*=2 is a D orbital, etc. and *m*=-*l*,-*l*+*1*,...,+*l*. *n* is the quantum number of the electron shell. $j_{n,l}(r)$ are the normalized spherical Bessel functions with *n*=1,2,3… and again *l*=0,1,2... The spherical Bessel functions can be written in the form:

$$j_{n,l}(kr) = \sqrt{\frac{2}{R^3}}\,\frac{1}{J_{n,l+\frac{3}{2}}(\alpha_{n,l})}\sqrt{\frac{\pi}{2kr}}\,J_{n,l+\frac{1}{2}}(kr) \tag{7.2}$$

where $J_{n,l+1/2}$ is a standard Bessel function, $k = \alpha_{n,l}/R$, R is the sphere radius in Å and $\alpha_{n,l}$ is the root of $j_{n,l}$. The zeroth order energy of the particle in a sphere is:

$$E_{n,l}^{(0)} = \frac{{\alpha_{n,l}}^2}{2\mathrm{R}^2} \tag{7.3}$$

The atoms constituting the ligands are considered as point charge perturbations. First-order degenerate perturbation theory is applied for all orbitals with $l \geq 1$. A non-degenerate version of the code is used to calculate the energy of the S orbitals.

In the presence of a perturbation, the correct zeroth order wavefunction of degenerate energy levels is a linear combination of the zeroth order non-degenerate wavefunctions:

$$\varphi^{(0)} = c_1\psi_{n,l,-l} + c_2\psi_{n,l,-l+1} + \ldots + c_{2l+1}\psi_{n,l,+l} \tag{7.4}$$

By solving the secular equation, we can obtain the first order energy and the zeroth order wavefunction (eigenvectors c_1, c_2…) of each energy level. The secular equation has the following form:

$$\mathbf{A}\vec{\mathrm{c}} = \mathrm{E}^{(1)}\vec{\mathrm{c}} \tag{7.5}$$

Where $\vec{\mathrm{c}}$ represents the eigenvectors, $\mathrm{E}^{(1)}$ the first order energy and **A** is a square matrix of dimension ($2l+1$):

$$\mathbf{A} = \begin{pmatrix} \langle \psi_{n,l,-l} | \hat{V} | \psi_{n,l,-l} \rangle & \cdots & \langle \psi_{n,l,-l} | \hat{V} | \psi_{n,l,+l} \rangle \\ \vdots & \ddots & \vdots \\ \langle \psi_{n,l,+l} | \hat{V} | \psi_{n,l,-l} \rangle & \cdots & \langle \psi_{n,l,+l} | \hat{V} | \psi_{n,l,+l} \rangle \end{pmatrix} \tag{7.6}$$

$\hat{V}$, the total perturbation exerted by the ligands, is:

$$\hat{V} = \sum_{i=1}^{N} \frac{-\mathrm{q_i}}{\sqrt{(\mathrm{x}-\mathrm{x_i})^2 + (\mathrm{y}-\mathrm{y_i})^2 + (\mathrm{z}-\mathrm{z_i})^2}} \tag{7.7}$$

where N is the number of perturbations, (x_i, y_i, z_i) are the coordinates of the i^{th} perturbation, and q_i is the charge of the i^{th} perturbation. It should be noted that $\hat{V}$ and **A** are Hermitian. Each matrix element of the secular equation corresponds to a triple integral over r, θ and ϕ coordinates:

$$\int_0^R \int_0^\pi \int_0^{2\pi} \psi_{n,l,m}^*(r,\theta,\phi)\hat{V}\psi_{n,l,m}(r,\theta,\phi) r^2 \sin\theta \, dr d\theta d\phi \tag{7.8}$$

In this equation, $\hat{V}$ is expressed in spherical coordinates. The triple integration was found to be impractical to solve analytically. Therefore, the integration was performed numerically. The sphere is divided into a grid. Using spherical coordinates to create the grid inside the sphere (evenly dividing r, θ, ϕ coordinates) yielded very inaccurate results since a larger density of points are generated near the poles than near the equator. In order to fix that issue, a Cartesian grid was created. Another advantage of the Cartesian grid is that it is not necessary to convert the perturbation $\hat{V}$ into spherical coordinates.

For each case studied in this work, the chosen grid size is the one for which the first order energy is converged for the highest l considered. As l increases, the number of nodes increases and therefore the grid size needs to be smaller relative to orbitals with smaller l. Although the grid is divided based on Cartesian coordinates, the coordinates of each point within the sphere are converted to spherical coordinates in order to calculate the wavefunctions for the orbitals of interest. We note that the center of mass of the nanoparticle must be located at the origin. However, there is no need to align the primary axis of the nanoparticle along the z axis.

Computational details

All energy calculations are computed with a code written in FORTRAN90. Bessel functions and Legendre Polynomial subroutines are taken from Fortran numerical recipes.[303] Calculation of the eigenvalues and eigenvectors of the secular matrix **A** are run using the zheev.f subroutine from the LAPACK 3.2 package.[304,305] The roots of the spherical Bessel functions were determined using an online calculator.[306] The test cases figures and the orbitals of the first test case are drawn using Matlab. $Au_{25}(SR)_{18}^-$, $Au_{102}(SR)_{44}$, $Au_{144}(SR)_{60}$ and the 3 nm sphere perturbations are drawn using MacMolPlot.[257] The perturbation coordinates for the $Au_{144}(SR)_{60}$ spherical case and the 3 nm NP are generated using a Matlab program written by J. Bowman that generates uniform points on a sphere.[307] Since a few of the resulting S-Au-S units are bent and a few sulfur atoms overlap some gold atoms, the sulfur atoms are manually arranged around the gold atoms to get linear S-Au-S units. Consequently, the arrangement of the units is not perfectly uniform. The density of states (DOS) spectra are fit with a Gaussian of 0.1 eV FWHM.

Description of the model systems

Test cases

In order to verify that the program is working correctly, five simple test cases are designed in which the spherical core is perturbed by negative point charges (Figure 7-1). These test configurations include axial (Case 1), square planar (Case 2), octahedral (Case 3), planar with eight perturbations (Case 4) and approximately spherical with eighteen perturbations (Case 5). In order to verify that no alignment along the *z* axis is necessary, two different possibilities are considered for Case 1: 1a) the two perturbations are along the z axis and 1b) the two perturbations are on opposite sides of the sphere but at a random orientation. The coordinates of the perturbations for each case are given in Appendix E. The core is a 3.00 Å radius sphere centered at the Cartesian coordinates (0,0,0) and divided using a 0.1 Å grid. Each perturbation is a single negative charge located 4.5 Å away from the center of the spherical core. The 1P and 1D orbital energies are calculated for each case by adding zeroth order and first order energies.

Figure 7-1. Test cases. A) Case 1a: Axial with perturbations aligned along the *z* axis. B) Case 1b: Axial with perturbations along a random axis. C) Case 2: Square planar. D) Case 3: Octahedral. E) Case 4: Planar with eight perturbations. F) Case 5: Quasi-spherical with 18 perturbations.

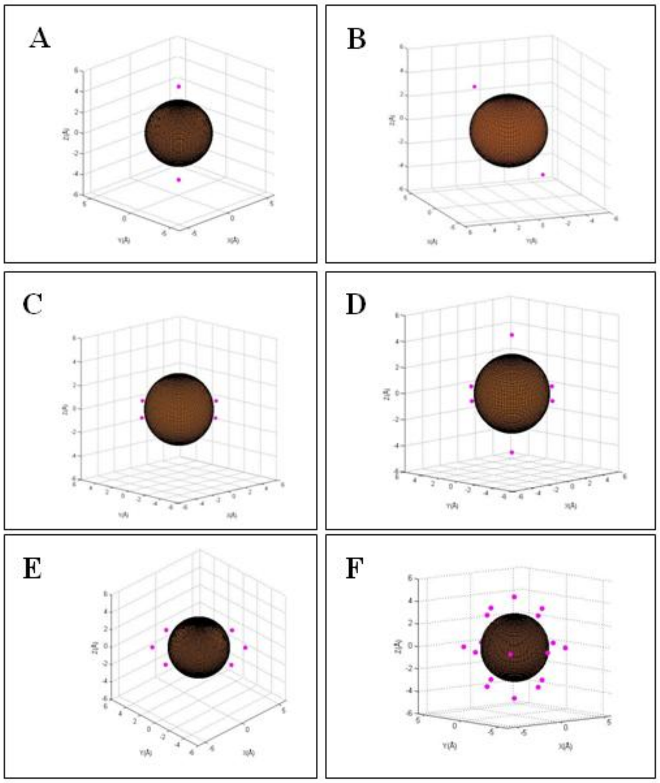

$Au_{25}(SR)_{18}^-$

The structure of $Au_{25}(SR)_{18}^q$ ($SR=SCH_2CH_2Ph$, SCH_3… and q=0,-1,+1) has been subject to numerous investigations.[73,308-310] It was eventually shown to have a Au_{13} icosahedral core with six $Au_2(SR)_3$ protecting units arranged in a quasi-tetrahedral fashion[73,309,310], as shown in Figure 7-2. The negatively charged cluster has a fully occupied 1P shell and is therefore very stable.

Figure 7-2. Optimized Xα/TZP.4f structure of the $Au_{25}(SR)_{18}^-$ cluster.

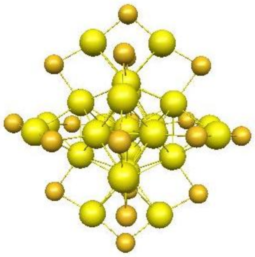

*The R group is not shown here. Orange: Sulfur. Yellow: Gold. Coordinates from Ref[78].

In order to model this nanoparticle, a 4.2 Å sphere is used to represent the core. This distance corresponds to the experimentally determined[73,310] and DFT calculated[78] bond length between the central gold atom and the outer gold core atoms (2.8 Å, close to the bulk Au-Au distance of 2.88 Å) plus half this bond length, which correlates to an approximate atomic radius for the outer gold core atom. The R group is not considered as a perturbation since its effect is likely to be much smaller than the gold or sulfur atoms. However, it must be remembered that depending on the nature of the R group, this perturbation may not be negligible. Gold atoms from the staples are considered perturbations with a +1 charge and sulfur atoms are considered perturbations of -1 charge. However, it should be noted that Au-S bonding is fairly covalent and therefore the magnitude of the partial charges on these atoms may be expected to be less than 1. The converged grid size is 0.2 Å. In order to investigate the influence of the size of the core in the energy level splitting, another set of calculations are run with a spherical core radius of 3.0 Å.

$Au_{102}(SR)_{44}$

The crystal structure of $Au_{102}(SR)_{44}$ with R=para-mercaptobenzoic acid (p-MBA) was determined by Jadzinsky in 2007.[76] The structure of the cluster is shown in Figure 7-3. It is made of an Au_{79} decahedral core protected by two $Au_2(SR)_3$ units similar to those discussed in the $Au_{25}(SR)_{18}$ case and 19 linear RS-Au-SR units. All those units constitute the perturbations. The partial charges considered are the same as for $Au_{25}(SR)_{18}^-$. We should emphasize that again the R group is not considered in this work. The distance between the center of mass of the cluster and the outer gold atom of the core is about 6.1 Å.[76] A 7.2 Å radius is considered to represent the spherical core. A grid size of 0.1 Å is used. The first order and zeroth order energies of the 1F, 2P, 1G, 2D, 1H, 3S and 1I orbitals are calculated and compared with the DFT data obtained by Walter et al.[80]

Figure 7-3. $Au_{102}(SR)_{44}$ crystal structure.

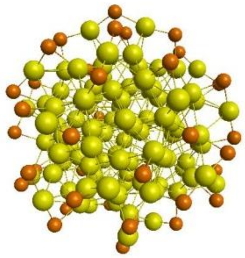

*The R group is omitted. Orange: Sulfur. Yellow: Gold. Coordinates from ref [76]

$Au_{144}(SR)_{60}$

DFT studies on $Au_{144}(SR)_{60}$ suggest a structure with an icosahedral Au_{114} core and thirty surrounding $Au(SR)_2$ motifs.[301] The optimized structure is shown in Figure 7-4A, with the R group omitted. The distance between the center and the outer gold atoms of the core is 7.10 Å.[301] In this work, $Au_{144}(SR)_{60}$ is modeled with a 8.5 Å core sphere, which corresponds to this distance plus half a Au-Au bond length. The S-Au-S perturbations are treated as point charges, similar to the two previous cases. The converged grid size is 0.1 Å. The first order and zeroth order energies of the 1S, 1P, 1D, 2S, 1F, 2P, 1G, 2D, 1H, 3S, 2F, 1I, 3P and 2G orbitals are calculated and compared with the data obtained by Lopez-Avecedo et al.[301] This range covers all occupied and several lowest unoccupied orbitals.

In order to determine how symmetry influences the splitting of the orbitals, a second geometry is examined in which the S-Au-S staples are uniformly spread out around the spherical core as shown in Figure 7-4B. In the DFT optimized structure, the average distance between the center of the sphere and the perturbations is 9.30 Å. Therefore, each perturbation in this case is located 9.30 Å away from the center of the sphere. The same set of orbital energies is calculated.

Figure 7-4. A) $Au_{144}(SR)_{60}$ optimized structure. B) Spherically spread out perturbations.

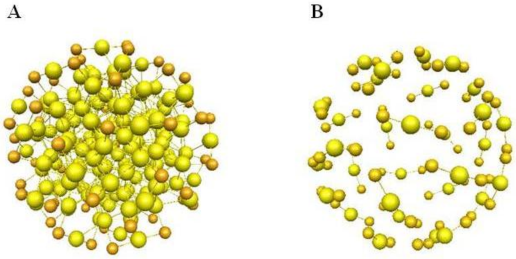

*The R group is omitted. Orange: Sulfur. Yellow: Gold. Coordinates of A) from Ref[301].

3nm nanoparticle

In order to create a nanoparticle in which the Au atoms in the S-Au-S unit lie at a distance of 1.5 nm from the center of the core, a radius of 1.415 nm is chosen for the spherical core. Therefore, the distance between the surface of the core and the perturbations is 0.85 Å, which is similar to the $Au_{144}(SR)_{60}$ nanoparticle. To determine the number of S-Au-S perturbations for this system, the ratio corresponding to surface area / number of units was considered to be identical to the $Au_{144}(SR)_{60}$ system:

$$\frac{A\left(Au_{144}\left(SR\right)_{60}\right)}{N\left(Au_{144}\left(SR\right)_{60}\right)}=\frac{A\left(3nm\ NP\right)}{N\left(3nm\ NP\right)}$$

where A is the surface area and N is the number of S-Au-S units. The surface area is proportional to the radius squared of the nanoparticle. We consider $r = R - 1.4$ where 1.4 is half of the Au-Au bond length in Å and R is the radius of the spherical core also in Å. The number of S-Au-S perturbations considered is:

$$\frac{r^2\left(3nm\ NP\right)}{r^2\left(Au_{144}\left(SR\right)_{60}\right)}N\left(Au_{144}\left(SR\right)_{60}\right)=\left(\frac{14.15-1.4}{8.5-1.4}\right)^2\times 30=96$$

The 96 S-Au-S motifs are uniformly spread around the sphere at a distance of 1.5 nm from the center of the sphere (Figure 7-5A). A similar nanoparticle with 64 S-Au-S motifs is also modelled (Figure 7-5B) in order to determine the effect of the number of perturbations on the electronic structure. The number of electrons in these clusters is estimated based on the electron density of the $Au_{144}(SR)_{60}$ cluster and calculated to be 388. However, this would lead to a partially filled shell. On the other hand, a cluster with 398 electrons would entirely fill up 25 shells. The zeroth order and first order energy of the 3F, 4P, 2I, 3G, 4D, 5S, 1N, 2J, 1L, 1M, 3H, 2K and 4F orbitals are calculated. They correspond to the six highest occupied and the seven lowest unoccupied orbitals, which would be the ones involved in electronic transitions. The converged grid size used for these calculations is 0.35375 Å, which was chosen to evenly divide into 1.415 nm.

Figure 7-5. Perturbations of the 3 nm sphere. A) 96 perturbations. B) 64 perturbations.

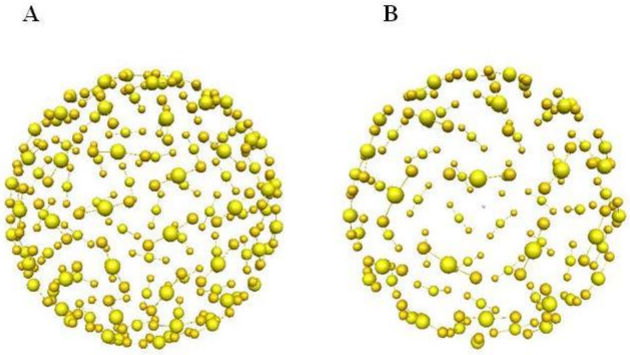

*Orange: Sulfur. Yellow: Gold.

Results and discussion

Test cases

Figure 7-6 shows the total energy (sum of zeroth order and first order) of the 1P and 1D orbitals for each of the five cases. The orbitals are labeled with the familiar notations P_x, P_y, P_z, D_{xy}, D_{xz}… except for the test case 1b since the alignment of the main axis with the z-axis is not respected. Instead, they are labeled P'_x, P'_y, P'_z, D'_{xy}, D'_{xz}… The splitting of the orbitals is as expected for all the test cases. Test case 1a shows that the P_z orbital lies higher in energy than the P_x and P_y orbitals, which are degenerate. The D_{z^2} orbital's energy is higher than the D_{yz} and D_{xz} orbitals (which are degenerate), which lie higher in energy than the D_{xy} and $D_{x^2-y^2}$ (which are also degenerate). Case 1b shows identical orbital splitting as case 1a. The P orbitals are plotted for these two cases in Appendix E. In each case, the three P orbitals are orthogonal with one of them pointing toward the perturbations.

As expected for the square planar case, the P_x and P_y energies are degenerate and lie higher in energy than the P_z. The energy of the $D_{x^2-y^2}$ orbital is higher than the energy of the D_{xy} orbital. The D_{xz} and D_{yz} orbitals come next and are degenerate, followed by the D_{z^2}. For the octahedral case, all P orbitals are degenerate. The D_{xz}, D_{xy} and D_{yz} are degenerate. The $D_{x^2-y^2}$ and D_{z^2} are also degenerate and lie higher in energy. As expected, the fourth case shows a similar splitting as the square planar case except that the D_{xy} and $D_{x^2-y^2}$ are degenerate. The last case shows an octahedral splitting. However, the energy difference between the two sets of D orbitals (0.12 eV) is about twice as small as the standard octahedral case (0.23 eV). The eighteen perturbations are arranged in an almost spherical manner and as a result, the energy of the orbital splitting is lower; however, the perturbations are not perfectly spherical so the splitting is found to be nonzero. The results from Figure 7-6 are consistent with known ligand-field splitting patterns. Since the splitting among P orbitals (max=0.64 eV) and among D orbitals (max=1.32 eV) are much less than the P-D energy difference (~5 eV), the perturbations should be weak enough that perturbation theory is valid. First order perturbation theory is sufficient to predict these patterns.

Figure 7-6. Orbital splitting for the test cases. A) Axial with perturbations along the z axis. B) Axial with perturbations along a random axis. C) Square planar. D) Octahedral. E) Planar with eight perturbations. F) Quasi-spherical with 18 perturbations. The orbital energies are in eV.

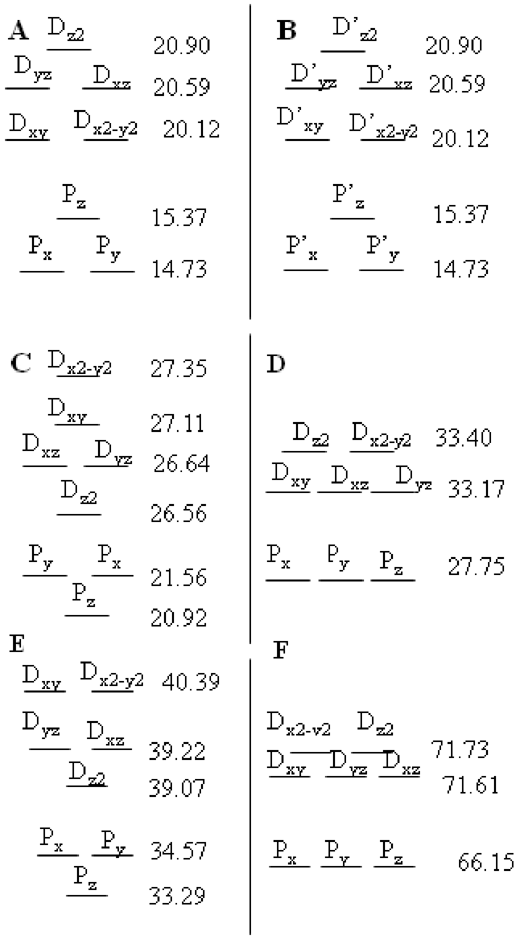
A
D_{z2} 20.90
D_{yz} D_{xz} 20.59
D_{xy} D_{x2-y2} 20.12
P_z 15.37
P_x P_y 14.73
B
D'_{z2} 20.90
D'_{yz} D'_{xz} 20.59
D'_{xy} D'_{x2-y2} 20.12
P'_z 15.37
P'_x P'_y 14.73
C
D_{x2-y2} 27.35
D_{xy} 27.11
D_{xz} D_{yz} 26.64
D_{z2} 26.56
P_y P_x 21.56
P_z 20.92
D
D_{z2} D_{x2-y2} 33.40
D_{xy} D_{xz} D_{yz} 33.17
P_x P_y P_z 27.75
E
D_{xy} D_{x2-y2} 40.39
D_{yz} D_{xz} 39.22
D_{z2} 39.07
P_x P_y 34.57
P_z 33.29
F
D_{x2-y2} D_{z2} 71.73
D_{xy} D_{yz} D_{xz} 71.61
P_x P_y P_z 66.15

$Au_{25}(SR)_{18}^-$

Figure 7-7A shows the 1P and 1D orbitals and their energies for $Au_{25}(SR)_{18}^-$ with a spherical core radius of 4.20 Å. These energies are calculated by adding the zeroth order and first order energies. The energies lie between 17.08 and 20.15 eV. These large positive values are due to the fact that we are considering a simple PIS model: the nuclei are not included. The 1P orbitals (HOMO) are degenerate. The 1D orbitals are split into 2 sets. The D_{xy}, D_{xz} and D_{yz} orbitals (LUMO+1) are 0.54 eV higher in energy than the $D_{x^2-y^2}$ and D_{z^2} orbitals (LUMO). The HOMO-LUMO gap is 2.49 eV.

Figure 7-7. A) $Au_{25}(SR)_{18}^-$ 1P and 1D orbitals and their energies in eV for a 4.2 Å spherical core. B) $Au_{25}(SR)_{18}^-$ 1P and 1D orbital energies in eV for a 3 Å spherical core.

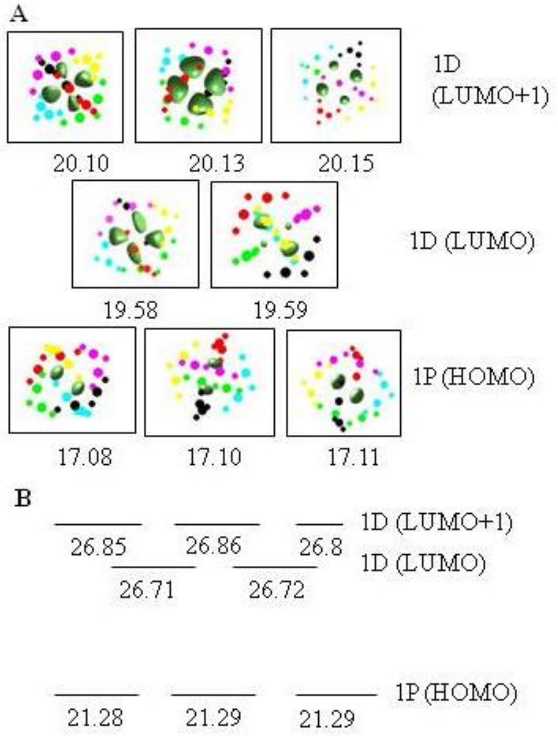

*Orbitals are in dark green. Each Au_2S_3 unit is represented with a different color. The bigger dots represent gold atoms and the smaller ones represent sulfur atoms.

This splitting agrees with the quasi-tetrahedral arrangement of the $Au_2(SR)_3$ units. As in the DFT calculations,[73,310] the orbitals making up the HOMO, LUMO and LUMO+1 levels are nearly degenerate, although a slight splitting occurs since the symmetry of the NP is not rigorously T_h. The DFT splitting between the two sets of D orbitals is 0.82 eV and the HOMO-LUMO gap is 1.48 eV. Therefore, the PIS model gives an orbital splitting that is comparable to DFT values but not quantitatively accurate. A few reasons for this may include the fact that the PIS model calculates the energy of orbitals within the core of the NP. Although the 1P and 1D orbitals are mainly located within the core of the nanoparticle, there is some ligand contribution.[73] In addition, electrons in the real case can spill out of the core, whereas they are constrained by an infinite potential in the PIS model. Other contributions to the inaccuracy of the energy gaps might include the absence of nuclei or the fact that orbital occupancies are not considered. Nevertheless, good qualitative results are obtained, including the right degeneracies and the correct orbital orderings. The PIS orbitals are very similar to the ones obtained with DFT:[73] the HOMO level is made of orbitals with a P character, the LUMO level is made of orbitals with $D_{x^2-y^2}$ and D_{z^2} character and the LUMO+1 is made of orbitals with D_{xy}, D_{xz} and D_{yz} character. However, the alignment of these orbitals is not always identical to DFT. In fact, some of these orbitals are oriented in a slightly different set of axes.

The orbital energies are between 21.28 and 26.86 eV for the 3.0 Å case, as shown in Figure 7-7B. The difference in range compared to the 4.20 Å case is mainly due to the zeroth order energy, which is inversely proportional to the radius of the spherical core squared (eq. 7.3). The D_{xy}, D_{xz} and D_{yz} orbitals (LUMO+1) are 0.14 eV higher in energy than the $D_{x^2-y^2}$ and D_{z^2} orbitals (LUMO) and the HOMO-LUMO gap is 5.43 eV. Consequently, as the core radius increases, the orbital splitting for a given shell increases but the energy between two different shells decreases.

Silver has a free-electron character similar to gold. Since the *d* band plays less of a role in silver than gold, the PIS model (which does not discriminate between elements) may provide more quantitative results. According to DFT, the silver cluster $Ag_{25}(SR)_{18}^-$ shows similar splitting as its gold counterpart.[73] The DFT calculated HOMO-LUMO energy gap is found to be 1.43 eV and the LUMO-LUMO+1 gap is 0.55 eV.[73] Thus, the HOMO-LUMO gap for both gold and silver is overestimated somewhat by the PIS model but the LUMO-LUMO+1 splitting for silver is well-reproduced by the PIS model. In the future, we may discriminate between elements by including the *d*-band or different spill-out parameters depending on the metal considered.

$Au_{102}(SR)_{44}$

Figure 7-8A shows the density of states diagram of $Au_{102}(SR)_{44}$ calculated with the PIS model. Figure 7-8B shows the DFT projected density of states within the Au_{79} core from Walter et al.[80]

Figure 7-8. A) $Au_{102}(SR)_{44}$ density of states spectrum using the PIS model. B) Projected density of states within the gold core region.

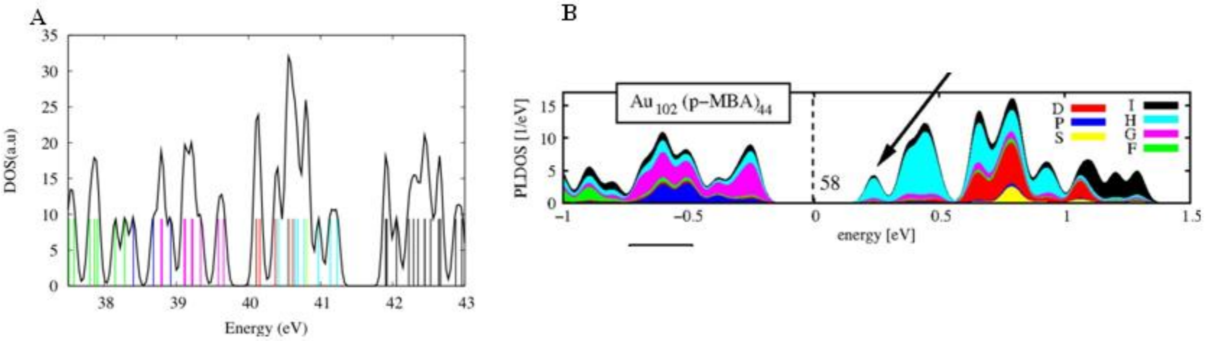

*Yellow: S. Blue: P. Red: D. Green: F. Magenta: G. Cyan: H. Black: I. B) is reprinted from Ref [80].(Copyright 2008 National Academy of Sciences, U.S.A.).

Both the PIS model and DFT show a set of occupied 1F orbitals followed by the 2P orbitals, which partially overlap the 1G. A gap of 0.4 eV occurs between the 1G and 1H orbitals with the two methods. It corresponds to the HOMO-LUMO gap. With the PIS model, the 2D orbitals partially overlap the 1H orbitals. However, there is a distinct set of 1H orbitals that does not overlap the 2D set with DFT. This feature is not reproduced with the PIS model. Additionally, contrary to DFT, the PIS model gives a large gap (0.7 eV) between the 1H and 1I orbitals. The orbital splittings are given in Table 7.1.

Table 7.1. Energy splitting (eV) of each set of orbitals of the $Au_{102}(SR)_{44}$ nanoparticle.

Orbitals	PIS model	DFT*
1F	0.8	0.2
2P	0.5	0.3
1G	0.9	0.5
2D	0.5	0.6
1H	1.1	0.8
1I	1.0	0.4

*Ref [80]

Overall, the splitting tends to be overestimated with the PIS model. In general, the PIS model gives good qualitative agreement with DFT but lacks quantitative accuracy. It should be emphasized that the core of this cluster has a decahedral symmetry which is not as spherical as the core of $Au_{25}(SR)_{18}^{-}$ or $Au_{144}(SR)_{60}$ which have icosahedral symmetry. Additionally, the p-MBA groups, which are not considered here, may influence the energy splittings and gaps. These calculations have also been run with a core radius of 7.5 Å, which corresponds to the distance between the center of mass of the cluster and the outer gold atom of the core plus half a gold-gold bond length. This DOS spectrum did not show any gap between the 1G and 1H orbitals, which again stresses the importance of the choice of radius.

$Au_{144}(SR)_{60}$

Figure 7-9A shows the density of states diagram calculated with the PIS model for the optimized structure. Figure 7-9B shows the DFT projected density of states within the Au_{114} core from Lopez-Acevedo et al.[301] and Figure 7-9C shows the density of states diagram calculated with the PIS model for uniformly spread perturbations. Tables 7.2 and 7.3 show the band gaps and energy splitting of the orbitals respectively for each of those three cases. The electronic structures obtained with the PIS model (Case A) and with DFT (Case B) for the DFT optimized structure are first discussed, followed by a discussion of the electronic structure obtained with the PIS model for uniformly distributed perturbations (Case C).

Figure 7-9. A) $Au_{144}(SR)_{60}$ density of states spectrum using the PIS model. B) Projected density of states within the gold core region. C) $Au_{144}(SR)_{60}$ density of states spectrum using PIS model with uniformly spherically spread out perturbations.

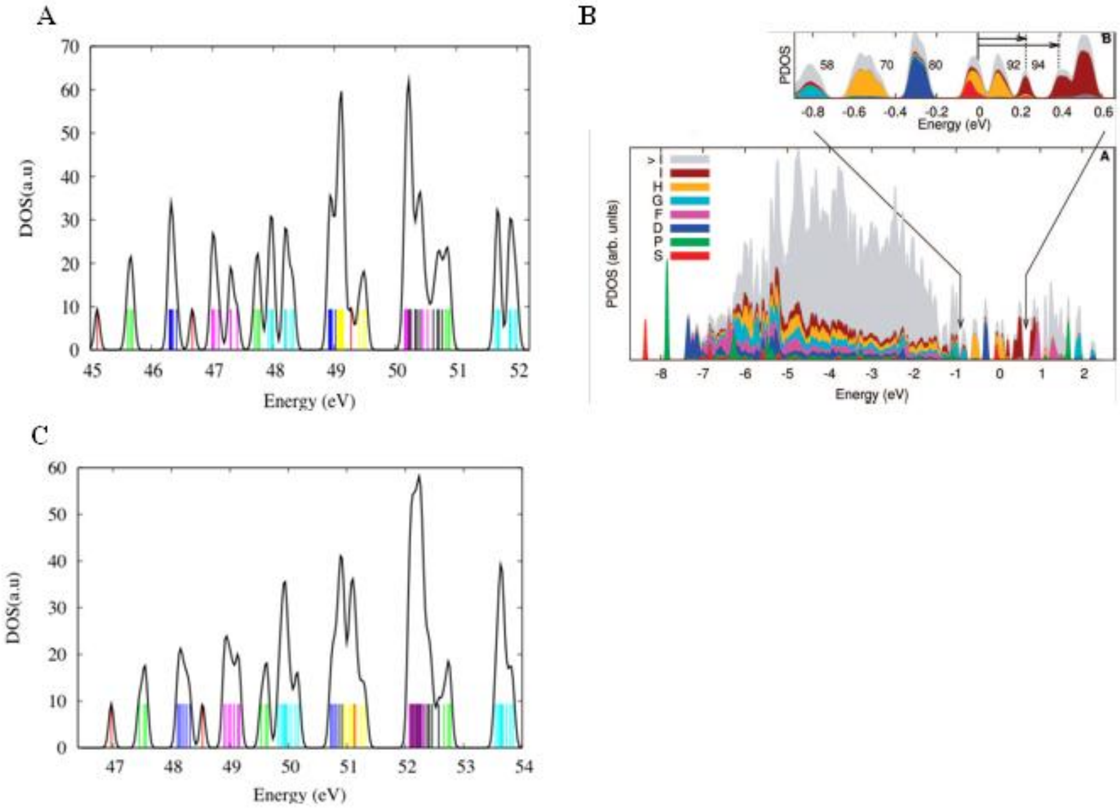

*Red: S. Green: P. Blue: D. Magenta: F. Turquoise: G. Yellow: H. Black: I. B) is reproduced with permission from Ref[301](Copyright 2009 American Chemical Society)

Comparison between the PIS model and DFT electronic structures for the optimized structure (Cases A and B).

Similar features between the two spectra are observed. First, the 1S, 1P and 1D orbitals show similar splitting. The gap between the 1S and 1P orbitals is 0.50 eV with both the PIS model and DFT. The PIS model overestimates the gap between the 1P and 1D orbitals by 0.16 eV. The next higher-energy orbitals are 2S, 1F, 2P and 1G. In the DFT calculations, the 2S, 1F and 2P orbitals overlap the *d*-band. The *d*-band originates from *d* electrons localized on the gold atoms and is not calculated with our model. The 1G orbital splitting is overestimated with our model. This could possibly be explained by the fact that the 1G orbitals partially overlap the *d* band in DFT calculations. A gap of 0.58 eV (Table 7.2) appears between the 1G and 2D orbitals with the PIS model, which is a bit larger than the 0.45 eV gap predicted by DFT for these orbitals. The 2D orbitals are split over 0.11 eV with the PIS model (Table 7.3) and about 0.06 eV with DFT. With DFT, the 1H orbitals are split into two main sets and the 2D orbitals fall between those two sets of 1H orbitals. Our model also predicts the splitting of the 1H orbitals into 2 sets but the 2D orbitals lie slightly lower in energy (0.03 eV) than the first set of 1H orbitals. The splitting of the 1H orbitals is underestimated by 0.27 eV with the PIS model. DFT calculations show that the 3S orbital overlaps the second set of 1H orbitals. With the PIS model, the 3S orbital falls between the two sets of 1H orbitals.

Table 7.2. Band gap energies (eV) of the $Au_{144}(SR)_{60}$ nanoparticle.

Orbitals	Case A	Case C	Case B[a]
1S→1P	0.50	0.48	0.50
1P→1D	0.60	0.54	0.44
1D→2S	0.26	0.22	NA[b]
2S→1F	0.33	0.38	NA[b]
1F→2P	0.29	0.37	NA[b]
2P→1G	0.15	0.19	NA[b]
1G→2D	0.58	0.55	0.45, 0.16[c]
1H→2F	0.64	0.75	0.76, 0.10[d]
2F→3P	0.29	0.37	0.18
3P→2G	0.75	0.78	0.18

a) Ref[301]
b) These orbitals overlap with the *d* band and therefore their energies could not be determined.
c) 1G→1H
d) 1H→1I

Table 7.3. Energy splitting (eV) of each set of orbitals of the $Au_{144}(SR)_{60}$ nanoparticle.

Orbitals	Case A	Case C	Case B[a]
1P	0.08	0.12	0.02
1D	0.12	0.21	0.07
1F	0.41	0.25	NA[b]
2P	0.07	0.11	NA[b]
1G	0.41	0.34	0.27
2D	0.11	0.19	0.06
1H	0.47	0.44	0.74
2F	0.37	0.22	0.53
1I	0.58	0.49	0.63
3P	0.07	0.11	0.02
2G	0.35	0.30	0.38

a) Ref[301]
b) These orbitals overlap with the *d* band and therefore their energies could not be determined.

The PIS model shows a large gap of 0.64 eV between the 1H and 2F orbitals. Therefore, the filling of the 1H shell would lead to a very stable cluster. However, $Au_{144}(SR)_{60}$ only possesses 84 metallic electrons according the superatom complex model.[301] According to the PIS model, 84 electrons would fill orbitals up to the 3S. There is a significant gap of 0.12 eV between the 3S orbitals and the second set of 1H orbitals that would contribute to the stability of the cluster. The PIS model shows that the 2F orbitals strongly overlap with the 1I orbitals. DFT also shows some overlap between the 2F and 1I orbitals but the 1I orbitals tend to have lower energies than the 2F orbitals. Similar to the 1H orbitals, the splitting of the 2F orbitals is underestimated by 0.16 eV with the PIS model. The splitting of the 1I orbitals with the PIS model (0.58 eV) is somewhat smaller than the one obtained with the DFT calculations (0.63 eV) but in the right range. Similarly to DFT calculations, the 3P and 2G orbitals appear at higher energy than the 2F and 1I orbitals. The gap between the 2F and 3P orbitals is 0.29 eV with the PIS model but only 0.18 eV with DFT. However, the gap between the 3P and 2G orbitals is much larger with the PIS model (0.75 eV) than with DFT calculations (about 0.18 eV). Most band gaps tend to be overestimated with the PIS model, but within a reasonable range. The only exception is the gap between the 3P and 2G orbitals which is overestimated by 0.57 eV.

Generally, the PIS model can reproduce many of the features of the density of states spectrum. However, since the charge-perturbed PIS is a rough model, accurate quantitative results are not obtained.

Comparison between the DFT optimized structure and uniformly spread perturbations (Cases A and C).

The PIS orbital energies for the uniformly spherically spread out perturbations are shown in Figure 7-9C and compared to those obtained using the DFT optimized structure (Figure 7-9A). The peaks in Figure 7-9C are sharper than those obtained on Figure 7-9A: the orbital energies for each set of orbitals are not as spread out as those calculated for the DFT optimized structure. This observation is particularly obvious for high *l* quantum numbers (F, G, H and I orbitals) as shown in Table 7.2, since these orbitals have many lobes and the perturbations are uniformly spread out around the spherical core. On the other hand, lower *l* (P and D orbitals) tend to look more spread out in the spherical case, which can be explained by the fact that they have fewer lobes and that the perturbations are not perfectly uniform around the sphere.

Additionally, the orbitals are shifted to higher energies (about 2 eV) in Figure 7-9C. This is due to the fact that in the uniformly arranged perturbations case, all the perturbations are chosen to be equidistant from the center of the sphere, which is not the case for the DFT optimized structure. Another interesting feature is that most of the gaps between different shells vary by less than 0.11 eV. Therefore, these energy gaps are not as affected by the arrangement of the perturbations as the orbital splitting is.

The data shows that the symmetry of the system plays a major role in determining the density of states spectrum, since it strongly influences orbital splitting. On the other hand, band gaps are not very affected by the arrangement of the perturbations.

3 nm NP

Figure 7-10 shows the density of states spectrum of the 3 nm nanoparticle with 96 and 64 perturbations. The two spectra are very similar, which shows that the number of perturbations does not significantly affect the electronic structure. As shown in Table 7.4, the splitting of the orbitals remains almost identical as the number of perturbation changes. We shall note that the orbital splitting is in general lower for this large nanoparticle than for the $Au_{144}(SR)_{60}$ cluster for a specific *l*. In fact, we can expect a decrease of the splitting of the orbitals as the radius of the nanoparticle increases and the arrangement of the perturbations become more and more spherical. We also note that, as found in the $Au_{25}(SR)_{18}^-$ case, if the core radius is decreased to 13.15 Å, the splitting of the orbitals becomes much lower. For instance, the splitting of the 1N orbitals decreases by 0.13 eV. The spectrum shifts to higher energy as the number of perturbations increases, which is expected since the orbital energies increase proportionally to the charge of the perturbations and each S-Au-S unit has a net negative charge. Both spectra show three main regions with a very large density of states. It is known that a large HOMO-LUMO gap and completely filled shells increase the system's stability: the electrons in the filled HOMO shell have low energy and cannot be easily removed. The LUMO has a high energy which means the system cannot accept any electrons. If this particle had 338 core electrons, it would be expected to be more stable since all the shells up to 2I would be completely filled and there is a gap of 0.09 eV between the 2I and 1M orbitals for the 96 perturbations case. In the 64 perturbation case, this gap increases to 0.13 eV. Similarly, this nanoparticle would also be quite stable if it had 452 electrons since there is an energy gap of 0.05 eV between two sets of 1N orbitals in the 96 perturbation case (0.06 eV in the 64 perturbation case). However, this arrangement does not lead to a fully occupied electronic shell. Overall, the size of the orbital gaps decreases as the particle becomes larger, and the 3 nm NP is closer to being "metallic" than $Au_{144}(SR)_{60}$.

Figure 7-10. Density of states spectra using PIS model of a 3 nm nanoparticle with A) 96 and B) 64 S-Au-S units.

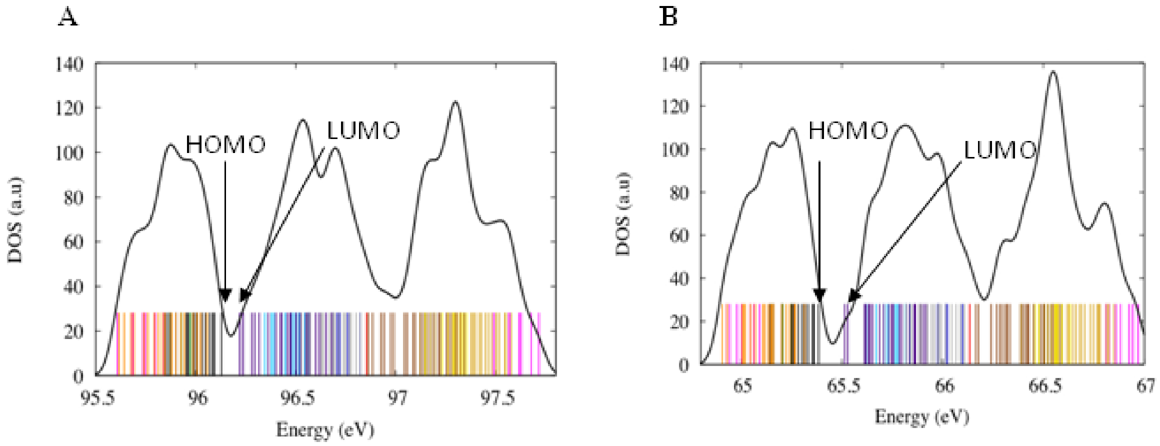

*Red: S. Green: P. Blue: D. Magenta: F. Turquoise: G. Yellow: H. Black: I. Grey: J. Golden: K. Orange: L. Indigo: M. Brown: N. One possible HOMO-LUMO gap leading to enhanced stability is denoted in both spectra.

Table 7.4. Energy spread of each set of orbitals for the 3 nm nanoparticle.

Orbitals	Orbital energy splitting (eV) with 96 perturbations	Orbital energy splitting (eV) with 64 perturbations
3F	0.23	0.16
1L	0.44	0.41
4P	0.10	0.10
2I	0.28	0.24
1M	0.46	0.40
3G	0.22	0.22
2J	0.29	0.29
4D	0.14	0.12
1N	0.46	0.42
3H	0.23	0.24
2K	0.31	0.30
4F	0.23	0.16

Final considerations

All the calculations performed in this work took no longer than a few minutes for each value of *l*, which makes this method very effective. The computational time required of course still depends on the size of the particle studied, the number of electron shells of interest, the number of perturbations considered and the grid size chosen. The results are qualitatively similar to those obtained with DFT, but quantitative accuracy in splitting energies and band gaps is still lacking. This model can potentially be improved by including interactions with the nuclei, for example by using a Jellium model, which would significantly lower the orbital energies. Another way to improve this model is to consider each atom in the ligand (the R group in our example). Finally, we could also include the *d*-band and introduce different spill-out parameters to discriminate between silver and gold, as explained in the results and discussion section. Of course, this would increase the computational time required.

Conclusions

In summary, a charge-perturbed particle-in-a-sphere model was created using first-order degenerate perturbation theory to calculate orbital energies of ligand-protected spherical gold nanoparticles. Atoms constituting the ligand motifs are described as point charge perturbations and the core is treated as a spherical well. Since spherical nanoparticles can be described with the superatom model,[22] the program uses the PIS model in conjunction with perturbation theory to determine the density of states of several spherical gold nanoparticles. The results are qualitatively similar to those obtained with DFT. The orbital energies are in agreement with expected ligand-field splitting patterns. The calculations performed on the $Au_{25}(SR)_{18}^{-}$ cluster show that the core radius plays a major role in the determination of the orbital splitting. The data obtained for the $Au_{144}(SR)_{60}$ nanoparticle shows that the symmetry of the perturbations greatly influences the electronic structure. However, the number of perturbations does not play a major part as long as the symmetry remains constant, as shown with the 3 nm nanoparticle case. As the nanoparticle size increases, the degree of orbital splitting decreases, which is most likely due to the nearly spherical arrangement of S-Au-S units. In addition, the energy gaps become smaller and the particle takes a metallic character.

A great advantage of this method is that it is computationally cheaper than DFT. The computational time required depends on the size of the particle studied, the number of perturbations considered and the grid size chosen. This model can be used for a wide variety of gold nanoparticles and ligands, if one is interested in getting the order of the superatom orbitals of a specific nanoparticle. The charge of the perturbations can be modulated depending on the atoms considered.

Acknowledgement

The authors thank Dr. Olga Lopez-Acevedo and Prof. Hannu Häkkinen (University of Jyväskylä, Finland) for sending DFT optimized coordinates and orbital energy data of $Au_{144}(SR)_{60}$. The authors thank Dr. Viktor Chikan (Kansas State University) for his help with Matlab programming.

Chapter 8 - Applications of the configuration interaction interpretation and extension to large nanoparticles

Introduction

In this section, we combine the findings described in the previous chapters to describe the evolution of the optical behavior of noble metal nanoparticles. We show that the CI model described in chapter 6 can reproduce the absorption features of several silver clusters and can be applied to any system size. In addition, we discuss the extension of this model to large noble metal nanoparticles.

Applications of the CI interpretation

In chapter 5, we showed that the high-energy, high-intensity β-band in acenes can be qualified as a plasmon. The reason for this is the constructive addition of the single-particle states HOMO-1→LUMO and HOMO→LUMO+1. In addition, we saw that the electron density shifts from one end of the molecule to the other upon excitation, as expected for a dipolar plasmon mode. Another excited state with lower energy and low oscillator strength (the α state) is also made of the same single-particle transitions. In this case, their dipole moment contributions interact destructively, explaining the low oscillator strength of the α state. This data is summarized in Table 8.1.

Table 8.1. Longitudinal modes of naphthalene at the LB94/TZP level of theory.[273]

Peak	Energy (eV)	Oscillator strength (a.u)	Transitions	Dipole moments contributions (a.u)	Transition densities*	|Isovalue|
α	4.09	0.000032	HOMO -1→ LUMO	2.2022	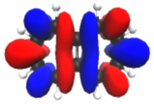	0.005
			HOMO→ LUMO+1	-2.1736		
β	5.60	1.107	HOMO -1→ LUMO	-1.8247	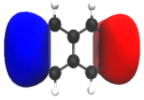	0.05
			HOMO →LUMO+1	-1.8267		

* The region where the electron density increases is in red. The region where the electron density decreases is in blue.

Application of the CI interpretation to the nanowire Ag_6

Is this behavior reproduced in noble metal nanoparticles? We already described the plasmon features of noble metal nanorods in terms of the constructive addition of single-particle transitions but we have not yet looked at the transition densities. We now take a closer look at the Ag_6 nanowire described in chapter 3. Table 8.2 shows the longitudinal and transverse excited state energies and oscillator strengths. The single-particle transitions and their contribution to the dipole moment of these excited states are also displayed.

Table 8.2. Longitudinal (L) and transverse (T) peak energies, oscillator strength and transition densities of the nanowire Ag_6 at the LB94/DZ level of theory. Single-particle states and dipole moments contributing to each peak are also given.

Peak	Energy (eV)	Oscillator strength (a.u.)	Excitations	Dipole moment contribution (a.u.)	Transition density side view*	Transition density end view*	|Isovalue|
L	1.98	1.74	$\Sigma_3 \rightarrow \Sigma_4$	-6.3581	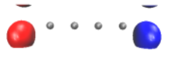	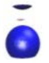	0.06
T1	6.86	0.67	$\Sigma_1 \rightarrow \Pi_1$	0.6997	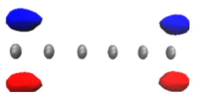	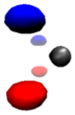	0.04
			$\Sigma_2 \rightarrow \Pi_2$	1.0356			
			$\Sigma_3 \rightarrow \Pi_3$	0.9631			
T2	5.75	0.0011	$\Sigma_1 \rightarrow \Pi_1$	0.3590	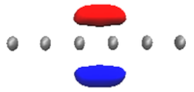	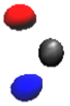	0.017
			$\Sigma_2 \rightarrow \Pi_2$	1.5259			
			$\Sigma_3 \rightarrow \Pi_3$	-1.8127			
T3	5.82	0.0013	$\Sigma_1 \rightarrow \Pi_1$	-1.9817	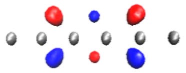	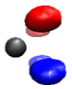	0.015
			$\Sigma_2 \rightarrow \Pi_2$	1.1369			
			$\Sigma_3 \rightarrow \Pi_3$	0.6165			

* The region where the electron density increases is in red. The region where the electron density decreases is in blue.

Only one single-particle transition contributes to the longitudinal mode. The electron density oscillates from one end of the molecule to the other, again as expected for a dipolar plasmon. As discussed in chapter 3, three $\Sigma_m \rightarrow \Pi_m$ (m=1, 2, 3) single-particle transitions contribute to the main transverse peak (labeled T1) and their dipole moment contributions add constructively. The electron density moves across the short axis of the system (as expected) and it is focused on the extremities of the wire. The same $\Sigma_m \rightarrow \Pi_m$ transitions contribute to two other transverse peaks in the absorption spectrum (labeled T2 and T3). However, their dipole moments add destructively, explaining the lower oscillator strength of these states. The transition densities of these two states also reveal the oscillation of the electron density across the short axis of the system. The electron density involved in these two states is much lower than the one involved in T1. This is shown by the lower isovalues used to plot these orbitals.

We now apply the CI model discussed in Chapter 6 to the transverse peak of this system. The values of α used correspond to the DFT calculated energy difference between the Π_m and Σ_m orbitals. At the LB94/DZ level of theory, these values are: $\alpha_1 = E(\Pi_1) - E(\Sigma_1) = 5.59$ eV, $\alpha_2 = E(\Pi_2) - E(\Sigma_2) = 5.69$ eV and $\alpha_3 = E(\Pi_3) - E(\Sigma_3) = 5.79$ eV. The coupling β values are assumed to be all equal and a value of 0.36 eV is taken to obtain the best fit with TDDFT. The best fit here is determined by the energy gap between the excited states. The CI and TDDFT results are given in Table 8.3.

Table 8.3. Comparison between TDDFT and CI excitation energies and oscillator strengths for the three excited states in Ag_6 resulting from the combination of the single-particle states $\Sigma_m \rightarrow \Pi_m$ (m=1, 2, 3).

Peak	TDDFT (LB94/DZ)		CI[a]	
	Energy (eV)	Oscillator strength (a.u.)	Energy (eV)	Oscillator strength[b] (a.u.)
T2	5.75	0.0013	5.27	0.0081
T3	5.82	0.0011	5.38	0.0089
T1	6.86	0.6653	6.42	2.9830

[a] The α values used for the CI matrix in eq. 6.2 are α_1 =5.59 eV, α_2=5.69 eV, α_3=5.79 eV and β=0.36 eV.

[b] The value given here is actually the oscillator strength enhancement, as explained in Chapter 6.

The excited state energies obtained with CI tend to be about 0.5 eV lower than the TDDFT values. The oscillator strengths enhancements give trends in very good agreement with TDDFT. Since the values of α are not exactly equal, the excited states T2 and T3 are not exactly degenerate and their oscillator strength is slightly higher than zero, as explained in chapter 6.

Application of the CI interpretation to the nanorod Ag_{71}^{-3}

Only one single-particle transition contributes to the longitudinal peak of the nanowires such as the Ag_6 described above. On the other hand, multiple transitions contribute to the longitudinal peak of wider systems, as discussed in chapter 4. Multiple single-particle transitions out of delocalized cylindrical orbitals contribute constructively to the high intensity longitudinal peak at 4.13 eV for the nanorod Ag_{71}^{-3}. Multiple low-energy excited states occur between 1.1 and 2.6 eV, arising from a destructive interaction of the same single-particle transitions. Again, these peaks are too weak to be observed experimentally. The strong longitudinal peak (plasmon) and one of these low-energy peaks are analyzed in Table 8.4. The electron density shifts from one end of the nanorod to the other in both of these excited states. This kind of motion is expected for a dipolar plasmon. However, we again note that the electron density involved in the strong longitudinal peak is higher than for the small peak, as suggested by the larger isovalue used to plot these orbitals. A direct application of the CI interpretation, as was done for Ag_6, is more difficult here since not all single-particle excitations out of the cylindrical orbitals contributing to this peak are printed out in the ADF program. In addition, a larger number of *d*-band orbitals may mix in due to their increased density of states with increasing system size. However, it is clear that the optical behavior of this system can be described in a similar way.

Table 8.4. Two longitudinal peak energies, oscillator strength and transition densities of the nanorod Ag_{71}^{-3} at the LB94/DZ level of theory.

Energy (eV)	Oscillator strength (a.u.)	Excitations	Contribution to dipole moment (a.u.)	Transition density side view	Transition density end view	|Isovalue|
4.13	5.14	$\Sigma_6 \rightarrow \Sigma_7$	1.1479	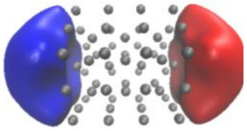	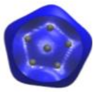	0.015
		$\Delta_4 \rightarrow \Delta_5$	1.8721			
		$2\Sigma_3 \rightarrow 2\Sigma_4$	0.8478			
		$\Pi_5 \rightarrow \Pi_6$	1.5081			
		$\Phi_3 \rightarrow \Phi_4$	1.0964			
		$2\Pi_2 \rightarrow 2\Pi_3$	0.8278			
1.46	0.0029	$\Sigma_6 \rightarrow \Sigma_7$	2.0691	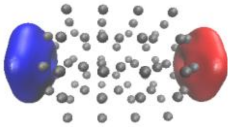	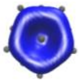	0.005
		$\Delta_4 \rightarrow \Delta_5$	1.3857			
		$2\Sigma_3 \rightarrow 2\Sigma_4$	0.5556			
		$\Pi_5 \rightarrow \Pi_6$	-9.3167			
		$\Phi_3 \rightarrow \Phi_4$	5.4624			

* The region where the electron density increases is in red. The region where the electron density decreases is in blue.

Application of the CI interpretation to the tetrahedral cluster Ag_{20}.

We discussed how the CI treatment can describe the plasmonic features of elongated systems. Can we apply it to any shape? The tetrahedral cluster Ag_{20} was previously studied using TDDFT.[177,209] At the LB94/TZP level of theory, this system has one strong peak in its absorption spectrum at 4.14 eV. Nine single-particle transitions between frontier orbitals contribute to this peak, as shown in Table 8.5. Their dipole moment contributions add constructively, giving this state a high oscillator strength. The same single-particle transitions contribute to eight other excited states between 2.17 and 3.12 eV, as shown in Table 8.6. These states have low oscillator strengths due to a destructive addition of the same single-particle transitions. The transitions densities of the strong peak and one of these weak states are shown in Table 8.5.

Table 8.5. Excited state energies, oscillator strength and transition densities of the tetrahedral Ag_{20} cluster at the LB94/TZP level of theory.

Energy (eV)	Oscillator strength (a.u.)	Transitions	Dipole moments (a.u.)	Transition density*	|Isovalue|
2.74	0.0192	HOMO-1 →LUMO+1	-1.576	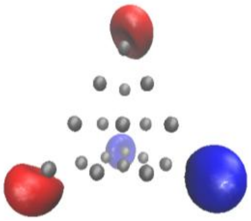	0.010
		HOMO → LUMO+2	2.8284		
		HOMO-2 → LUMO	-1.1909		
		HOMO → LUMO+2	0.6464		
		HOMO-1 →LUMO	-0.9814		
		HOMO →LUMO+3	-0.4312		
		HOMO-1 →LUMO+3	0.3975		
		HOMO-2 → LUMO+3	-0.2251		
		HOMO → LUMO	0.0608		
4.14	3.0047	HOMO-2 → LUMO	-1.1957	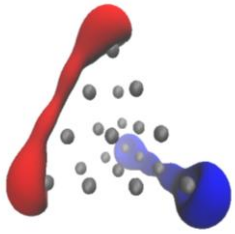	0.044
		HOMO →LUMO+3	-1.5952		
		HOMO-1 →LUMO+2	-1.3647		
		HOMO-1 →LUMO	-1.4425		
		HOMO → LUMO+2	-0.818		
		HOMO-1 →LUMO+1	-0.686		
		HOMO-1 →LUMO+3	-0.2421		
		HOMO-2 → LUMO+3	-0.1266		
		HOMO → LUMO	-0.0801		

* The region where the electron density increases is in red. The region where the electron density decreases is in blue.

For the state at 4.14 eV, the electron density moves from one edge of the cluster to the opposite one. The electron density change tends to be larger at the vertices of the system. For the state at 2.74 eV, a similar shift of the electron density is observed. Again, the electron density involved in the excitation is higher in the 4.14eV state, as shown by the higher isovalue used in the plot. The strong peak at 4.14 eV can therefore be attributed to a plasmon according to the scheme used so far.

The CI interpretation is applied to this system as well. The nine single-particle transitions shown in Table 8.5 are considered in the CI matrix. As in the Ag_6 case discussed above, the diagonal elements α of the CI matrix are the DFT energy differences between the two orbitals involved in the transition. At the LB94/TZP level of theory, these values are: α_1=2.41 eV, α_2=2.63 eV, α_3=2.64 eV, α_4=2.27 eV, α_5=2.46 eV, α_6=2.55 eV, α_7=2.80 eV, α_8=2.95 eV and α_9=2.09 eV. The coupling β considered is 0.15 eV. This value is chosen in the same manner as the one chosen for Ag_6 (such as to obtain the best splittings in comparison with TDDFT). Both CI and TDDFT results are reported in Table 8.6. Both methods show excellent agreement. Like in the Ag_6 case, the excited state energies are lower with CI. In addition, both CI and TDDFT show that the oscillator strengths of the 8 lower excited states are very low whereas the excited state of the high energy state is very high. Again, since the nine single-particle transitions are not exactly degenerate, the 8 low-energy excited states have non-zero oscillator strength.

Table 8.6. Comparison between TDDFT and CI excitation energies and oscillator strengths for the excited states in the tetrahedral cluster Ag_{20}.

TDDFT (LB94/TZP)		CI[a]	
Energy (eV)	Oscillator strength (a.u.)	Energy (eV)	Oscillator strength[b] (a.u.)
2.17	2.69E-03	1.97	0.048
2.36	3.03E-03	2.15	0.039
2.54	7.54E-03	2.28	0.011
2.65	4.01E-04	2.35	0.032
2.74	1.92E-02	2.43	0.024
2.81	6.88E-03	2.49	0.00055
2.93	1.33E-08	2.60	0.069
3.12	1.62E-02	2.75	0.078
4.14	3.0047	3.78	8.70

[a] The α values used for the CI matrix in eq. 6.2 are α_1=2.41 eV, α_2=2.63 eV, α_3=2.64 eV, α_4=2.27 eV, α_5=2.46 eV, α_6=2.55 eV, α_7=2.80 eV, α_8=2.95 eV, α_9=2.09 eV and β=0.15 eV.

[b] The value given here is the oscillator strength enhancement, as explained in Chapter 6.

Discussion: Extension of the CI interpretation to large nanoparticles

We showed in this chapter that the CI formalism in chapters 5 and 6 can successfully model the optical behavior of metallic clusters of various shapes. The plasmon of metallic clusters results from a constructive addition of nearly degenerate single-particle transitions. These transitions occur between delocalized orbitals resulting from a linear combination of the valence *s* orbitals of the metal atoms. As the size of the cluster increases, the number of single-particle transitions contributing to the plasmon peak increases due to the increasing density of states of these orbitals. This density of states increase was shown using the charge-perturbed particle-in-a-sphere model for gold nanoparticles in chapter 7 (Figures 7-7 to 7-10). For large nanoparticles, a large number of transitions between these delocalized orbitals have the same symmetry and similar energies. They can interact constructively to make a plasmon, as described above. The intensity of the plasmon peak increases with the number of single-particle contributions (Chapter 6). Therefore, the intensity of the resulting plasmon peak will become very high for large systems. Thus, one cause of the evolution from the discrete absorption spectrum of clusters to the plasmon peak of nanoparticle can be assigned to the increasing number of transitions involved in the CI. (As shown in chapter 7, another cause of the evolution is the decreased ligand-field splitting as the nanoparticle increases in size.) For small clusters, the density of states of delocalized orbitals is small. Few allowed transitions are close enough in energy to interact and make a plasmon. A discrete absorption spectrum is therefore obtained. We emphasize that for small gold clusters, excitations out of the *d*-band also contribute to the absorption spectrum since these localized orbitals may be close in energy to the delocalized ones. Overall, as the size of the system increases the number of transitions that can interact increases, giving birth to the plasmon.

Chapter 9 - Effects of Silver Doping on the Geometric and Electronic Structure and Optical Absorption Spectra of the $\mathbf{Au_{25-\mathit{n}}Ag_{\mathit{n}}(SH)_{18}^{-}}$ (*n* = 1, 2, 4, 6, 8, 10, 12) Bimetallic Nanoclusters

Reproduced with permission from:
Guidez, E. B.; Mäkinen, V.; Häkkinen, H.; Aikens, C. M. *J. Phys. Chem. C* **2012**, *116*, 20617.
Copyright 2012 American Chemical Society.

Abstract

The effect of silver doping of the $Au_{25}(SH)_{18}^{-}$ nanoparticle is studied by investigating $Au_{25-n}Ag_n(SH)_{18}^{-}$ (n = 1, 2, 4, 6, 8, 10, 12) systems using density functional theory (DFT). For $n = 1$, doping of the icosahedral shell of the metal core is energetically more favorable than doping of the metal-thiolate units or the center of the core. For $n \geq 2$, only doping of the core surface is considered and arrangements where the silver dopants are in close proximity tend to be slightly less favorable. However, energy differences are small and all conformations are accessible under experimental conditions. Boltzmann-averaged excitation spectra for these systems show similar features to the undoped $Au_{25}(SH)_{18}^{-}$. The main differences include a blue shift of the low-energy HOMO-LUMO (1P→1D) peak and an increased intensity of the peak at 2.5 eV as the number of doping silver atoms increases. Silver doping lowers the energy of ligand-based orbitals and facilitates the transitions between the superatom orbitals. Silver-doped systems show broader excitation spectra due to a breaking of the symmetry of the superatom orbitals.

Introduction

Small thiolate-stabilized gold and silver nanoparticles with diameters on the order of 1-2 nm exhibit structured optical absorption spectra with multiple peaks rather than the single, sharp peak of larger nanoparticles.[311-314] These optical characteristics provide a fingerprint of the nanoparticle core size and lead to interesting applications related to luminescence, nonlinear optical properties, etc.[315,316] The geometric structures of several nanoparticles in this size range have been characterized by x-ray crystallography, including $Au_{25}(SR)_{18}^{-/0}$,[73,297,310] $Au_{38}(SR)_{24}$,[74] and $Au_{102}(SR)_{44}$,[76] and it is now known that these systems are composed of a metal core surrounded by oligomeric –S–Au–S– or –S–Au–S–Au–S– motifs often called “staples”. This Au-S interface structure is found also in certain cases in self-assembled monolayers of thiolates on Au(111) (for a recent review, see Ref [317]). The $Au_{25}(SR)_{18}^{-}$ nanocluster has a 13-atom icosahedral core surrounded by six –S–Au–S–Au–S– units. Because the outermost valence electrons of gold (6s) and silver (5s) are relatively free-electron-like, these nanoparticles exhibit electron shell structure similar to that of sodium or other simple metal clusters; however for ligand-stabilized nanoparticles, the “free-electron” count n_e of a cluster with stoichiometry Au(or $Ag)_N X_M L_S^z$ (X = one-electron-withdrawing or -localizing ligand; L = Lewis base type ligand) can be determined by $n_e = N - M - z$, where N is the number of valence s electrons from the metal atoms and z is the global charge of the cluster.[80,260] $Au_{25}(SR)_{18}^{-}$ has $n_e = 8$ corresponding to an electronic shell structure with three highest occupied P-like orbitals and five lowest unoccupied D-like orbitals that can be revealed either by using a projection onto spherical harmonics approach or by examining Kohn-Sham orbitals.[73,80,83,309] Such orbitals are sometimes referred to as “superatom” orbitals since they originate from the linear combination of the gold 6s orbitals in the cluster and look like the familiar atomic orbitals. These superatom orbitals are delocalized over the core.[83] In the $Au_{25}(SR)_{18}^{-}$ system, the D-like orbitals split into two or more sets depending on the arrangement of the ligands.[82,83]

Doping of these nanoparticles has been of interest since Murray and co-workers demonstrated via mass spectrometry that a single Pd atom could be doped into the $Au_{25}(SR)_{18}^{-}$ cluster.[318] Density functional theory (DFT) calculations showed that the resulting cluster is most stable if Pd replaces the central core atom rather than gold atoms in the outer core or staple motifs.[319,320] A later combined experimental and theoretical study further supported the idea that the most stable cluster is indeed $Pd@Au_{24}(SR)_{18}$, proposed a neutral charge state, and suggested that this nanoparticle is more stable than the pure $Au_{25}(SR)_{18}^{-}$ system;[321] other recent work from this group indicates that the two central atoms of $Au_{38}(SR)_{24}$ can also be replaced by Pd, leading to a cluster with greater stability than the pure system.[322] Because of the interest in doped nanoparticles, the properties of $M@Au_{24}(SR)_{18}^{q}$ core-shell clusters with over 15 different metal atoms M including Ag, Cu, Pt, and Mn as the central atom have been studied by a number of researchers using DFT.[323-326]

Silver doping of gold nanoparticles is of interest since silver nanoparticles typically have strong plasmonic properties; in addition, the lattice constants of silver and gold are nearly identical so the two noble metals can be mixed in various proportions. Previous DFT work on doping of a single Ag atom into $Au_{25}(SR)_{18}^-$ indicated that the most favorable position for the silver atom is on the surface of the core rather than at the center of the core or in the staple motifs.[320] Other atoms such as Cd and Mn also appear to be most stable in this position.[168,320,327] Recently, it has been shown that approximately 11 silver atoms can be doped into $Au_{25}(SR)_{18}^-$ [Ref [181]] and up to 60 silver atoms can be doped into the $Au_{144}(SR)_{60}$ system.[328] Using DFT calculations, Malola and Häkkinen showed that the most favorable sites for silver doping of the icosahedral $Au_{144}(SR)_{60}$ nanoparticle are on the surface of the metal core, and this enhances the electronic shell structure of the particle.[329] Monte Carlo calculations using a MAEAM potential also find that silver atoms preferentially segregate to the surface layer of larger bare Au-Ag alloy nanoparticles,[330] which suggests that this phenomenon is not restricted to small thiolate-stabilized nanoparticles.

Previously, Negishi et al. reported a continuous change in the low-energy intraband transitions in silver-doped $Au_{25}(SR)_{18}^-$ nanoparticles.[181] They found that the optical absorption spectrum of their most highly doped system is close to the theoretical time-dependent DFT calculations of Aikens on a related $Ag_{13}Au_{12}(SH)_{18}^-$ nanoparticle.[83] In this work, we examine the absorption spectra of a series of $Au_{25-n}Ag_n(SH)_{18}^-$ (n = 1, 2, 4, 6, 8, 10, 12) bimetallic nanoparticles in order to determine the origin of the observed continuous change of the electronic structure and optical absorption.

Computational details

Calculations were run using density functional theory as implemented in the codes ADF2010.01[110] and GPAW.[331,332] In the ADF program, a triple-zeta polarized basis set with the frozen core approximation was used for all calculations. Relativistic effects were considered using the zeroth order regular approximation (ZORA).[115,116] All geometry optimizations were performed with the LDA functional Xα since LDA functionals reproduce Au-Au distances well. Single point energies are also reported at the LB94/TZP level of theory[146] using the Xα geometries. Excitation calculations were run at the LB94/TZP level and the frozen core approximation was also used. Excitation spectra were convoluted using a Gaussian with a FWHM value of 0.2 eV. A set of test calculations were run also with the GPAW code, by using the LDA parameterization by Perdew and Wang (LDA-PW).[104] The code uses the projector augmented wave (PAW) method[333] in a real-space grid. A grid spacing of 0.2 Å was used. $Ag(4d^{10}5s^1)$, $Au(5d^{10}6s^1)$ and $S(3s^23p^4)$ electrons were treated as valence and the inner electrons were included in a frozen core density. The setups for Au and Ag include scalar-relativistic effects. In geometry optimizations, 0.05 eV/Å convergence criterion for residual forces in atoms was used without any symmetry constraints.

Geometry optimizations and excitation calculations were performed on several isomers of each $Au_{25-n}Ag_n(SH)_{18}^-$ cluster (n = 1, 2, 4, 6, 8, 10, 12, 13). All the isomers studied are shown in Appendix F. Except for n = 1, only dopants on the surface of the core were considered since it is the most favorable position, as shown in the next section. For each even value of n between 2 and 10, the excitation spectra of the different isomers were Boltzmann-averaged using the procedure described here. The Boltzmann weight (BW) of each isomer (i) at room temperature was calculated using the following formula:

$$BW(i) = \frac{e^{-\frac{E_i}{kT}}}{\sum_j e^{-\frac{E_j}{kT}}}$$

where k is the Boltzmann constant (8.6173324 x 10^{-5} eV/K), T the temperature (298 K), and E_i is the energy of the isomer relative to the most stable structure. The sum j is over all isomers for a specific value of n. The intensity of each LB94/TZP excitation was multiplied by the Boltzmann weight of the isomer considered. The Boltzmann-averaged excitation spectrum was generated by convoluting all the obtained transitions for each n value with Gaussian functions with a FWHM of 0.2 eV.

Results and discussion

The effect of the position of the doping atom on the geometry, stability and excitation spectrum of the cluster will be addressed in detail in this section.

$Au_{24}Ag(SH)_{18}^-$

One silver dopant can occupy three distinct positions: on the surface of the core (1a), in one of the protecting staples (1b) and in the center (1c), as shown in Figure 9-1.

Figure 9-1. Geometry of the $Au_{24}Ag(SH)_{18}^{-}$ isomers at the Xα/TZP level of theory.

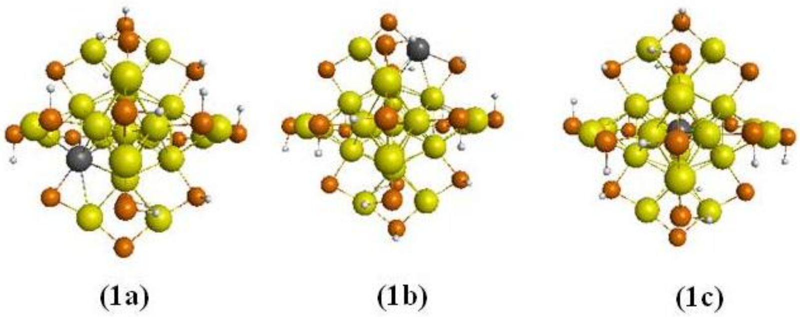
(1a) (1b) (1c)

*Key: Yellow=gold, gray= silver, orange= sulfur, white= hydrogen

Table 9.1 shows the relative energies and HOMO-LUMO gap of these relaxed systems at three levels of theory. Although the Xα, LDA-PW, and LB94 numbers differ, the trends are the same. 1a is the most stable structure, followed by 1b and 1c, in qualitative agreement with Ref [320]. This is in contrast to the $PdAu_{24}(SR)_{18}^{2-}$ case where the palladium occupying the central position was found to be the most stable, followed by the core surface position and the ligand shell position (calculated with the PBE and TPSS exchange-correlation functionals).[319] Experiment also suggests that the center position is preferred for Pd.[321]

Table 9.1. Relative energies and HOMO-LUMO gaps of the silver mono-substituted $Au_{24}Ag(SH)_{18}^{-}$ clusters (eV).

	Relative energies			HOMO-LUMO gap		
	Xα	LDA-PW	LB94	Xα	LDA-PW	LB94
1a	0	0	0	1.32	1.39	1.39
1b	0.11	0.14	0.30	1.32	1.36	1.41
1c	0.65	0.40	0.78	1.12	1.18	1.21

The HOMO-LUMO gaps obtained with LDA-PW and LB94 are comparable and Xα gives only slightly lower values. The HOMO-LUMO gaps for complexes 1a and 1b are similar, with values of 1.39 and 1.41 eV respectively at the LB94 level of theory. The HOMO-LUMO gap of complex 1c is 1.21 eV, which is 0.18 eV lower than isomer 1a. In comparison, the $PdAu_{24}(SR)_{18}^{2-}$ case exhibits a 1.25 eV HOMO-LUMO gap for the center doping position.[319] In contrast, the core surface and ligand shell doping positions showed considerably lower HOMO-LUMO gaps of 0.91 and 0.86 eV respectively.[319] Since large HOMO-LUMO gaps are often associated with stability, these results show that the silver dopant prefers to occupy the core surface whereas the palladium prefers to occupy the center. Jiang and Dai demonstrated that silver has a lower interaction energy with the $Au_{24}(SR)_{18}$ framework than palladium at the PBE/def2-TZVP level of theory,[23] which is in accordance with our observations. The energy of the substitution reaction $Au_{25}(SR)_{18}^{-} + n\text{Ag} \rightarrow Au_{25-n}(SR)_{18}^{-} + n\text{Au}$ was calculated for all the values of n considered and for all the positions of silver, as shown in Table 9.2. For $n = 1$, the reaction energy is much higher for the substitution of the center gold atom than any other position. DFT calculations on silver-doped $Au_{144}(SR)_{60}$ also show that it is more favorable for silver to occupy the outer shell of the cluster core.[329] Silver doping in the inner icosahedral shell of the core and in the staple units of $Au_{144}(SR)_{60}$ leads to much less stable clusters.[329] Average bond distances between the center atom and the surface of the core as well as distances between the edge sulfur atoms of each unit and the adjacent gold or silver atom of the core are shown in Table F.1 of Appendix F. Doping of the $Au_{25}(SH)_{18}^{-}$ system somewhat affects the geometry of the cluster. The average length between the center atom and the core surface is 2.78 Å for 1c and 2.79 Å for 1a and 1b. For system 1c, all center-surface distances are almost equal, with a deviation up to 0.01 Å. However, center-core distances of 1a are 2.78 ± 0.04 Å. This larger deviation is due to the fact that the bond length between the center gold atom and the silver atom on the surface is 2.83 Å. Additionally, the bond length between the core gold atom opposite to the silver atom and the center atom is 2.82 Å. This 0.05 Å elongation is interesting since gold and silver have approximately the same size and similar bulk lattice constants. Similar to 1c, 1b shows little variation in the center-core distances. The average bond length between sulfur atoms and the adjacent atom on the surface of the core is 2.41 Å for 1b and 2.42 Å for 1c, with a very small deviation for both cases. The average for case 1a is 2.42 Å but a large deviation of 0.09 Å occurs. This deviation is due to the long distance between silver and sulfur (2.51 Å). This is very comparable to the Ag-S distance at the metal core – sulfur interface (2.52 Å) found in the PBE calculation of the most stable silver-doped $Au_{144}(SR)_{60}$ cluster which has a core-shell composition of $Au_{54}Ag_{60}(RSAuSR)_{60}$.[329]

Table 9.2. Au_{25}+*n*Ag → Au_{25-n}Ag + *n*Au reaction energies per silver atom in eV at the Xα/TZP level of theory.

n	configuration	ΔE/n
1	a (surface)	0.79
	b (unit)	0.90
	c (center)	1.44
2	a	0.79
	b	0.80
	c	0.81
4	a	0.81
	b	0.82
	c	0.82
	d	0.83
	e	0.83
	f	0.85
6	a	0.84
	b	0.84
	c	0.84
	d	0.85
	e	0.85
	f	0.85
	g	0.86
	h	0.86
8	a	0.86
	b	0.86
	c	0.86
	d	0.86
	e	0.86
	f	0.87
10	a	0.86
	b	0.87
	c	0.87
12	surface	0.88

Excitation spectra of the three silver-doped species are shown in Figure 9-2. The $Au_{25}(SH)_{18}^{-}$ excitation spectrum was also calculated at the LB94/TZP level of theory (Figure F-1 of Appendix F) and is similar to the one previously calculated at the SAOP/TZP level of theory.[83]

Figure 9-2. Excitation spectra of the A) 1a, B) 1b and C) 1c $Au_{24}Ag(SH)_{18}^{-}$ isomers at the LB94/TZP level of theory.

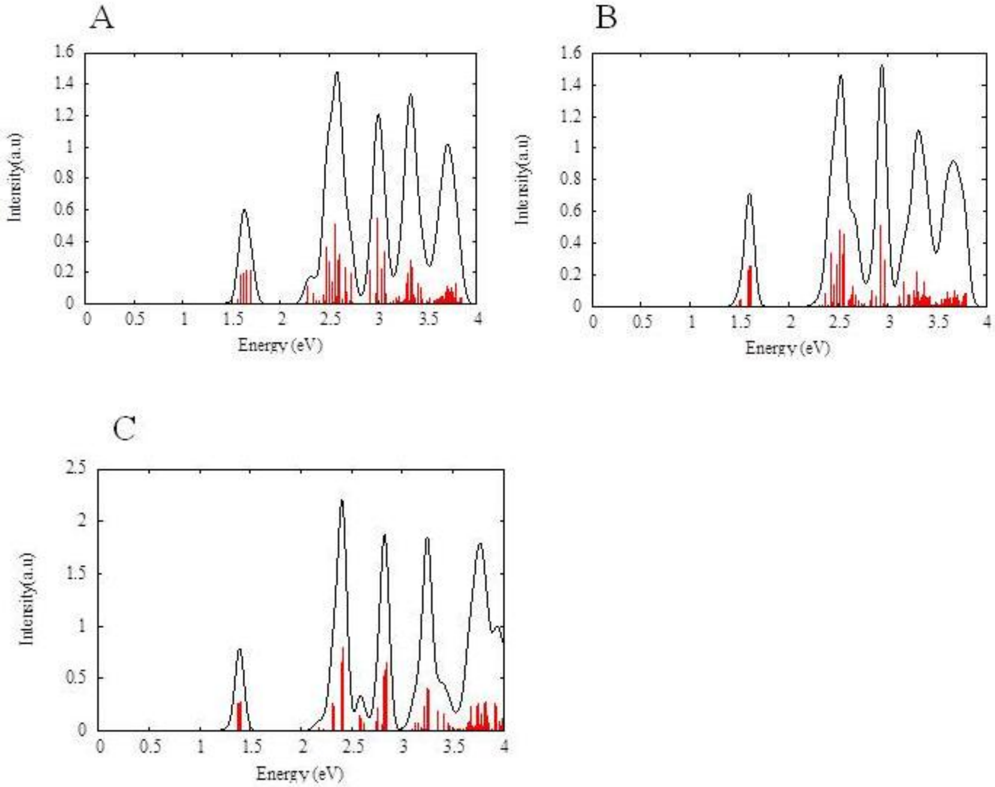

The first peak at 1.60 eV is assigned to transitions originating from the approximately triply degenerate 1P superatom orbitals (HOMO) to the doubly degenerate set of 1D orbitals (LUMO), which corresponds to the peak at 1.63 eV at the SAOP/TZP level of theory.[83] The peak at 2.48 eV is assigned to transitions from an approximately triply degenerate set of a_u orbitals originating from the staple motifs to the LUMO. This peak also occurs at 2.48 eV at the SAOP/TZP level of theory and corresponds to transitions from the triply degenerate HOMO-2 to LUMO.[83] Orbitals below the HOMO are composed of sulfur p orbitals and of d orbitals from the gold on the staples. The peak at 2.55 eV is assigned to transitions from the HOMO to the LUMO+1 orbitals (a triply degenerate set of 1D orbitals) and corresponds to the peak at 2.60 eV at the SAOP/TZP level.[83] At 2.66 eV, we have transitions from the HOMO orbital to the LUMO+2 orbital, corresponding to the 2S superatom orbital.[83] The excitation spectrum of 1c is very similar to the spectrum of the undoped system described above. The sharp low-energy HOMO-LUMO peak appears at 1.39 eV. The peak at 2.31 eV corresponds to interband transitions from the triply degenerate ligand-based orbitals (here HOMO-1) to the LUMO. The peak at 2.40 eV is assigned to HOMO-LUMO+1 transitions. The peak at 2.58 eV corresponds to transitions from the HOMO to the LUMO+3 orbital (1P→2S). Higher energy peaks are assigned to additional interband transitions. System 1a shows an excitation spectrum that is much broader than 1c, although the main features are similar to the undoped system. This can be explained by the breaking of the symmetry of the system when the doping silver occupies the surface of the core. For instance, the low energy peak of 1a, corresponding to a HOMO-LUMO transition in the $Au_{25}(SH)_{18}^-$ system, extends from 1.56 to 1.70 eV. The silver atom splits the degeneracy of the superatom orbitals, leading to a broader spectrum. Case 1b also shows a slightly more split spectrum than 1c. Since the silver atom is in a staple unit, it does not change the core orbitals very much. However, the ligand orbitals that contribute are affected,[83] leading to some splitting in the spectrum.

$Au_{23}Ag_2(SH)_{18}^-$

We now consider two silver atoms doping the surface of the icosahedral core of the system. Three configurations are obtained, as shown in Figure 9-3.

Figure 9-3. Geometries of the $Au_{23}Ag_2(SH)_{18}^-$ isomers at the Xα/TZP level of theory.

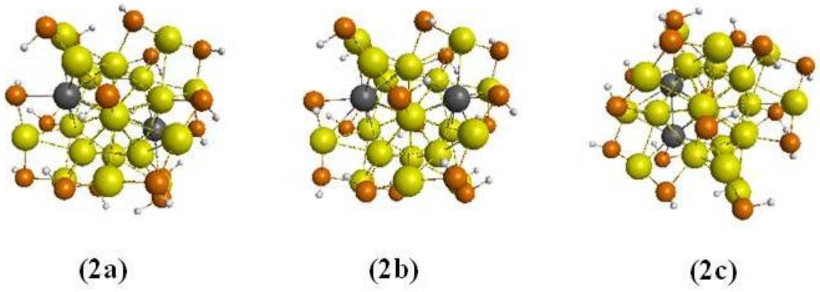

* Color coding same as Figure 9-1.

Case 2a has two silver atoms aligned with an axis through the gold center, giving a system with higher symmetry than the other two cases. Case 2b has two nonadjacent silver atoms. Case 2c has two adjacent silver atoms on the surface of the core. Bond lengths follow similar trends as case 1a discussed previously (Table F-2 of Appendix F). Distances between the center core and the silver atoms are 0.08, 0.05 and 0.03 Å longer than distances between the center gold and another gold atom on the surface for cases 2a, 2b and 2c respectively. The distance between silver and the neighboring sulfur are also 0.11 Å longer than corresponding gold-sulfur distances for case 2a and 0.1 Å for cases 2b and 2c. Relative energies and HOMO-LUMO gaps are given in Table 9.3.

Table 9.3. Relative energies and HOMO-LUMO gaps of the silver bi-substituted $Au_{23}Ag_2(SH)_{18}^-$ cluster (eV).

	Relative energies			HOMO-LUMO gap		
	Xα	LDA-PW	LB94	Xα	LDA-PW	LB94
2a	0	0	0.04	1.25	1.30	1.30
2b	0.03	0	0	1.36	1.41	1.43
2c	0.05	0.04	0.05	1.37	1.39	1.44

We note that the relative energies of the three systems are much closer than in the uni-doped case, within a 0.05 eV range. Moreover, substitution reaction energies are very similar for the three systems. Therefore, all configurations can potentially occur under experimental conditions. Xα, LDA-PW and LB94 give slightly different trends. With Xα, longer distances between the silver atoms lead to more stable systems. With LB94 single point calculations at the Xα geometries, the non-adjacent arrangement (2b) of the silver atoms is more favorable than the opposite arrangement (2a). LDA-PW data shows that 2a and 2b have the same energy. However, it should be again emphasized that the energy differences are in the order of hundredths of an electronvolt. The HOMO-LUMO gap of 2a is 0.13 eV smaller than 2b with LB94, and 0.11 eV smaller than 2b with Xα and LDA-PW. 2b and 2c show similar HOMO-LUMO gaps. High HOMO-LUMO gaps lead to increased stability since removal of an electron from the HOMO or addition of an electron in the LUMO becomes difficult. 2a has a significantly lower HOMO-LUMO gap than the other two isomers but only a slightly lower energy.

The excitation spectra are shown in Figure 9-4. The main features are also similar to the $Au_{25}(SH)_{18}^-$ system described above. Although 2a has the highest symmetry, it shows a higher splitting than 2b and 2c.

Figure 9-4. Excitation spectra of the A) 2a, B) 2b and C) 2c $Au_{23}Ag_2(SH)_{18}^-$ isomers at the LB94/TZP level of theory.

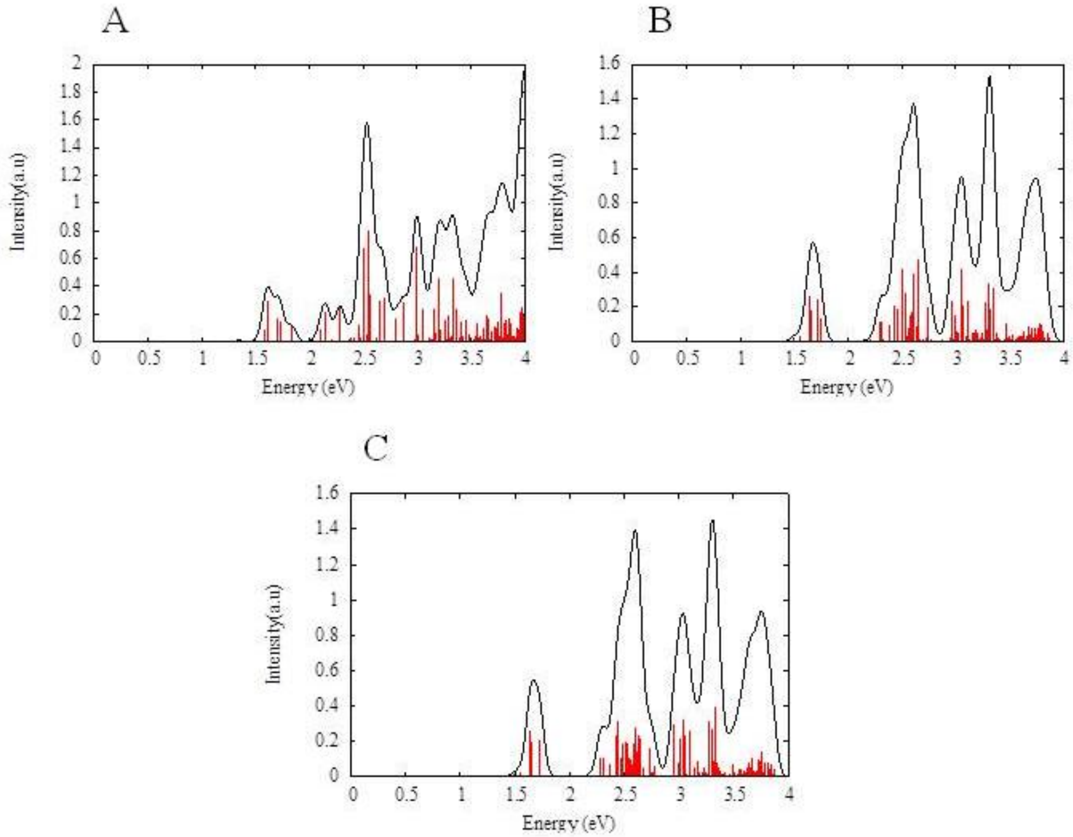

Table 9.4. Superatom orbital splitting of the three $Au_{23}Ag_2(SH)_{18}^-$ isomers (eV) at the LB94/TZP level of theory.

	2a	2b	2c
1P (“HOMO”)	0.292	0.159	0.159
First 1D set (“LUMO”)	0.165	0.075	0.061
Second 1D set (“LUMO+1”)	0.139	0.063	0.063

Orbital energy splittings for these three cases are summarized in Table 9.4. The splitting of the 1P orbitals is identical for cases 2b and 2c but almost twice as high for 2a. The two sets of 1D orbitals also show a much higher splitting for 2a than 2b and 2c. This is in accordance with the fact that 2b and 2c show similar excitation spectra and 2a has a significantly split spectrum. Figure 9-5 shows the frontier orbitals of case 2a. The lobes of the 1P orbitals are not exactly aligned with the axis pointing at the two silver atoms but instead are aligned along an axis pointing toward silver and an adjacent gold atom. The energy of this orbital is more affected by the silver atoms than the other two 1P orbitals, which causes the greater observed energy splitting. The $1D_z^2$-like orbital is oriented similarly to the 1P orbital discussed above. One 1D orbital in the second set has two lobes pointing almost directly at the silver atoms. Therefore, the orientation of the superatom orbital is determined by the position of the silver atoms and the silver atoms affect the spread of the orbital energies.

Figure 9-5. Frontier orbitals of $Au_{23}Ag_2(SH)_{18}^-$ (2a) at the LB94/TZP level of theory.

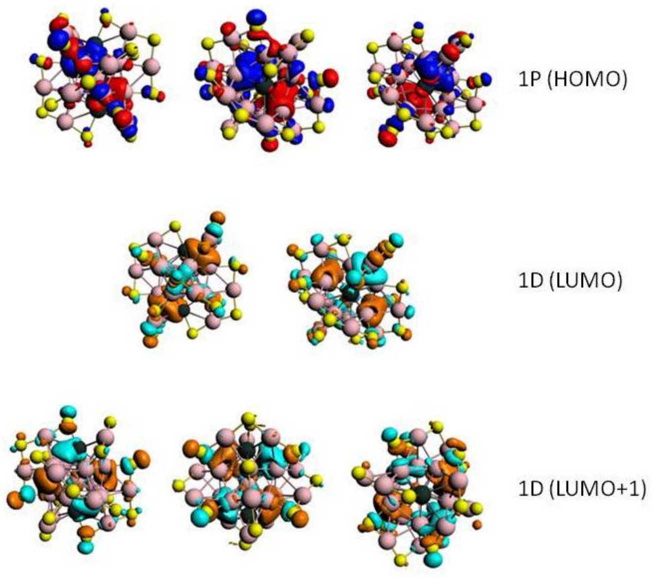

Key: Yellow: sulfur, pink: gold, black: silver. Contour value=0.02

$Au_{25-n}Ag_n(SH)_{18}^-$ (n=4, 6, 8, 10)

A number of configurations with 4, 6, 8 and 10 silver atoms doping the surface have been studied. All the isomers for each value of *n* are shown in Figure F-2 to F-5 of Appendix F. Tables 9.5 to 9.8 show relative energies and HOMO-LUMO gaps for *n* = 4, 6, 8 and 10 at the Xα, LDA-PW and LB94 level of theory. All three levels of theory give similar results.

Table 9.5. Relative energies and HOMO-LUMO gaps of the silver tetra-substituted $Au_{21}Ag_4(SH)_{18}^-$ cluster (eV).

	Relative energies			HOMO-LUMO gap		
	Xα	LDA-PW	LB94	Xα	LDA-PW	LB94
4a	0	0	0	1.44	1.44	1.49
4b	0.02	0.01	0.01	1.42	1.43	1.47
4c	0.03	0.06	0.01	1.35	1.34	1.40
4d	0.07	0.06	0.06	1.24	1.29	1.29
4e	0.07	0.08	0.07	1.43	1.44	1.49
4f	0.14	0.16	0.13	1.33	1.33	1.40

Table 9.6. Relative energies and HOMO-LUMO gaps of the $Au_{19}Ag_6(SH)_{18}^-$ cluster (eV).

	Relative energies			HOMO-LUMO gap		
	Xα	LDA-PW	LB94	Xα	LDA-PW	LB94
6a	0	0.02	0.02	1.56	1.56	1.61
6b	0.01	0	0.01	1.56	1.60	1.62
6c	0.02	0.03	0	1.51	1.56	1.57
6d	0.05	0.04	0.11	1.52	1.56	1.58
6e	0.05	0.07	0.05	1.51	1.58	1.58
6f	0.07	0.08	0.04	1.23	1.30	1.27
6g	0.12	0.12	0.13	1.51	1.52	1.57
6h	0.13	0.18	0.16	1.53	1.56	1.60

The relative energies are again relatively close for each isomer, which shows that there is no strongly preferred arrangement of the silver atoms at the surface of the core. However, we can see that the arrangements where the silver atoms are close to each other tend to be slightly less favored. For instance, 4f has four silver atoms connected at the surface of the core and its energy is 0.14 eV higher than the lowest energy structure at the Xα level of theory. Similarly, for six silver dopants, the capped structure where all the silver atoms are adjacent (6h) is 0.13 eV higher in energy than the lowest-energy isomer. The second highest energy isomer 6g is similar to 4f but with an additional two silver atoms also adjacent.

For *n* = 8, there are more silver atoms in the core than gold. The structures with the most packed arrangement of the silver atoms are slightly less favored but the relative energies are all within 0.08 eV at the Xα level. These trends are somewhat reflected in the substitution reaction energies. Substitution reactions become less favorable as more gold atoms are substituted, as displayed in Table 9.2.

Table 9.7. Relative energies and HOMO-LUMO gaps of the $Au_{17}Ag_8(SH)_{18}^-$ cluster (eV).

	Relative energies			HOMO-LUMO gap		
	Xα	LDA-PW	LB94	Xα	LDA-PW	LB94
8a	0	0	0	1.51	1.52	1.57
8b	0.01	0.03	0.02	1.41	1.41	1.44
8c	0.01	0.03	0.02	1.54	1.54	1.59
8d	0.04	0.08	0.04	1.42	1.42	1.45
8e	0.05	0.08	0.07	1.53	1.53	1.58
8f	0.08	0.1	0.14	1.39	1.39	1.43

We note that for *n* = 10, the three possible isomers are similar to those obtained with *n* = 2 (with silver and gold swapped on the surface of the core). 10a is the most favorable at the Xα level of theory while 10b is the most favorable at the LB94 level. It is interesting to note that the opposite arrangement of gold atoms around the core is the least favorable at the LB94 level.

Table 9.8. Relative energies and HOMO-LUMO gaps of the $Au_{15}Ag_{10}(SH)_{18}^-$ cluster (eV).

	Relative energies			HOMO-LUMO gap		
	Xα	LDA-PW	LB94	Xα	LDA-PW	LB94
10a	0	0	0.07	1.51	1.52	1.56
10b	0.06	0.06	0	1.61	1.60	1.65
10c	0.1	0.08	0.03	1.59	1.62	1.64

It should be emphasized that the relative energy differences of all isomers for a specific *n* are small and all structures may be accessible at room temperature. Consequently, we looked at the Boltzmann-averaged spectra for all *n*, as displayed in Figure 9-6.

Figure 9-6. Boltzmann-averaged excitation spectra of $Au_{25\text{-}n}Ag_n(SH)_{18}^-$ nanoclusters at the LB94/TZP level of theory.

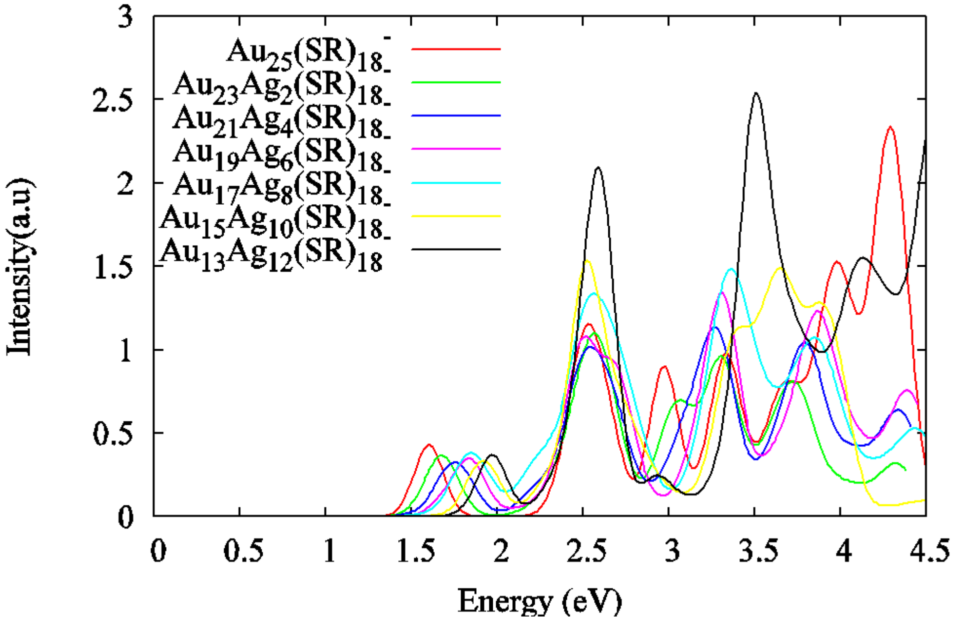

Individual excitation spectra are shown in Appendix F (Figures F-6 to F-9). The individual spectra are very split but the Boltzmann averaged curves show similar features to the $Au_{25}(SH)_{18}^-$ system. Although silver and gold atoms have a singly occupied *s* orbital, their optical properties differ due to the strong relativistic effects in gold. Relativistic effects lead to the contraction of the electron cloud of gold. As a result, the 5*d* orbitals of the gold atom are very close to the singly occupied 6*s* orbital. On the other hand, there is a large gap between the 4*d* and 5*s* orbitals of silver. For highly doped species, the superatom orbitals become more separated from ligand-based orbitals. The low-energy peak, which corresponds to the intraband HOMO-LUMO transition, shifts from 1.60 eV to 2 eV as the number of doping silver atoms increases. This is in accordance with the observed increasing HOMO-LUMO (1P-1D) gap with increasing *n*. The peak intensity remains almost constant. This blue shift of the HOMO-LUMO peak (from 1.59 eV to 1.85 eV) with increasing *n* was previously observed experimentally by Negishi et al. for similar $Au_{25\text{-}n}Ag_n(SR)_{18}^-$ clusters.[181] The intensity also remained quasi-constant.[181] The transitions responsible for the 2.5 eV peak originate from ligand orbitals to LUMO for the undoped system, as discussed previously. As *n* becomes larger, 1P→ 1D and 1P→ 2S transitions take over. These transitions are more intense than the interband transitions. We note that the high contribution of the superatom orbitals for this peak was previously observed for the fully-doped core system at the SAOP/TZP level of theory.[83] The peak at 3.3 eV shifts to 3.5 eV as the number of silver atoms increases and its intensity increases as well. This peak corresponds mainly to interband transitions. This can also be explained by the fact that the ligand orbitals become lower in energy and more separated from the superatom orbitals.

$Au_{13}Ag_{12}(SH)_{18}^-$

The system with 12 silver atoms on the core surface has also been studied (Figure 9-7). The bond length between the center gold atom and the silver atoms is 2.79 Å, similar to the distances obtained for the mono-substituted systems. The distance between silver and the adjacent sulfur is 2.54 Å, which is 0.03 Å longer than the silver-sulfur distance for the mono-substituted system 1a.

Figure 9-7. Geometry of the $Au_{13}Ag_{12}(SH)_{18}^-$ nanocluster at the Xα/TZP level of theory.

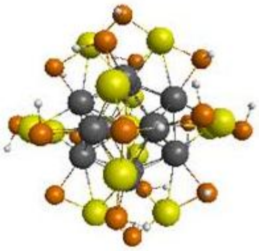

(12)

***** Color coding same as Figure 9-1.

The excitation spectrum of $Au_{13}Ag_{12}(SH)_{18}^-$ is shown in Figure 9-8. The peak at 1.97 eV is the HOMO→LUMO (1P→1D) peak, similar to the other spectra. The peak at 2.51 eV corresponds to HOMO→LUMO+1 (1P→1D) transitions. The peak at 2.61 eV corresponds mainly to 1P→2S transitions. Similar features were obtained at the SAOP/TZP level of theory for the fully doped core $Ag_{13}Au_{12}(SR)_{18}^-$ system.[83] The HOMO-LUMO peak of the $Ag_{13}Au_{12}(SR)_{18}^-$ system is at

1.83 eV, the HOMO→LUMO+1 peak at 2.34 eV and the HOMO→ LUMO+2 (1P→2S) transition at 2.53 eV.[83] The substitution of the center atom does not significantly affect the spectrum, which is in accordance with the results obtained above for case 1c.

Figure 9-8. Excitation spectrum of the $Au_{13}Ag_{12}(SH)_{18}^-$ nanocluster at the LB94/TZP level of theory.

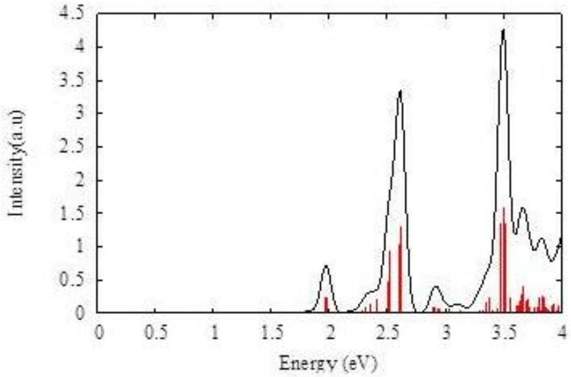

Conclusions

The surface of the core is the preferred position for silver doping into $Au_{25}(SH)_{18}^-$. The core center position is highly unfavorable. Several isomers of silver-doped $Au_{25-n}Ag_n(SR)_{18}^-$ nanoparticles have been studied with $n = 1, 2, 4, 8, 10$ and 12 doping silver atoms. For $n \geq 2$, only doping of the core surface was considered. In general, arrangements where the silver atoms are close to each other tend to be less favorable but all isomers should be accessible under experimental conditions. However, their relative abundance in the experiment may depend on the details (kinetic factors) of the growth that cannot be addressed in this study. Silver doping on the surface of the core does not affect the overall shape of the optical absorption spectrum but gives some additional orbital splitting due to the breaking of the symmetry of the nanoparticle. The optical gap determined by the position of the HOMO→LUMO peak (1P→1D) shifts to higher energy with increasing *n*, which is in qualitative agreement with the experiment of Negishi and co-workers.[181] The intensity of the peak at 2.5 eV increases as the number of silver doping atoms increases due to the increasing contribution of superatom 1P→ 1D and 1P→2S transitions. The high energy peak that corresponds to interband transitions shifts to higher energy as the number of doping silver atoms increases. During nanoparticle growth, any possible arrangement of the silver atoms in the nanoparticle may possibly occur, leading to a mixture of isomers. However, if one can control the number of silver atoms in the nanoparticle, it could be possible to tune optical properties such as the HOMO-LUMO gap and the shape of the optical absorption spectra.

Acknowledgements

This material is based upon work supported by the Air Force Office of Scientific Research under AFOSR Award No. FA9550-09-1-0451 (CMA) and by the Academy of Finland (HH). The computations were performed at Kansas State University and at CSC – the Finnish IT Center for Science in Espoo.

Chapter 10 - Conclusions

In summary, I showed that the absorption spectra of silver and gold clusters can be directly related to the plasmonic behavior of larger nanoparticles using time-dependent density functional theory. The frontier orbitals of silver and gold clusters are delocalized over the entire structure and result from a linear combination of the singly occupied *s* orbital of the atoms. They look like the familiar hydrogen-like orbitals for spherical clusters and are labeled 1S, 1P, 1D, … I showed that the splitting of these orbitals due to the ligand field can be qualitatively reproduced by a charge-perturbed particle-in-a-sphere model. For nanorods, the frontier orbitals have cylindrical symmetry and are labeled Σ, Π, Δ, … The strong absorption features of noble metal clusters can be assigned to a constructive addition of single-particle transitions between these delocalized orbitals. As the size of the particle increases, the density of states of these orbitals increases. Therefore, the number of interacting single-particle transitions increases, resulting in the strong plasmon peak observed in larger nanoparticles.

A simple CI treatment can reproduce the main absorption features (plasmons) of noble metal particles of various sizes. CI was previously used by Pariser to explain the absorption spectrum of linear polycyclic hydrocarbons and I showed that plasmons also occur in these systems.

The TDDFT absorption spectra of silver and gold nanorods with up to 71 atoms were compared. Two main plasmon modes occur in these systems: the longitudinal mode which corresponds to the constructive addition of the dipole moment contributions of $\Sigma\rightarrow\Sigma$, $\Pi\rightarrow\Pi$, $\Delta\rightarrow\Delta$, … single-particle transitions and a transverse mode, which corresponds to the constructive addition of the dipole moment contributions of $\Sigma\rightarrow\Pi$, $\Pi\rightarrow\Sigma$, $\Pi\rightarrow\Delta$, … single-particle transitions. Gold nanorods have a much broader absorption spectrum due to the numerous excitations out of the *d*-band. In addition, transitions out of the *d*-band orbitals and cylindrical delocalized orbitals may interact for systems with low aspect ratios since they have similar energies, making the longitudinal plasmon peak difficult to identify. As the aspect ratio increases, the energy gap between the cylindrical orbitals involved in the longitudinal mode decreases. Therefore, transitions within these orbitals become lower in energy than the excitations out of the *d*-band and the plasmon peak becomes well-defined.

I finally analyzed the effect of silver doping on the absorption spectrum of the $Au_{25}(SH)_{18}^{-}$ cluster. Doping at the core surface is energetically preferred. An increased silver content yields a blue-shift of the low energy HOMO-LUMO peak and an increased intensity of the high energy absorption peaks. With increasing silver content, the *d*-band excitations become higher in energy, which results in a larger contribution of intraband excitations to the absorption spectrum.

References

(1) Halas, N. J.; Lal, S.; Chang, W.-S.; Link, S.; Nordlander, P. *Chem. Rev.* **2011**, *111*, 3913.

(2) Chen, H.; Shao, L.; Li, Q.; Wang, J. *Chem. Soc. Rev.* **2013**.

(3) Zhou, X.; Liu, G.; Yu, J.; Fan, W. *J. Mater. Chem.* **2012**, *22*, 21337.

(4) Ozbay, E. *Science* **2006**, *311*, 189.

(5) Shinji, H.; Takayuki, O. *J. Phys. D: Appl. Phys.* **2012**, *45*, 433001.

(6) Jain, P.; Huang, X.; El-Sayed, I.; El-Sayed, M. *Plasmonics* **2007**, *2*, 107.

(7) Kauranen, M.; Zayats, A. V. *Nat Photon* **2012**, *6*, 737.

(8) Okamoto, H.; Imura, K. *J. Phys. Chem. Lett.* **2013**, *4*, 2230.

(9) Willets, K. A.; Van Duyne, R. P. *Annu. Rev. Phys. Chem.* **2007**, *58*, 267.

(10) Link, S.; El-Sayed, M. A. *Int. Rev. Phys. Chem.* **2000**, *19*, 409.

(11) Mark, D. T.; Md Muntasir, H.; Min, G. *New J. Phys.* **2010**, *12*, 083062.

(12) Rodríguez-Fernández, J.; Pérez-Juste, J.; García de Abajo, F. J.; Liz-Marzán, L. M. *Langmuir* **2006**, *22*, 7007.

(13) Chen, Y.-S.; Choi, H.; Kamat, P. V. *J. Am. Chem. Soc.* **2013**, *135*, 8822.

(14) Hirakawa, T.; Kamat, P. V. *Langmuir* **2004**, *20*, 5645.

(15) Jiang, S.; Win, K. Y.; Liu, S.; Teng, C. P.; Zheng, Y.; Han, M.-Y. *Nanoscale* **2013**, *5*, 3127.

(16) Mahmoud, M. A.; El-Sayed, M. A. *J. Phys. Chem. Lett.* **2013**, *4*, 1541.

(17) Saha, K.; Agasti, S. S.; Kim, C.; Li, X.; Rotello, V. M. *Chem. Rev.* **2012**, *112*, 2739.

(18) Abramczyk, H.; Brozek-Pluska, B. *Chem. Rev.* **2013**, *113*, 5766.

(19) Giannini, V.; Fernández-Domínguez, A. I.; Heck, S. C.; Maier, S. A. *Chem. Rev.* **2011**, *111*, 3888.

(20) Arvizo, R. R.; Bhattacharyya, S.; Kudgus, R. A.; Giri, K.; Bhattacharya, R.; Mukherjee, P. *Chem. Soc. Rev.* **2012**, *41*, 2943.

(21) Valley, N.; Greeneltch, N.; Van Duyne, R. P.; Schatz, G. C. *J. Phys. Chem. Lett.* **2013**, 2599.

(22) Chakraborty, I.; Bag, S.; Landman, U.; Pradeep, T. *J. Phys. Chem. Lett.* **2013**, *4*, 2769.

(23) Shimizu, T.; Teranishi, T.; Hasegawa, S.; Miyake, M. *J. Phys. Chem. B* **2003**, *107*, 2719.

(24) Link, S.; El-Sayed, M. *J. Phys. Chem. B* **1999**, *103*, 4212.

(25) Ringe, E.; Langille, M. R.; Sohn, K.; Zhang, J.; Huang, J.; Mirkin, C. A.; Van Duyne, R. P.; Marks, L. D. *J. Phys. Chem. Lett.* **2012**, *3*, 1479.

(26) Burda, C.; Chen, X.; Narayanan, R.; El-Sayed, M. A. *Chem. Rev.* **2005**, *105*, 1025.

(27) Fernanda Cardinal, M.; Rodríguez-González, B.; Alvarez-Puebla, R. n. A.; Pérez-Juste, J.; Liz-Marzán, L. M. *J. Phys. Chem. C* **2010**, *114*, 10417.

(28) Link, S.; Wang, Z. L.; El-Sayed, M. A. *J. Phys. Chem. B* **1999**, *103*, 3529.

(29) Link, S.; Mohamed, M. B.; El-Sayed, M. A. *J. Phys. Chem. B* **1999**, *103*, 3073.

(30) Kelly, K. L.; Coronado, E.; Zhao, L. L.; Schatz, G. C. *J. Phys. Chem. B* **2002**, *107*, 668.

(31) Pietrobon, B.; McEachran, M.; Kitaev, V. *ACS Nano* **2008**, *3*, 21.

(32) Duan, J.; Park, K.; MacCuspie, R. I.; Vaia, R. A.; Pachter, R. *J. Phys. Chem. C* **2009**, *113*, 15524.

(33) Eustis, S.; El-Sayed, M. A. *Chem. Soc. Rev.* **2006**, *35*, 209.

(34) Huang, X.; El-Sayed, I. H.; Qian, W.; El-Sayed, M. A. *J. Am. Chem. Soc.* **2006**, *128*, 2115.

(35) Chen, R.; Zheng, X.; Qian, H.; Wang, X.; Wang, J.; Jiang, X. *Biomat. Sci.* **2013**, *1*, 285.

(36) Huang, X.; Neretina, S.; El-Sayed, M. A. *Adv. Mater.* **2009**, *21*, 4880.

(37) Brioude, A.; Pileni, M. P. *J. Phys. Chem. B* **2005**, *109*, 23371.

(38) Oubre, C.; Nordlander, P. *J. Phys. Chem. B* **2004**, *108*, 17740.

(39) Kreibig, U.; Vollmer, M. *Optical properties of metal clusters*; Springer, 1995.

(40) Jain, P. K.; Eustis, S.; El-Sayed, M. A. *J. Phys. Chem. B* **2006**, *110*, 18243.

(41) Mie, G. *Ann. Phys.* **1908**, *25*, 377.

(42) Alvarez, M. M.; Khoury, J. T.; Schaaff, T. G.; Shafigullin, M. N.; Vezmar, I.; Whetten, R. L. *J. Phys. Chem. B* **1997**, *101*, 3706.

(43) Gans, R. *Ann. Phys.* **1915**, *47*, 270.

(44) Bohren, C. F.; Huffman, D. R. *Absorption and scattering of light by small particles*; John Wiley & Sons, 2008.

(45) Jain, P. K.; Lee, K. S.; El-Sayed, I. H.; El-Sayed, M. A. *J. Phys. Chem. B* **2006**, *110*, 7238.

(46) Coronado, E. A.; Schatz, G. C. *J. Chem. Phys.* **2003**, *119*, 3926.

(47) Selby, K.; Vollmer, M.; Masui, J.; Kresin, V.; de Heer, W. A.; Knight, W. D. *Phys. Rev. B* **1989**, *40*, 5417.

(48) Selby, K.; Kresin, V.; Masui, J.; Vollmer, M.; de Heer, W. A.; Scheidemann, A.; Knight, W. D. *Phys. Rev. B* **1991**, *43*, 4565.

(49) Harbich, W.; Fedrigo, S.; Buttet, J. *Chem. Phys. Lett.* **1992**, *195*, 613.

(50) Harb, M.; Rabilloud, F.; Simon, D.; Rydlo, A.; Lecoultre, S.; Conus, F.; Rodrigues, V.; Félix, C. *J. Chem. Phys.* **2008**, *129*.

(51) Tiggesbäumker, J.; Köller, L.; Meiwes-Broer, K.-H.; Liebsch, A. *Phys. Rev. A* **1993**, *48*, R1749.

(52) Fedrigo, S.; Harbich, W.; Buttet, J. *Phys. Rev. B* **1993**, *47*, 10706.

(53) Kresin, V. V. *Phys. Rev. B* **1995**, *51*, 1844.

(54) Gedney, S. *Introduction to the Finite-Difference Time-Domain (FDTD) Method for Electromagnetics*; Morgan & Claypool Publishers, 2011.

(55) Draine, B. T.; Flatau, P. J. *Journal of the Optical Society of America A* **1994**, *11*, 1491.

(56) Wu, Y.; Nordlander, P. *J. Phys. Chem. C* **2009**, *114*, 7302.

(57) Duval Malinsky, M.; Kelly, K. L.; Schatz, G. C.; Van Duyne, R. P. *J. Phys. Chem. B* **2001**, *105*, 2343.

(58) Hou, X.; Zhang, X.; Chen, S.; Fang, Y.; Li, N.; Zhai, X.; Liu, Y. *Colloids Surf., A* **2011**, *384*, 345.

(59) Mullin, J.; Valley, N.; Blaber, M. G.; Schatz, G. C. *J. Phys. Chem. A* **2012**, *116*, 9574.

(60) Baishya, K.; Idrobo, J. C.; Öğüt, S.; Yang, M.; Jackson, K.; Jellinek, J. *Phys. Rev. B* **2008**, *78*, 075439.

(61) Charlé, K. P.; Schulze, W.; Winter, B. *Z Phys D - Atoms, Molecules and Clusters* **1989**, *12*, 471.

(62) Beck, D. E. *Phys. Rev. B* **1987**, *35*, 7325.

(63) Ekardt, W.; Penzar, Z. *Solid State Commun.* **1986**, *57*, 661.

(64) Aikens, C. M.; Li, S.; Schatz, G. C. *J. Phys. Chem. C* **2008**, *112*, 11272.

(65) Burgess, R. W.; Keast, V. J. *J. Phys. Chem. C* **2011**, *115*, 21016.

(66) Liao, M.-S.; Bonifassi, P.; Leszczynski, J.; Ray, P. C.; Huang, M.-J.; Watts, J. D. *J. Phys. Chem. A* **2010**, *114*, 12701.

(67) Malola, S.; Lehtovaara, L.; Enkovaara, J.; Häkkinen, H. *ACS Nano* **2013**, *7*, 10263.

(68) Morton, S. M.; Silverstein, D. W.; Jensen, L. *Chem. Rev.* **2011**, *111*, 3962.

(69) Piccini, G.; Havenith, R. W. A.; Broer, R.; Stener, M. *J. Phys. Chem. C* **2013**, *117*, 17196.

(70) Johnson, H. E.; Aikens, C. M. *J. Phys. Chem. A* **2009**, *113*, 4445.

(71) Bae, G.-T.; Aikens, C. M. *J. Phys. Chem. C* **2012**, *116*, 10356.

(72) Durante, N.; Fortunelli, A.; Broyer, M.; Stener, M. *J. Phys. Chem. C* **2011**, *115*, 6277.

(73) Zhu, M.; Aikens, C. M.; Hollander, F. J.; Schatz, G. C.; Jin, R. *J. Am. Chem. Soc.* **2008**, *130*, 5883.

(74) Qian, H.; Eckenhoff, W. T.; Zhu, Y.; Pintauer, T.; Jin, R. *J. Am. Chem. Soc.* **2010**, *132*, 8280.

(75) Nimmala, P. R.; Yoon, B.; Whetten, R. L.; Landman, U.; Dass, A. *J. Phys. Chem. A* **2013**, *117*, 504.

(76) Jadzinsky, P. D.; Calero, G.; Ackerson, C. J.; Bushnell, D. A.; Kornberg, R. D. *Science* **2007**, *318*, 430.

(77) Negishi, Y.; Sakamoto, C.; Ohyama, T.; Tsukuda, T. *J. Phys. Chem. Lett.* **2012**, *3*, 1624.

(78) Aikens, C. M. *J. Phys. Chem. A* **2009**, *113*, 10811.

(79) Häkkinen, H.; Walter, M.; Grönbeck, H. *J. Phys. Chem. B* **2006**, *110*, 9927.

(80) Walter, M.; Akola, J.; Lopez-Acevedo, O.; Jadzinsky, P. D.; Calero, G.; Ackerson, C. J.; Whetten, R. L.; Grönbeck, H.; Häkkinen, H. *Proc. Natl. Acad. Sci.* **2008**, *105*, 9157.

(81) Provorse, M. R.; Aikens, C. M. *J. Am. Chem. Soc.* **2010**, *132*, 1302.

(82) Aikens, C. M. *J. Phys. Chem. Lett.* **2010**, *1*, 2594.

(83) Aikens, C. M. *J. Phys. Chem. C* **2008**, *112*, 19797.

(84) Aikens, C. M. *J. Phys. Chem. Lett.* **2010**, *2*, 99.

(85) Link, S.; El-Sayed, M. A. *J. Phys. Chem. B* **1999**, *103*, 8410.

(86) Yurkin, M. A.; Hoekstra, A. G. *J. Quant. Spectrosc. Radiat. Transfer* **2007**, *106*, 558.

(87) Taflove, A. *Computational Electrodynamics: The Finite - Difference Time - Domain Method*; Artech House, Incorporated, 1995.

(88) Chen, H.; McMahon, J. M.; Ratner, M. A.; Schatz, G. C. *J. Phys. Chem. C* **2010**, *114*, 14384.

(89) Aikens, C. M.; Schatz, G. C. *J. Phys. Chem. A* **2006**, *110*, 13317.

(90) Li, W.-K.; Blinder, S. M. *J. Chem. Educ.* **2010**, *88*, 71.

(91) Pyykkö, P. *Chem. Rev.* **1988**, *88*, 563.

(92) Grant, I. P. *Relativistic Quantum Theory of Atoms and Molecules: Theory and Computation (Springer Series on Atomic, Optical, and Plasma Physics)*; Springer-Verlag New York, Inc., 2006.

(93) Pyykkö, P. *Chem. Rev.* **2011**, *112*, 371.

(94) Autschbach, J. *J. Chem. Phys.* **2012**, *136*.

(95) Levine, I. N. *Quantum chemistry. 5. th*; New York, Prentice Hall, 1991.

(96) Parr, R. G.; Yang, W. *Density-functional theory of atoms and molecules*; Oxford university press, 1989; Vol. 16.

(97) Koch, W.; Holthausen, M. C. *A chemist's guide to density functional theory*; Wiley-Vch Weinheim, 2001; Vol. 2.

(98) Parr, R. G. *Annu. Rev. Phys. Chem.* **1983**, *34*, 631.

(99) Hohenberg, P.; Kohn, W. *Phys. Rev.* **1964**, *136*, B864.

(100) Kohn, W.; Sham, L. J. *Phys. Rev.* **1965**, *140*, A1133.

(101) Vosko, S. H.; Wilk, L.; Nusair, M. *Can. J. Phys.* **1980**, *58*, 1200.

(102) Becke, A. D. *Phys. Rev. A* **1988**, *38*, 3098.

(103) Perdew, J. P. *Phys. Rev. B* **1986**, *33*, 8822.

(104) Perdew, J. P.; Wang, Y. *Phys. Rev. B* **1992**, *45*, 13244.

(105) Perdew, J. P.; Burke, K.; Ernzerhof, M. *Phys. Rev. Lett.* **1996**, *77*, 3865.

(106) Tao, J.; Perdew, J. P.; Staroverov, V. N.; Scuseria, G. E. *Phys. Rev. Lett.* **2003**, *91*, 146401.

(107) Zhao, Y.; Truhlar, D. G. *J. Chem. Phys.* **2006**, *125*.

(108) Lee, C.; Yang, W.; Parr, R. G. *Phys. Rev. B* **1988**, *37*, 785.

(109) Adamo, C.; Barone, V. *J. Chem. Phys.* **1999**, *110*, 6158.

(110) te Velde, G.; Bickelhaupt, F. M.; Baerends, E. J.; Fonseca Guerra, C.; van Gisbergen, S. J. A.; Snijders, J. G.; Ziegler, T. *J. Comput. Chem.* **2001**, *22*, 931.

(111) Szabo, A.; Ostlund, N. S. *Modern Quantum Chemistry: Introduction to Advanced Electronic Structure Theory*; Dover Publications, 1996.

(112) Dirac, P. A. M. *Proc. R. Soc. London, Ser. A* **1928**, *117*, 610.

(113) Dirac, P. A. M. *Proc. R. Soc. London, Ser. A* **1930**, *126*, 360.

(114) van Lenthe, E.; Baerends, E. J.; Snijders, J. G. *J. Chem. Phys.* **1993**, *99*, 4597.

(115) van Lenthe, E.; Baerends, E. J.; Snijders, J. G. *J. Chem. Phys.* **1994**, *101*, 9783.

(116) van Lenthe, E.; Ehlers, A.; Baerends, E.-J. *J. Chem. Phys.* **1999**, *110*, 8943.

(117) Ullrich, C. A. *Time-Dependent Density-Functional Theory: Concepts and Applications*; OUP Oxford, 2012.

(118) Dreuw, A.; Head-Gordon, M. *Chem. Rev.* **2005**, *105*, 4009.

(119) Marques, M. A. L.; Gross, E. K. U. *Annu. Rev. Phys. Chem.* **2004**, *55*, 427.

(120) Chong, D. P. *Recent advances in density functional methods*; World Scientific, 1995; Vol. 1.

(121) van Gisbergen, S. J. A.; Snijders, J. G.; Baerends, E. J. *Comput. Phys. Commun.* **1999**, *118*, 119.

(122) Tagar, Z. A.; Sirajuddin; Memon, N.; Agheem, M. H.; Junejo, Y.; Hassan, S. S.; Kalwar, N. H.; Khattak, M. I. *Sens. Actuators, B* **2011**, *157*, 430.

(123) Judita, P.; Jurgita, L.; Diana, A.; Prosyčeva, I. *Radiat. Prot. Dosim.* **2010**, *139*, 353.

(124) Sun, Y. *J. Phys. Chem. C* **2010**, *114*, 2127.

(125) Temple, T. L.; Bagnall, D. M. *J. Appl. Phys.* **2011**, *109*, 084343.

(126) Zhang, J. Z. *J. Phys. Chem. Lett.* **2010**, *1*, 686.

(127) Parab, H. J.; Chen, H. M.; Lai, T.-C.; Huang, J. H.; Chen, P. H.*et al. J. Phys. Chem. C* **2009**, *113*, 7574.

(128) González, A. L.; Noguez, C.; Ortiz, G. P.; Rodríguez-Gattorno, G. *J. Phys. Chem. B* **2005**, *109*, 17512.

(129) Wiley, B. J.; Im, S. H.; Li, Z.-Y.; McLellan, J.; Siekkinen, A.; Xia, Y. *J. Phys. Chem. B* **2006**, *110*, 15666.

(130) Jin, R.; Cao, Y.; Mirkin, C. A.; Kelly, K. L.; Schatz, G. C.; Zheng, J. G. *Science* **2001**, *294*, 1901.

(131) Schmucker, A. L.; Harris, N.; Banholzer, M. J.; Blaber, M. G.; Osberg, K. D.; Schatz, G. C.; Mirkin, C. A. *ACS Nano* **2010**, *4*, 5453.

(132) Jain, P. K.; El-Sayed, M. A. *Chem. Phys. Lett.* **2010**, *487*, 153.

(133) Khan, S. A.; Senapati, D.; Senapati, T.; Bonifassi, P.; Fan, Z.; Singh, A. K.; Neeley, A.; Hill, G.; Ray, P. C. *Chem. Phys. Lett.* **2011**, *512*, 92.

(134) Koponen, L.; Tunturivuori, L. O.; Puska, M. J.; Hancock, Y. *J Chem Phys* **2010**, *132*, 214301.

(135) Szymańska-Chargot, M.; Gruszecka, A.; Smolira, A.; Bederski, K.; Gluch, K.; Cytawa, J.; Michalak, L. *J. Alloys Compd.* **2009**, *486*, 66.

(136) Sánchez-Iglesias, A.; Pastoriza-Santos, I.; Pérez-Juste, J.; Rodríguez-González, B.; Garcia de Abajo, F. J.; Liz-Marzán, L. M. *Adv. Mater.* **2006**, *18*, 2529.

(137) Seo, D.; Yoo, C. I.; Chung, I. S.; Park, S. M.; Ryu, S.; Song, H. *J. Phys. Chem. C* **2008**, *112*, 2469.

(138) Kasture, M.; Sastry, M.; Prasad, B. L. V. *Chem. Phys. Lett.* **2010**, *484*, 271.

(139) El-Sayed, A. M.; Al-Sherbini *Mater. Chem. Phys.* **2010**, *121*, 349.

(140) Ni, W.; Ambjörnsson, T.; Apell, S. P.; Chen, H.; Wang, J. *Nano Lett.* **2009**, *10*, 77.

(141) Yan, J.; Gao, S. *Phys. Rev. B* **2008**, *78*, 235413.

(142) Yan, J.; Yuan, Z.; Gao, S. *Phys. Rev. Lett.* **2007**, *98*, 216602.

(143) Kim, H.; Xiang, C.; Guell, A. G.; Penner, R. M.; Potma, E. O. *J. Phys. Chem. C* **2008**, *112*, 12721.

(144) Lian, K.-Y.; Salek, P.; Jin, M.; Ding, D. *J. Chem. Phys.* **2009**, *130*, 174701.

(145) Schipper, P. R. T.; Gritsenko, O. V.; van Gisbergen, S. J. A.; Baerends, E. J. *J. Chem. Phys.* **2000**, *112*, 1344.

(146) van Leeuwen, R.; Baerends, E. J. *Phys. Rev. A* **1994**, *49*, 2421.

(147) Hu, L.; Kim, H. S.; Lee, J.-Y.; Peumans, P.; Cui, Y. *ACS Nano* **2010**, *4*, 2955.

(148) Gao, C.; Zhang, Q.; Lu, Z.; Yin, Y. *J. Am. Chem. Soc.* **2011**, *133*, 19706.

(149) Koenigsmann, C.; Scofield, M. E.; Liu, H.; Wong, S. S. *J. Phys. Chem. Lett.* **2012**, *3*, 3385.

(150) Novo, C.; Funston, A. M.; Mulvaney, P. *Nat Nano* **2008**, *3*, 598.

(151) Chuntonov, L.; Bar-Sadan, M.; Houben, L.; Haran, G. *Nano Lett.* **2011**, *12*, 145.

(152) Grubisic, A.; Schweikhard, V.; Baker, T. A.; Nesbitt, D. J. *ACS Nano* **2012**, *7*, 87.

(153) Kim, S.; Imura, K.; Lee, M.; Narushima, T.; Okamoto, H.; Jeong, D. H. *Phys. Chem. Chem. Phys.* **2013**, *15*, 4146.

(154) Loumaigne, M.; Vasanthakumar, P.; Richard, A.; Débarre, A. *ACS Nano* **2012**, *6*, 10512.

(155) Nappa, J.; Revillod, G.; Abid, J.-P.; Russier-Antoine, I.; Jonin, C.; Benichou, E.; Girault, H. H.; Brevet, P. F. *Faraday Discuss.* **2004**, *125*, 145.

(156) Zheng, J.; Zhou, C.; Yu, M.; Liu, J. *Nanoscale* **2012**, *4*, 4073.

(157) Hutter, E.; Fendler, J. H. *Adv. Mater.* **2004**, *16*, 1685.

(158) Dreaden, E. C.; Alkilany, A. M.; Huang, X.; Murphy, C. J.; El-Sayed, M. A. *Chem. Soc. Rev.* **2012**, *41*, 2740.

(159) Gagner, J. E.; Shrivastava, S.; Qian, X.; Dordick, J. S.; Siegel, R. W. *J. Phys. Chem. Lett.* **2012**, *3*, 3149.

(160) Nose, K.; Pissuwan, D.; Goto, M.; Katayama, Y.; Niidome, T. *Nanoscale* **2012**, *4*, 3776.

(161) Ho, F. H.; Wu, Y.-H.; Ujihara, M.; Imae, T. *Analyst* **2012**, *137*, 2545.

(162) Lu, G.; Hou, L.; Zhang, T.; Liu, J.; Shen, H.; Luo, C.; Gong, Q. *J. Phys. Chem. C* **2012**, *116*, 25509.

(163) Zhu, Y.; Xu, L.; Ma, W.; Xu, Z.; Kuang, H.; Wang, L.; Xu, C. *Chem. Commun.* **2012**, *48*, 11889.

(164) Joshi, G. K.; McClory, P. J.; Muhoberac, B. B.; Kumbhar, A.; Smith, K. A.; Sardar, R. *J. Phys. Chem. C* **2012**, *116*, 20990.

(165) Lee, K.-S.; El-Sayed, M. A. *J. Phys. Chem. B* **2006**, *110*, 19220.

(166) Li, C.-Z.; Male, K. B.; Hrapovic, S.; Luong, J. H. T. *Chem. Commun.* **2005**, 3924.

(167) Tian, L.; Chen, E.; Gandra, N.; Abbas, A.; Singamaneni, S. *Langmuir* **2012**, *28*, 17435.

(168) Chikkaveeraiah, B. V.; Bhirde, A. A.; Morgan, N. Y.; Eden, H. S.; Chen, X. *ACS Nano* **2012**, *6*, 6546.

(169) Jokerst, J. V.; Cole, A. J.; Van de Sompel, D.; Gambhir, S. S. *ACS Nano* **2012**, *6*, 10366.

(170) Zhou, W.; Liu, X.; Ji, J. *J. Mater. Chem.* **2012**, *22*, 13969.

(171) Wang, J.; Dong, B.; Chen, B.; Jiang, Z.; Song, H. *Dalton Trans.* **2012**, *41*, 11134.

(172) Lusic, H.; Grinstaff, M. W. *Chem. Rev.* **2013**, *113*, 1641.

(173) Lim, J. K.; Imura, K.; Nagahara, T.; Kim, S. K.; Okamoto, H. *Chem. Phys. Lett.* **2005**, *412*, 41.

(174) Khlebtsov, B. N.; Khlebtsov, N. G. *J. Phys. Chem. C* **2007**, *111*, 11516.

(175) Gulati, A.; Liao, H.; Hafner, J. H. *J. Phys. Chem. B* **2006**, *110*, 22323.

(176) Sherry, L. J.; Jin, R.; Mirkin, C. A.; Schatz, G. C.; Van Duyne, R. P. *Nano Lett.* **2006**, *6*, 2060.

(177) Brewer, K. E.; Aikens, C. M. *J. Phys. Chem. A* **2010**, *114*, 8858.

(178) Li, Z.; Zhu, Z.; Liu, W.; Zhou, Y.; Han, B.; Gao, Y.; Tang, Z. *J. Am. Chem. Soc.* **2012**, *134*, 3322.

(179) Szunerits, S.; Boukherroub, R. *Chem. Commun.* **2012**, *48*, 8999.

(180) Guidez, E. B.; Mäkinen, V.; Häkkinen, H.; Aikens, C. M. *J. Phys. Chem. C* **2012**, *116*, 20617.

(181) Negishi, Y.; Iwai, T.; Ide, M. *Chem. Commun.* **2010**, *46*, 4713.

(182) Olson, T. Y.; Schwartzberg, A. M.; Orme, C. A.; Talley, C. E.; O'Connell, B.; Zhang, J. Z. *J. Phys. Chem. C* **2008**, *112*, 6319.

(183) Ma, Y.; Qu, Y. *Nanoscale* **2012**, *4*, 3036.

(184) He, J.; Zhang, P.; Babu, T.; Liu, Y.; Gong, J.; Nie, Z. *Chem. Commun.* **2013**, *49*, 576.

(185) Kundu, S. *J. Mater. Chem. C* **2013**, *1*, 831.

(186) Ni, C.; Hassan, P. A.; Kaler, E. W. *Langmuir* **2005**, *21*, 3334.

(187) Jana, N. R.; Gearheart, L.; Murphy, C. J. *Chem. Commun.* **2001**, 617.

(188) Zhu, C.; Peng, H.-C.; Zeng, J.; Liu, J.; Gu, Z.; Xia, Y. *J. Am. Chem. Soc.* **2012**, *134*, 20234.

(189) Pietrobon, B.; McEachran, M.; Kitaev, V. *ACS Nano* **2009**, *3*, 21.

(190) Navarro, J. R. G.; Werts, M. H. V. *Analyst* **2013**, *138*, 583.

(191) N'Gom, M.; Ringnalda, J.; Mansfield, J. F.; Agarwal, A.; Kotov, N.; Zaluzec, N. J.; Norris, T. B. *Nano Lett.* **2008**, *8*, 3200.

(192) Becker, J.; Zins, I.; Jakab, A.; Khalavka, Y.; Schubert, O.; Sönnichsen, C. *Nano Lett.* **2008**, *8*, 1719.

(193) Abidi, W.; Selvakannan, P. R.; Guillet, Y.; Lampre, I.; Beaunier, P.; Pansu, B.; Palpant, B.; Remita, H. *J. Phys. Chem. C* **2010**, *114*, 14794.

(194) Guiton, B. S.; Iberi, V.; Li, S.; Leonard, D. N.; Parish, C. M.*et al. Nano Lett.* **2011**, *11*, 3482.

(195) Guidez, E. B.; Aikens, C. M. *Nanoscale* **2012**, *4*, 4190.

(196) Dhoni, M. S.; Ji, W. *J. Phys. Chem. C* **2011**, *115*, 20359.

(197) Liao, M.-S.; Bonifassi, P.; Leszczynski, J.; Ray, P. C.; Huang, M.-J.; Watts, J. D. *J. Phys. Chem. A* **2010**, *114*, 12701.

(198) Johnson, H. E.; Aikens, C. M. *J. Phys. Chem. A* **2009**, *113*, 4445.

(199) Guidez, E. B.; Aikens, C. M. *Phys. Chem. Chem. Phys.* **2012**, *14*, 4287.

(200) Ivanov, S. A.; Arachchige, I.; Aikens, C. M. *J. Phys. Chem. A* **2011**, *115*, 8017.

(201) Provorse, M. R.; Aikens, C. M. *J. Am. Chem. Soc.* **2010**, *132*, 1302.

(202) Chakraborty, I.; Govindarajan, A.; Erusappan, J.; Ghosh, A.; Pradeep, T.; Yoon, B.; Whetten, R. L.; Landman, U. *Nano Lett.* **2012**, *12*, 5861.

(203) Pyykkö, P.; Desclaux, J. P. *Acc. Chem. Res.* **1979**, *12*, 276.

(204) Desclaux, J. P.; Pyykkö, P. *Chem. Phys. Lett.* **1976**, *39*, 300.

(205) Pyykkö, P. *Angew. Chem. Int. Ed.* **2004**, *43*, 4412.

(206) Guidez, E. B.; Aikens, C. M. *Nanoscale* **2012**, *4*, 4190.

(207) Johnson, C. J.; Dujardin, E.; Davis, S. A.; Murphy, C. J.; Mann, S. *J. Mater. Chem.* **2002**, *12*, 1765.

(208) Lopez-Acevedo, O.; Tsunoyama, H.; Tsukuda, T.; Häkkinen, H.; Aikens, C. M. *J. Am. Chem. Soc.* **2010**, *132*, 8210.

(209) Bae, G.-T.; Aikens, C. M. *J. Phys. Chem. A* **2012**, *116*, 8260.

(210) Liu, X.-J.; Hamilton, I.; Krawczyk, R. P.; Schwerdtfeger, P. *J. Comput. Chem.* **2012**, *33*, 311.

(211) Clar, E. *Polycyclic hydrocarbons*; Academic Press: London, **1964**; Vol. 1,2.

(212) Ramdahl, T. *Handbook of polycyclic aromatic hydrocarbons*; CRC Press **1985**; Vol. 2.

(213) Schön, J. H.; Kloc, C.; Bucher, E.; Batlogg, B. *Nature* **2000**, *403*, 408.

(214) Schön, J. H.; Berg, S.; Kloc, C.; Batlogg, B. *Science* **2000**, *287*, 1022.

(215) Wang, C.; Dong, H.; Hu, W.; Liu, Y.; Zhu, D. *Chem. Rev.* **2011**, *112*, 2208.

(216) Kippelen, B.; Bredas, J.-L. *Energy Environ. Sci.* **2009**, *2*, 251.

(217) Bendikov, M.; Wudl, F.; Perepichka, D. F. *Chem. Rev.* **2004**, *104*, 4891.

(218) Anthony, J. E. *Chem. Rev.* **2006**, *106*, 5028.

(219) Zade, S. S.; Bendikov, M. *Angew. Chem. Int. Ed.* **2010**, *49*, 4012.

(220) Reddy, A. R.; Bendikov, M. *Chem. Commun.* **2006**, *0*, 1179.

(221) Mondal, R.; Tönshoff, C.; Khon, D.; Neckers, D. C.; Bettinger, H. F. *J. Am. Chem. Soc.* **2009**, *131*, 14281.

(222) Tönshoff, C.; Bettinger, H. F. *Angew. Chem. Int. Ed.* **2010**, *49*, 4125.

(223) Cioslowski, J. *J. Chem. Phys.* **1993**, *98*, 473.

(224) Qu, Z.; Zhang, D.; Liu, C.; Jiang, Y. *J. Phys. Chem. A* **2009**, *113*, 7909.

(225) Hajgato, B.; Szieberth, D.; Geerlings, P.; De Proft, F.; Deleuze, M. S. *J. Chem. Phys.* **2009**, *131*, 224321.

(226) Coulson, C. A. *Proc. Phys. Soc.* **1948**, *60*, 257.

(227) Dierksen, M.; Grimme, S. *J. Phys. Chem. A* **2004**, *108*, 10225.

(228) Grimme, S.; Parac, M. *ChemPhysChem* **2003**, *4*, 292.

(229) Houk, K. N.; Lee, P. S.; Nendel, M. *J. Org. Chem.* **2001**, *66*, 5517.

(230) Bendikov, M.; Duong, H. M.; Starkey, K.; Houk, K. N.; Carter, E. A.; Wudl, F. *J. Am. Chem. Soc.* **2004**, *126*, 7416.

(231) Hachmann, J.; Dorando, J. J.; Aviles, M.; Chan, G. K.-L. *J. Chem. Phys.* **2007**, *127*, 134309.

(232) Karcher, W.; Fordham, R.; Dubois, J.; Glaude, P.; Ligthart, J. *Spectral atlas of polycyclic aromatic compounds*, 1985.

(233) Sony, P.; Shukla, A. *Phys. Rev. B* **2007**, *75*, 155208.

(234) Platt, J. R. *J. Chem. Phys.* **1949**, *17*, 484.

(235) Biermann, D.; Schmidt, W. *J. Am. Chem. Soc.* **1980**, *102*, 3163.

(236) Ham, N. S.; Ruedenberg, K. *J. Chem. Phys.* **1956**, *25*, 13.

(237) Pariser, R. *J. Chem. Phys.* **1956**, *24*, 250.

(238) Wong, B. M.; Hsieh, T. H. *J. Chem. Theory Comput.* **2010**, *6*, 3704.

(239) Richard, R. M.; Herbert, J. M. *J. Chem. Theory Comput.* **2011**, *7*, 1296.

(240) Krykunov, M.; Grimme, S.; Ziegler, T. *J. Chem. Theory Comput.* **2012**, *8*, 4434.

(241) Fei, Z.; Andreev, G. O.; Bao, W.; Zhang, L. M.; S. McLeod, A.*et al. Nano Lett.* **2011**, *11*, 4701.

(242) Hartmann, N.; Piredda, G.; Berthelot, J.; Colas des Francs, G.; Bouhelier, A.; Hartschuh, A. *Nano Lett.* **2011**, *12*, 177.

(243) Chen, J.; Badioli, M.; Alonso-Gonzalez, P.; Thongrattanasiri, S.; Huth, F.*et al. Nature* **2012**, *487*, 77.

(244) Ju, L.; Geng, B.; Horng, J.; Girit, C.; Martin, M.*et al. Nat Nano* **2011**, *6*, 630.

(245) Manjavacas, A.; Nordlander, P.; García de Abajo, F. J. *ACS Nano* **2012**, *6*, 1724.

(246) Manjavacas, A.; Marchesin, F.; Thongrattanasiri, S.; Koval, P.; Nordlander, P.; Sánchez-Portal, D.; García de Abajo, F. J. *ACS Nano* **2013**, *7*, 3635.

(247) Balzarotti, F.; Stefani, F. D. *ACS Nano* **2012**, *6*, 4580.

(248) Chang, S.; Li, Q.; Xiao, X.; Wong, K. Y.; Chen, T. *Energy Environ. Sci.* **2012**, *5*, 9444.

(249) Parac, M.; Grimme, S. *Chem. Phys.* **2003**, *292*, 11.

(250) Goerigk, L.; Grimme, S. *J. Chem. Theory Comput.* **2011**, *7*, 3272.

(251) Shao, Y.; Molnar, L. F.; Jung, Y.; Kussmann, J.; Ochsenfeld, C.*et al. Phys. Chem. Chem. Phys.* **2006**, *8*, 3172.

(252) Rohrdanz, M. A.; Martins, K. M.; Herbert, J. M. *J. Chem. Phys.* **2009**, *130*, 054112.

(253) Yanai, T.; Tew, D. P.; Handy, N. C. *Chem. Phys. Lett.* **2004**, *393*, 51.

(254) Wong, B. M.; Cordaro, J. G. *J. Chem. Phys.* **2008**, *129*, 214703.

(255) Dunning, J. T. H. *J. Chem. Phys.* **1989**, *90,* 1007.

(256) Martin, R. L. *J. Chem. Phys.* **2003**, *118,* 4775.

(257) Bode, B. M.; Gordon, M. S. *J. Mol. Graphics Modell.* **1998**, *16*, 133.

(258) Humphrey, W.; Dalke, A.; Schulten, K. *J. Mol. Graph.* **1996**, *14,* 33.

(259) Bernadotte, S.; Evers, F.; Jacob, C. R. *J. Phys. Chem. C* **2013**, *117,* 1863.

(260) de Heer, W. A. *Rev. Mod. Phys.* **1993**, *65,* 611.

(261) de Heer, W. A.; Selby, K.; Kresin, V.; Masui, J.; Vollmer, M.; Chatelain, A.; Knight, W. D. *Phys. Rev. Lett.* **1987**, *59*, 1805.

(262) Duthler, C. J.; Johnson, S. E.; Broida, H. P. *Phys. Rev. Lett.* **1971**, *26*, 1236.

(263) Mann, D. M.; Broida, H. P. *J. Appl. Phys.* **1973**, *44*, 4950.

(264) Herrmann, A.; Hofmann, M.; Leutwyler, S.; Schumacher, E.; Wöste, L. *Chem. Phys. Lett.* **1979**, *62*, 216.

(265) Nordlander, P.; Oubre, C.; Prodan, E.; Li, K.; Stockman, M. I. *Nano Lett.* **2004**, *4*, 899.

(266) Nordlander, P.; Prodan, E. *Nano Lett.* **2004**, *4*, 2209.

(267) Tame, M. S.; McEnery, K. R.; Ozdemir, S. K.; Lee, J.; Maier, S. A.; Kim, M. S. *Nat Phys* **2013**, *9,* 329.

(268) Qin, H. L.; Wang, D.; Huang, Z. L.; Wu, D. M.; Zeng, Z. C.; Ren, B.; Xu, K.; Jin, J. *J. Am. Chem. Soc.* **2013**, *135,* 12544.

(269) Ringe, E.; Sharma, B.; Henry, A.-I.; Marks, L. D.; Van Duyne, R. P. *Phys. Chem. Chem. Phys.* **2013**, *15*, 4110.

(270) Zhao, Y.; Xu, L.; Liz-Marzán, L. M.; Kuang, H.; Ma, W.*et al. J. Phys. Chem. Lett.* **2013**, *4,* 641.

(271) Jain, P. K.; Huang, X.; El-Sayed, I. H.; El-Sayed, M. A. *Acc. Chem. Res.* **2008**, *41*, 1578.

(272) Hsiao, Y.-S.; Charan, S.; Wu, F.-Y.; Chien, F.-C.; Chu, C.-W.; Chen, P.; Chen, F.-C. *J. Phys. Chem. C* **2012**, *116*, 20731.

(273) Guidez, E. B.; Aikens, C. M. *J. Phys. Chem. C* **2013**, *117*, 21466.

(274) Christensen, J.; Manjavacas, A.; Thongrattanasiri, S.; Koppens, F. H. L.; García de Abajo, F. J. *ACS Nano* **2011**, *6*, 431.

(275) Grigorenko, A. N.; Polini, M.; Novoselov, K. S. *Nat Photon* **2012**, *6*, 749.

(276) Wu, D.; Yan, K.; Zhou, Y.; Wang, H.; Lin, L.; Peng, H.; Liu, Z. *J. Am. Chem. Soc.* **2013**.

(277) Guidez, E. B.; Aikens, C. M. *J. Phys. Chem. C* **2013**, *117*, 12325.

(278) Bini, D.; Benedetto, F. *CALCOLO* **1996**, *33*, 1.

(279) Charutz, D. M.; Ron, S.; Eisenberg, E.; Baer, M. *Chem. Phys. Lett.* **1995**, *244*, 299.

(280) Gilibert, M.; Baram, A.; Last, I.; Szichman, H.; Baer, M. *J. Chem. Phys.* **1993**, *99*, 3503.

(281) Albert, V. V.; Badaeva, E.; Kilina, S.; Sykora, M.; Tretiak, S. *J. Lumin.* **2011**, *131*, 1739.

(282) Guidez, E. B.; Aikens, C. M. *Phys. Chem. Chem. Phys.* **2012**, *14*, 4287.

(283) Abad, J. M.; Sendroiu, I. E.; Gass, M.; Bleloch, A.; Mills, A. J.; Schiffrin, D. J. *J. Am. Chem. Soc.* **2007**, *129*, 12932.

(284) Balasubramanian, R.; Guo, R.; Mills, A. J.; Murray, R. W. *J. Am. Chem. Soc.* **2005**, *127*, 8126.

(285) Wu, Z.; Suhan, J.; Jin, R. *J. Mater. Chem.* **2009**, *19*, 622.

(286) Dass, A.; Guo, R.; Tracy, J. B.; Balasubramanian, R.; Douglas, A. D.; Murray, R. W. *Langmuir* **2007**, *24*, 310.

(287) Cheng, P. P. H.; Silvester, D.; Wang, G.; Kalyuzhny, G.; Douglas, A.; Murray, R. W. *J. Phys. Chem. B* **2006**, *110*, 4637.

(288) Sardar, R.; Shumaker-Parry, J. S. *J. Am. Chem. Soc.* **2011**, *133*, 8179.

(289) Varnavski, O.; Ramakrishna, G.; Kim, J.; Lee, D.; Goodson, T. *J. Am. Chem. Soc.* **2009**, *132*, 16.

(290) Shaw, C. F. *Chem. Rev.* **1999**, *99*, 2589.

(291) Di Gianvincenzo, P.; Marradi, M.; Martínez-Ávila, O. M.; Bedoya, L. M.; Alcamí, J.; Penadés, S. *Bioorg. Med. Chem. Lett.* **2010**, *20*, 2718.

(292) Zhu, Y.; Qian, H.; Zhu, M.; Jin, R. *Adv. Mater.* **2010**, *22*, 1915.

(293) Kumar, S. S.; Kwak, K.; Lee, D. *Anal. Chem.* **2011**, *83*, 3244.

(294) Miller, S. A.; Womick, J. M.; Parker, J. F.; Murray, R. W.; Moran, A. M. *J. Phys. Chem. C* **2009**, *113*, 9440.

(295) Parker, J. F.; Choi, J.-P.; Wang, W.; Murray, R. W. *J. Phys. Chem. C* **2008**, *112*, 13976.

(296) Choi, J.-P.; Fields-Zinna, C. A.; Stiles, R. L.; Balasubramanian, R.; Douglas, A. D.; Crowe, M. C.; Murray, R. W. *J. Phys. Chem. C* **2010**, *114*, 15890.

(297) Zhu, M.; Eckenhoff, W. T.; Pintauer, T.; Jin, R. *J. Phys. Chem. C* **2008**, *112*, 14221.

(298) Wu, Z.; Jin, R. *Nano Lett.* **2010**, *10*, 2568.

(299) Han, Y.-K.; Kim, H.; Jung, J.; Choi, Y. C. *J. Phys. Chem. C* **2010**, *114*, 7548.

(300) Zhu, M.; Aikens, C. M.; Hendrich, M. P.; Gupta, R.; Qian, H.; Schatz, G. C.; Jin, R. *J. Am. Chem. Soc.* **2009**, *131*, 2490.

(301) Lopez-Acevedo, O.; Akola, J.; Whetten, R. L.; Grönbeck, H.; Häkkinen, H. *J. Phys. Chem. C* **2009**, *113*, 5035.

(302) Goldsmith, M.-R.; George, C. B.; Zuber, G.; Naaman, R.; Waldeck, D. H.; Wipf, P.; Beratan, D. N. *Phys. Chem. Chem. Phys.* **2006**, *8*, 63.

(303) Press, W. H. *Numerical recipes in Fortran 77: the art of scientific computing*; Cambridge university press, 1992; Vol. 1.

(304) Anderson, E. *LAPACK Users' guide*; Siam, 1999; Vol. 9.

(305) Anderson, E.; Bai, Z.; Bischof, C.; Demmel, J.; Dongarra, J.*et al. LAPACK Users' guide*; Society for Industrial and Applied Mathematics Philadelphia, 1995.

(306) http://keisan.casio.com

(307) http://mathworks.de/matlabcentral/newsreader/view_thread/21747

(308) Iwasa, T.; Nobusada, K. *Chem. Phys. Lett.* **2007**, *441*, 268.

(309) Akola, J.; Walter, M.; Whetten, R. L.; Häkkinen, H.; Grönbeck, H. *J. Am. Chem. Soc.* **2008**, *130*, 3756.

(310) Heaven, M. W.; Dass, A.; White, P. S.; Holt, K. M.; Murray, R. W. *J. Am. Chem. Soc.* **2008**, *130*, 3754.

(311) Schaaff, T. G.; Shafifullin, M. N.; Khoury, J. T.; Vezmar, I.; Whetten, R. L.*et al. J. Phys. Chem. B* **1997**, *101*, 7885.

(312) Wyrwas, R. B.; Alvarez, M. M.; Khoury, J. T.; Price, R. C.; Schaaff, T. G.; Whetten, R. L. *Eur. Phys. J. D* **2007**, *43*, 91.

(313) Negishi, Y.; Nobusada, K.; Tsukuda, T. *J. Am. Chem. Soc.* **2005**, *127*, 5261.

(314) Kumar, S.; Bolan, M. D.; Bigioni, T. P. *J. Am. Chem. Soc.* **2010**, *132*, 13141.

(315) Bigioni, T. P.; Whetten, R. L.; Dag, Ö. *J. Phys. Chem. B* **2000**, *104*, 6983.

(316) Ramakrishna, G.; Varnavski, O.; Kim, J.; Lee, D.; Goodson, T. *J. Am. Chem. Soc.* **2008**, *130*, 5032.

(317) Hakkinen, H. *Nat. Chem.* **2012**, *4*, 443.

(318) Fields-Zinna, C. A.; Crowe, M. C.; Dass, A.; Weaver, J. E. F.; Murray, R. W. *Langmuir* **2009**, *25*, 7704.

(319) Kacprzak, K. A.; Lehtovaara, L.; Akola, J.; Lopez-Acevedo, O.; Häkkinen, H. *Phys. Chem. Chem. Phys.* **2009**, *11*, 7123.

(320) Walter, M.; Moseler, M. *J. Phys. Chem. C* **2009**, *113*, 15834.

(321) Negishi, Y.; Kurashige, W.; Niihori, Y.; Iwasa, T.; Nobusada, K. *Phys. Chem. Chem. Phys.* **2010**, *12*, 6219.

(322) Negishi, Y.; Igarashi, K.; Munakata, K.; Ohgake, W.; Nobusada, K. *Chem. Commun.* **2012**, *48*, 660.

(323) Jiang, D.-e.; Dai, S. *Inorg. Chem.* **2009**, *48*, 2720.

(324) Jiang, D.-e.; Whetten, R. L. *Phys. Rev. B* **2009**, *80*, 115402.

(325) Ulises Reveles, J.; Clayborne, P. A.; Reber, A. C.; Khanna, S. N.; Pradhan, K.; Sen, P.; Pederson, M. R. *Nat. Chem.* **2009**, *1*, 310.

(326) Akola, J.; Kacprzak, K. A.; Lopez-Acevedo, O.; Walter, M.; Grönbeck, H.; Häkkinen, H. *J. Phys. Chem. C* **2010**, *114*, 15986.

(327) Zhou, M.; Cai, Y. Q.; Zeng, M. G.; Zhang, C.; Feng, Y. P. *Appl. Phys. Lett.* **2011**, *98*, 143103/1.

(328) Kumara, C.; Dass, A. *Nanoscale* **2011**, *3*, 3064.

(329) Malola, S.; Häkkinen, H. *J. Phys. Chem. Lett.* **2011**, *2*, 2316.

(330) Deng, L.; Hu, W.; Deng, H.; Xiao, S.; Tang, J. *J. Phys. Chem. C* **2011**, *115*, 11355.

(331) Enkovaara, J.; Rostgaard, C.; Mortensen, J. J.; Chen, J.; Dułak, M.*et al. J. Phys.: Condens. Matter* **2010**, *22*, 253202.

(332) Mortensen, J. J.; Hansen, L. B.; Jacobsen, K. W. *Phys. Rev. B* **2005**, *71*, 035109.

(333) Blöchl, P. E. *Phys. Rev. B* **1994**, *50*, 17953.

Appendix A - Supporting information for “Theoretical analysis of the optical excitation spectra of silver and gold nanowires”

Silver nanowires

Figure A-1. Neutral silver nanowires excitation spectra with SAOP/DZ.

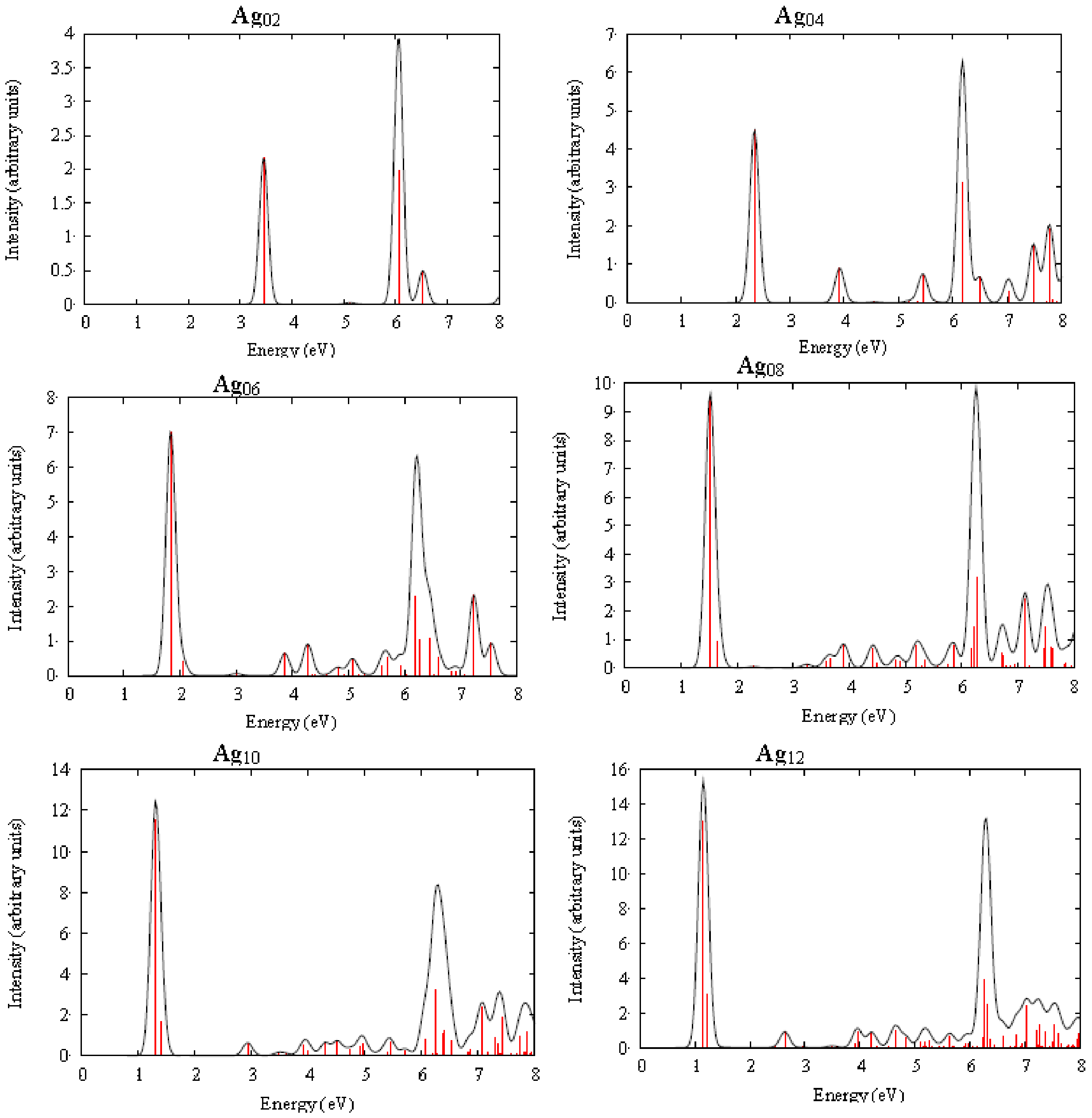
Ag02

Ag04

Ag06

Ag08

Ag10

Ag12

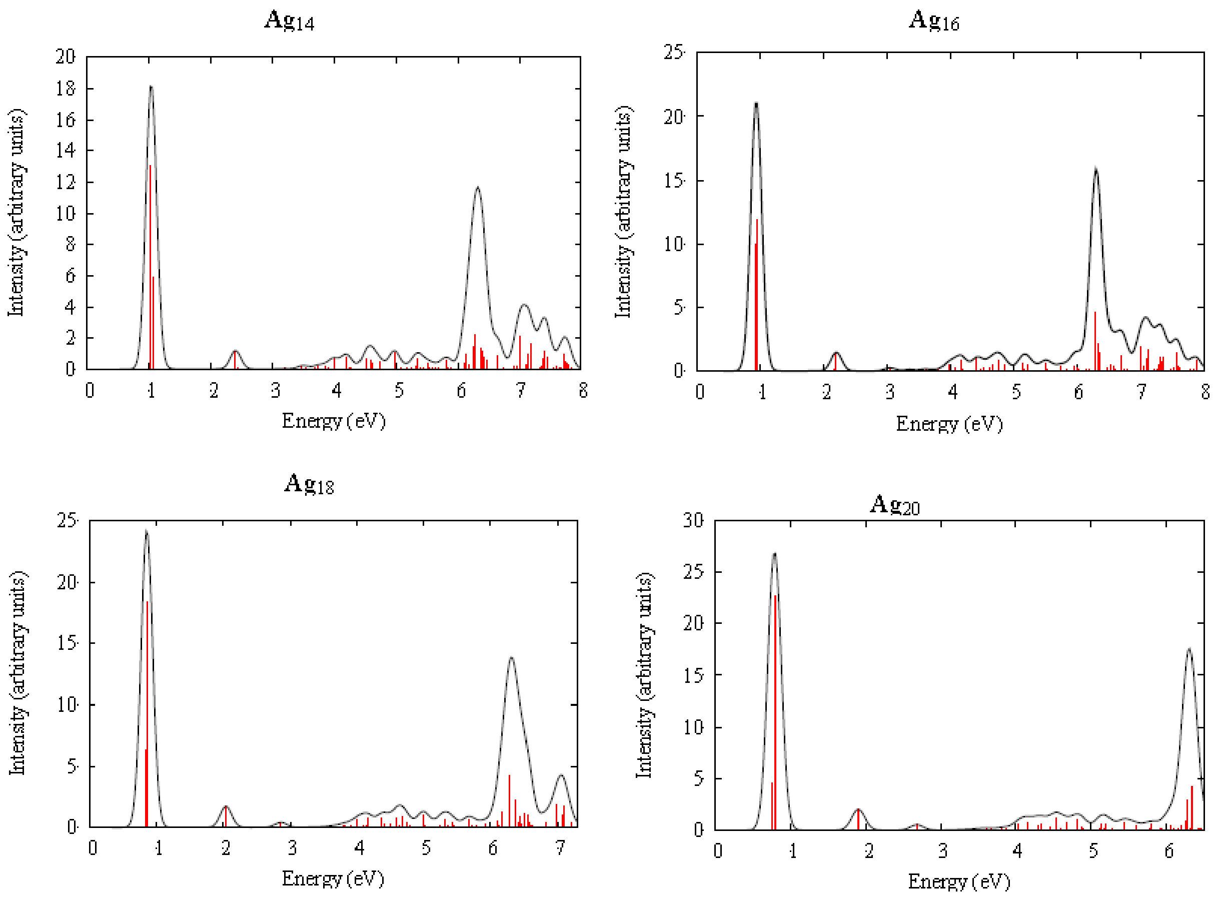

Figure A-2. Positively charged silver nanowires excitation spectra with SAOP/DZ.

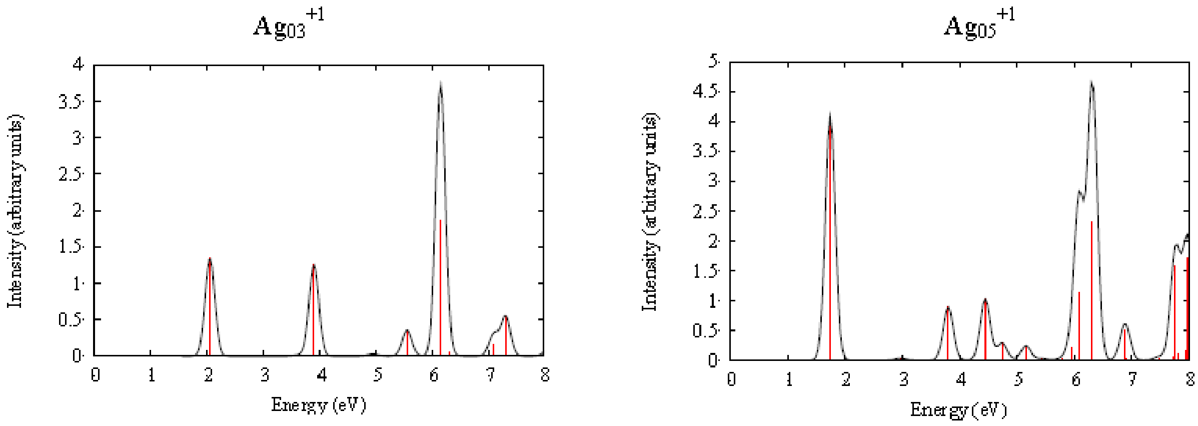

Ag_{07}^{+1}

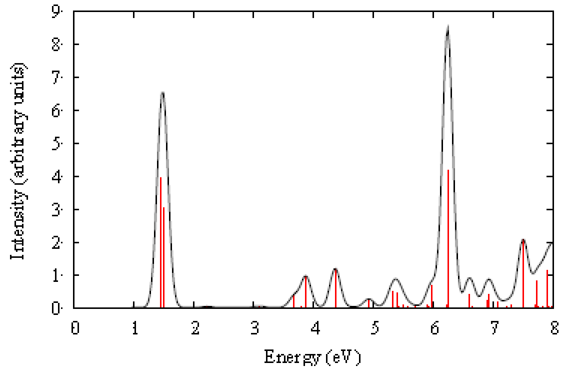

Ag_{09}^{+1}

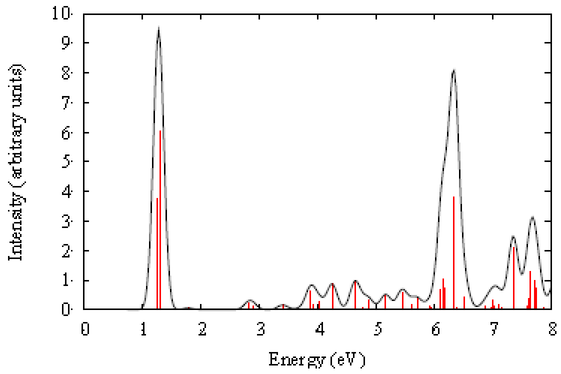

Ag_{11}^{+1}

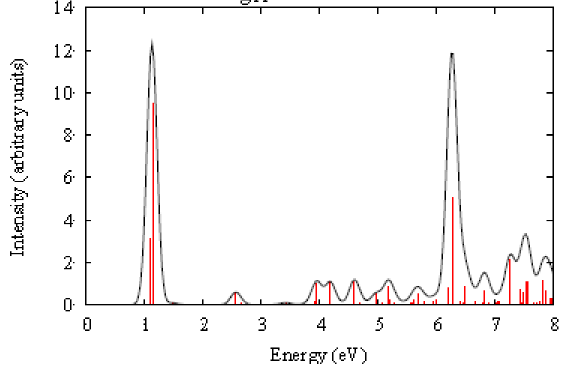

Ag_{13}^{+1}

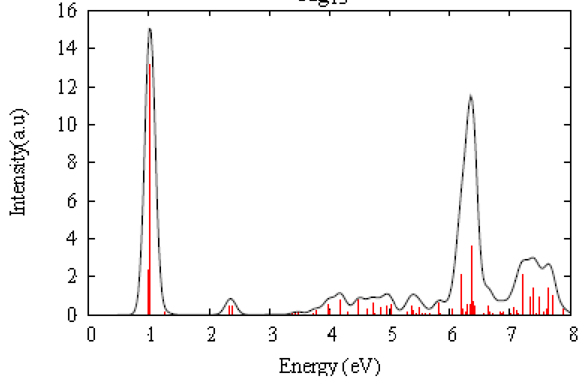

Ag_{15}^{+1}

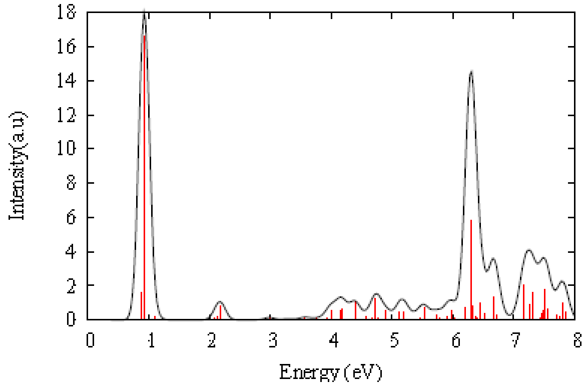

Ag_{17}^{+1}

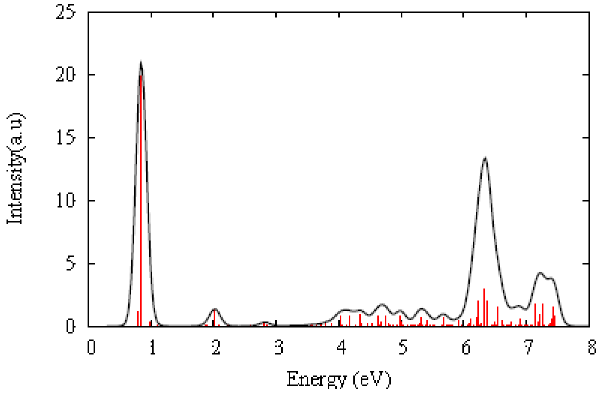

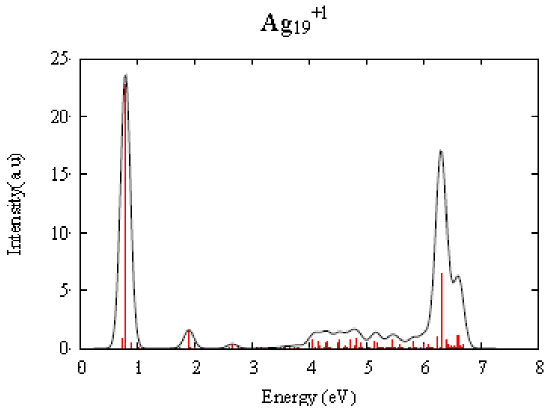

Figure A-3. Negatively charged silver nanowires excitation spectra with SAOP/DZ.

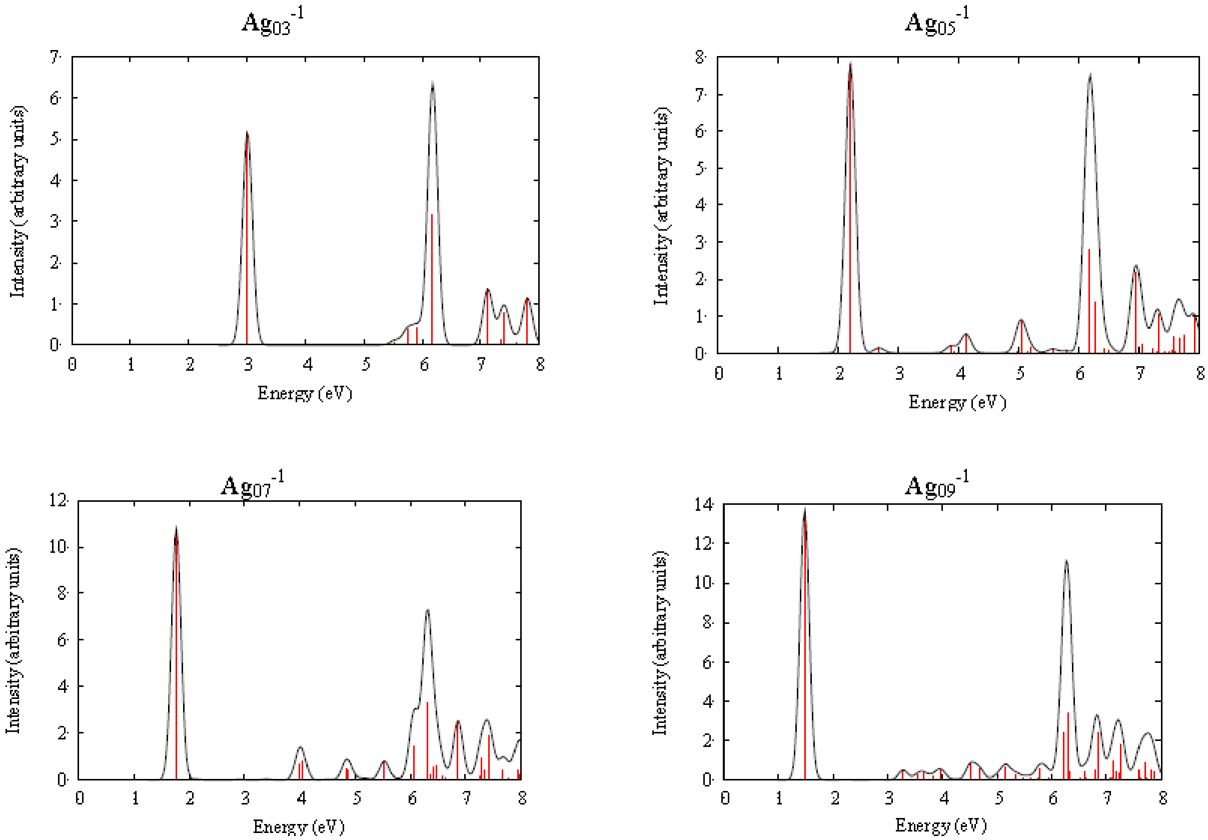

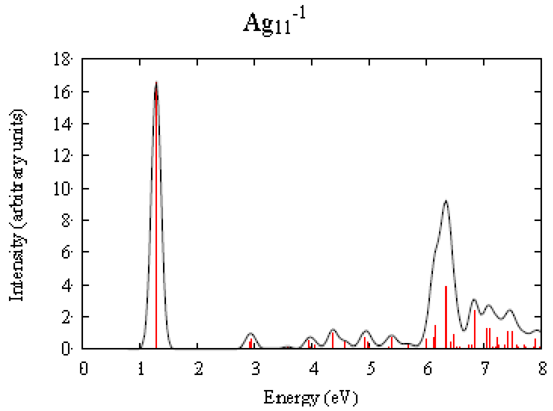
Ag_{11}^{-1}
Intensity (arbitrary units)
0
2
4
6
8
10
12
14
16
18
Energy (eV)
0
1
2
3
4
5
6
7
8

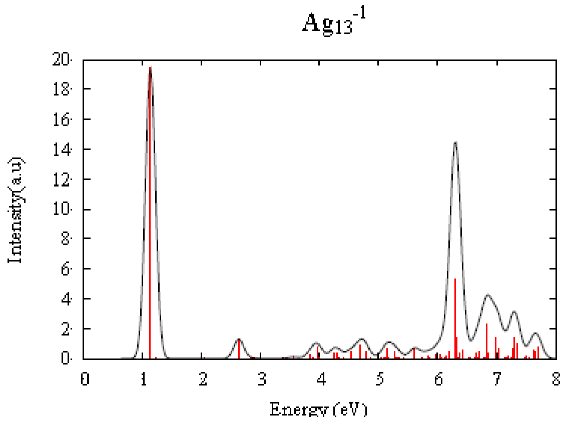
Ag_{13}^{-1}
Intensity(a.u)
0
2
4
6
8
10
12
14
16
18
20
Energy (eV)
0
1
2
3
4
5
6
7
8

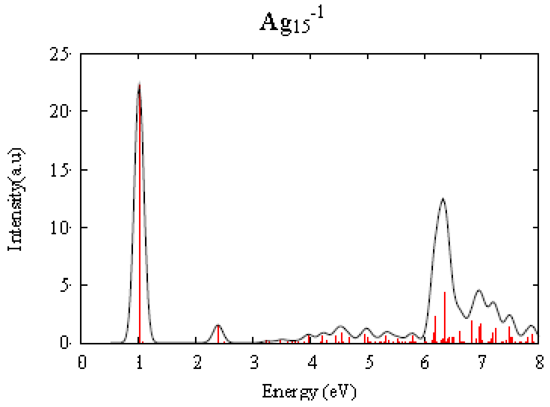
Ag_{15}^{-1}
Intensity(a.u)
0
5
10
15
20
25
Energy (eV)
0
1
2
3
4
5
6
7
8

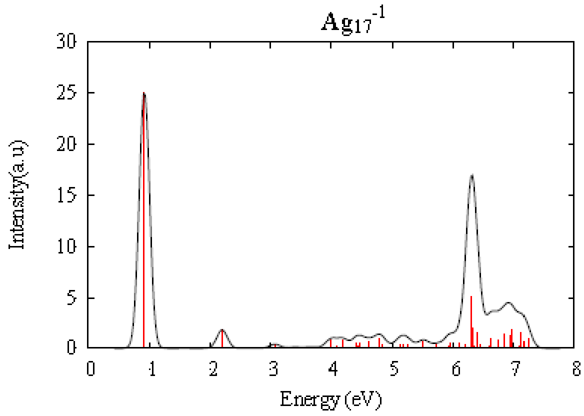
Ag_{17}^{-1}
Intensity(a.u)
0
5
10
15
20
25
30
Energy (eV)
0
1
2
3
4
5
6
7
8

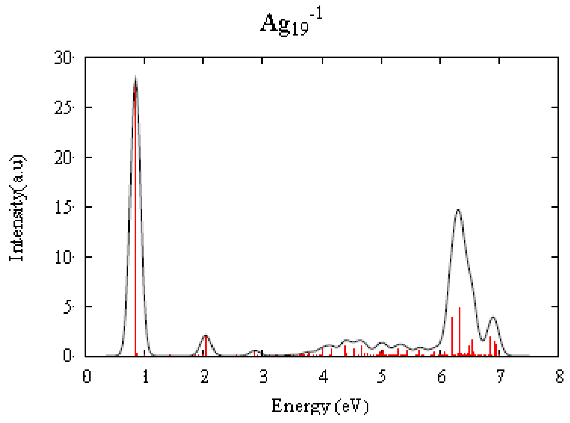
Ag_{19}^{-1}
Intensity(a.u)
0
5
10
15
20
25
30
Energy (eV)
0
1
2
3
4
5
6
7
8

Figure A-4. Neutral silver nanowires excitation spectra with LB94/DZ.

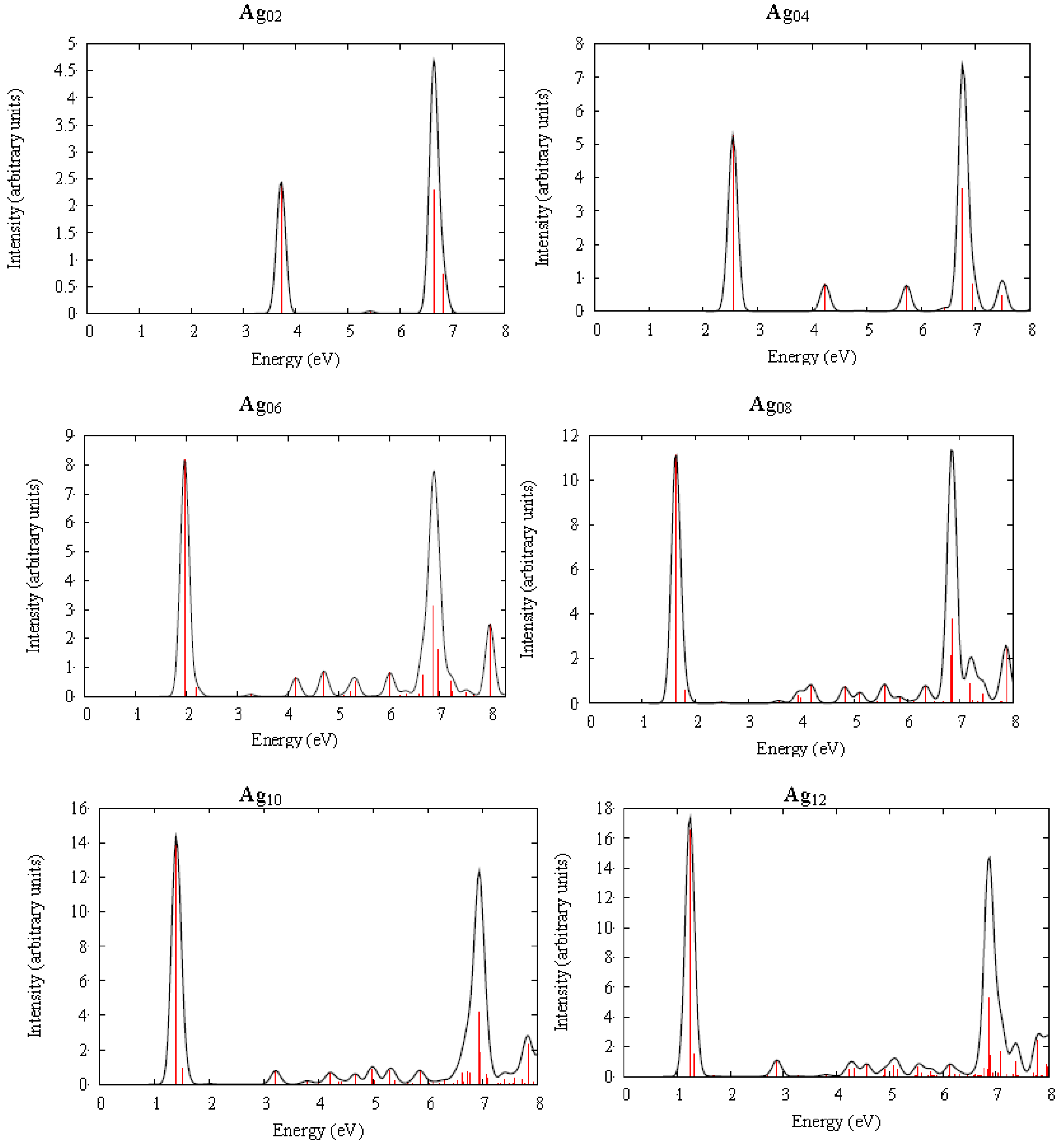

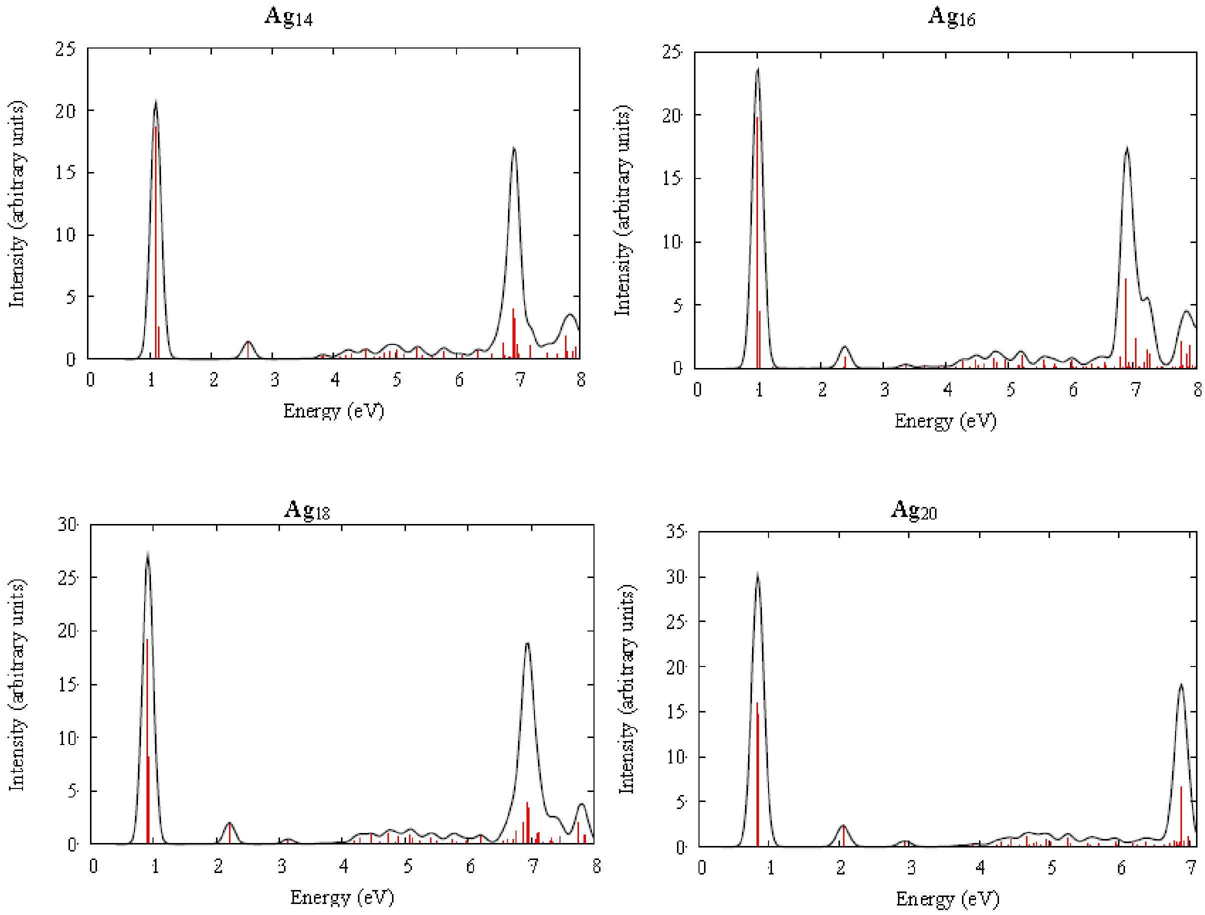

Figure A-5. Positively chaged silver nanowires excitation spectra with LB94/DZ.

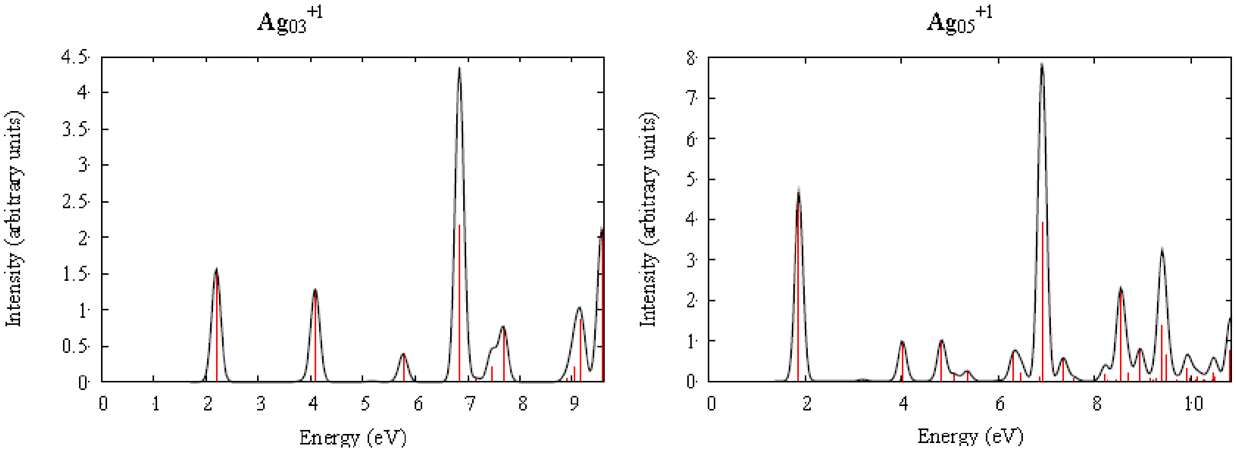

Ag_{07}^{+1}

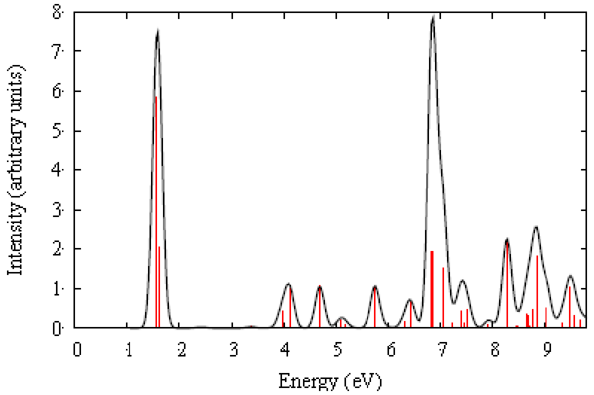

Ag_{09}^{+1}

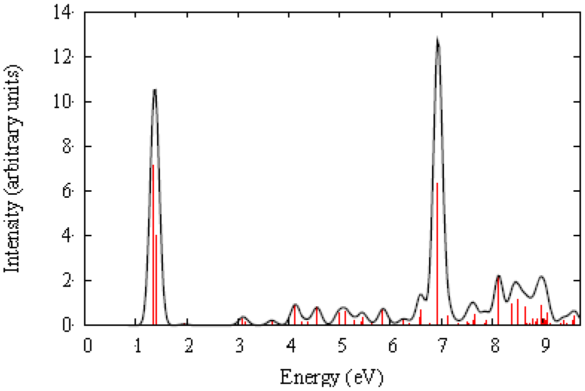

Ag_{11}^{+1}

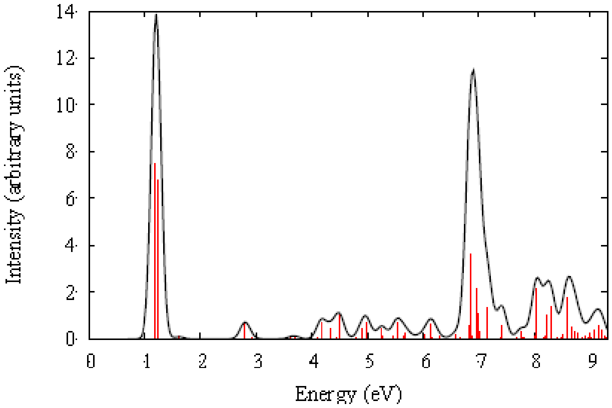

Ag_{13}^{+1}

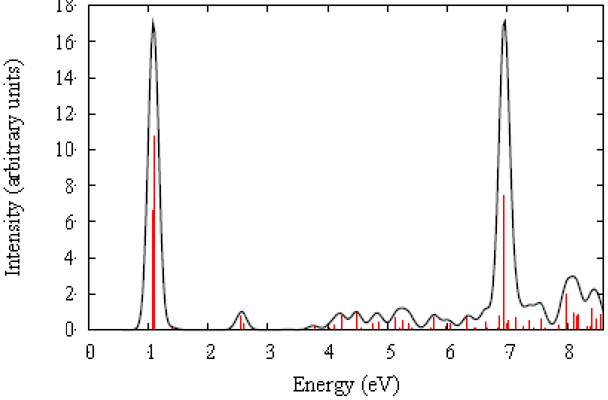

Ag_{15}^{+1}

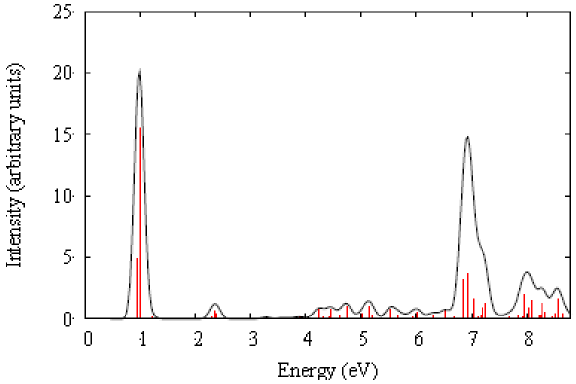

Ag_{17}^{+1}

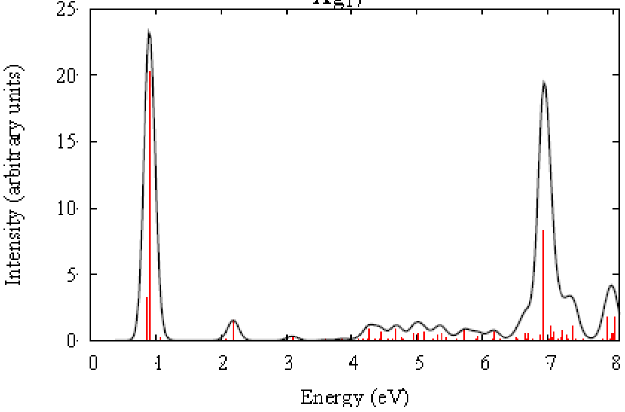

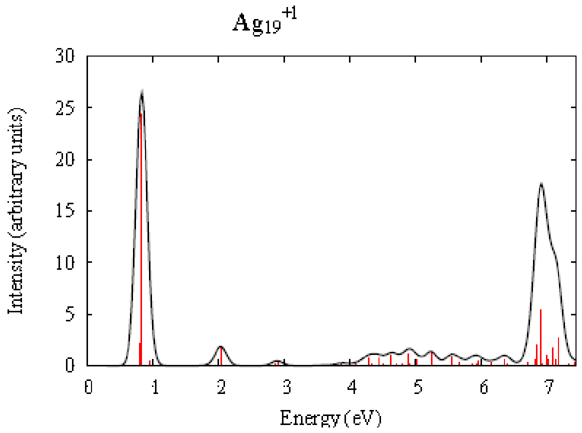
Ag_{19}^{+1}

Figure A-6. Negatively charged silver nanowires excitation spectra with LB94/DZ.

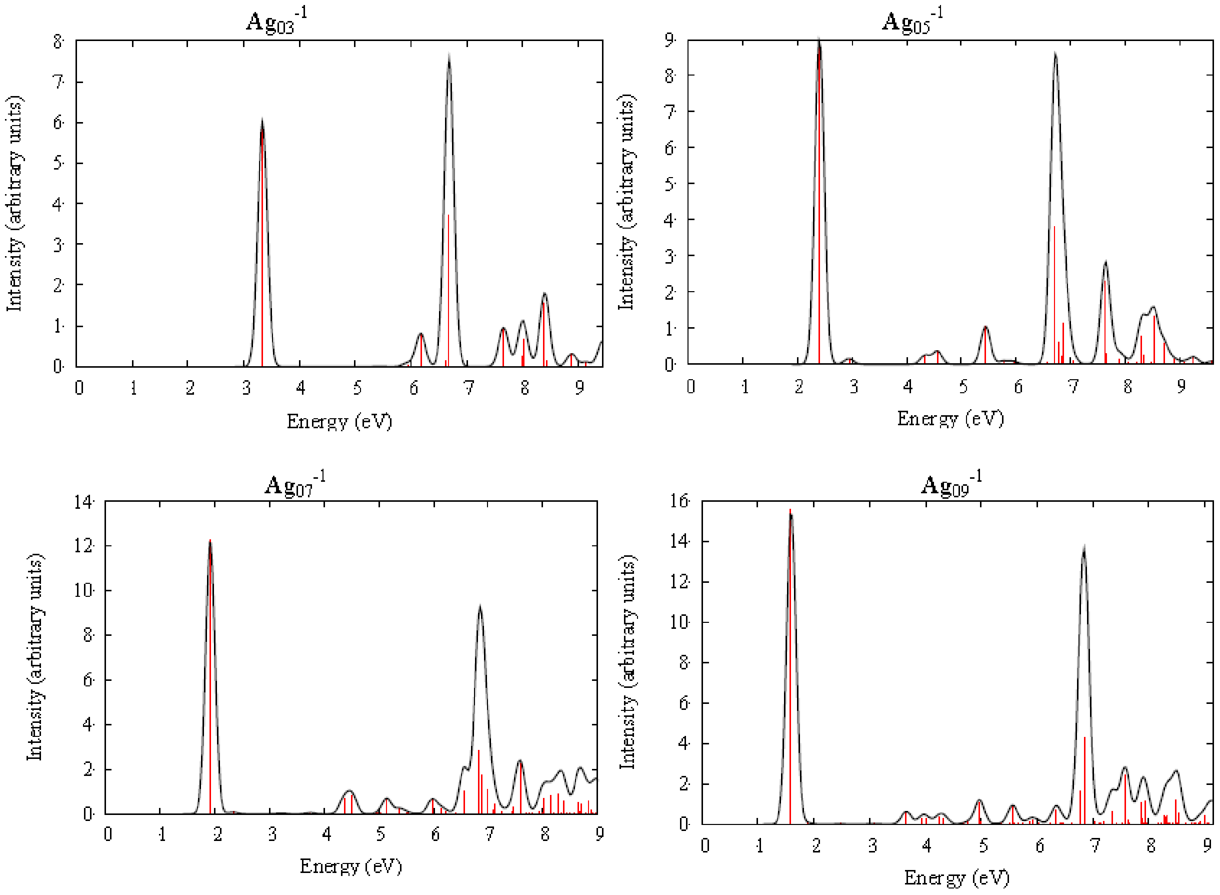
Ag_{03}^{-1}

Ag_{05}^{-1}

Ag_{07}^{-1}

Ag_{09}^{-1}

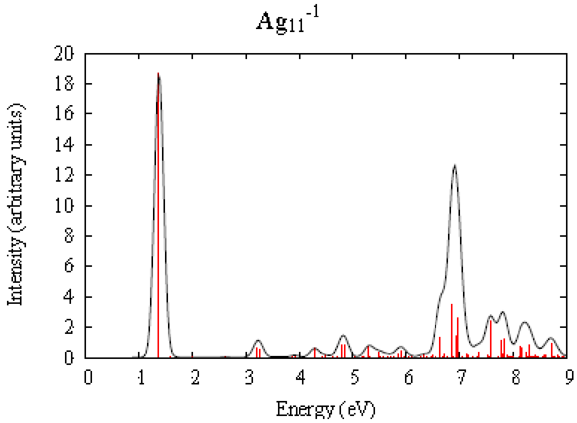
Ag_{11}^{-1}
Intensity (arbitrary units)
0
2
4
6
8
10
12
14
16
18
20
Energy (eV)
0
1
2
3
4
5
6
7
8
9

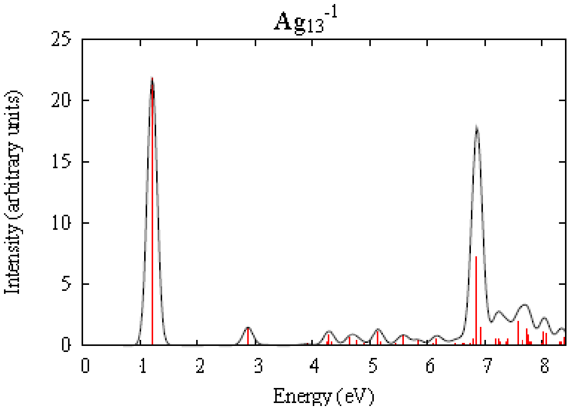
Ag_{13}^{-1}
Intensity (arbitrary units)
0
5
10
15
20
25
Energy (eV)
0
1
2
3
4
5
6
7
8

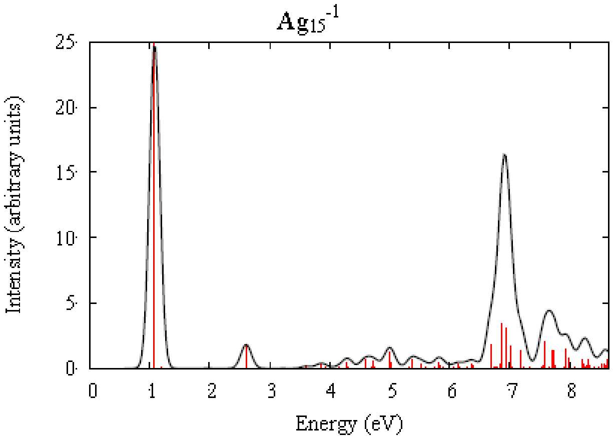
Ag_{15}^{-1}
Intensity (arbitrary units)
0
5
10
15
20
25
Energy (eV)
0
1
2
3
4
5
6
7
8

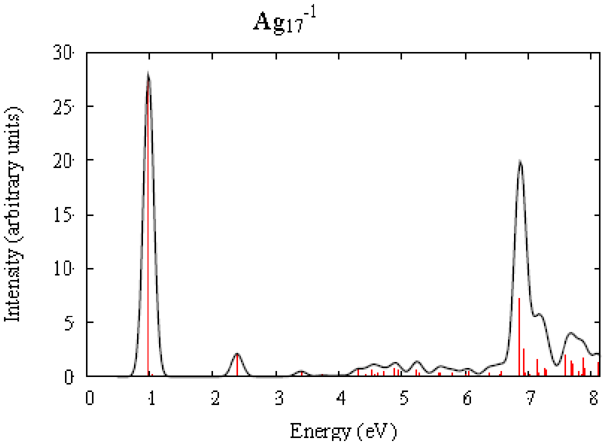
Ag_{17}^{-1}
Intensity (arbitrary units)
0
5
10
15
20
25
30
Energy (eV)
0
1
2
3
4
5
6
7
8

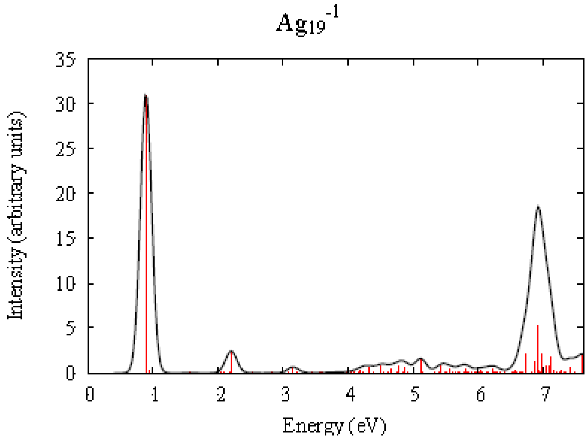
Ag_{19}^{-1}
Intensity (arbitrary units)
0
5
10
15
20
25
30
35
Energy (eV)
0
1
2
3
4
5
6
7

Gold nanowires

Figure A-7. Neutral gold nanowires excitation spectra with SAOP/DZ.

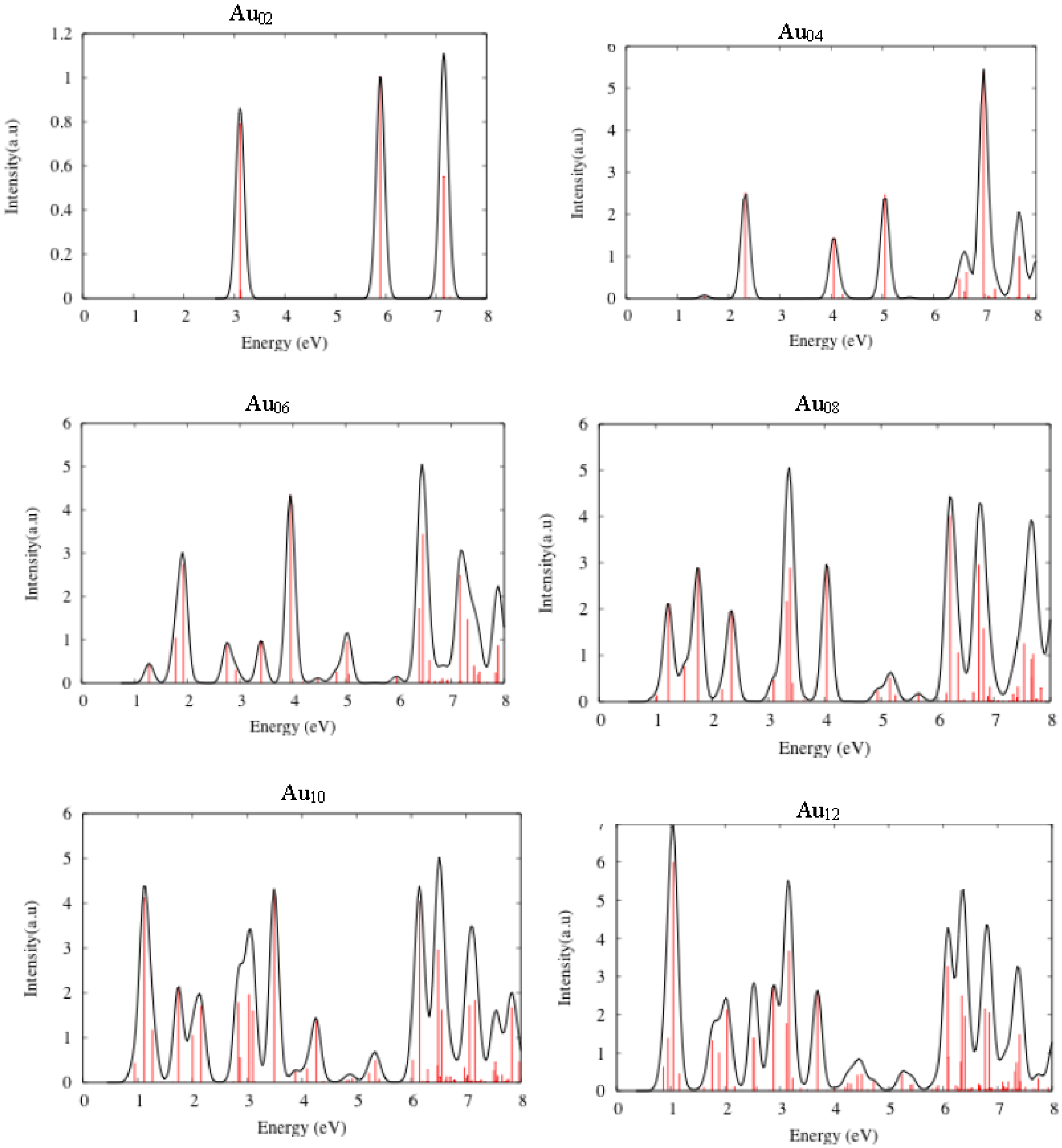

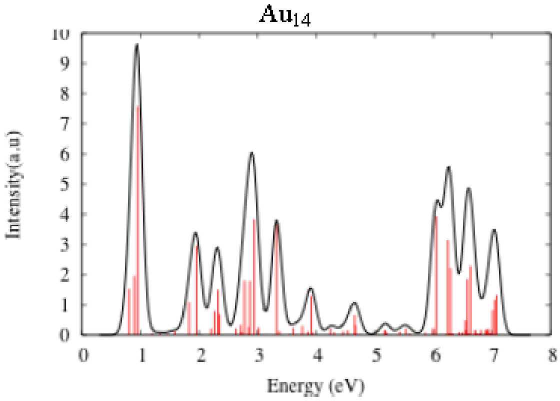
Au$_{14}$

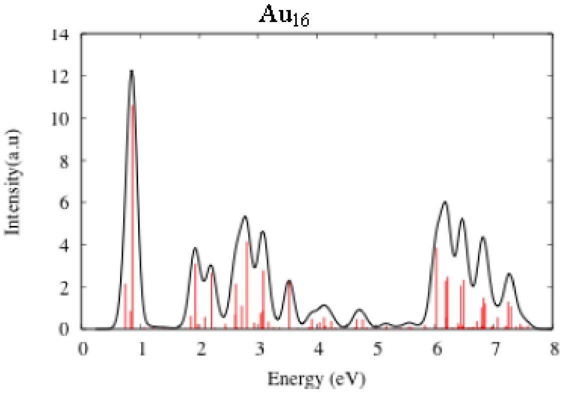
Au$_{16}$

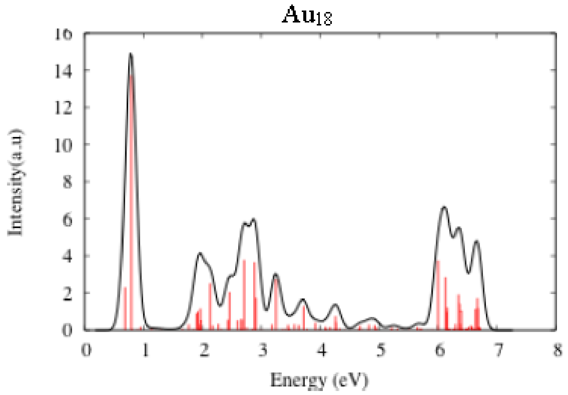
Au$_{18}$

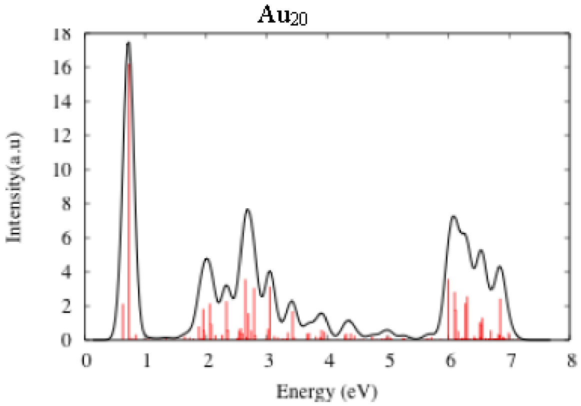
Au$_{20}$

Figure A-8. Positively charged gold nanowires excitation spectra with SAOP/DZ.

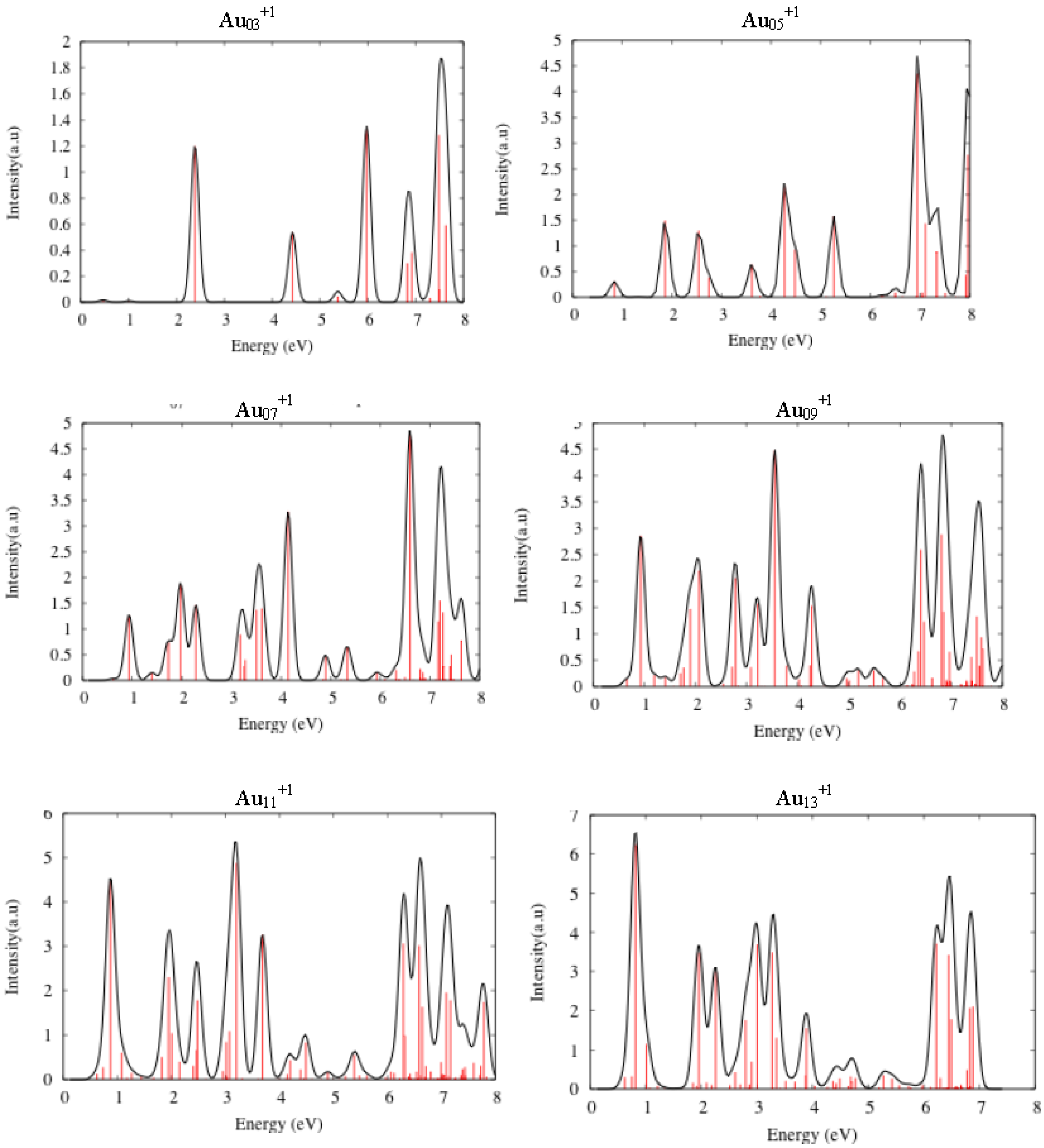

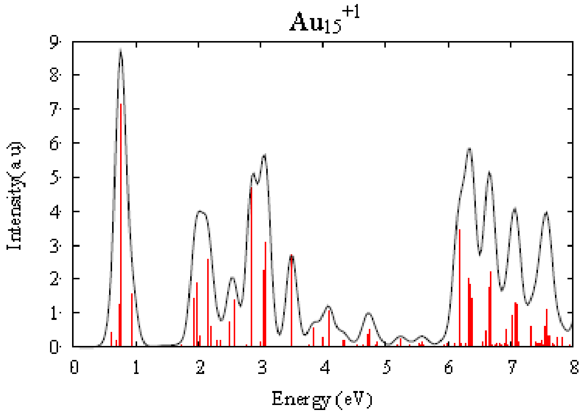
Au$_{15}^{+1}$

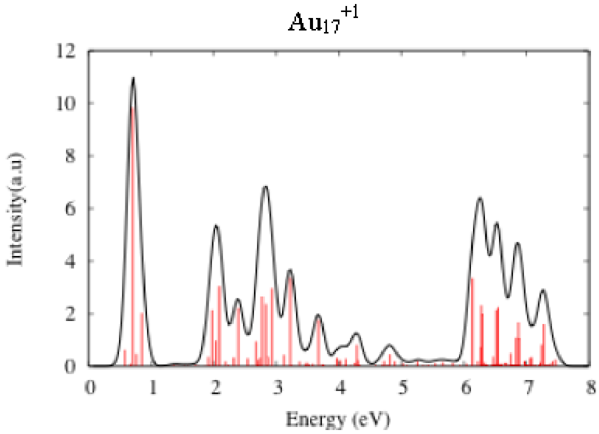
Au$_{17}^{+1}$

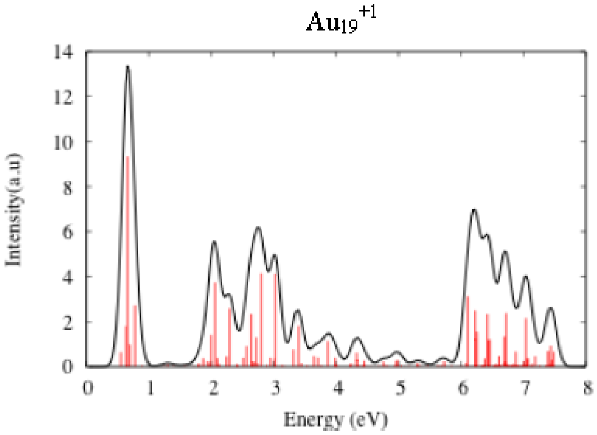
Au$_{19}^{+1}$

Figure A-9. Negatively charged gold nanowires excitation spectra with SAOP/DZ.

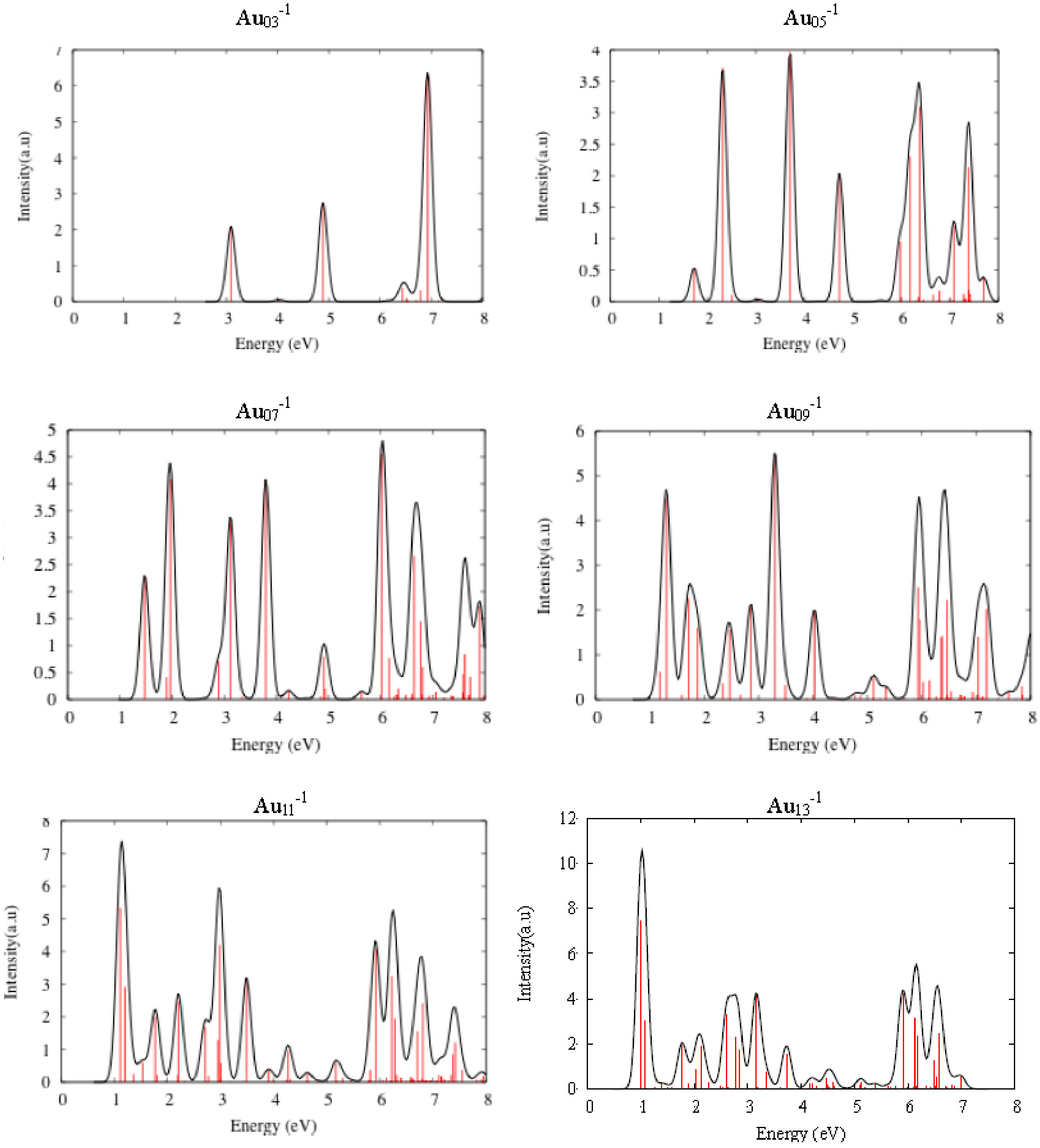

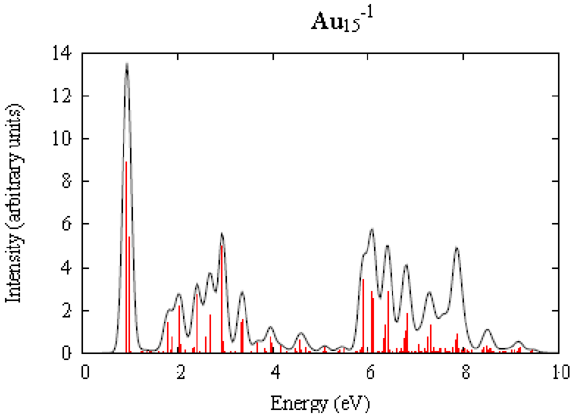

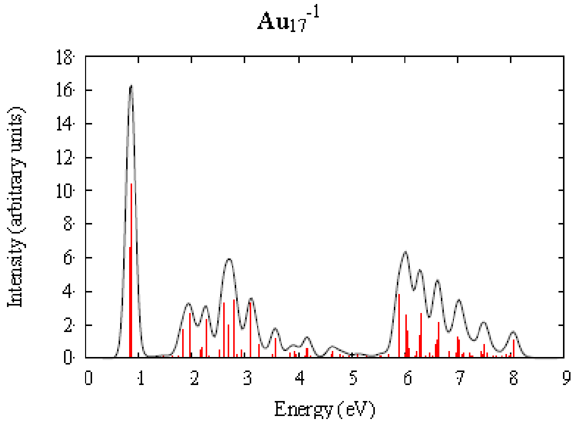

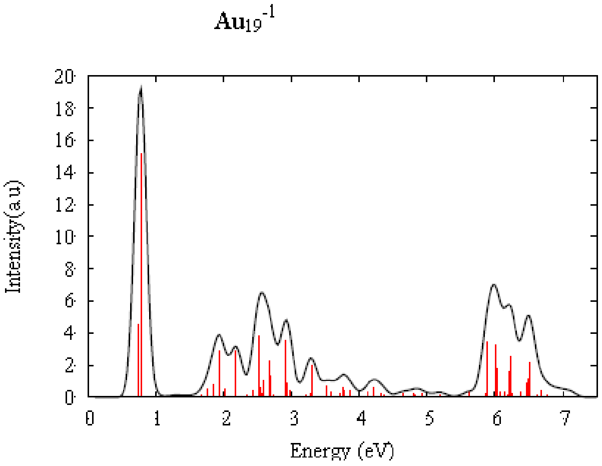

Figure A-10. Neutral gold nanowires excitation spectra with LB94/DZ.

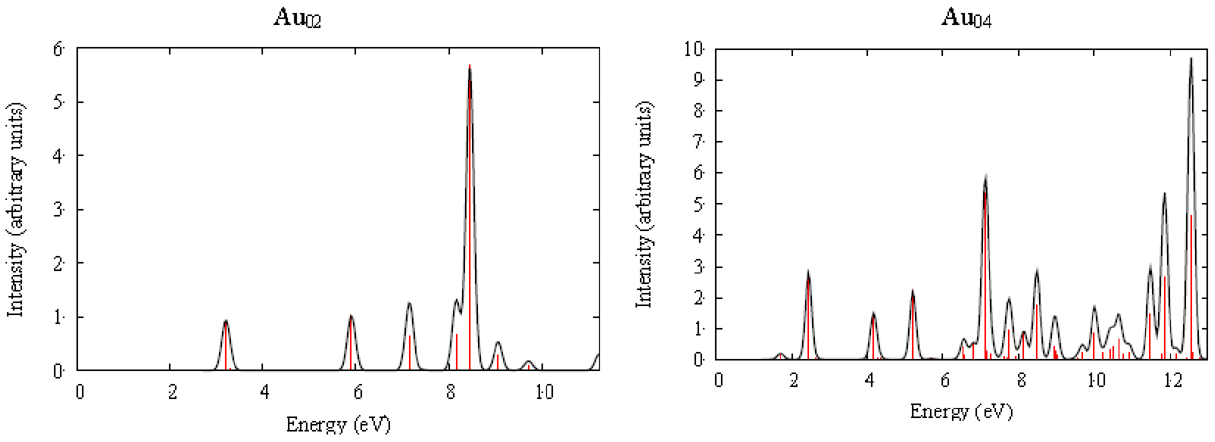

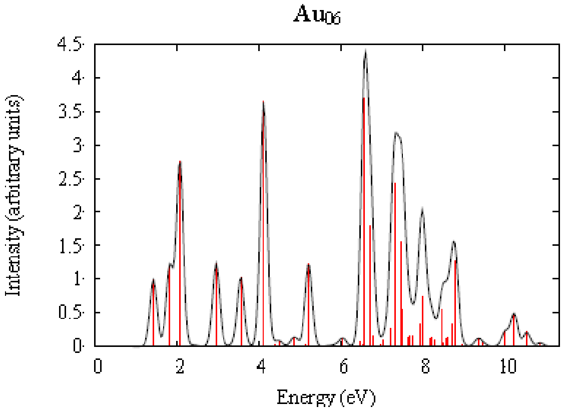
Au06
Intensity (arbitrary units)
4.5
4
3.5
3
2.5
2
1.5
1
0.5
0
0
2
4
6
8
10
Energy (eV)

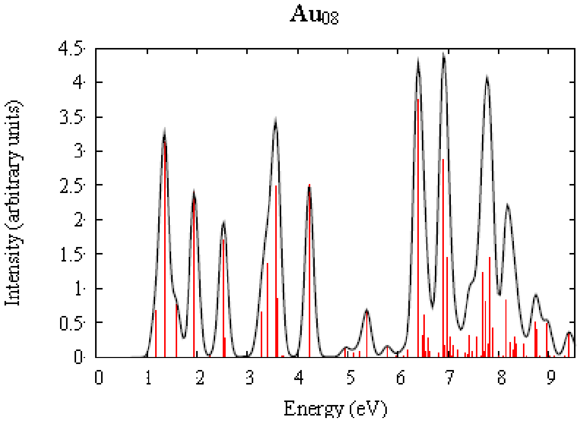
Au08
Intensity (arbitrary units)
4.5
4
3.5
3
2.5
2
1.5
1
0.5
0
0
1
2
3
4
5
6
7
8
9
Energy (eV)

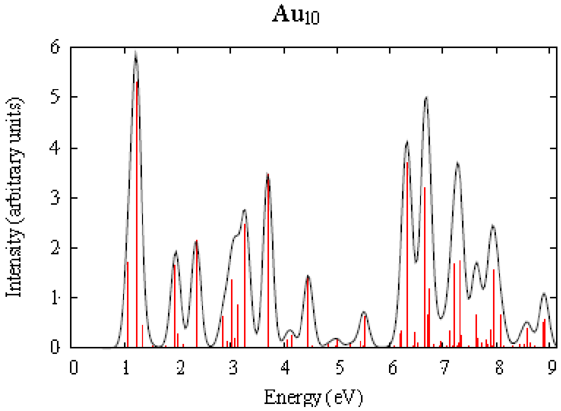
Au10
Intensity (arbitrary units)
6
5
4
3
2
1
0
0
1
2
3
4
5
6
7
8
9
Energy (eV)

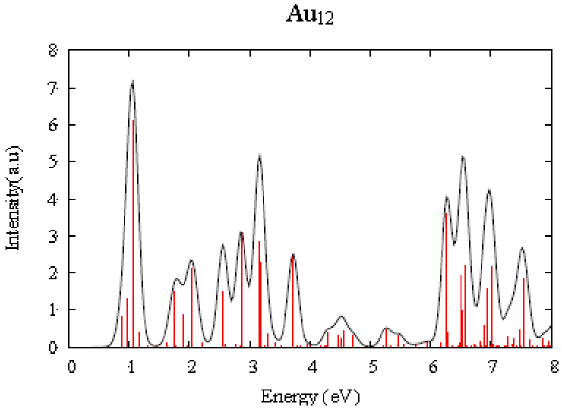
Au12
Intensity(a.u)
8
7
6
5
4
3
2
1
0
0
1
2
3
4
5
6
7
8
Energy (eV)

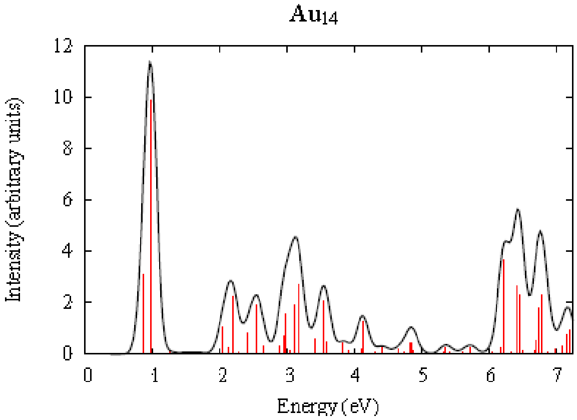
Au14
Intensity (arbitrary units)
12
10
8
6
4
2
0
0
1
2
3
4
5
6
7
Energy (eV)

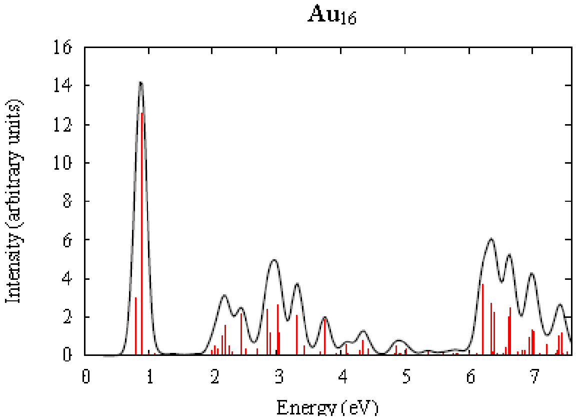
Au16
Intensity (arbitrary units)
16
14
12
10
8
6
4
2
0
0
1
2
3
4
5
6
7
Energy (eV)

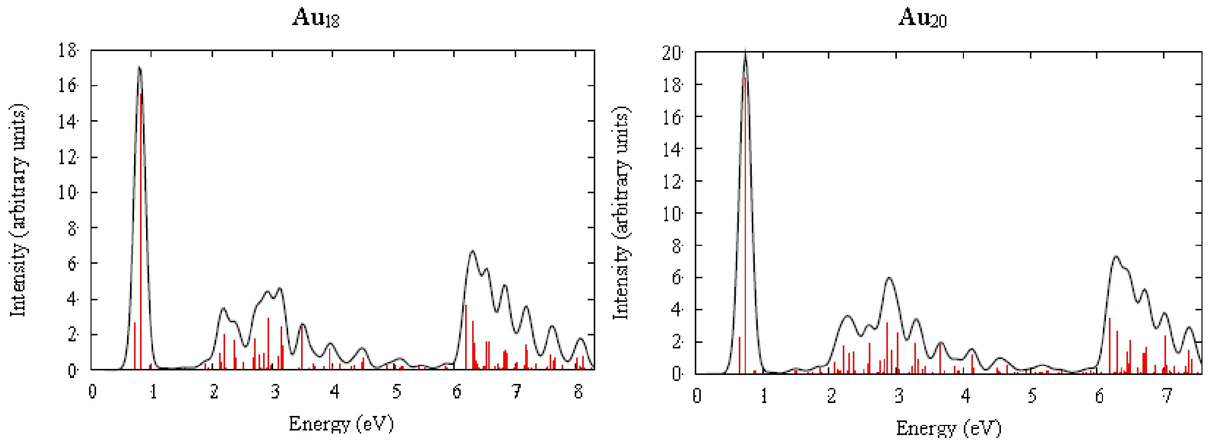

Figure A-11. Positively charged gold nanowires excitation spectra with LB94/DZ.

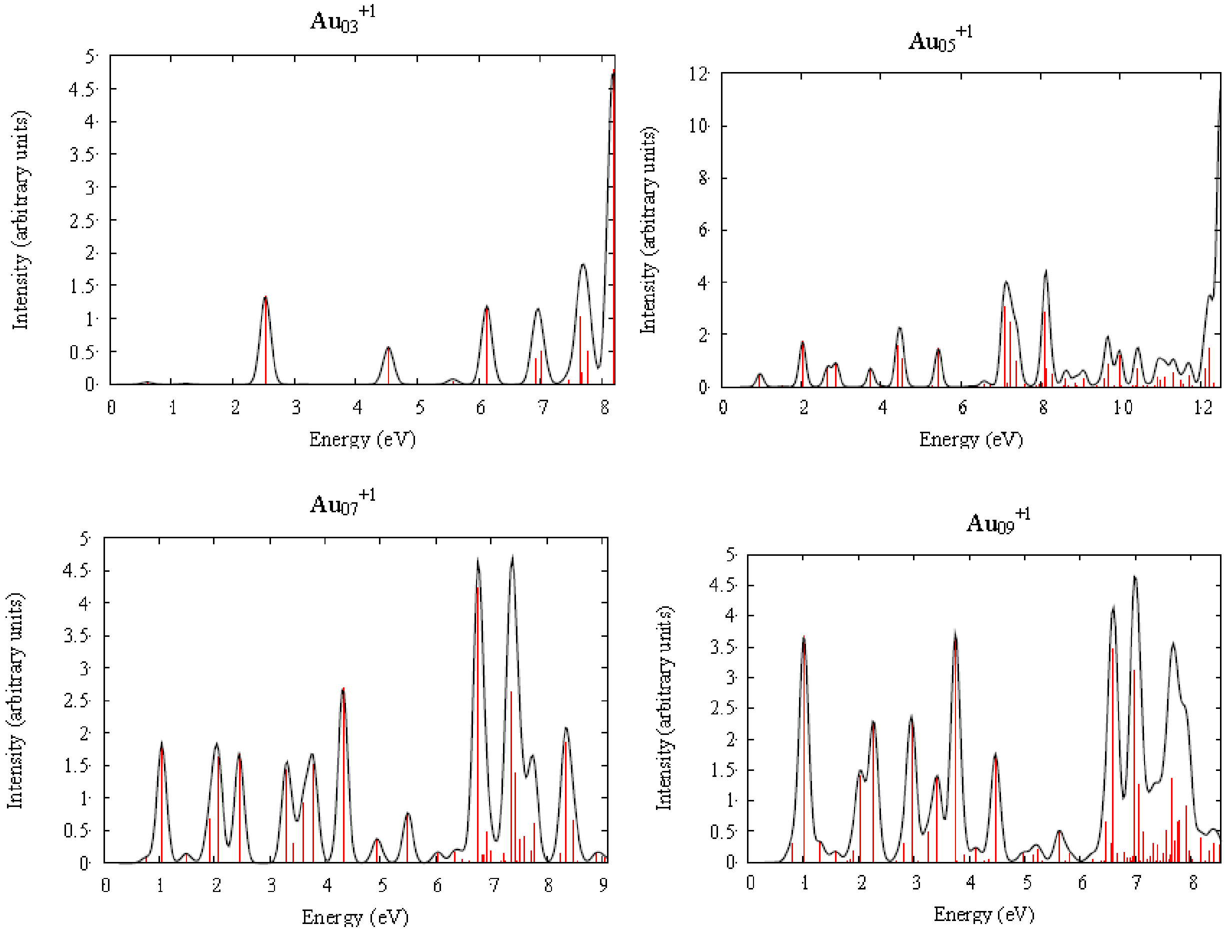

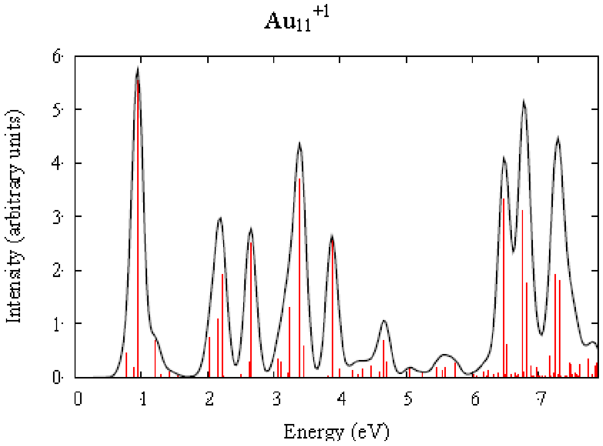

Au_{11}^{+1}
Intensity (arbitrary units)
0
1
2
3
4
5
6
Energy (eV)
0
1
2
3
4
5
6
7

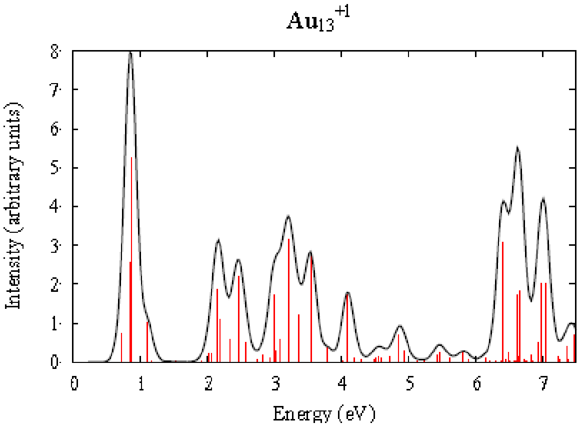

Au_{13}^{+1}
Intensity (arbitrary units)
0
1
2
3
4
5
6
7
8
Energy (eV)
0
1
2
3
4
5
6
7

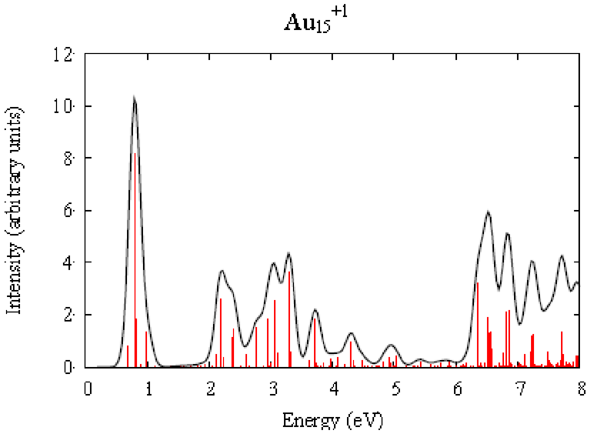

Au_{15}^{+1}
Intensity (arbitrary units)
0
2
4
6
8
10
12
Energy (eV)
0
1
2
3
4
5
6
7
8

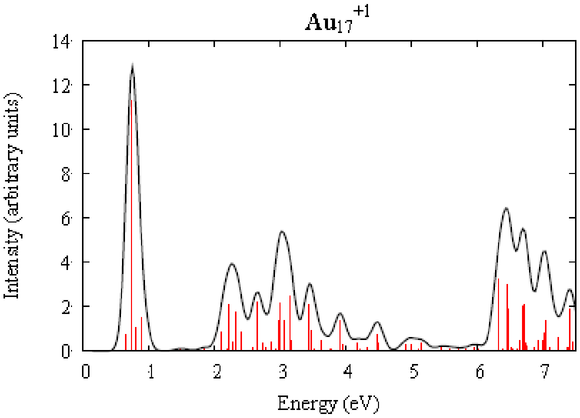

Au_{17}^{+1}
Intensity (arbitrary units)
0
2
4
6
8
10
12
14
Energy (eV)
0
1
2
3
4
5
6
7

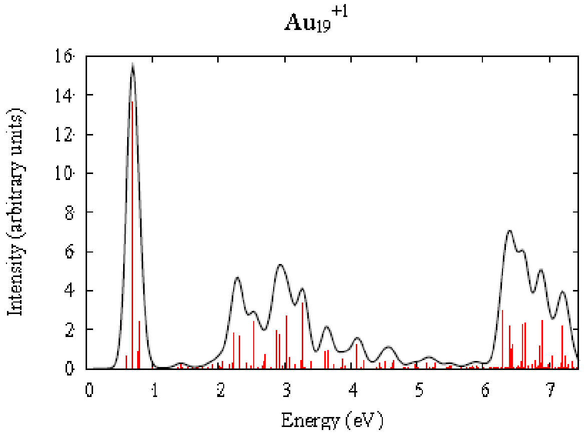

Au_{19}^{+1}
Intensity (arbitrary units)
0
2
4
6
8
10
12
14
16
Energy (eV)
0
1
2
3
4
5
6
7

Figure A-12. Negatively charged gold nanowires excitation spectra with LB94/DZ.

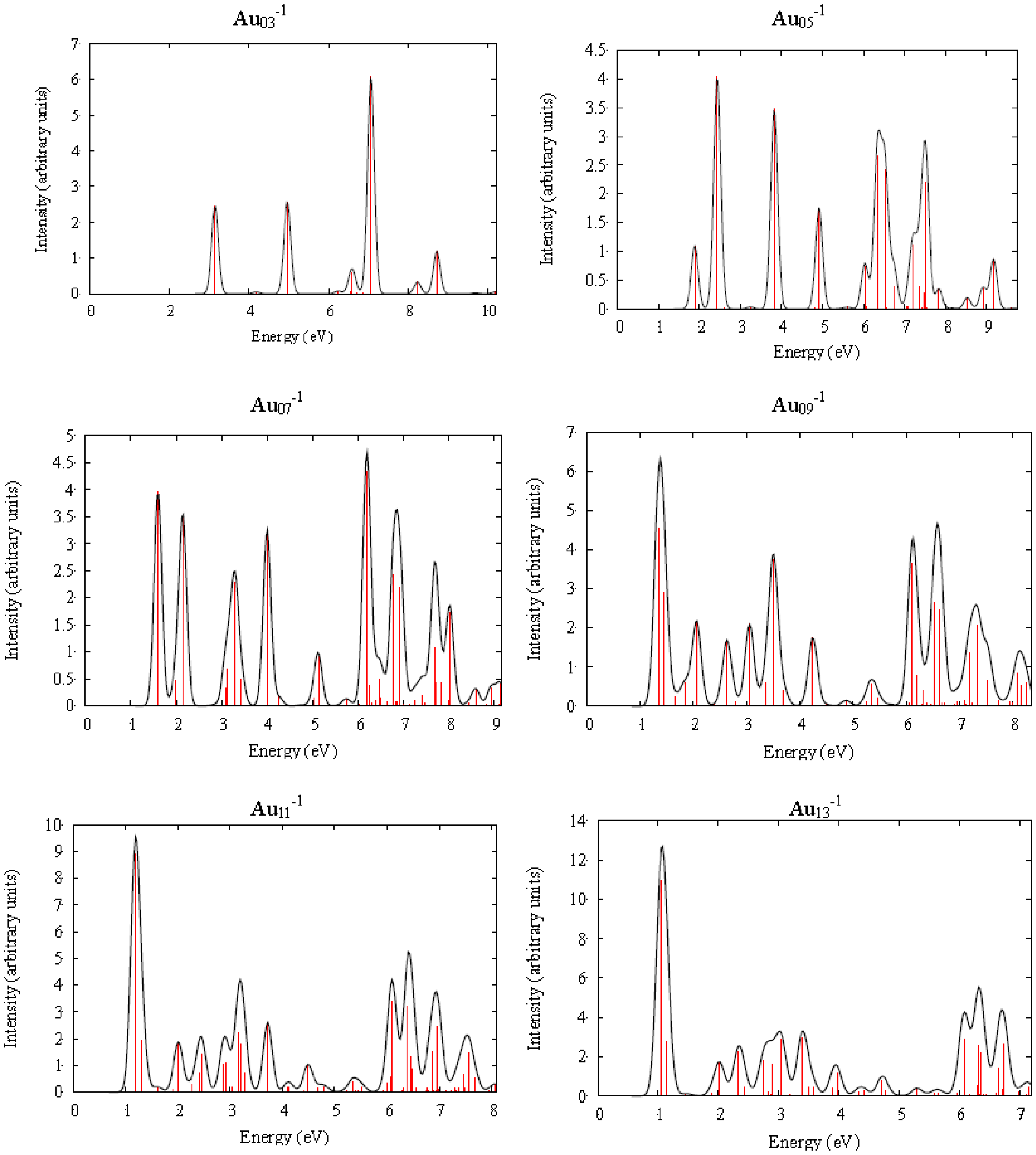

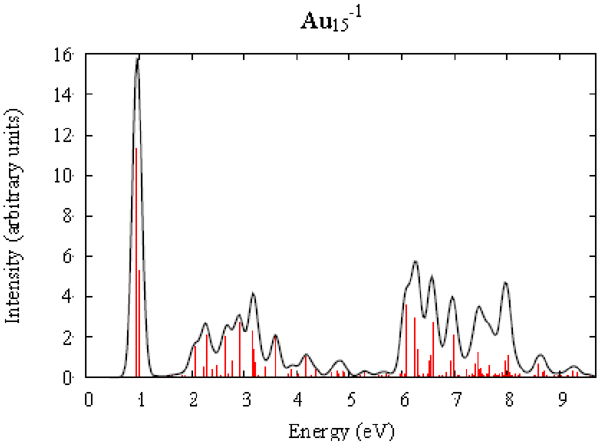
Au$_{15}^{-1}$

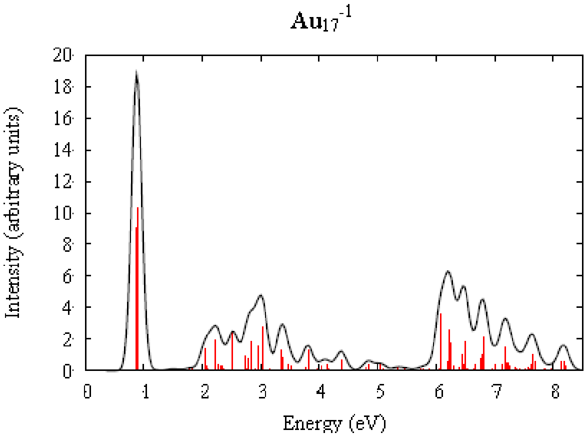
Au$_{17}^{-1}$

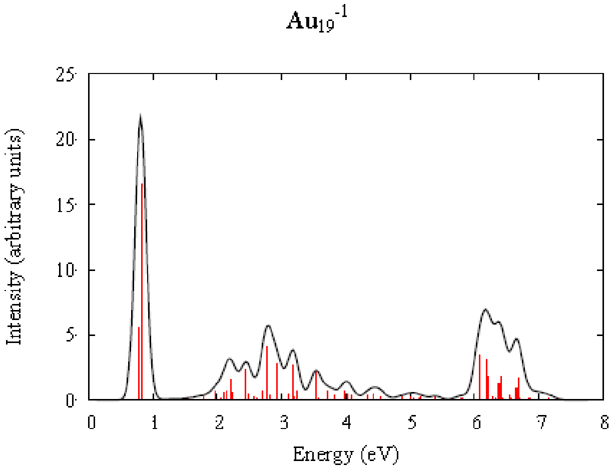
Au$_{19}^{-1}$

Appendix B - Supporting information for “Diameter-Dependence of the Excitation spectra of Silver and Gold Nanorods”

Figure B-1. Excitation spectra of star-shaped silver nanorods at the LB94/DZ level of theory.

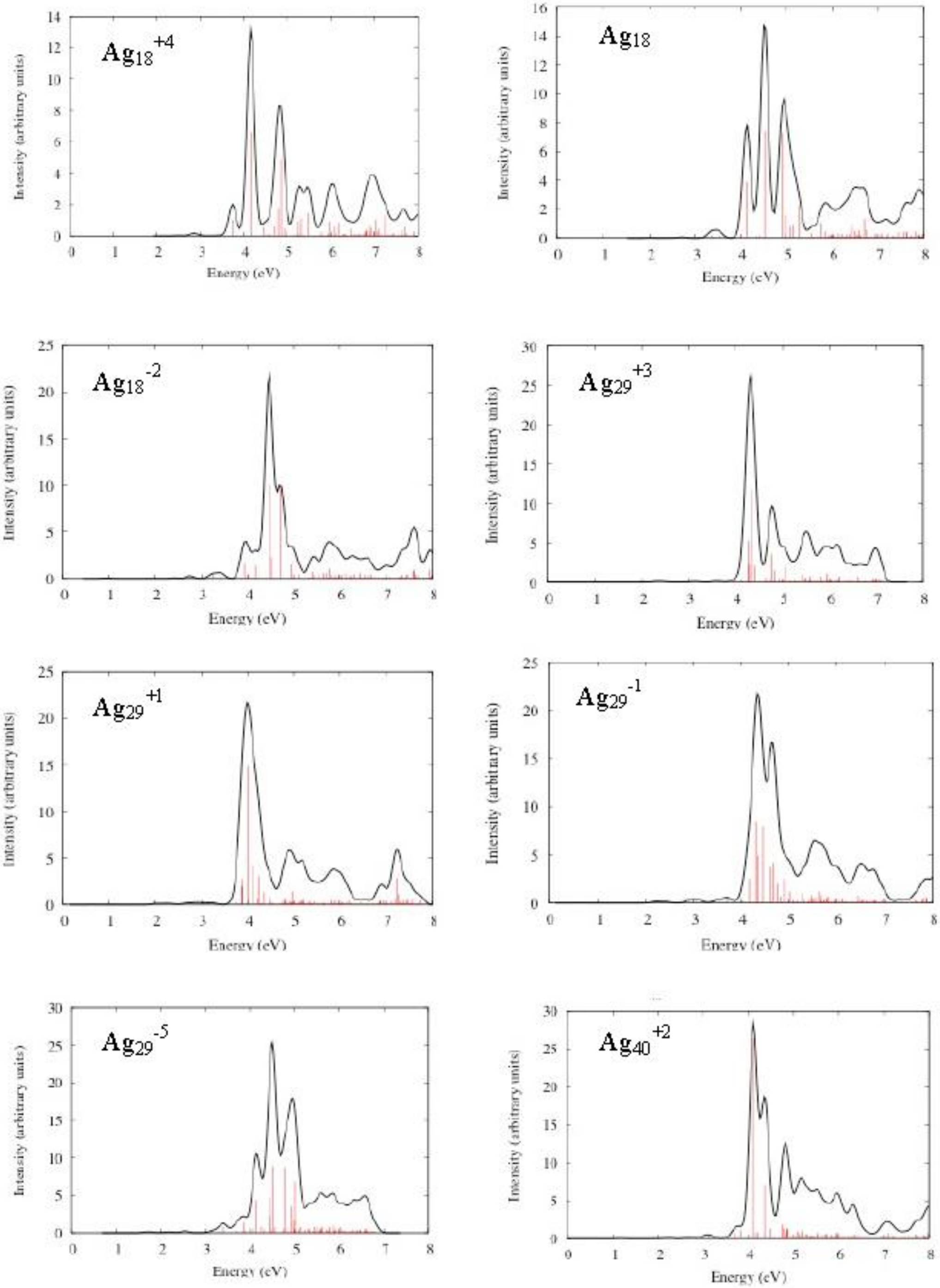

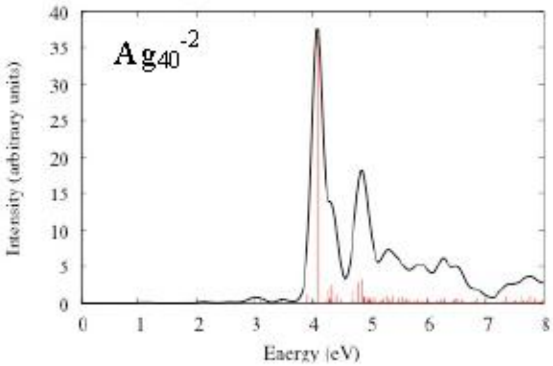
Ag_{40}^{-2}
Intensity (arbitrary units)
Energy (eV)
0 5 10 15 20 25 30 35 40
0 1 2 3 4 5 6 7 8

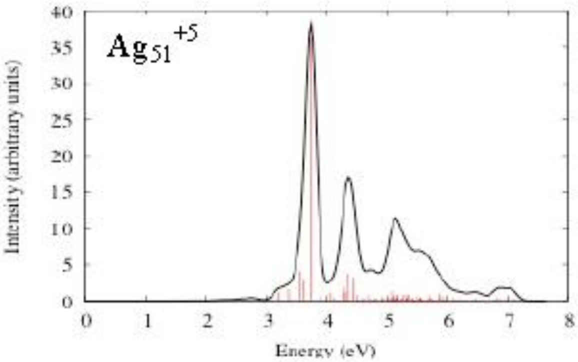
Ag_{51}^{+5}
Intensity (arbitrary units)
Energy (eV)
0 5 10 15 20 25 30 35 40
0 1 2 3 4 5 6 7 8

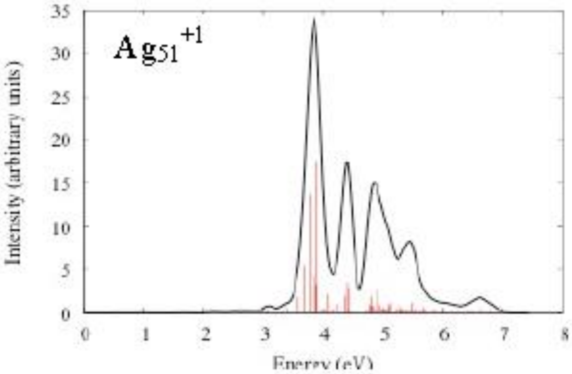
Ag_{51}^{+1}
Intensity (arbitrary units)
Energy (eV)
0 5 10 15 20 25 30 35
0 1 2 3 4 5 6 7 8

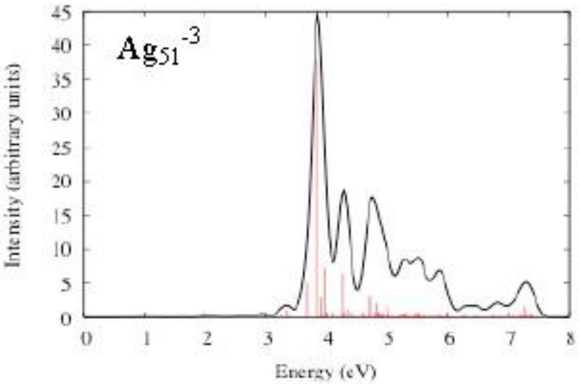
Ag_{51}^{-3}
Intensity (arbitrary units)
Energy (eV)
0 5 10 15 20 25 30 35 40 45
0 1 2 3 4 5 6 7 8

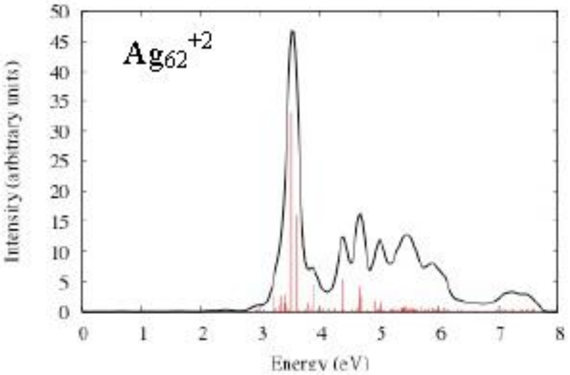
Ag_{62}^{+2}
Intensity (arbitrary units)
Energy (eV)
0 5 10 15 20 25 30 35 40 45 50
0 1 2 3 4 5 6 7 8

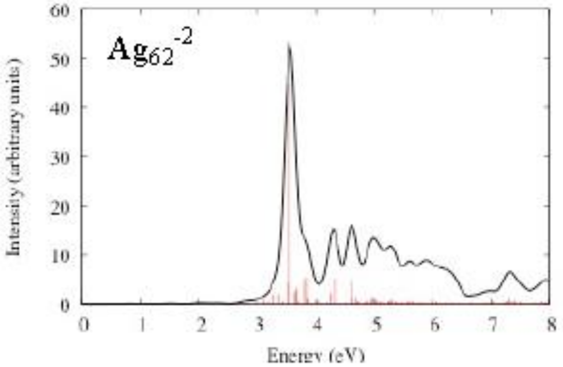
Ag_{62}^{-2}
Intensity (arbitrary units)
Energy (eV)
0 10 20 30 40 50 60
0 1 2 3 4 5 6 7 8

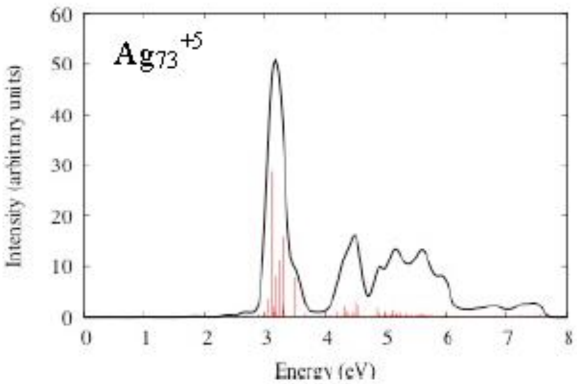
Ag_{73}^{+5}
Intensity (arbitrary units)
Energy (eV)
0 10 20 30 40 50 60
0 1 2 3 4 5 6 7 8

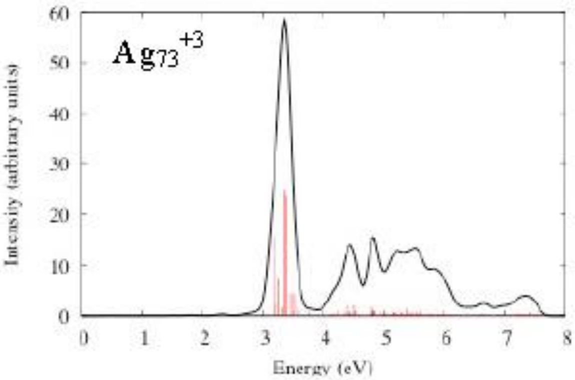
Ag_{73}^{+3}
Intensity (arbitrary units)
Energy (eV)
0 10 20 30 40 50 60
0 1 2 3 4 5 6 7 8

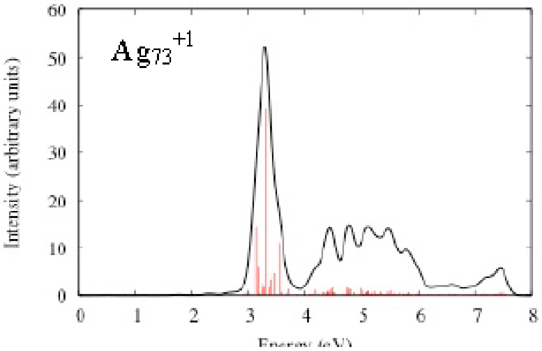
Ag73+1
Intensity (arbitrary units)
0
10
20
30
40
50
60
0
1
2
3
4
5
6
7
8
Energy (eV)

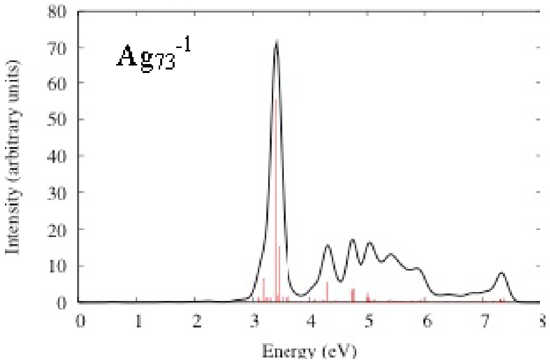
Ag73-1
Intensity (arbitrary units)
0
10
20
30
40
50
60
70
80
0
1
2
3
4
5
6
7
Energy (eV)

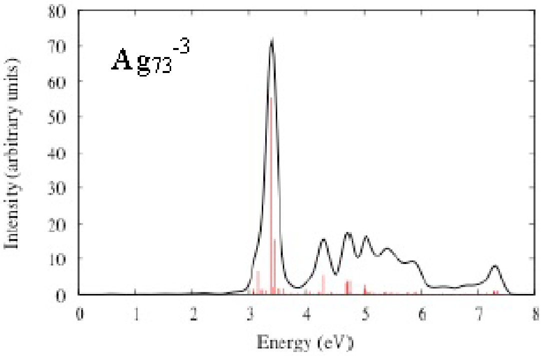
Ag73-3
Intensity (arbitrary units)
0
10
20
30
40
50
60
70
80
0
1
2
3
4
5
6
7
8
Energy (eV)

Figure B-2. Excitation spectra of large pentagon-shaped silver nanorods at the LB94/DZ level of theory.

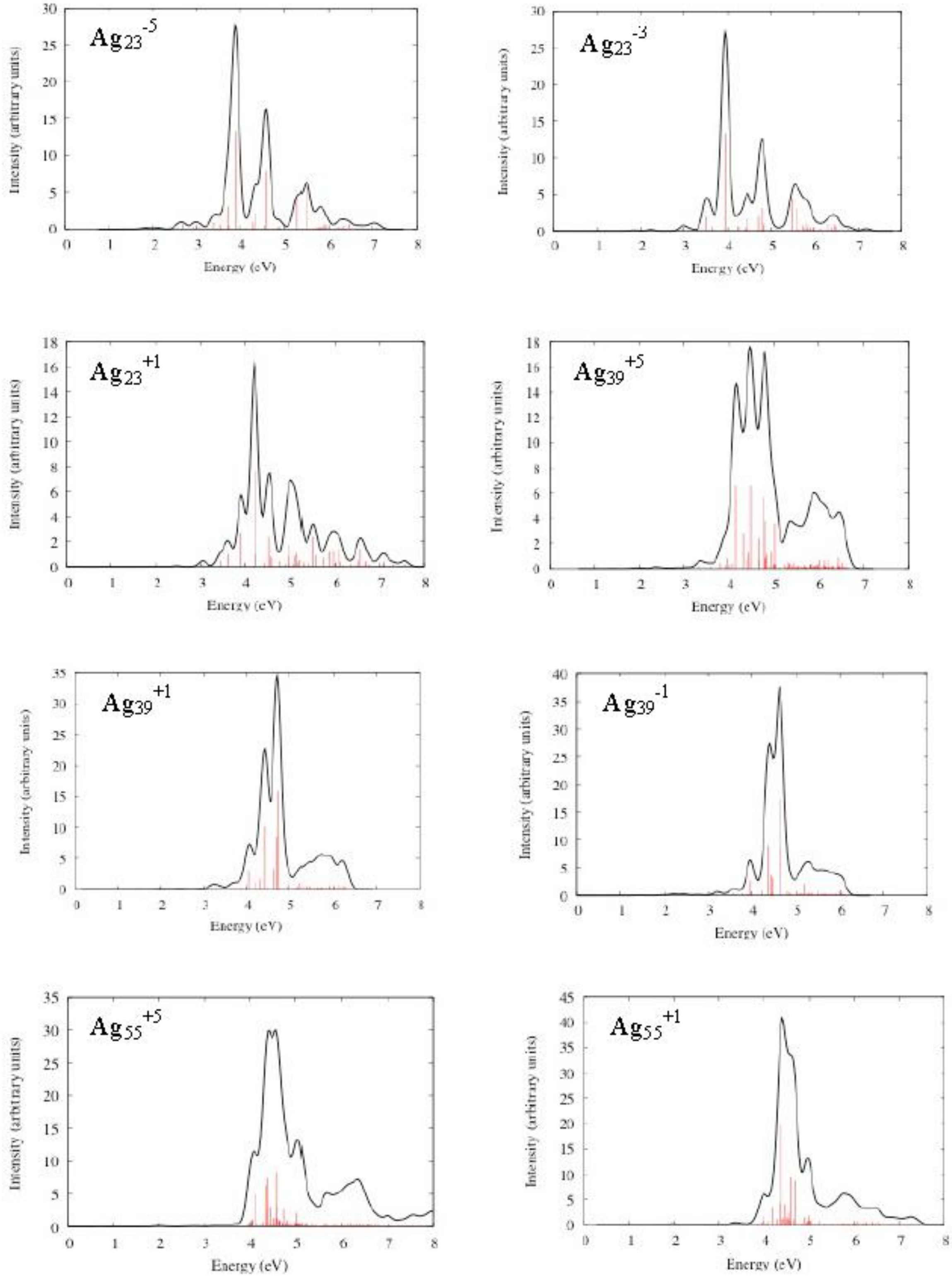

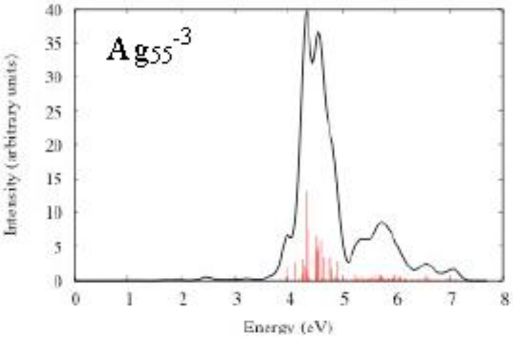
Ag_{55}^{-3}
Intensity (arbitrary units)
0
5
10
15
20
25
30
35
40
0
1
2
3
4
5
6
7
8
Energy (eV)

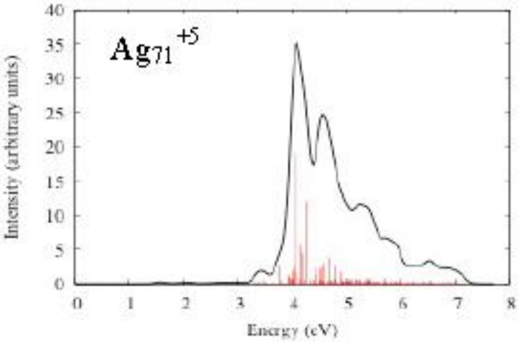
Ag_{71}^{+5}
Intensity (arbitrary units)
0
5
10
15
20
25
30
35
40
0
1
2
3
4
5
6
7
8
Energy (eV)

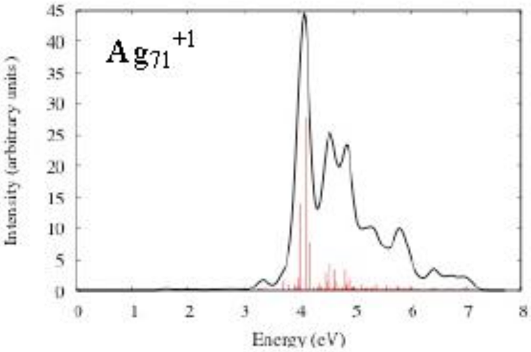
Ag_{71}^{+1}
Intensity (arbitrary units)
0
5
10
15
20
25
30
35
40
45
0
1
2
3
4
5
6
7
8
Energy (eV)

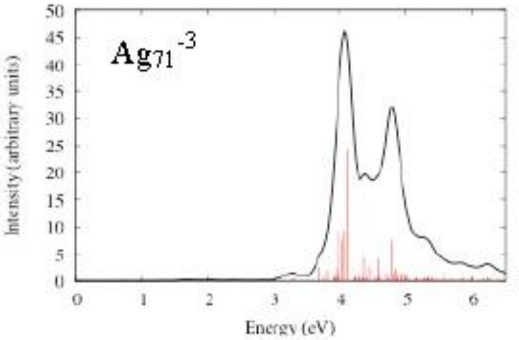
Ag_{71}^{-3}
Intensity (arbitrary units)
0
5
10
15
20
25
30
35
40
45
50
0
1
2
3
4
5
6
Energy (eV)

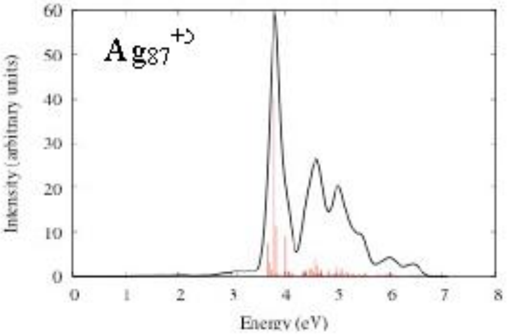
Ag_{87}^{+5}
Intensity (arbitrary units)
0
10
20
30
40
50
60
0
1
2
3
4
5
6
7
8
Energy (eV)

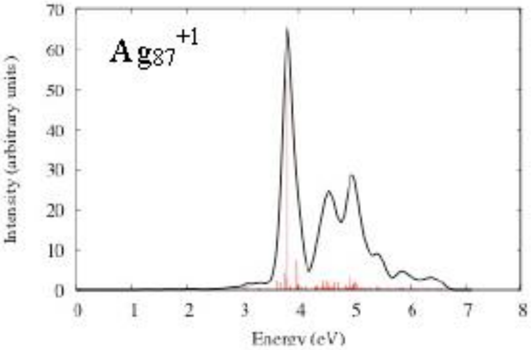
Ag_{87}^{+1}
Intensity (arbitrary units)
0
10
20
30
40
50
60
70
0
1
2
3
4
5
6
7
8
Energy (eV)

Figure B-3. Excitation spectra of small pentagon-shaped gold nanorods at the LB94/DZ level of theory.

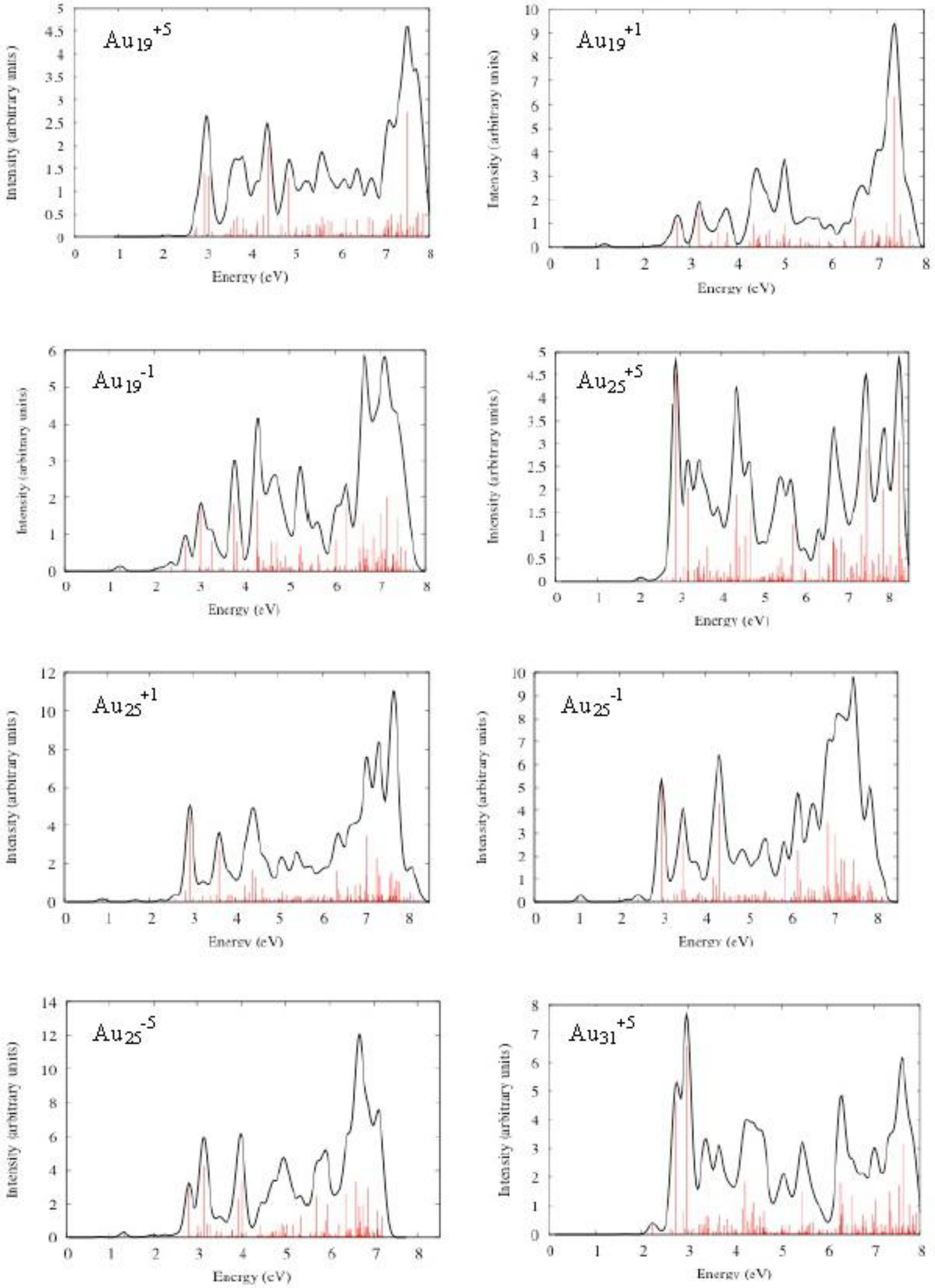

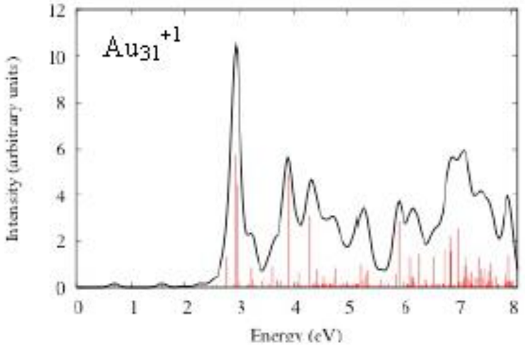
Au_{31}^{+1}
Intensity (arbitrary units)
0 2 4 6 8 10 12
0 1 2 3 4 5 6 7 8
Energy (eV)

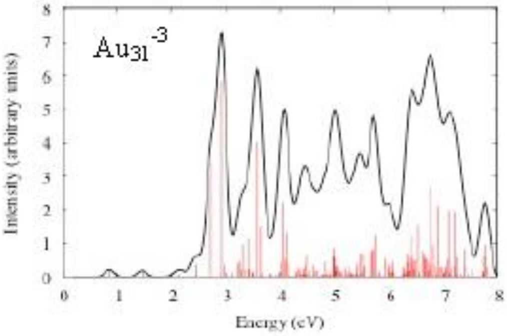
Au_{31}^{-3}
Intensity (arbitrary units)
0 1 2 3 4 5 6 7 8
0 1 2 3 4 5 6 7 8
Energy (eV)

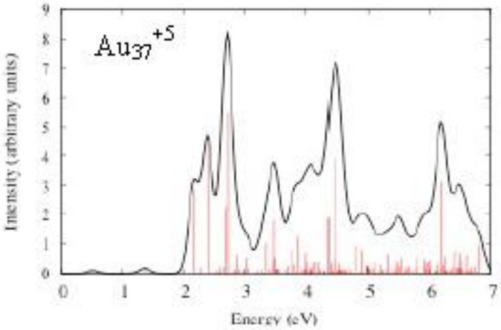
Au_{37}^{+5}
Intensity (arbitrary units)
0 1 2 3 4 5 6 7 8 9
0 1 2 3 4 5 6 7
Energy (eV)

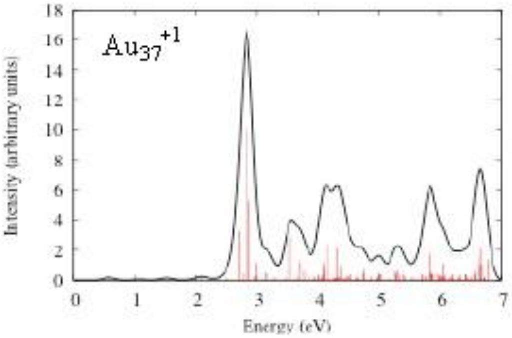
Au_{37}^{+1}
Intensity (arbitrary units)
0 2 4 6 8 10 12 14 16 18
0 1 2 3 4 5 6 7
Energy (eV)

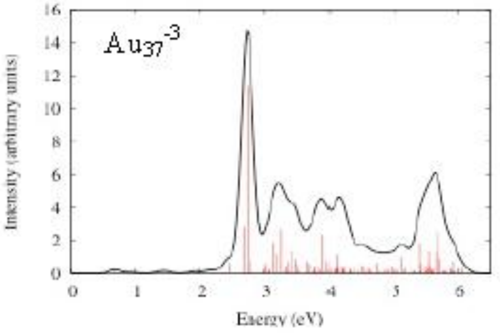
Au_{37}^{-3}
Intensity (arbitrary units)
0 2 4 6 8 10 12 14 16
0 1 2 3 4 5 6
Energy (eV)

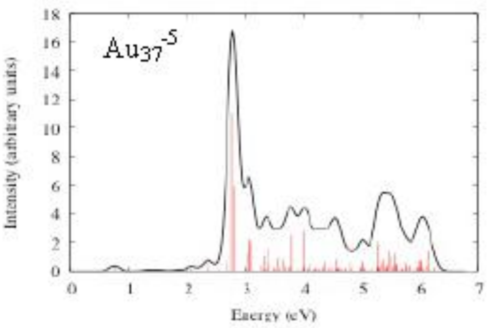
Au_{37}^{-5}
Intensity (abitrary units)
0 2 4 6 8 10 12 14 16 18
0 1 2 3 4 5 6 7
Energy (eV)

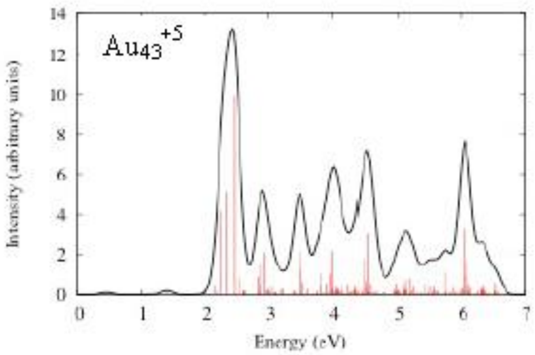
Au_{43}^{+5}
Intensity (abitrary units)
0 2 4 6 8 10 12 14
0 1 2 3 4 5 6 7
Energy (eV)

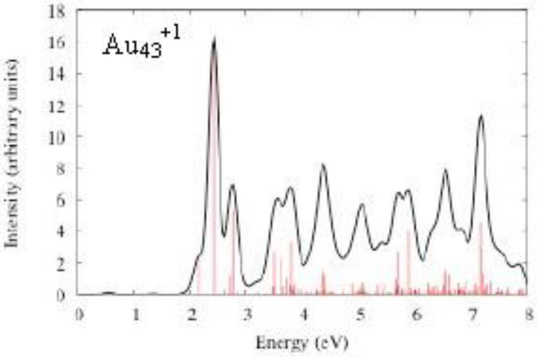
Au_{43}^{+1}
Intensity (arbitrary units)
0 2 4 6 8 10 12 14 16 18
0 1 2 3 4 5 6 7 8
Energy (eV)

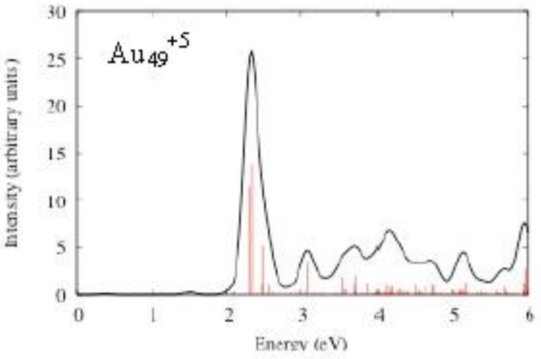
Au_{49}^{+5}
Intensity (arbitrary units)
Energy (eV)
0
5
10
15
20
25
30
0
1
2
3
4
5
6

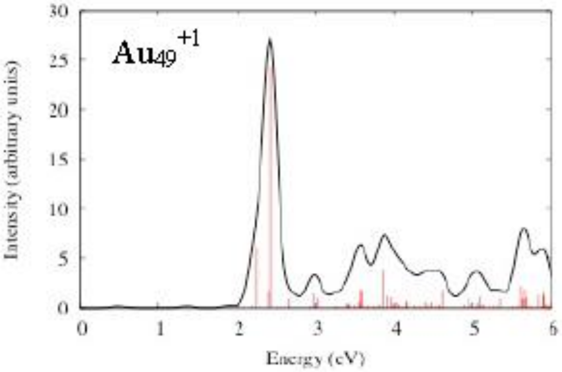
Au_{49}^{+1}
Intensity (arbitrary units)
Energy (eV)
0
5
10
15
20
25
30
0
1
2
3
4
5
6

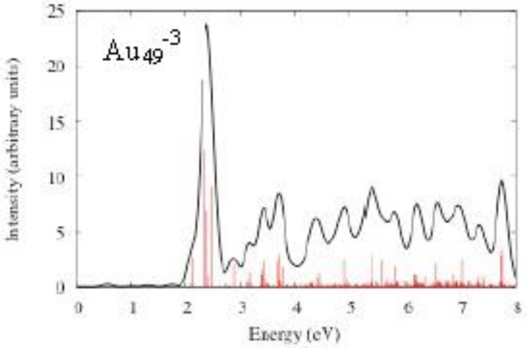
Au_{49}^{-3}
Intensity (arbitrary units)
Energy (eV)
0
5
10
15
20
25
0
1
2
3
4
5
6
7
8

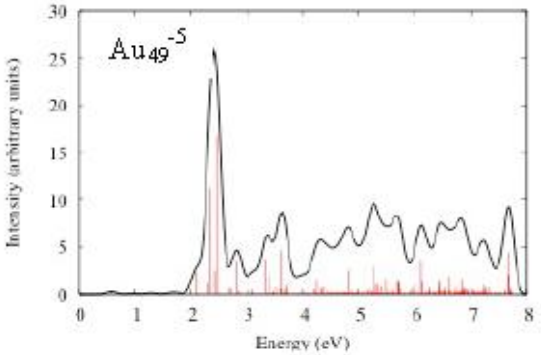
Au_{49}^{-5}
Intensity (arbitrary units)
Energy (eV)
0
5
10
15
20
25
30
0
1
2
3
4
5
6
7
8

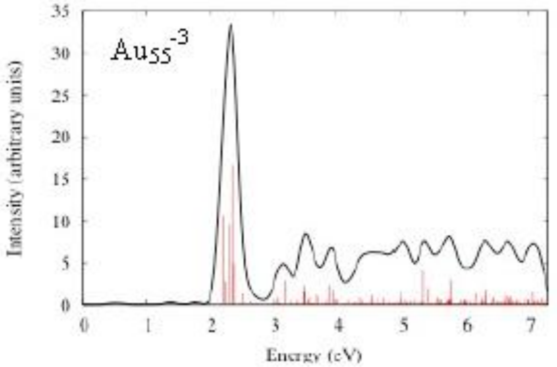
Au_{55}^{-3}
Intensity (arbitrary units)
Energy (eV)
0
5
10
15
20
25
30
35
0
1
2
3
4
5
6
7

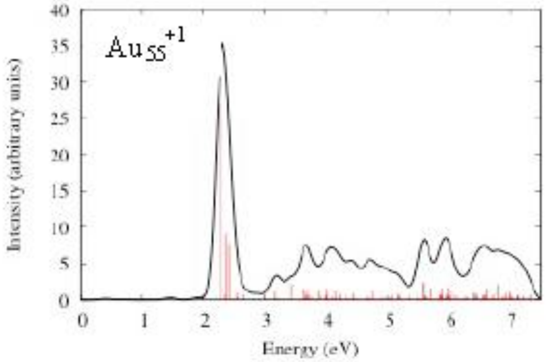
Au_{55}^{+1}
Intensity (arbitrary units)
Energy (eV)
0
5
10
15
20
25
30
35
40
0
1
2
3
4
5
6
7

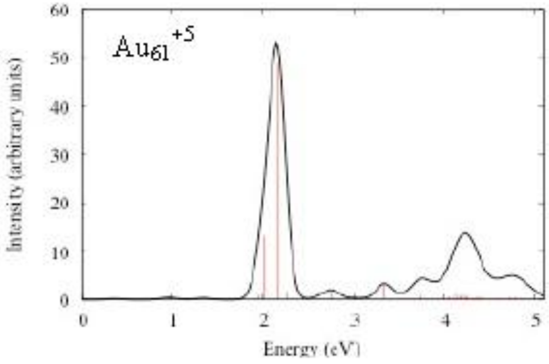
Au_{61}^{+5}
Intensity (arbitrary units)
Energy (eV)
0
10
20
30
40
50
60
0
1
2
3
4
5

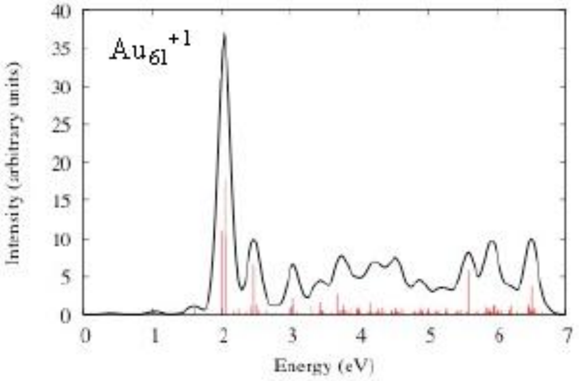
Au_{61}^{+1}
Intensity (arbitrary units)
Energy (eV)
0
5
10
15
20
25
30
35
40
0
1
2
3
4
5
6
7

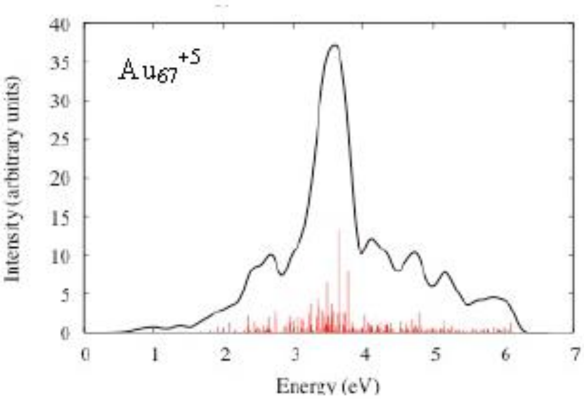
Au_{67}^{+5}
Intensity (arbitrary units)
Energy (eV)
0
5
10
15
20
25
30
35
40
0
1
2
3
4
5
6
7

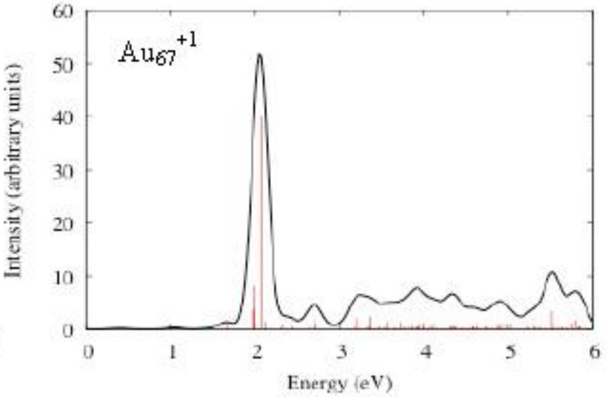
Au_{67}^{+1}
Intensity (arbitrary units)
Energy (eV)
0
10
20
30
40
50
60
0
1
2
3
4
5
6

Figure B-4. Excitation spectra of star-shaped nanorods at the LB94/DZ level of theory.

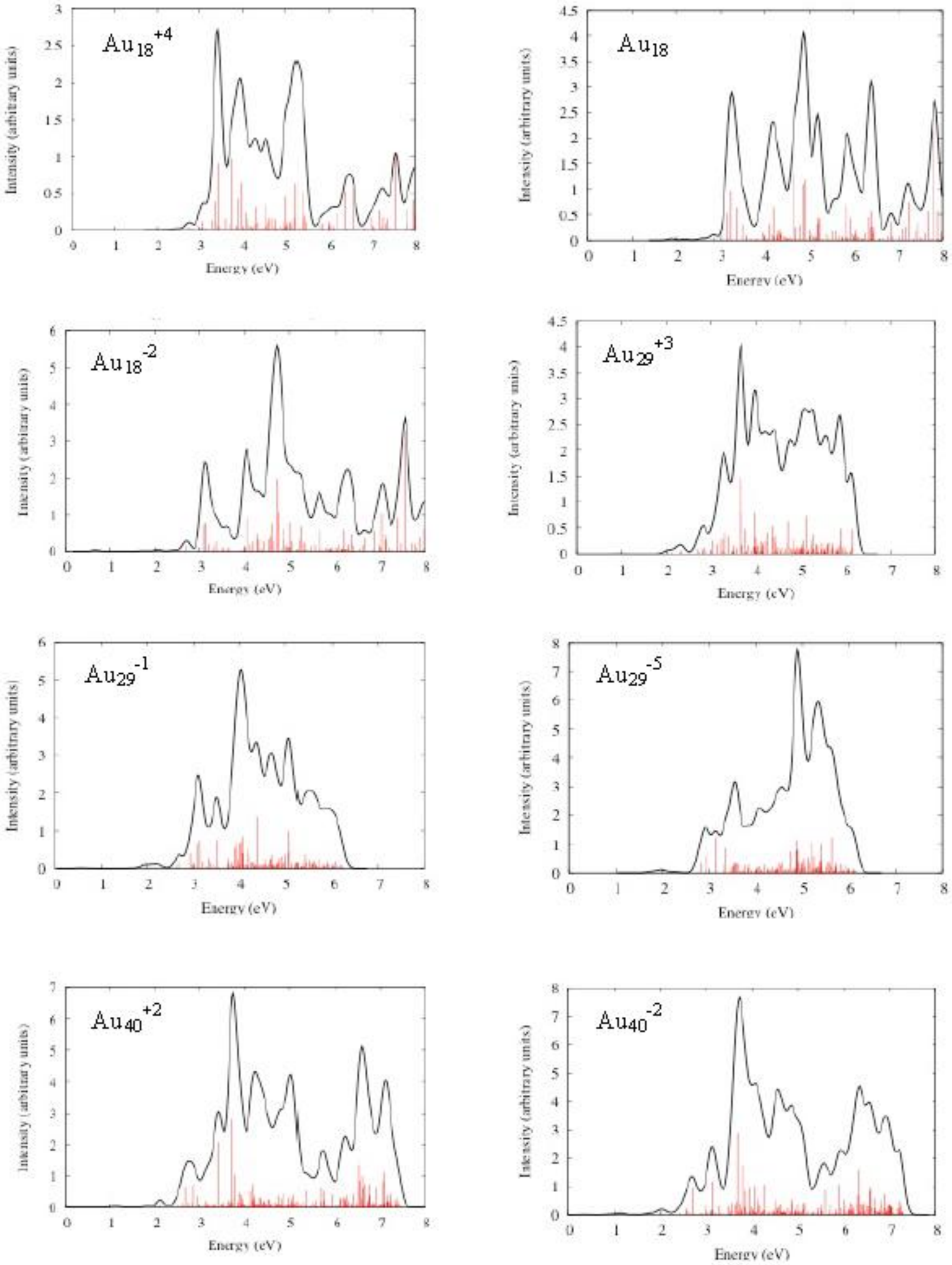

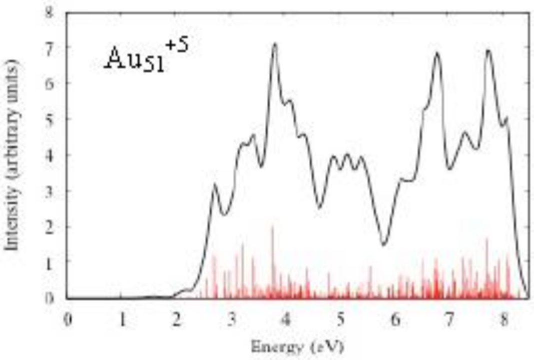
Au_{51}^{+5}
Intensity (arbitrary units)
Energy (eV)
0 1 2 3 4 5 6 7 8

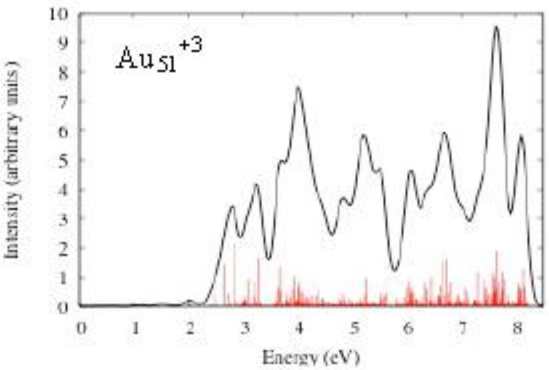
Au_{51}^{+3}
Intensity (arbitrary units)
Energy (eV)
0 1 2 3 4 5 6 7 8 9 10

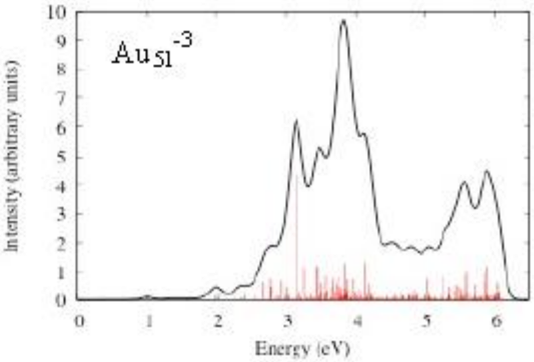
Au_{51}^{-3}
Intensity (arbitrary units)
Energy (eV)
0 1 2 3 4 5 6 7 8 9 10

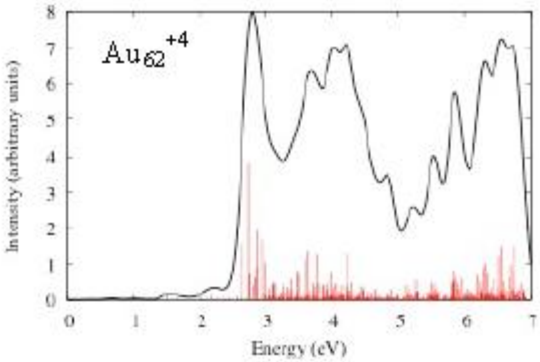
Au_{62}^{+4}
Intensity (arbitrary units)
Energy (eV)
0 1 2 3 4 5 6 7 8

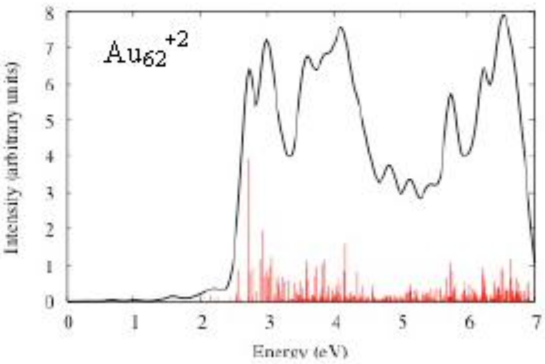
Au_{62}^{+2}
Intensity (arbitrary units)
Energy (eV)
0 1 2 3 4 5 6 7 8

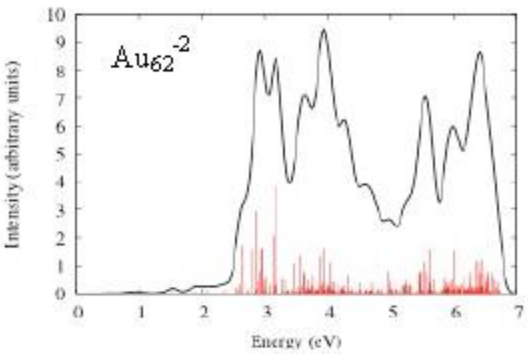
Au_{62}^{-2}
Intensity (arbitrary units)
Energy (eV)
0 1 2 3 4 5 6 7 8 9 10

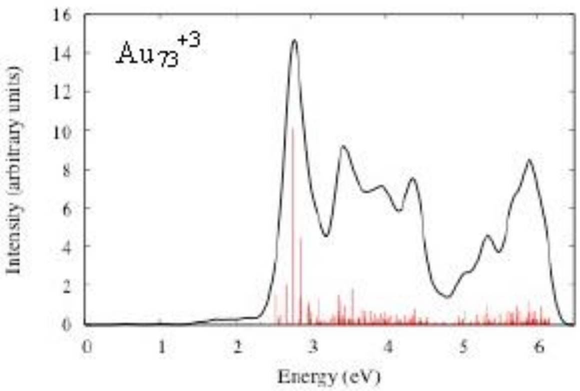
Au_{73}^{+3}
Intensity (arbitrary units)
Energy (eV)
0 2 4 6 8 10 12 14 16
0 1 2 3 4 5 6

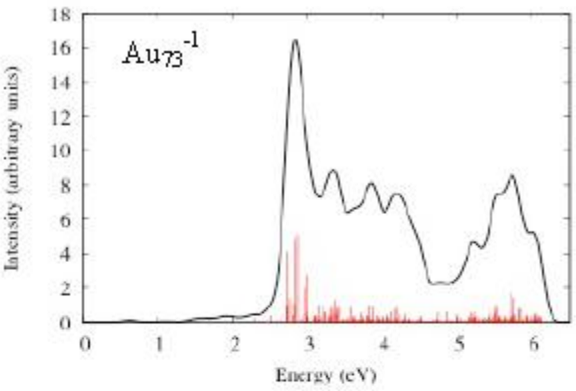
Au_{73}^{-1}
Intensity (arbitrary units)
Energy (eV)
0 2 4 6 8 10 12 14 16 18
0 1 2 3 4 5 6

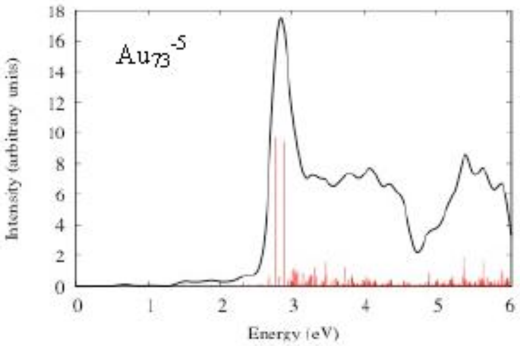
Au_{73}^{-5}
Intensity (arbitrary units)
Energy (eV)
0
2
4
6
8
10
12
14
16
18
0
1
2
3
4
5
6

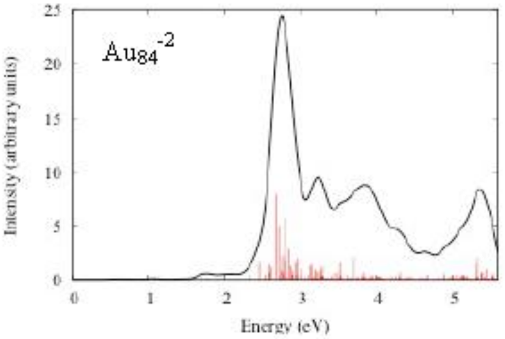
Au_{84}^{-2}
Intensity (arbitrary units)
Energy (eV)
0
5
10
15
20
25
0
1
2
3
4
5

Figure B-5. Excitation spectra of large pentagon-shaped gold nanorods at the LB94/DZ level of theory.

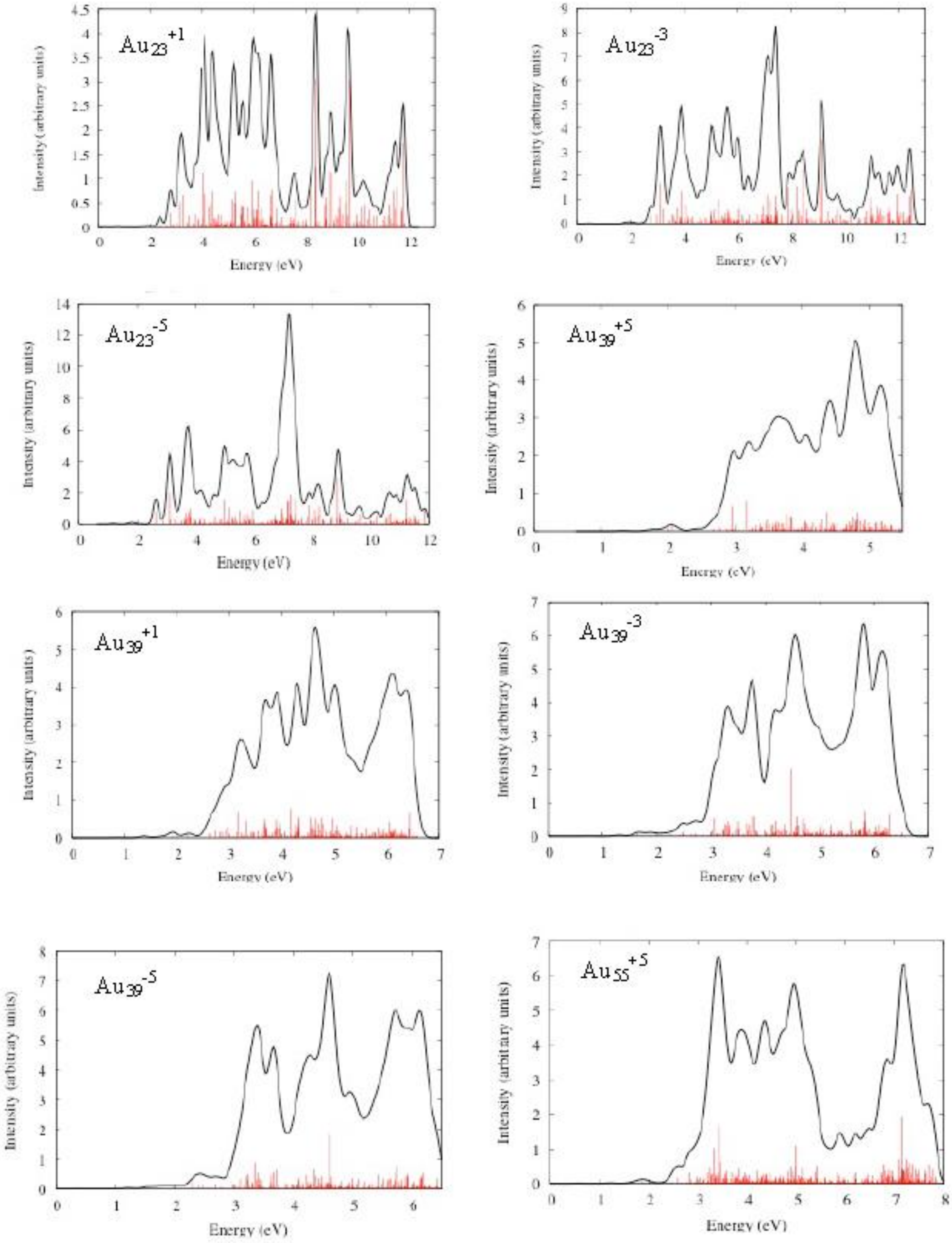

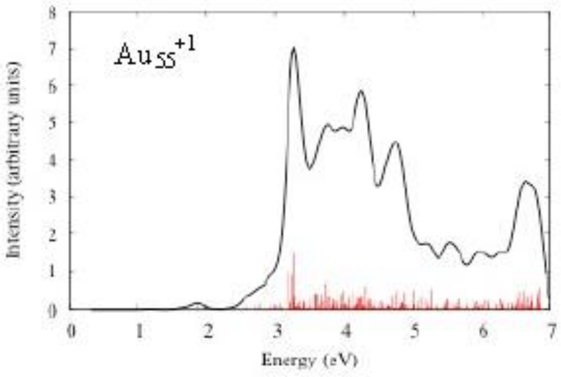

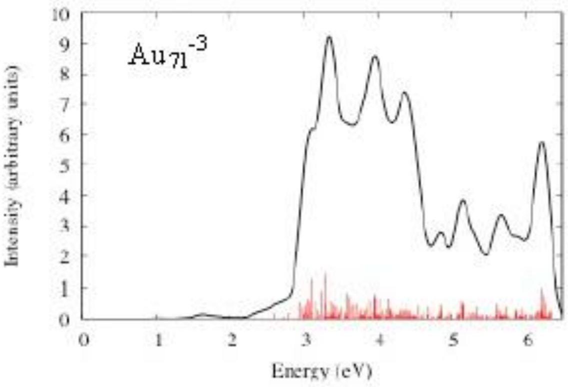

Figure B-6. Longitudinal peak wavelengths of positively charged and negatively charged A) star-shaped and B) large pentagon-shaped silver nanorods.

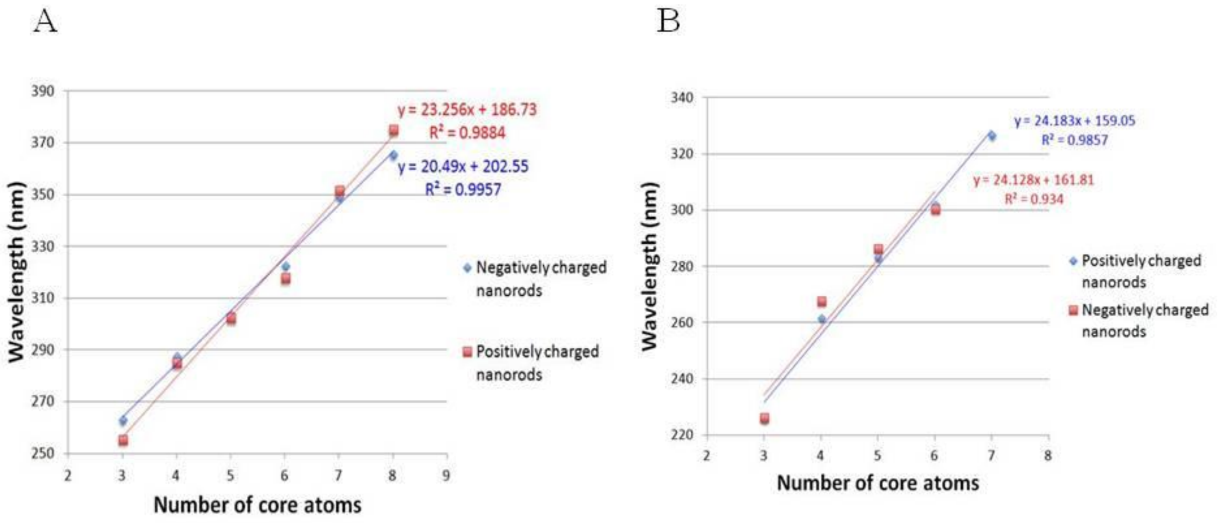

Table B.1. Longitudinal and transverse peak energies of negatively charged star-shaped silver nanorods.

System	Aspect ratio (L/2R)	Longitudinal peak (nm)	Transverse peak 1 (nm)	Transverse peak 2 (nm)	HOMO-LUMO gap (eV)
Ag_{18}^{-2}	0.88	263.01	278.15	276.94	0.76
Ag_{29}^{-1}	1.17	287.51	285.32	267.39	0.58
Ag_{40}^{-2}	1.53	303.51	284.91	254.76	0.21
Ag_{51}^{-3}	1.78	322.65	290.47	260.10	0.29
Ag_{62}^{-2}	2.12	349.26	287.15	268.55	0.14
Ag_{73}^{-1}	2.46	365.57	287.26	261.20	0.06
Ag_{84}^{-2}	2.80	392.76	286.95	257.94	0.19

Table B.2. Longitudinal and transverse peak energies of negatively charged large pentagon-shaped silver nanorods.

System	Aspect ratio (L/2R)	Longitudinal peak (nm)	Transverse peak 1 (nm)	Transverse peak 2 (nm)	HOMO-LUMO gap (eV)
Ag_{23}^{-3}	0.56	226.41	314.68	258.30	0.18
Ag_{39}^{-5}	0.94	267.97	283.91	267.39	0.02
Ag_{55}^{-3}	1.15	286.54	288.34	270.71	0.04
Ag_{71}^{-3}	1.48	300.64	303.88	258.30	0.24

Table B.3. Energy, oscillator strength, and transitions involved in the main longitudinal peak of the small pentagon-shaped Au_{67}^{+1} nanorod.

Energy (eV)	Intensity (a.u)	Transitions	z-component of transition dipole moment (a.u.)	Weight
2.0714	8.5160	Π_8 (HOMO-4) → Π_9 (LUMO+3)	-8.0604	0.2901
		Σ_{11} (HOMO) → Σ_{12} (LUMO+7)	-3.0604	0.1007
		Σ_{11} (HOMO) → 2 Σ_4 (LUMO+9)	-2.3431	0.0934
		Δ_3 (HOMO-1) → Δ_4 (LUMO)	-1.7648	0.0536

Figure B-7. Kohn-Sham orbitals for the transitions involved in the high intensity longitudinal peak of the small pentagon-shaped nanorods Au_{67}^{+1}. Contour value=0.01.

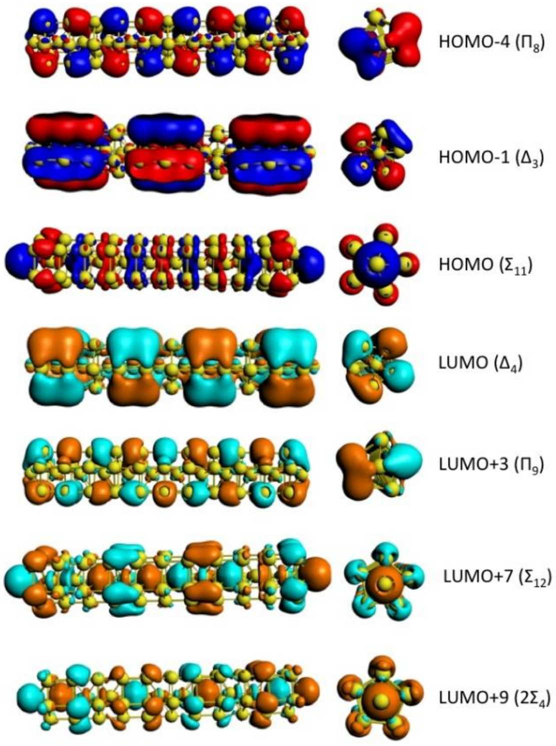
HOMO-4 (Π_8)
HOMO-1 (Δ_3)
HOMO (Σ_{11})
LUMO (Δ_4)
LUMO+3 (Π_9)
LUMO+7 (Σ_{12})
LUMO+9 ($2\Sigma_4$)

Appendix C - Supporting information for "Origin and TDDFT Benchmarking of the Plasmon Resonance in Acenes"

Figure C-1. Natural transition orbitals involved in the α and β-peak at the ωPBEh/cc-pVTZ level of theory.

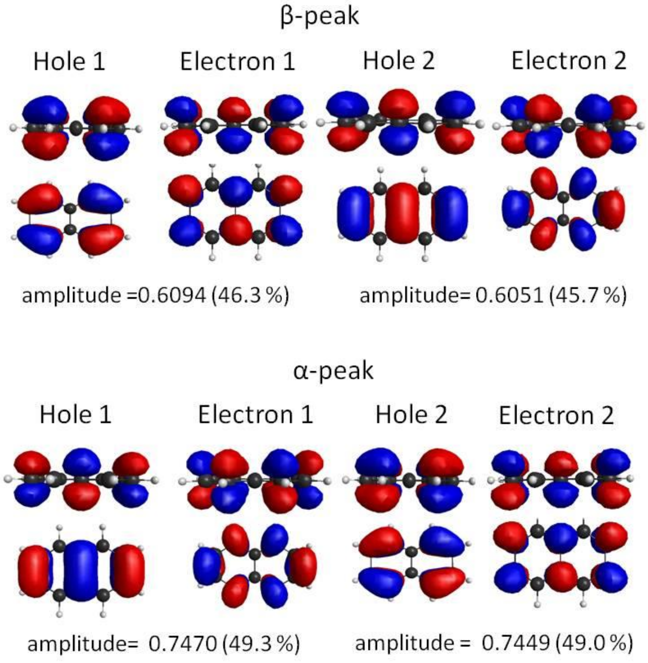
β-peak
Hole 1
Electron 1
Hole 2
Electron 2
amplitude =0.6094 (46.3 %)
amplitude= 0.6051 (45.7 %)
α-peak
Hole 1
Electron 1
Hole 2
Electron 2
amplitude= 0.7470 (49.3 %)
amplitude = 0.7449 (49.0 %)

Appendix D - Supporting information for "Plasmon Resonance Analysis with Configuration Interaction"

Table D.1. Energies and oscillator strengths for varying values of α_1 (case 2). Case 1 is shown in red.

$\Delta\alpha_1$ (%)	α_1 (eV)	E_1 (eV)	S_1 (a.u)	E_2 (eV)	S_2 (a.u)	E_3 (eV)	S_3 (a.u)
-50	2.5	4.5	0	2.3417	0.4448	5.6583	2.5552
-40	3.0	4.5	0	2.8139	0.3684	5.6861	2.6315
-30	3.5	4.5	0	3.2753	0.2752	5.7247	2.7248
-20	4.0	4.5	0	3.7192	0.1661	5.7808	2.8338
-10	4.5	4.5	0	4.134	0.0566	5.866	2.9433
-5	4.75	4.5	0	4.3246	0.0164	5.9254	2.9836
-1	4.95	4.5	0	4.4663	0.0007	5.9837	2.9991
0	5.0	4.5	0	4.5	0.0000	6	3.0000
1	5.05	4.5	0	4.533	0.0008	6.017	2.9991
5	5.25	4.5	0	4.6569	0.0203	6.0931	2.9798
10	5.5	4.5	0	4.7929	0.0858	6.2071	2.9142
20	6.0	4.5	0	5	0.1044	6.5	2.8958
30	6.5	4.5	0	5.134	0.1245	6.866	2.8751
40	7.0	4.5	0	5.2192	0.1945	7.2808	2.8056
50	7.5	4.5	0	5.2753	0.3334	7.7247	2.6664

Analytical derivation of the behavior of the energies E_2 and E_3 with increasing value of α_1 (case 2).

The second and third eigenvalue expressions can be divided into two ε-dependent terms. The first term is $\mathrm{T}_1 = \alpha + \frac{1}{2}(\varepsilon + \beta)$, which increases linearly with ε. This term is the same for both E_2 and E_3. The second term is $\mathrm{T}_2 = \pm\frac{1}{2}\sqrt{9\beta^2 - 2\beta\varepsilon + \varepsilon^2}$. The plus sign is for E_3 and the negative sign is for E_2. The expression under the square root is quadratic. We note that the value $\sqrt{9\beta^2 - 2\beta\varepsilon + \varepsilon^2}$ is always positive regardless of the value of ε since β is real. For the eigenvalue E_2, T_2 increases with increasing ε until it reaches its maximum value $\varepsilon = \beta = 0.5$. For $\varepsilon > \beta$, T_2 decreases. As a result, E_2 is expected to become larger until ε reaches the value of β. Due to the opposite sign of T_2, the opposite behavior is expected for E_3. E_3 therefore becomes larger with increasing ε when $\varepsilon > \beta$.

The values of T_1 and T_2 for the E_2 and E_3 peaks for the CI matrix given by eq. 12 are given in Tables S2 and S3. When α_1 increases from 2.5 to 5.5 eV, both T_1 and T_2 become larger and therefore E_2 does as well. When α_1 becomes larger than 5.5 eV ($\varepsilon > \beta$), T_2 starts to decrease and E_2 starts to stabilize. The peak at E_3 (the plasmon peak) shows the opposite behavior: its energy slowly increases when α_1 shifts from 2.5 to 5.5 eV ($\varepsilon < \beta$) and quickly rises when α_1 becomes larger than 5.5 eV, as explained by the opposite sign of T_2 in the analytical expression.

Table D.2. Values of T_1 and T_2 for the E_2 peak (case 2).

α_1 (eV)	ε (eV)	E_2 (eV)	T_1 (eV)	T_2 (eV)
2.5	-2.5	2.3417	4.0000	-1.6583
3	-2	2.8139	4.2500	-1.4361
3.5	-1.5	3.2753	4.5000	-1.2247
4	-1	3.7192	4.7500	-1.0308
4.5	-0.5	4.1340	5.0000	-0.8660
4.75	-0.25	4.3246	5.1250	-0.8004
4.95	-0.05	4.4663	5.2250	-0.7587
5	0	4.5000	5.2500	-0.7500
5.05	0.05	4.5330	5.2750	-0.7420
5.25	0.25	4.6569	5.3750	-0.7181
5.5	0.5	4.7929	5.5000	-0.7071
6	1	5.0000	5.7500	-0.7500
6.5	1.5	5.1340	6.0000	-0.8660
7	2	5.2192	6.2500	-1.0308
7.5	2.5	5.2753	6.5000	-1.2247

Table D.3. Values of T_1 and T_2 for the E_3 peak (case 2).

α_1 (eV)	ε (eV)	E_3 (eV)	T_1 (eV)	T_2 (eV)
2.5	-2.5	5.6583	4.0000	1.6583
3	-2	5.6861	4.2500	1.4361
3.5	-1.5	5.7247	4.5000	1.2247
4	-1	5.7808	4.7500	1.0308
4.5	-0.5	5.8660	5.0000	0.8660
4.75	-0.25	5.9254	5.1250	0.8004
4.95	-0.05	5.9837	5.2250	0.7587
5	0	6.0000	5.2500	0.7500
5.05	0.05	6.0170	5.2750	0.7420
5.25	0.25	6.0931	5.3750	0.7181
5.5	0.5	6.2071	5.5000	0.7071
6	1	6.5000	5.7500	0.7500
6.5	1.5	6.8660	6.0000	0.8660
7	2	7.2808	6.2500	1.0308
7.5	2.5	7.7247	6.5000	1.2247

Table D.4. Eigenvectors of the CI matrix for case 2 where α_1=2.5 eV.

	E_1= 4.5 eV	E_2= 2.3417 eV	E_3= 5.6583 eV
A_1	0	0.9758	0.2185
A_2	0.7071	-0.1545	0.6900
A_3	-0.7071	-0.1545	0.6900
$\|A_1+A_2+A_3\|^2$	0	0.4448	2.5552

Table D.5. Eigenvectors of the CI matrix for case 2 where α_1=3.0 eV.

	E_1= 4.5 eV	E_2= 2.8139 eV	E_3= 5.6861 eV
A_1	0	0.9671	0.2546
A_2	0.7071	-0.1800	0.6838
A_3	-0.7071	-0.1800	0.6838
$\|A_1+A_2+A_3\|^2$	0	0.3684	2.6315

Table D.6. Eigenvectors of the CI matrix for case 2 where α_1=3.5 eV.

	E_1= 4.5 eV	E_2= 3.2753 eV	E_3= 5.7247 eV
A_1	0	0.9530	0.3029
A_2	0.7071	-0.2142	0.6739
A_3	-0.7071	-0.2142	0.6739
$\|A_1+A_2+A_3\|^2$	0	0.2752	2.7248

Table D.7. Eigenvectors of the CI matrix for case 2 where α_1=4.0 eV.

	E_1= 4.5 eV	E_2= 3.7192 eV	E_3= 5.7808 eV
A_1	0	0.9294	0.3690
A_2	0.7071	-0.2610	0.6572
A_3	-0.7071	-0.2610	0.6572
$\|A_1+A_2+A_3\|^2$	0	0.1661	2.8338

Table D.8. Eigenvectors of the CI matrix for case 2 where α_1=4.5 eV.

	E_1= 4.5 eV	E_2= 4.1340 eV	E_3= 5.8660 eV
A_1	0	0.8881	0.4597
A_2	0.7071	-0.3251	0.6280
A_3	-0.7071	-0.3251	0.6280
$\|A_1+A_2+A_3\|^2$	0	0.0.0566	2.9432

Table D.9. Eigenvectors of the CI matrix for case 2 where α_1=4.75 eV.

	E_1= 4.5 eV	E_2= 4.3246 eV	E_3= 5.9254 eV
A_1	0	0.8569	0.5155
A_2	0.7071	-0.3645	0.6059
A_3	-0.7071	-0.3645	0.6059
$\|A_1+A_2+A_3\|^2$	0	0.0164	2.9836

Table D.10. Eigenvectors of the CI matrix for case 2 where α_1=4.95 eV.

	E_1= 4.5 eV	E_2= 4.4663 eV	E_3= 5.9837 eV
A_1	0	0.8254	0.5646
A_2	0.7071	-0.3992	0.5836
A_3	-0.7071	-0.3992	0.5836
$\|A_1+A_2+A_3\|^2$	0	0.0007	2.9991

Table D.11. Eigenvectors of the CI matrix for case 2 where α_1=5.05 eV.

	E_1= 4.5 eV	E_2= 4.533 eV	E_3= 6.017 eV
A_1	0	0.8072	0.5902
A_2	0.7071	-0.4174	0.5708
A_3	-0.7071	-0.4174	0.5708
$\|A_1+A_2+A_3\|^2$	0	0.0008	2.9991

Table D.12. Eigenvectors of the CI matrix for case 2 where α_1=5.25 eV.

	E_1= 4.5 eV	E_2= 4.6569 eV	E_3= 6.0931 eV
A_1	0	0.7662	0.6426
A_2	0.7071	-0.4544	0.5418
A_3	-0.7071	-0.4544	0.5418
$\|A_1+A_2+A_3\|^2$	0	0.0203	2.9798

Table D.13. Eigenvectors of the CI matrix for case 2 where α_1=5.5 eV.

	E_1= 4.5 eV	E_2= 4.7929 eV	E_3= 6.2071 eV
A_1	0	0.7071	0.7071
A_2	0.7071	-0.5	0.5
A_3	-0.7071	-0.5	0.5
$\|A_1+A_2+A_3\|^2$	0	0.0858	2.9142

Table D.14. Eigenvectors of the CI matrix for case 2 where α_1=6.0 eV.

	E_1= 4.5 eV	E_2= 5.0 eV	E_3= 6.5 eV
A_1	0	0.5774	0.8165
A_2	0.7071	-0.5774	0.4082
A_3	-0.7071	-0.5774	0.4082
$\|A_1+A_2+A_3\|^2$	0	0.3334	2.6663

Table D.15. Eigenvectors of the CI matrix for case 2 where α_1=6.5 eV.

	E_1= 4.5 eV	E_2= 5.134 eV	E_3= 6.866 eV
A_1	0	0.4597	-0.8881
A_2	0.7071	-0.628	-0.3251
A_3	-0.7071	-0.628	-0.3251
$\|A_1+A_2+A_3\|^2$	0	0.6341	2.3664

Table D.16. Eigenvectors of the CI matrix for case 2 where α_1=7 eV.

	E_1= 4.5 eV	E_2= 5.2192 eV	E_3= 7.2808 eV
A_1	0	0.369	-0.9294
A_2	0.7071	-0.6572	-0.261
A_3	-0.7071	-0.6572	-0.261
$\lvert A_1+A_2+A_3\rvert^2$	0	0.8938	2.1066

Table D.17. Eigenvectors of the CI matrix for case 2 where α_1=7.5 eV.

	E_1= 4.5 eV	E_2= 5.2753 eV	E_3= 7.7247 eV
A_1	0	0.3029	-0.953
A_2	0.7071	-0.6739	-0.2142
A_3	-0.7071	-0.6739	-0.2142
$\lvert A_1+A_2+A_3\rvert^2$	0	1.0918	1.9083

Table D.18. Energies and oscillator strengths for different values of α_3 (case 3).

$\Delta\alpha_3$(%)	α_3 (eV)	E_1 (eV)	S_1 (a.u)	E_2 (eV)	S_2 (a.u)	E_3 (eV)	S_3 (a.u)
-50	2.5	2.359	0.4952	4.8207	0.3329	6.3202	2.1718
-40	3	2.836	0.4273	4.8272	0.3408	6.3368	2.2317
-30	3.5	3.3038	0.3407	4.8373	0.3520	6.3589	2.3074
-20	4	3.7554	0.2290	4.8554	0.3681	6.3892	2.4028
-10	4.5	4.1723	0.0918	4.8946	0.3846	6.4331	2.5236
-5	4.75	4.3532	0.0284	4.9339	0.3785	6.4628	2.5931
-1	4.95	4.4741	0.0012	4.9841	0.3469	6.4919	2.6517
0	5.0	4.5	0.0000	5.0	0.3334	6.5	2.6664
1	5.05	4.5241	0.0012	5.0174	0.3173	6.5085	2.6814
5	5.25	4.6015	0.0279	5.1014	0.2331	6.5471	2.7390
10	5.5	4.6624	0.0832	5.2304	0.1160	6.6072	2.8009
20	6	4.7192	0.1661	5.5	0.0000	6.7808	2.8338
30	6.5	4.7429	0.2070	5.714	0.1151	7.0431	2.6778
50	7.5	4.7629	0.2290	5.9437	0.3681	7.7934	2.4028

Table D.19. Eigenvectors of the CI matrix for case 3 where α_3=2.5 eV.

	E_1= 2.3590 eV	E_2= 4.8207 eV	E_3= 6.3202 eV
A_1	-0.1120	-0.4248	-0.8983
A_2	-0.1643	0.8995	-0.4048
A_3	0.9800	0.1023	-0.1706
$\lvert A_1+A_2+A_3\rvert^2$	0.4952	0. 3329	2.1718

Table D.20. Eigenvectors of the CI matrix for case 3 where α_3=3.0 eV.

	E_1= 2.8360 eV	E_2= 4.8272 eV	E_3= 6.3368 eV
A_1	-0.1227	-0.4338	-0.8926
A_2	-0.1964	0.8922	-0.4067
A_3	0.9728	0.1254	-0.1947
$\lvert A_1+A_2+A_3\rvert^2$	0.4273	0.3408	2.2317

Table D.21. Eigenvectors of the CI matrix for case 3 where α_3=3.5 eV.

	E_1= 3.3038 eV	E_2= 4.8373 eV	E_3= 6.3589 eV
A_1	-0.1329	-0.4477	-0.8843
A_2	-0.2440	0.8795	-0.4086
A_3	0.9606	0.1615	-0.2261
$\lvert A_1+A_2+A_3\rvert^2$	0.3407	0.3520	2.3074

Table D.22. Eigenvectors of the CI matrix for case 3 where α_3=4.0 eV.

	E_1= 3.7554 eV	E_2= 4.8554 eV	E_3= 6.3892 eV
A_1	-0.1371	-0.4706	-0.8716
A_2	-0.3213	0.8535	-0.4103
A_3	0.9370	0.2238	-0.2683
$\lvert A_1+A_2+A_3\rvert^2$	0.2290	0.3681	2.4028

Table D.23. Eigenvectors of the CI matrix for case 3 where α_3=4.5 eV.

	E_1= 4.1723 eV	E_2= 4.8946 eV	E_3= 6.4331eV
A_1	-0.1141	-0.5122	-0.8512
A_2	-0.4623	0.7858	-0.4109
A_3	0.8794	0.3466	-0.3265
$\|A_1+A_2+A_3\|^2$	0.0918	0.3846	2.5237

Table D.24. Eigenvectors of the CI matrix for case 3 where α_3=4.75 eV.

	E_1= 4.3532 eV	E_2= 4.9339 eV	E_3= 6.4628eV
A_1	-0.0734	-0.5434	-0.8363
A_2	-0.5738	0.7088	-0.4102
A_3	0.8157	0.4497	-0.3639
$\|A_1+A_2+A_3\|^2$	0.0284	0.3785	2.5931

Table D.25. Eigenvectors of the CI matrix for case 3 where α_3=4.95 eV.

	E_1= 4.4741 eV	E_2= 4.9841 eV	E_3= 6.4919 eV
A_1	0.0172	0.5708	-0.8209
A_2	0.6803	-0.6084	-0.4088
A_3	-0.7328	-0.5514	-0.3988
$\|A_1+A_2+A_3\|^2$	0.0012	0.3469	2.6517

Table D.26. Eigenvectors of the CI matrix for case 3 where α_3=5.05 eV.

	E_1= 4.5241 eV	E_2= 5.0174 eV	E_3= 6.5085 eV
A_1	-0.0181	0.5836	0.8118
A_2	0.7332	-0.5443	0.4076
A_3	-0.6798	-0.6026	0.4180
$\|A_1+A_2+A_3\|^2$	0.0012	0.3173	2.6814

Table D.27. Eigenvectors of the CI matrix for case 3 where α_3=5.25 eV.

	E_1= 4.6015 eV	E_2= 5.1014 eV	E_3= 6.5471 eV
A_1	-0.0929	-0.6056	0.7903
A_2	0.8219	0.4014	0.4042
A_3	-0.5621	0.6870	0.4605
$\|A_1+A_2+A_3\|^2$	0.0279	0.2331	2.7390

Table D.28. Eigenvectors of the CI matrix for case 3 where α_3=5.5 eV.

	E_1= 4.6624 eV	E_2= 5.2304 eV	E_3= 6.6072 eV
A_1	-0.1721	-0.6318	0.7558
A_2	0.8877	0.2332	0.3971
A_3	-0.4271	0.7392	0.5207
$\|A_1+A_2+A_3\|^2$	0.0832	0.1160	2.8009

Table D.29. Eigenvectors of the CI matrix for case 3 where α_3=6.0 eV.

	E_1= 4.7192 eV	E_2= 5.50 eV	E_3= 6.7808 eV
A_1	0.2610	0.7071	0.6572
A_2	-0.9294	0	0.3690
A_3	0.2610	-0.7071	0.6572
$\|A_1+A_2+A_3\|^2$	0.1917	0	2.8338

Table D.30. Eigenvectors of the CI matrix for case 3 where α_3=6.5 eV.

	E_1= 4.7429 eV	E_2= 5.7140 eV	E_3= 7.0431 eV
A_1	0.3005	0.7928	-0.5302
A_2	-0.9365	0.1398	0.3217
A_3	0.1810	-0.5932	0.7844
$\|A_1+A_2+A_3\|^2$	0.2070	0.1151	2.6778

Table D.31. Eigenvectors of the CI matrix for case 3 where α_3=7 eV.

	E_1= 4.7554 eV	E_2= 5.8554 eV	E_3= 7.3892 eV
A_1	0.3213	0.8535	0.4103
A_2	-0.9370	0.2238	0.2683
A_3	-0.1371	-0.4706	0.8716
$\|A_1+A_2+A_3\|^2$	0.2290	0.3681	2.4028

Table D.32. Eigenvectors of the CI matrix for case 3 where α_3=7.5 eV.

	E_1= 4.7629 eV	E_2= 5.9437 eV	E_3= 7.7934 eV
A_1	0.3339	0.8871	0.3188
A_2	-0.9362	0.2726	0.2220
A_3	0.1100	-0.3726	0.9215
$\|A_1+A_2+A_3\|^2$	0.2423	0.6195	2.1380

Table D.33. Energies and oscillator strengths for varying values of β_{12} (case 4).

$\Delta\beta_{12}$(%)	β_{12} (eV)	E_1 (eV)	S_1 (a.u)	E_2 (eV)	S_2 (a.u)	E_3 (eV)	S_3 (a.u)
-50	0.25	4.75	0	4.4069	0.0203	5.8431	2.9798
-40	0.3	4.7	0	4.4272	0.0128	5.8728	2.9870
-30	0.35	4.65	0	4.4466	0.0071	5.9034	2.9929
-20	0.4	4.6	0	4.4652	0.0031	5.9348	2.9971
-10	0.45	4.55	0	4.483	0.0008	5.967	2.9991
-5	0.475	4.525	0	4.4916	0.0002	5.9834	2.9998
-1	0.495	4.505	0	4.4983	$7.29*10^{-6}$	5.9967	2.9998
0	0.5	4.5	0	4.5	0.0000	6	3.0005
1	0.505	4.495	0	4.5017	$7.84*10^{-6}$	6.0033	3.0002
5	0.525	4.475	0	4.5082	0.0002	6.0168	2.9998
10	0.55	4.45	0	4.5163	0.0007	6.0337	2.9991
20	0.6	4.4	0	4.5319	0.0028	6.0681	2.9971
30	0.65	4.35	0	4.5468	0.0062	6.1032	2.9936
40	0.7	4.3	0	4.561	0.0107	6.139	2.9894
50	0.75	4.25	0	4.5746	0.0164	6.1754	2.9836

Table D.34. Eigenvectors of the CI matrix for case 4 where β_{12}=0.25 eV.

	E_1= 4.75 eV	E_2= 4.4069 eV	E_3= 5.8431 eV
A_1	0.7071	0.4544	0.5418
A_2	-0.7071	0.4544	0.5418
A_3	0	-0.7662	0.6426
$\|A_1+A_2+A_3\|^2$	0	0.0203	2.9798

Table D.35. Eigenvectors of the CI matrix for case 4 where β_{12}=0.3 eV.

	E_1= 4.70 eV	E_2= 4.4272 eV	E_3= 5.8728 eV
A_1	0.7071	0.4451	0.5494
A_2	-0.7071	0.4451	0.5494
A_3	0	-0.7770	0.6295
$\|A_1+A_2+A_3\|^2$	0	0.0128	2.9870

Table D.36. Eigenvectors of the CI matrix for case 4 where β_{12}=0.35 eV.

	E_1= 4.65 eV	E_2= 4.4466 eV	E_3= 5.9034 eV
A_1	0.7071	0.4358	0.5568
A_2	-0.7071	0.4358	0.5568
A_3	0	-0.7875	0.6163
$\|A_1+A_2+A_3\|^2$	0	0.0071	2.9929

Table D.37. Eigenvectors of the CI matrix for case 4 where β_{12}=0.40 eV.

	E_1= 4.60 eV	E_2= 4.4652 eV	E_3= 5.9348 eV
A_1	0.7071	0.4266	0.5640
A_2	-0.7071	0.4266	0.5640
A_3	0	-0.7975	0.6033
$\|A_1+A_2+A_3\|^2$	0	0.0031	2.9971

Table D.38. Eigenvectors of the CI matrix for case 4 where β_{12}=0.45 eV.

	E_1= 4.55 eV	E_2= 4.483 eV	E_3= 5.967 eV
A_1	0.7071	0.4174	0.5708
A_2	-0.7071	0.4174	0.5708
A_3	0	-0.8072	0.5902
$\lvert A_1+A_2+A_3\rvert^2$	0	0.0008	2.9991

Table D.39. Eigenvectors of the CI matrix for case 4 where β_{12}=0.475 eV.

	E_1= 4.5250 eV	E_2= 4.4916 eV	E_3= 5.9834 eV
A_1	0.7071	0.4128	0.5741
A_2	-0.7071	0.4128	0.5741
A_3	0	-0.8119	0.5838
$\lvert A_1+A_2+A_3\rvert^2$	0	0.0002	2.9998

Table D.40. Eigenvectors of the CI matrix for case 4 where β_{12}=0.495 eV.

	E_1= 4.5050 eV	E_2= 4.4983 eV	E_3= 5.9967 eV
A_1	0.7071	0.4092	0.5767
A_2	-0.7071	0.4092	0.5767
A_3	0	-0.8156	0.5786
$\lvert A_1+A_2+A_3\rvert^2$	0	$7.29*10^{-6}$	2.9998

Table D.41. Eigenvectors of the CI matrix for case 4 where β_{12}=0.505 eV.

	E_1= 4.495 eV	E_2= 4.5017 eV	E_3= 6.0033 eV
A_1	0.7071	0.4073	0.578
A_2	-0.7071	0.4073	0.578
A_3	0	-0.8174	0.5761
$\lvert A_1+A_2+A_3\rvert^2$	0	$7.84*10^{-6}$	3.000

Table D.42. Eigenvectors of the CI matrix for case 4 where β_{12}=0.525 eV.

	E_1= 4.475 eV	E_2= 4.5082 eV	E_3= 6.0168 eV
A_1	0.7071	0.4037	0.5805
A_2	-0.7071	0.4037	0.5805
A_3	0	-0.821	0.571
$\lvert A_1+A_2+A_3\rvert^2$	0	0.0002	2.9998

Table D.43. Eigenvectors of the CI matrix for case 4 where β_{12}=0.55 eV.

	E_1= 4.45 eV	E_2= 4.5163 eV	E_3= 6.0337 eV
A_1	0.7071	0.3992	0.5836
A_2	-0.7071	0.3992	0.5836
A_3	0	-0.8254	0.5646
$\lvert A_1+A_2+A_3\rvert^2$	0	0.0007	2.9991

Table D.44. Eigenvectors of the CI matrix for case 4 where β_{12}=0.60 eV.

	E_1= 4.40 eV	E_2= 4.5319 eV	E_3= 6.0681 eV
A_1	0.7071	0.3903	0.5896
A_2	-0.7071	0.3903	0.5896
A_3	0	-0.8338	0.5520
$\lvert A_1+A_2+A_3\rvert^2$	0	0.0028	2.9971

Table D.45. Eigenvectors of the CI matrix for case 4 where β_{12}=0.65 eV.

	E_1= 4.35 eV	E_2= 4.5468 eV	E_3= 6.1032 eV
A_1	0.7071	0.3816	0.5953
A_2	-0.7071	0.3816	0.5953
A_3	0	-0.8419	0.5396
$\lvert A_1+A_2+A_3\rvert^2$	0	0.0062	2.9939

Table D.46. Eigenvectors of the CI matrix for case 4 where β_{12}=0.70 eV.

	E_1= 4.30 eV	E_2= 4.5610 eV	E_3= 6.1390 eV
A_1	0.7071	0.3730	0.6008
A_2	-0.7071	0.3730	0.6008
A_3	0	-0.8496	0.5274
$\lvert A_1+A_2+A_3\rvert^2$	0	0.0108	2.9891

Table D.47. Eigenvectors of the CI matrix for case 4 where β_{12}=0.75 eV.

	E_1= 4.25 eV	E_2= 4.5746 eV	E_3= 6.1754 eV
A_1	0.7071	0.3645	0.6059
A_2	-0.7071	0.3645	0.6059
A_3	0	-0.8569	0.5155
$\lvert A_1+A_2+A_3\rvert^2$	0	0.0164	2.9836

Table D.48. Energies and oscillator strengths for varying values of β_{23} (case 5).

$\Delta\beta_{23}$(%)	β_{23} (eV)	E_1 (eV)	S_1 (a.u)	E_2 (eV)	S_2 (a.u)	E_3 (eV)	S_3 (a.u)
-50	0.25	4.3303	0.0220	4.7551	0.0077	5.9146	2.9705
-40	0.3	4.3493	0.0144	4.7069	0.0067	5.9438	2.9787
-30	0.35	4.3669	0.0084	4.6593	0.0059	5.9737	2.9856
-20	0.4	4.3825	0.0039	4.6131	0.0051	6.0045	2.9912
-10	0.45	4.3946	0.0010	4.5695	0.0042	6.0359	2.9950
-5	0.475	4.3985	0.0003	4.5496	0.0036	6.0519	2.9960
-1	0.495	4.3999	0.00001	4.5352	0.0030	6.0649	2.9971
0	0.5	4.4	0.0000	4.5319	0.0028	6.0681	2.9971
1	0.505	4.3999	0.00001	4.5287	0.0027	6.0714	2.9974
5	0.525	4.3981	0.0002	4.5174	0.0019	6.0845	2.9977
10	0.55	4.3918	0.0009	4.5072	0.0010	6.101	2.9981
20	0.6	4.3654	0.0021	4.5	0.0000	6.1346	2.9977
30	0.65	4.3268	0.0027	4.5043	0.0009	6.1688	2.9964
40	0.7	4.2828	0.0028	4.5135	0.0035	6.2037	2.9939
50	0.75	4.2363	0.0027	4.5245	0.0071	6.2392	2.9901

Table D.49. Eigenvectors of the CI matrix for case 5 where β_{23}=0.25 eV.

	E_1= 4.3303 eV	E_2= 4.7551 eV	E_3= 5.9146 eV
A_1	0.7573	0.0717	0.6491
A_2	-0.5431	0.6211	0.5650
A_3	-0.3627	-0.7804	0.5093
$\|A_1+A_2+A_3\|^2$	0.0220	0.0077	2.9705

Table D.50. Eigenvectors of the CI matrix for case 5 where β_{23}=0.30 eV.

	E_1= 4.3493 eV	E_2= 4.7069 eV	E_3= 5.9438 eV
A_1	0.7647	0.0960	0.6372
A_2	-0.5515	0.6091	0.5700
A_3	-0.3334	-0.7872	0.5188
$\|A_1+A_2+A_3\|^2$	0.0144	0.0067	2.9787

Table D.51. Eigenvectors of the CI matrix for case 5 where β_{23}=0.35 eV.

	E_1= 4.3669 eV	E_2= 4.6593 eV	E_3= 5.9737 eV
A_1	0.7696	0.1296	0.6253
A_2	-0.5665	0.5903	0.5750
A_3	-0.2946	-0.7967	0.5277
$\|A_1+A_2+A_3\|^2$	0.0084	0.0059	2.9856

Table D.52. Eigenvectors of the CI matrix for case 5 where β_{23}=0.40 eV.

	E_1= 4.3825 eV	E_2= 4.6131 eV	E_3= 6.0045 eV
A_1	0.7692	0.1792	0.6133
A_2	-0.5926	0.5591	0.5799
A_3	-0.2390	-0.8095	0.5362
$\|A_1+A_2+A_3\|^2$	0.0039	0.0051	2.9912

Table D.53. Eigenvectors of the CI matrix for case 5 where β_{23}=0.45 eV.

	E_1= 4.3946 eV	E_2= 4.5695 eV	E_3= 6.0359 eV
A_1	0.7559	0.2598	0.6014
A_2	-0.6371	0.5021	0.5848
A_3	-0.1507	-0.8252	0.5443
$\|A_1+A_2+A_3\|^2$	0.0010	0.0042	2.9950

Table D.54. Eigenvectors of the CI matrix for case 5 where β_{23}=0.475 eV.

	E_1= 4.3985 eV	E_2= 4.5496 eV	E_3= 6.0519 eV
A_1	0.7383	0.3166	0.5955
A_2	-0.6690	0.4556	0.5872
A_3	-0.0854	-0.8320	0.5482
$\|A_1+A_2+A_3\|^2$	0.0003	0.0036	2.9960

Table D.55. Eigenvectors of the CI matrix for case 5 where β_{23}=0.495 eV.

	E_1= 4.3999 eV	E_2= 4.5352 eV	E_3= 6.0649 eV
A_1	0.7147	0.3743	0.5908
A_2	-0.6991	0.4051	0.5891
A_3	-0.0188	-0.8341	0.5513
$\|A_1+A_2+A_3\|^2$	0.00001	0.0030	2.9971

Table D.56. Eigenvectors of the CI matrix for case 5 where β_{23}=0.505 eV.

	E_1= 4.3999 eV	E_2= 4.5287 eV	E_3= 6.0714 eV
A_1	0.6987	0.4070	0.5884
A_2	-0.7152	0.3746	0.5901
A_3	-0.0197	-0.8331	0.5528
$\|A_1+A_2+A_3\|^2$	0.00001	0.0027	2.9974

Table D.57. Eigenvectors of the CI matrix for case 5 where β_{23}=0.525 eV.

	E_1= 4.3981 eV	E_2= 4.5174 eV	E_3= 6.0845 eV
A_1	0.6562	0.4781	0.5837
A_2	-0.7470	0.3026	0.5920
A_3	0.1064	-0.8245	0.5557
$\|A_1+A_2+A_3\|^2$	0.0002	0.0019	2.9977

Table D.58. Eigenvectors of the CI matrix for case 5 where β_{23}=0.55 eV.

	E_1= 4.3918 eV	E_2= 4.5072 eV	E_3= 6.1010 eV
A_1	0.5846	0.5695	0.5779
A_2	-0.7797	0.1973	0.5943
A_3	0.2244	-0.7980	0.5593
$\|A_1+A_2+A_3\|^2$	0.009	0.0010	2.9981

Table D.59. Eigenvectors of the CI matrix for case 5 where β_{23}=0.60 eV.

	E_1= 4.3654 eV	E_2= 4.5000 eV	E_3= 6.1346 eV
A_1	-0.4235	-0.7071	0.5663
A_2	0.8008	0	0.5989
A_3	-0.4235	0.7071	0.5663
$\|A_1+A_2+A_3\|^2$	0.0021	0	2.9977

Table D.60. Eigenvectors of the CI matrix for case 5 where β_{23}=0.65 eV.

	E_1= 4.3268 eV	E_2= 4.5043 eV	E_3= 6.1688 eV
A_1	-0.3061	-0.7736	0.5548
A_2	0.7883	0.1207	0.6034
A_3	-0.5338	0.6220	0.5729
$\|A_1+A_2+A_3\|^2$	0.0027	0.0009	2.9964

Table D.61. Eigenvectors of the CI matrix for case 5 where β_{23}=0.70 eV.

	E_1= 4.2828 eV	E_2= 4.5135 eV	E_3= 6.2037 eV
A_1	-0.2347	0.8060	0.5435
A_2	0.7724	-0.1849	0.6077
A_3	-0.5902	-0.5624	0.5791
$\|A_1+A_2+A_3\|^2$	0.0028	0.0035	2.9939

Table D.62. Eigenvectors of the CI matrix for case 5 where β_{23}=0.75 eV.

	E_1= 4.2363 eV	E_2= 4.5245 eV	E_3= 6.2392 eV
A_1	-0.1898	0.8250	0.5323
A_2	0.7598	-0.2200	0.6118
A_3	-0.6219	-0.5205	0.5851
$\|A_1+A_2+A_3\|^2$	0.0027	0.0071	2.9901

Table D.63. Energies and oscillator strengths for varying values of β (case 6).

β (eV)	E_1 (eV)	S_1 (a.u)	E_2 (eV)	S_2 (a.u)	E_3 (eV)	S_3 (a.u)
0	5.0000	1.0000	5.1000	1.0000	5.2000	1.0000
0.001	5.0000	0.9704	5.1000	0.9994	5.2000	1.0300
0.005	4.9996	0.8578	5.1000	0.9853	5.2004	1.1569
0.01	4.9986	0.7331	5.0998	0.9426	5.2016	1.3241
0.05	4.9755	0.2291	5.0855	0.3681	5.2389	2.4031
0.1	4.9325	0.0832	5.0461	0.1160	5.3214	2.8009
0.2	4.8370	0.0245	4.9520	0.0295	5.5110	2.9460
0.3	4.7387	0.0114	4.8539	0.0130	5.7074	2.9756
0.4	4.6396	0.0066	4.7549	0.0072	5.9055	2.9863
0.5	4.5401	0.0043	4.6555	0.0046	6.1044	2.9912
1	4.0412	0.0011	4.1566	0.0011	7.1022	2.9977
2	3.0417	0.0003	3.1572	0.0003	9.1011	2.9995

Table D.64. Eigenvectors of the CI matrix for case 6 where β=0.

	E_1= 5.0000 eV	E_2= 5.1000 eV	E_3= 5.2000 eV
A_1	1	0	0
A_2	0	1	0
A_3	0	0	1
$\lvert A_1+A_2+A_3\rvert^2$	1	1	1

Table D.65. Eigenvectors of the CI matrix for case 6 where β=0.001 eV.

	E_1= 5.0000 eV	E_2= 5.1000 eV	E_3= 5.2000 eV
A_1	0.9999	0.0099	0.005
A_2	-0.0099	0.9999	0.01
A_3	-0.0049	-0.0101	0.9999
$\lvert A_1+A_2+A_3\rvert^2$	0.9704	0.9994	1.0300

Table D.66. Eigenvectors of the CI matrix for case 6 where β=0.005 eV.

	E_1= 4.9996 eV	E_2= 5.1000 eV	E_3= 5.2004 eV
A_1	0.9985	0.0473	0.0262
A_2	-0.0486	0.9975	0.051
A_3	-0.0237	-0.0522	0.9984
$\lvert A_1+A_2+A_3\rvert^2$	0.8579	0.9853	1.1569

Table D.67. Eigenvectors of the CI matrix for case 6 where β=0.01 eV.

	E_1= 4.9986 eV	E_2= 5.0998 eV	E_3= 5.2016 eV
A_1	0.9946	0.0884	0.0544
A_2	-0.0937	0.9902	0.1031
A_3	-0.0447	-0.1077	0.9932
$\lvert A_1+A_2+A_3\rvert^2$	0.733078	0.942647	1.32411

Table D.68. Eigenvectors of the CI matrix for case 6 where β=0.05 eV.

	E_1= 4.9755 eV	E_2= 5.0855 eV	E_3= 5.2389 eV
A_1	0.937	0.2238	0.2683
A_2	-0.3213	0.8535	0.4103
A_3	-0.1371	-0.4706	0.8716
$\|A_1+A_2+A_3\|^2$	0.2291	0.3681	2.4031

Table D.69. Eigenvectors of the CI matrix for case 6 where β=0.10 eV.

	E_1= 4.9325 eV	E_2= 5.0461 eV	E_3= 5.3214 eV
A_1	0.8877	0.2332	0.3971
A_2	-0.4271	0.7392	0.5207
A_3	-0.1721	-0.6318	0.7558
$\|A_1+A_2+A_3\|^2$	0.0832	0.1160	2.8009

Table D.70. Eigenvectors of the CI matrix for case 6 where β=0.2 eV.

	E_1= 4.8370 eV	E_2= 4.9520 eV	E_3= 5.5110 eV
A_1	0.846	0.2261	0.4828
A_2	-0.4973	0.6611	0.5618
A_3	-0.1922	-0.7154	0.6718
$\|A_1+A_2+A_3\|^2$	0.0245	0.0295	2.9460

Table D.71. Eigenvectors of the CI matrix for case 6 where β=0.3 eV.

	E_1= 4.7387 eV	E_2= 4.8539 eV	E_3= 5.7074 eV
A_1	0.8288	0.2219	0.5137
A_2	-0.5231	0.6333	0.5703
A_3	-0.1988	-0.7414	0.641
$\|A_1+A_2+A_3\|^2$	0.0114	0.0130	2.9756

Table D.72. Eigenvectors of the CI matrix for case 6 where β=0.4 eV.

	E_1= 4.6396 eV	E_2= 4.7549 eV	E_3= 5.9055 eV
A_1	0.8195	0.2195	0.5295
A_2	-0.5364	0.6193	0.5734
A_3	-0.2021	-0.7538	0.6252
$\|A_1+A_2+A_3\|^2$	0.0066	0.0072	2.9863

Table D.73. Eigenvectors of the CI matrix for case 6 where β=0.5 eV.

	E_1= 4.5401 eV	E_2= 4.6555 eV	E_3= 6.1044 eV
A_1	0.8136	0.218	0.539
A_2	-0.5444	0.6109	0.5748
A_3	-0.204	-0.7611	0.6157
$\|A_1+A_2+A_3\|^2$	0.0043	0.0046	2.9912

Table D.74. Eigenvectors of the CI matrix for case 6 where β=1.0 eV.

	E_1= 4.0412 eV	E_2= 4.1566 eV	E_3= 7.1022 eV
A_1	0.8015	0.2148	0.5581
A_2	-0.5608	0.5941	0.5767
A_3	-0.2077	-0.7752	0.5966
$\|A_1+A_2+A_3\|^2$	0.0011	0.0011	2.9977

Table D.75. Eigenvectors of the CI matrix for case 6 where β=2.0 eV.

	E_1= 3.0417 eV	E_2= 3.1572 eV	E_3= 9.1011 eV
A_1	0.7952	0.2131	0.5677
A_2	-0.569	0.5857	0.5772
A_3	-0.2095	-0.782	0.587
$\|A_1+A_2+A_3\|^2$	0.00028	0.00028	2.9995

Table D.76. Eigenvectors of the CI matrix for case 7 where $\beta_{13}= \beta_{23}=0$.

	E_1= 4.5475 eV	E_2= 5.2000 eV	E_3= 5.5525 eV
A_1	-0.7415	0	0.671
A_2	0.671	0	0.7415
A_3	0	1	0
$\|A_1+A_2+A_3\|^2$	0.0050	1	1.9952

Table D.77. Eigenvectors of the CI matrix for case 7 where $\beta_{13}= \beta_{23}=0.001$ eV.

	E_1= 4.5475 eV	E_2= 5.2000 eV	E_3= 5.5525 eV
A_1	0.7415	0.0026	0.671
A_2	-0.671	0.003	0.7414
A_3	-0.0001	-1	0.004
$\|A_1+A_2+A_3\|^2$	0.0050	0.9888	2.0062

Table D.78. Eigenvectors of the CI matrix for case 7 where $\beta_{13}= \beta_{23}=0.005$ eV.

	E_1= 4.5475 eV	E_2= 5.1999 eV	E_3= 5.5526 eV
A_1	0.7415	0.013	0.6709
A_2	-0.671	0.0152	0.7413
A_3	-0.0005	-0.9998	0.02
$\|A_1+A_2+A_3\|^2$	0.0049	0.9440	2.0512

Table D.79. Eigenvectors of the CI matrix for case 7 where $\beta_{13}= \beta_{23}=0.01$ eV.

	E_1= 4.5475 eV	E_2= 5.1994 eV	E_3= 5.5531 eV
A_1	0.7415	0.026	0.6705
A_2	-0.671	0.0304	0.7408
A_3	-0.0011	-0.9992	0.04
$\|A_1+A_2+A_3\|^2$	0.0048	0.8889	2.1062

Table D.80. Eigenvectors of the CI matrix for case 7 where $\beta_{13}=\beta_{23}$=0.05 eV.

	E_1= 4.5475 eV	E_2= 5.1864 eV	E_3= 5.5661 eV
A_1	0.7417	0.1231	0.6593
A_2	-0.6707	0.1441	0.7276
A_3	-0.0054	-0.9819	0.1894
$\|A_1+A_2+A_3\|^2$	0.0043	0.5108	2.4847

Table D.81. Eigenvectors of the CI matrix for case 7 where $\beta_{13}=\beta_{23}$=0.1 eV.

	E_1= 4.5474 eV	E_2= 5.1505 eV	E_3= 5.6021 eV
A_1	0.7425	0.2142	0.6347
A_2	-0.6698	0.2531	0.6981
A_3	-0.0111	-0.9434	0.3314
$\|A_1+A_2+A_3\|^2$	0.0038	0.2267	2.7696

Appendix E - Supporting Information for “Development of a charge-perturbed particle-in-a-sphere model for nanoparticle electronic structure”

Coordinates of the perturbations for the test cases

- Case 1a: P1(0,0,4.5); P2 (0,0,-4.5)
- Case 1b: P1(-1.2287,-2.3450,-3.6388); P2 (1.2287,2.3450,3.6388)
- Case 2: P1(0,4.5,0); P2 (0,-4.5,0); P3(4.5,0,0); P4 (-4.5,0,0)
- Case 3: P1(0,4.5,0); P2 (0,-4.5,0); P3(4.5,0,0); P4 (-4.5,0,0); P5(0,0,4.5); P6 (0,0,-4.5)
- Case 4: P1(0,4.5,0); P2 (0,-4.5,0); P3(4.5,0,0); P4 (-4.5,0,0); P5(3.18198,3.18198,0); P6 (3.18198, -3.181980); P7(-3.18198,-3.18198,0); P8 (-3.18198, 3.18198,0)
- Case 5: P1(0,4.5,0); P2 (0,-4.5,0); P3(4.5,0,0); P4 (-4.5,0,0); P5(0,0,4.5); P6 (0,0,-4.5); P7(-3.18198,-3.18198,0); P8 (-3.18198, 3.18198,0); P9(3.18198,3.18198,0); P10 (3.18198, -3.181980,0); P11(0,3.18198,3.18198); P12 (0,3.18198, -3.181980); P13(0,-3.18198,-3.18198); P14(0,-3.18198, 3.18198); P15(3.18198,0,3.18198); P16 (3.18198,0, -3.181980); P17(-3.18198,0,-3.18198); P18(-3.18198,0,3.18198)

Figure E-1. A) P orbitals of test case 1a and B) P orbitals of test case 1b. Green: Orbitals. Magenta: Point charge perturbations.

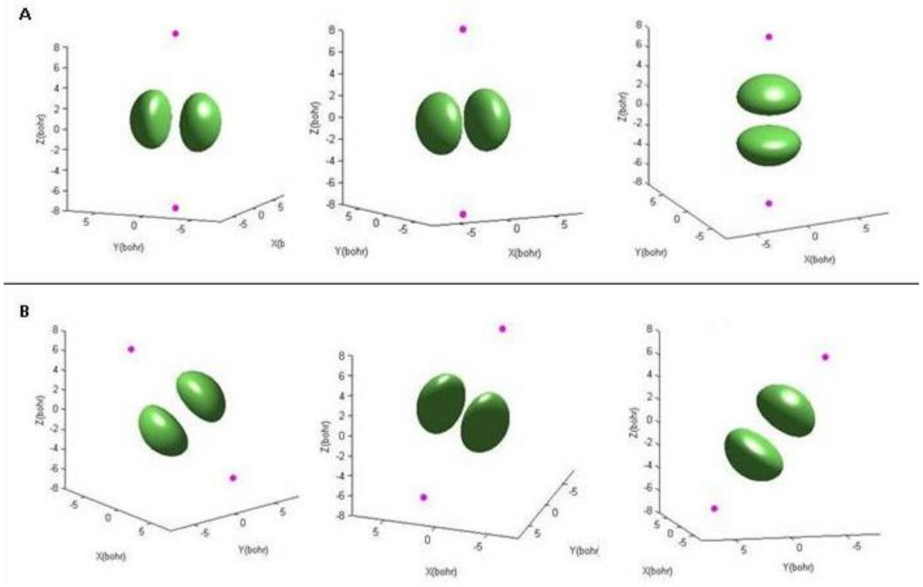

Appendix F - Supporting information for "Effects of Silver Doping on the Geometric and Electronic Structure and Optical Absorption Spectra of the $Au_{25-n}Ag_n(SH)_{18}^-$ (n = 1, 2, 4, 6, 8, 10, 12) Bimetallic Nanoclusters"

Table F.1. $Au_{24}Ag(SH)_{18}^-$ bond lengths calculated at the Xα/TZP level of theory.

Isomer	Center-Surface (Å)	Sulfur-adjacent core atom (Å)
1a (Surface)	2.79 (±0.04)	2.42 (±0.09)
1b (Unit)	2.79 (±0.02)	2.41 (±0.01)
1c (Center)	2.78 (±0.01)	2.42 (±0.01)

Table F.2. $Au_{23}Ag_2(SH)_{18}^-$ average bond lengths (in Å) calculated at the Xα/TZP level of theory.

	Opposite	Non-adjacent	Adjacent
Au(center)-Ag	2.85	2.83	2.81
Au(center)-Au (surface)	2.77	2.78	2.78
S-Ag	2.53	2.51	2.51
S-Au (surface)	2.42	2.41	2.41

Figure F-1. Excitation spectrum of $Au_{25}(SH)_{18}^-$ at the LB94/TZP level of theory.

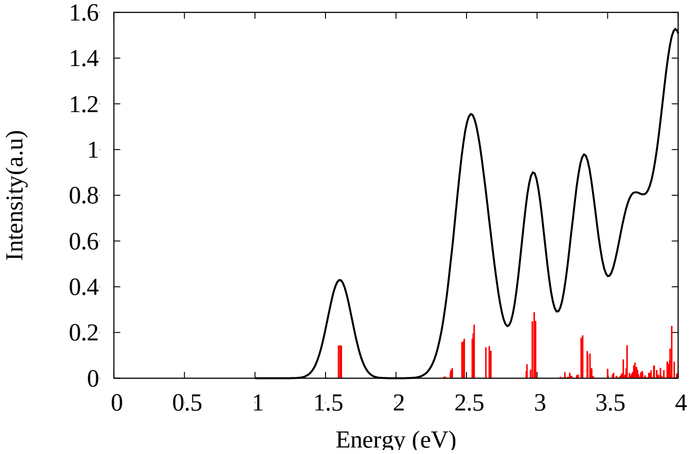

Figure F-2. Geometries of the $Au_{21}Ag_4(SH)_{18}^-$ isomers at the Xα/TZP level of theory.

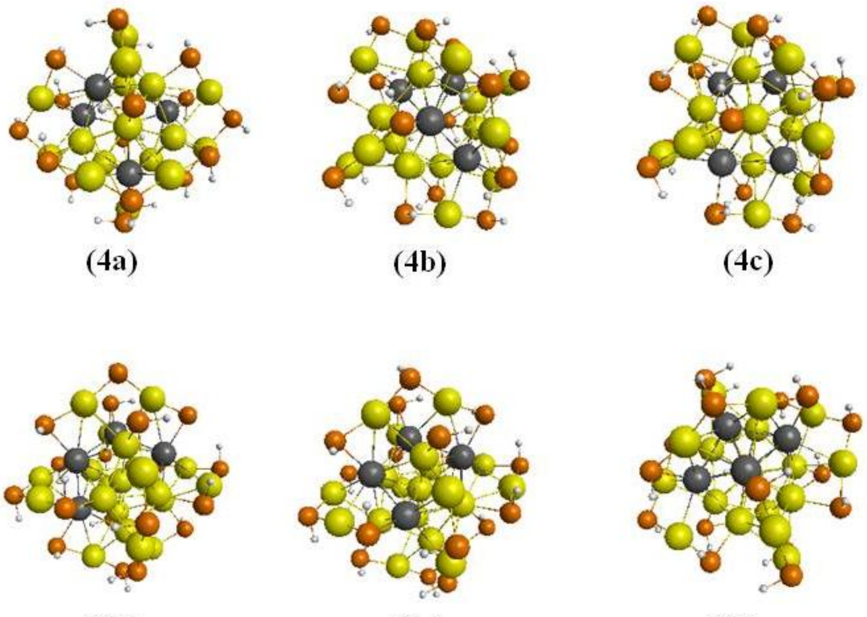
(4a) (4b) (4c)

(4d) (4e) (4f)

Figure F-3. Geometries of the $Au_{19}Ag_6(SH)_{18}^-$ isomers at the Xα/TZP level of theory

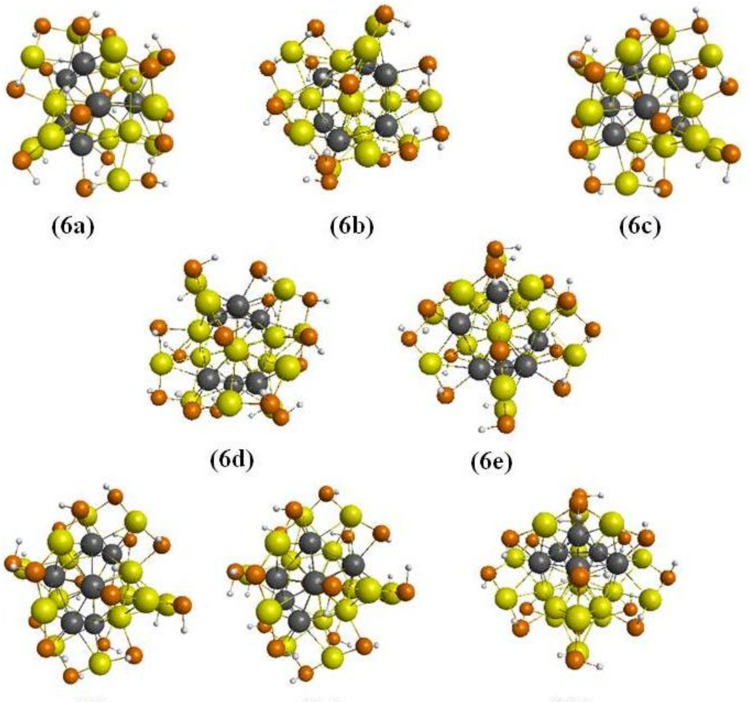
(6a) (6b) (6c)

(6d) (6e)

(6f) (6g) (6h)

Figure F-4. Geometries of the $Au_{17}Ag_8(SH)_{18}^-$ isomers at the Xα/TZP level of theory.

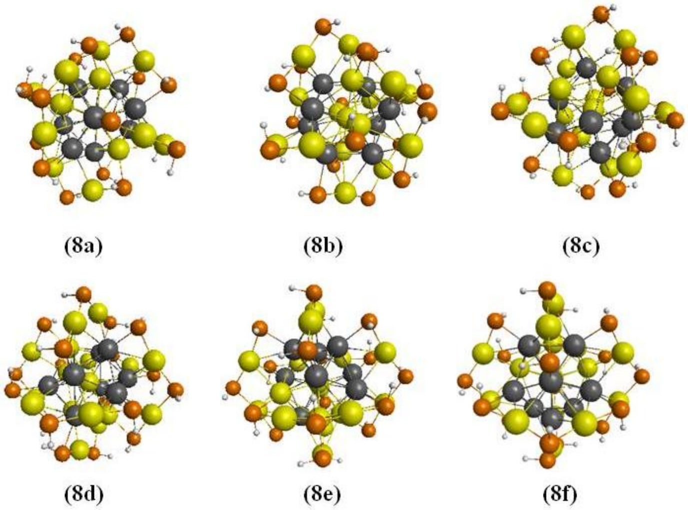
(8a) (8b) (8c)

(8d) (8e) (8f)

Figure F-5. Geometries of the $Au_{15}Ag_{10}(SH)_{18}^-$ isomers at the Xα/TZP level of theory.

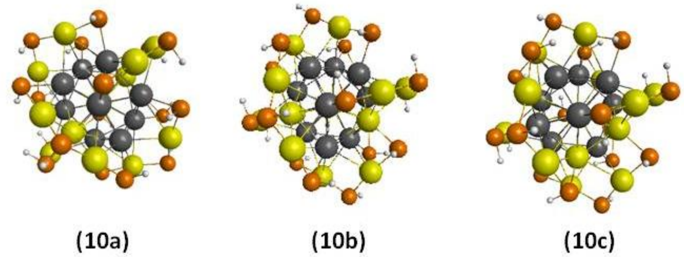
(10a) (10b) (10c)

Figure F-6. Excitation spectra of the A) 4a, B) 4b and C) 4c D) 4d E) 4e and F) 4f $Au_{21}Ag_4(SH)_{18}^-$ isomers at the LB94/TZP level of theory.

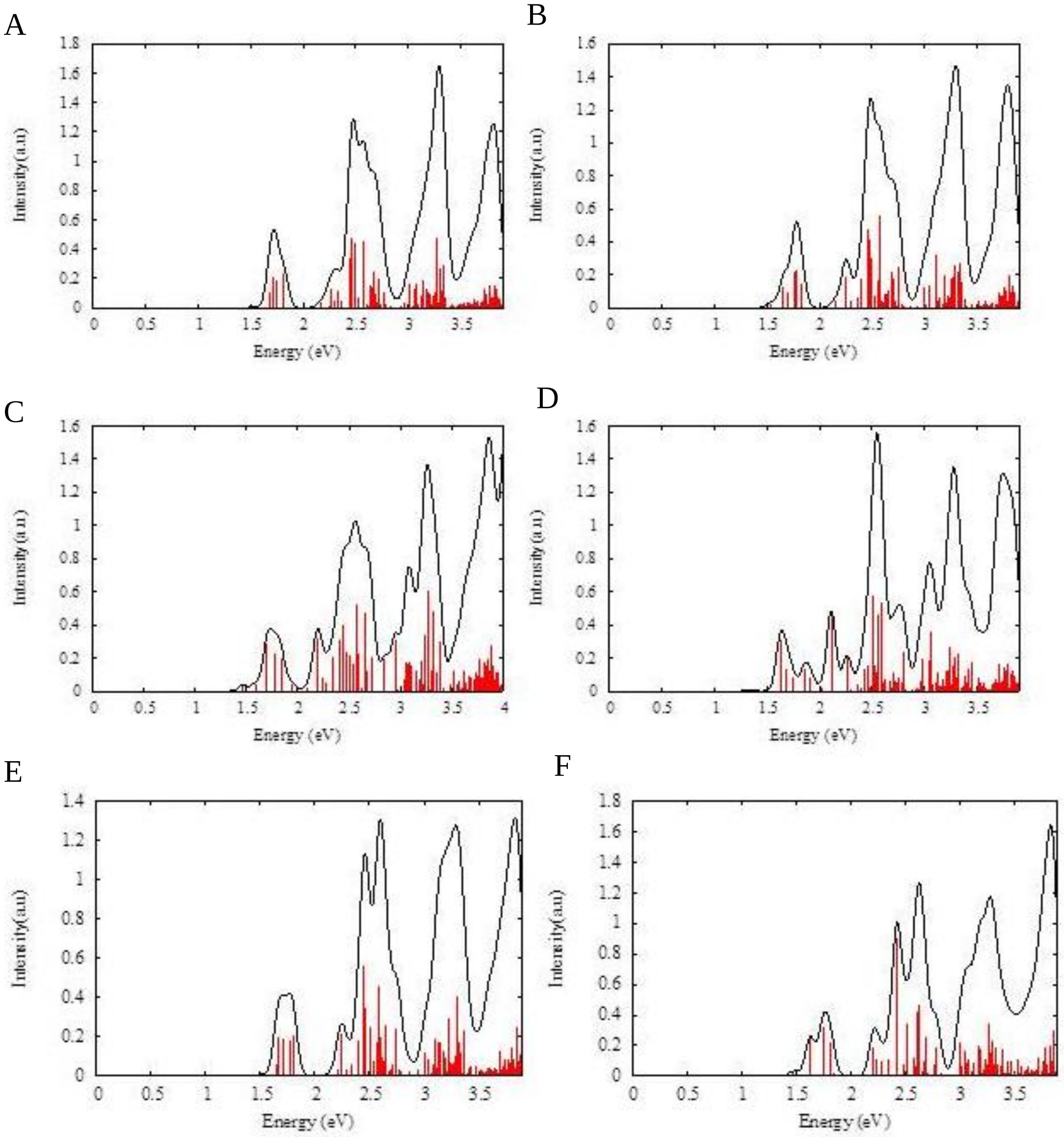

Figure F-7. Excitation spectra of the A) 6a, B) 6b and C) 6c D) 6d E) 6e and F) 6f G) 6g and H) 6h $Au_{19}Ag_6(SH)_{18}^-$ isomers at the LB94/TZP level of theory.

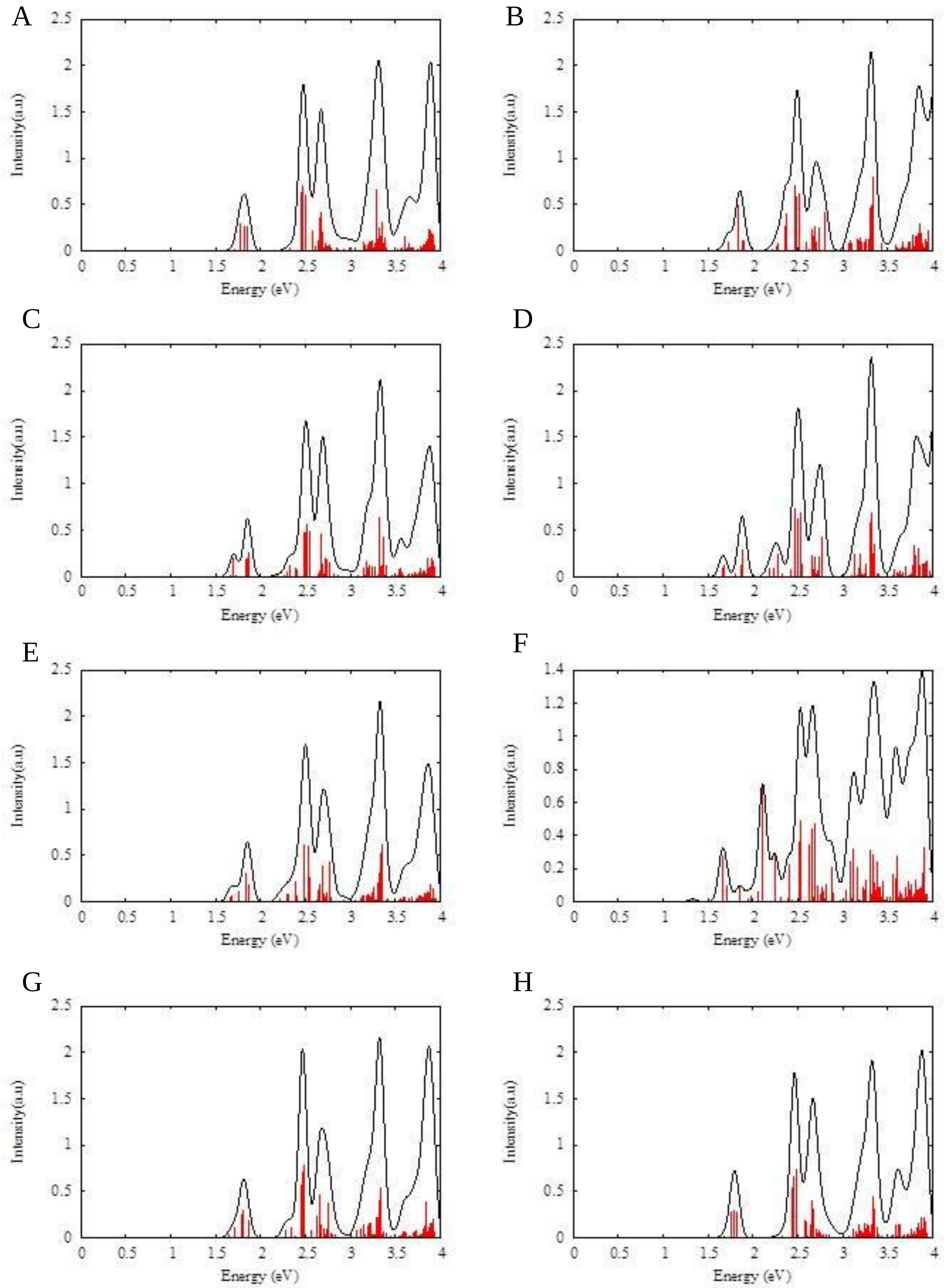

Figure F-8. Excitation spectra of the A) 8a, B) 8b and C) 8c D) 8d E) 8e and F) 8f $Au_{17}Ag_8(SH)_{18}^-$ isomers at the LB94/TZP level of theory.

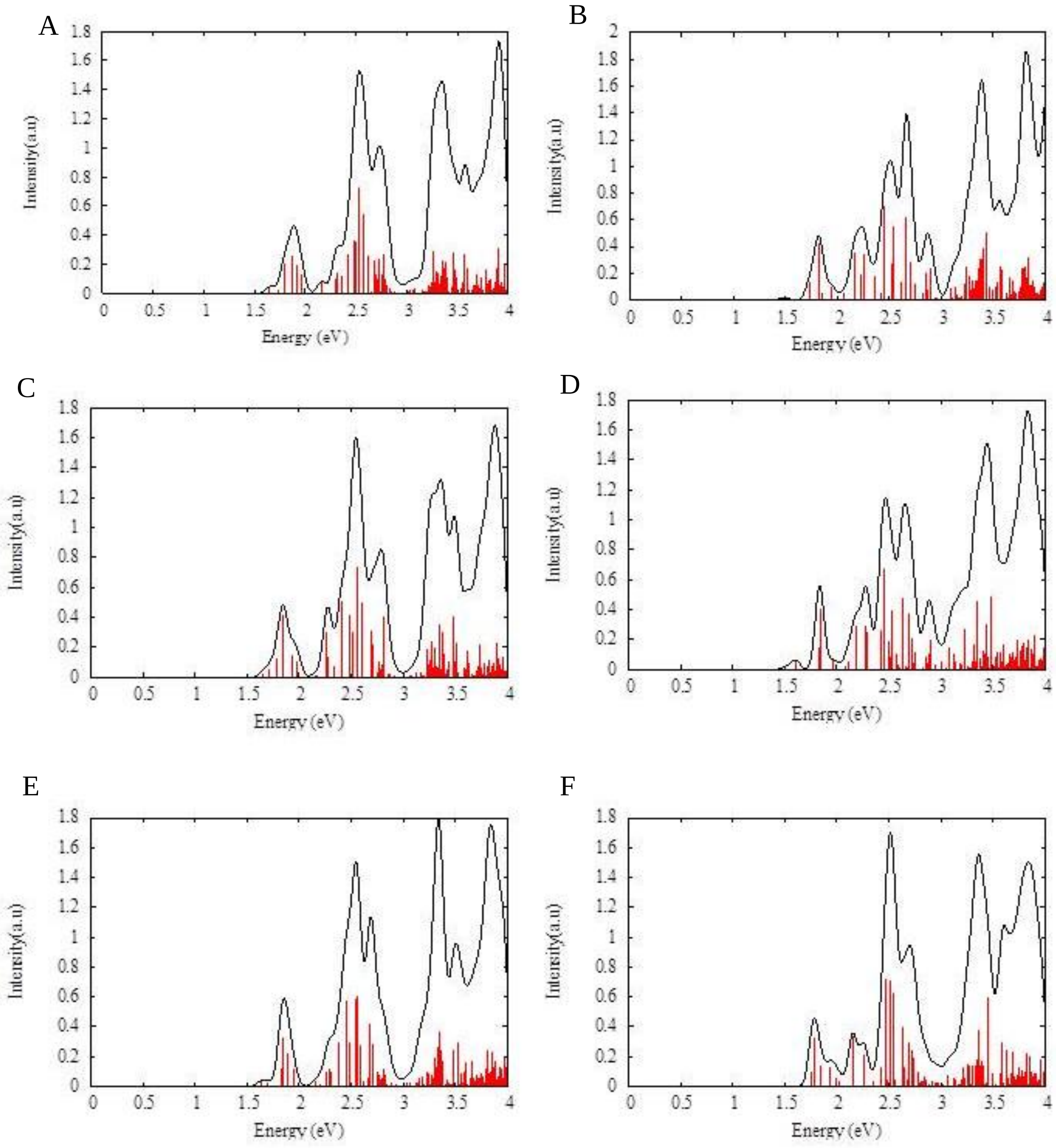

Figure F-9. Excitation spectra of the A) 10a, B) 10b and C) 10c $Au_{15}Ag_{10}(SH)_{18}^{-}$ isomers at the LB94/TZP level of theory.